Dissertation

submitted to the

Combined Faculties of the Natural Sciences and Mathematics

of the

Ruperto-Carola-University of Heidelberg, Germany

for the degree of

Doctor of Natural Sciences

Put forward by

Nikolas Dimitriadis

born in: Waiblingen

Oral examination: 11.07.2018

Real-time multispectral fluorescence and reflectance imaging for intraoperative applications

Referees:

Prof. Dr. Marcus Motzkus
Prof. Dr. Bernd Jähne

ABSTRACT

Fluorescence guided surgery supports doctors by making unrecognizable anatomical or pathological structures become recognizable. For instance, cancer cells can be targeted with one fluorescent dye whereas muscular tissue, nerves or blood vessels can be targeted by other dyes to allow distinction beyond conventional color vision.

Consequently, intraoperative imaging devices should combine multispectral fluorescence with conventional reflectance color imaging over the entire visible and near-infrared spectral range at video rate, which remains a challenge.

In this work, the requirements for such a fluorescence imaging device are analyzed in detail. A concept based on temporal and spectral multiplexing is developed, and a prototype system is build. Experiments and numerical simulations show that the prototype fulfills the design requirements and suggest future improvements.

The multispectral fluorescence image stream is processed to present fluorescent dye images to the surgeon using linear unmixing. However, artifacts in the unmixed images may not be noticed by the surgeon. A tool is developed in this work to indicate unmixing inconsistencies on a per pixel and per frame basis.

In-silico optimization and a critical review suggest future improvements and provide insight for clinical translation.

ZUSAMMENFASSUNG

Fluoreszenz kann Chirurgen während Operationen unterstützen, indem ansonsten mit bloßem Auge nicht erkennbare anatomische Strukturen sichtbar gemacht werden. So können zum Beispiel Tumorzellen mit einem Farbstoff markiert werden und Muskelgewebe, Nervenstränge oder Blutgefäße mit anderen Farbstoffen gefärbt werden. Somit kann zwischen den verschiedenen Gewebearten besser differenziert werden.

Die gleichzeitige Aufnahme von Fluoreszenz- und konventionellen Farbbildern im sichtbaren und nahinfrarot Bereich in Videorate stellt nach wie vor eine Herausforderung dar.

Diese Arbeit analysiert und spezifiziert zuerst die Anforderungen an ein solches Gerät. Daraufhin wird ein Konzept, welches auf spektralem und zeitlichem Multiplexing beruht, entwickelt und ein Prototyp wird realisiert. Experimente und numerische Simulationen belegen, dass der Prototyp die Anforderungen erfüllt.

Die multispektralen Bilddaten müssen verarbeitet werden, um den Chirurgen mit den diagnostisch relevanten Informationen versorgen zu können. Artefakte in diesen Bildern werden vom Chirurgen unter Umständen nicht erkannt. Eine neuartige Methode wird entwickelt, welche Inkonsistenzen in den diagnostischen Informationen für jeden Pixel auf Basis eines einzelnen Bildes vorhersagt.

Die numerische Optimierung von Systemparametern und eine abschließende kritische Betrachtung liefern Ansatzpunkte für zukünftige Verbesserungen und zeigen den Weg zur klinischen Anwendung auf.

CONTENTS

PUBLICATIONS

PEER-REVIEWED PUBLICATIONS

- Nikolas Dimitriadis, Bartłomiej Grychtol, Martin Theuring, Tobias Behr, Christian Sippel, and Nikolaos C. Deliolanis. “Spectral and temporal multiplexing for multispectral fluorescence and reflectance imaging using two color sensors”. In: *Optics Express* 25.11 (May 2017), p. 12812. DOI:10.1364/OE.25.012812.
- Nikolas Dimitriadis, Bartłomiej Grychtol, Lars Maertins, Tobias Behr, George Themelis, and Nikolaos C. Deliolanis. “Simultaneous real-time multicomponent fluorescence and reflectance imaging method for fluorescence-guided surgery”. In: *Optics Letters* 41.6 (Mar. 2016), p. 1173. DOI:10.1364/OL.41.001173.

PATENT APPLICATIONS

- Nikolas Dimitriadis and Nikolaos Deliolanis. “Methods And Means For Multispectral Imaging”. Patent WO 2015/185662. Dec. 2015.
- Nikolas Dimitriadis and Nikolaos Deliolanis. “Methods And Means For Multispectral Imaging”. Patent WO 2015/185661. Dec. 2015.

CONFERENCE PRESENTATIONS

- Nikolas Dimitriadis, Martin Theuring, Bartłomiej Grychtol, Lars Maertins, Matthias Kolibabka, Eric Brandhorst, Hans-Peter Hammes, and Nikolaos C. Deliolanis. “Single-Sensor Real-Time Multispectral Fluorescence and Color Imaging Platform for Image Guided Surgery.” In: *SPIE BiOS, Molecular-Guided Surgery: Molecules, Devices, and Applications II* BO112-1 (2016).
- Nikolas Dimitriadis, Bartłomiej Grychtol, Martin Theuring, Tobias Behr, and Nikolaos C. Deliolanis. "Real-time intraoperative multispectral fluorescence and color imaging platform for the visible and near infra-red region." In: *SPIE BiOS, Advanced Biomedical and Clinical Diagnostic and Surgical Guidance Systems XIV* BO201-43 (2016).

- Nikolas Dimitriadis, Martin Theuring, Bartłomiej Grychtol, Max Kriegmair, and Nikolaos C. Deliolanis. "A system for multispectral real-time fluorescence guided cystoscopy." In: *Computer Assisted Radiology and Surgery Proceedings of the 30th International Congress and Exhibition* 1–286 (2016). DOI:10.1007/s11548-016-1412-5.
- Nikolas Dimitriadis, Bartłomiej Grychtol, Martin Theuring, Tobias Behr, Lars Maertins, and Nikolaos C. Deliolanis. "Real-time multispectral fluorescence and reflectance imaging using a single sensor camera for surgery." In: *European Molecular Imaging Meeting* 12/2 #77 (2015).

NOMENCLATURE

5-ALA 5-aminolevulinic acid

5-ALA 5-aminolevuliniv acid

AOTF acousto optical tunable filter

CASSI coded aperture snapshot imager

CMOS complementary metal-oxide-semicoductor

CT computed tomography

CTIS computed tomography image spectroscopy

EMA European Medicines Agency

FDA Food and Drug Administration

FITC fluorescein isothiocyanate

FOV field of view

FPGA fiel programmable gate array

HSI hyperspectral imaging

ICA independent component analysis

ICCD intensified CCD

ICG indocyanine green

IFS integral field spectrometry

IMS image mapping spectrometry

LCTF liquid crystal tunable filter

MEMS micomechanical mirror scanning devices

MEMS micro-electromechanical systems

MP megapixel

MRI magnetic resonance imaging

MRS magnetic resonance spectroscopy

MSBS multispectral beam splitting

NMF nonnegative matrix factorization

PARAFAC parallel factor analysis

PCA principal component analysis

PET positron emission tomography

PPIX protoporphyrin IX

US ultrasound

SYMBOLS AND UNITS

MATHEMATICAL SYMBOLS

λ	wavelength
c	detection channel
f	fluorescent dye
$q_c(\lambda)$	spectral quantum efficiency for a sensor channel c at wavelength λ
$\eta(\lambda_c)$	relative detection efficiency for a dye with emission center wavelength λ_c
$e(\lambda)$	normalized emission spectrum
$\boldsymbol{m}_L$	color correction Luther matrix
δ_S	Luther error
$\boldsymbol{m}_M$	color correction Munsell matrix
$\Delta E_{00}(C_1, C_2)$	color difference between colors C_1 and C_2 according to CIEDE2000
$\overline{\Delta E_{00}}$	average color difference CIEDE2000 of a fixed set of Munsell colors
$s(c, \lambda)$	spectral sensitivity with respect to incident light in units of power spectral density
$r(t, \lambda)$	spectral reflectivity of color tone t at wavelength λ
$L(l, \lambda)$	illuminant l spectrum at wavelength λ in units of power spectral density
$A_S(l, t, c)$	sensor response of sensor channel c to the Munsell color t illuminated with light l
$B_S(l, t, c)$	response of the channel c of sensor S to the Munsell colors t illuminated with light l in XYZ color space.
Φ	light flux
$\boldsymbol{\kappa}(f)$	spectral signature of a fluorescent dye f
$\boldsymbol{m}$	mixing matrix
$m(c, f)$	mixing matrix coefficients

$\boldsymbol{u}$	unmixing matrix
$u(f,c)$	unmixing matrix coefficients
ξ	pixel location specified by one pixel row and column
$\boldsymbol{Y}(\xi)$	multispectral image data at location ξ
$\boldsymbol{X}(\xi)$	multispectral fluorescence component data at location ξ
$\boldsymbol{\Sigma}_Y(\xi)$	covariance matrix of image $\boldsymbol{Y}(\xi)$
$\Sigma_Y(c,c,\xi)$	covariance matrix elements of matrix $\boldsymbol{\Sigma}_Y(\xi)$ for channels c
$\boldsymbol{\mu}_Y(\xi)$	mean distribution parameter image for $\boldsymbol{Y}(\xi)$
$\hat{\boldsymbol{\mu}}_Y(\xi)$	estimated distribution parameter mean for $\boldsymbol{Y}(\xi)$
SNR	signal to noise ratio
$\boldsymbol{R}_Y(\xi)$	unmixing residuals for image data $\boldsymbol{Y}(\xi)$ at location ξ
$\boldsymbol{\varepsilon}_Y(\xi)$	standardized unmixing residual for image data $\boldsymbol{Y}(\xi)$ at location ξ
$T_Y(\xi)$	T-score of image data $\boldsymbol{Y}(\xi)$ for pixel location ξ
$\mathcal{P}\left(\mu\right)$	Poisson distribution with parameter μ
$\mathcal{N}\left(\mu,\Sigma\right)$	normal distribution with parameters mean μ and variance Σ
$\chi^2(k)$	chi-squared distribution with parameter k as number of degrees of freedom

UNITS

M	molar
m	meter
J	joule
s	second
W	watt
e^-	electron
lp	line pair
deg	angular degree
fps	frames per second
px	pixel

MP mega pixel; number of data points of a multispectral data set; it is common practice to refer to a number of data points as »resolution«, for example »the sensor has a resolution of 5 MP«, but it means that the sensor records images with 5 million data points

UNIT PREFIXES

p pico, $\times 10^{-12}$

n nano, $\times 10^{-9}$

µ micro, $\times 10^{-6}$

m milli, $\times 10^{-3}$

c centi, $\times 10^{-2}$

k kilo, $\times 10^{3}$

M mega, $\times 10^{6}$

G giga, $\times 10^{9}$

1 INTRODUCTION

Cancer is one of the major causes of death due to noncommunicable diseases worldwide. Every year around 2‰ of the world population are diagnosed with cancer and in 2010 1 out of 7 deaths was caused by cancer [1, 2]. This highlights the need to develop novel treatments. Three major treatments exist and complement each other: surgical cancer resection, pharmaceutical therapy, and radiotherapy.

For cancer diagnostics, a variety of volumetric 3D imaging techniques have been clinically established: computed tomography (CT), positron emission tomography (PET), magnetic resonance spectroscopy (MRS), magnetic resonance tomography (MRI), and ultrasound (US) [3, 4]. These imaging techniques revolutionized diagnostic procedures and improved treatment planning and evaluation.

During cancer resection surgeons rely for the most part on their vision [5]. But the tissue that needs to be resected is not always easy to distinguish from the surrounding tissue by eye as illustrated in Figure 1.1. In fact, hemoglobin is a very strong absorber and often dominates the appearance of tissue. As a result, some structures like nerve tracts may inadvertently be severed if they remain hidden. Also, scar tissue, which is typically caused by repetitive surgeries can be hard to distinguish from cancer tissue [6]. However, accurate cancer boundary identification is important because complete cancer resection is beneficial for the outcome for many cancer types [7–11].

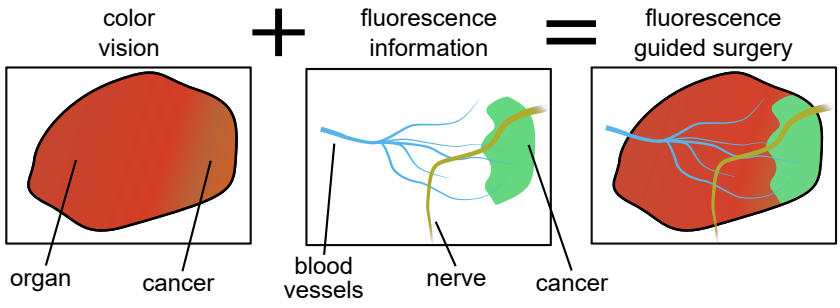

Figure 1.1: Impact of fluorescence guided surgery: Schematic illustration of an organ with cancer tissue, nerves and blood vessels. In the color image, which corresponds to the view of the surgeon, it is very challenging to identify the cancer. Both nerves and blood vessels cannot be identified. In fluorescence guided surgery, cancer tissue, nerves, and blood vessels are labeled with different fluorescent dyes. Only these dyes are seen in the fluorescence image. The final image which is presented to the surgeon during fluorescence guided surgery fuses the color image with information from the fluorescence image.

Consequently, advanced imaging technologies are required to support the surgeon. Though, integrating the established imaging technologies (CT, MRI, MRS, PET, and US) into the surgical work-flow is challenging – all the information generated by these techniques needs to be combined in real-time with what the surgeon can see [6].

Fluorescence guided surgery has the potential to close that gap. It enhances the color vision of a doctor with functional, anatomical or pathological information by fluorescence imaging. For example, it can help surgeons to accurately resect a cancer without damaging a hidden nerve. It has therefore become increasingly popular and gained acceptance in the medical community over the last decade. Nevertheless, only few applications have been clinically established so far and still lack of flexible targeting strategies [5, 12–16].

Recent advances in biomedical research demonstrate the capacity of fluorescence guidance in combination with specific targeting strategies. Clinical trials combining modern dyes with antibodies are awaited [17–21].

One example of a clinical scenario in which the labeling of cancer tissue supports the surgeon to distinguish cancerous from healthy tissue is shown in Figure 1.2A. The experiment, published by van Dam *et al.*, combines color imaging with a specific antibody to identify ovarian cancer tissue using a single fluorescent dye [22].

But the capabilities of clinical fluorescence imaging go far beyond imaging one single dye. Additional dyes facilitate identification of different structures. For example, Whitney *et al.* marked cancer tissue with one dye and labeled nerve tissue with a second dye to visualize both tissues separately, as shown in Figure 1.2B [23].

In all medical targeting techniques, dye molecules attach to every tissue type when circulating in the body with a different affinity. This can result in non-perfect labeling. To overcome this issue, Tichauer *et al.* combine two dyes: one with affinity to cancer and another dye with no affinity to the cancer [24]. Figure 1.2C shows a color image of the cancer, the distributions of both dyes and a combined fluorescence image with an improved cancer-to-background ratio.

With numerous novel staining techniques and dyes being developed and pushed towards clinical translation, which challenges remain to make fluorescence guided surgery a clinical gold standard?

On the one hand, the biomedical targeting techniques need to be further translated into clinical practice and the performance needs to be evaluated in clinical studies. On the other hand, the sophisticated imaging scenarios call for advanced instrumentation with seamless integration into clinical scenarios. Thus, a new imaging method is required which delivers combined color and fluorescence images in real-time to the surgeon.

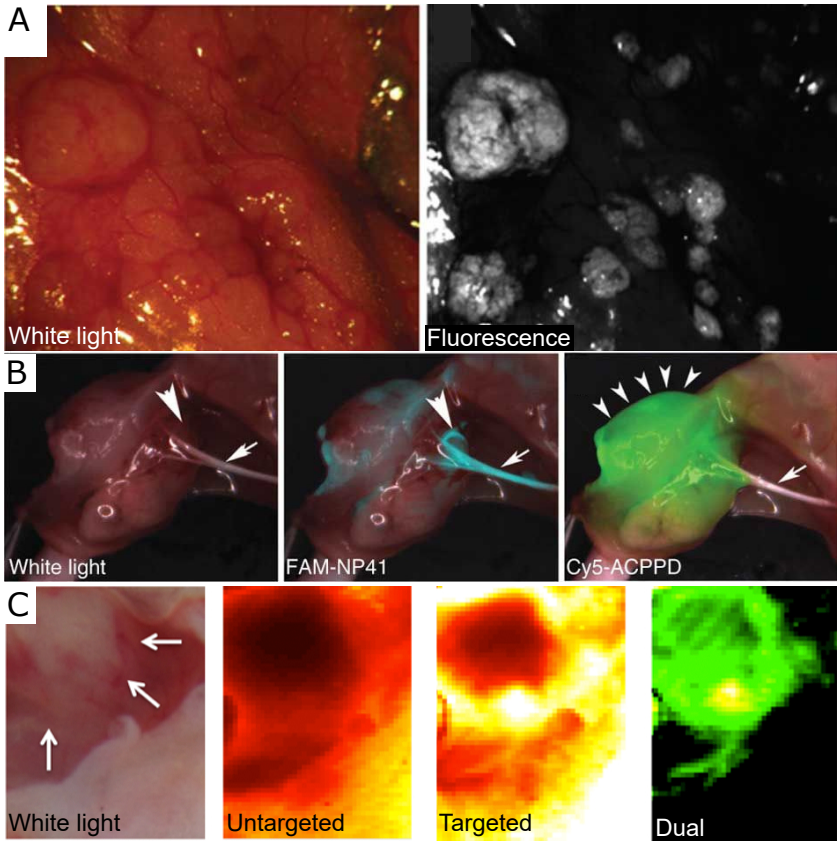

Figure 1.2: Clinical and preclinical example images demonstrating the potential of fluorescence guided surgery. A) White light color image and fluorescence image *ex vivo* of human tissue containing ovarian carcinoma labeled with the fluorescent dye FITC [22]. Adapted by permission from Macmillan Publishers Ltd: Nature Medicine [22], copyright 2011. B) Dual labeling scenario to differentiate nerve and cancer tissue: The white light color image on the left shows part of the sciatic nerve (white arrow) in a mouse with a mammary cancer. The center image displays the color image combined with the nerve fluorescence signal (FAM-NP41) in cyan. The right image shows the color image combined with the cancer fluorescence (Cy5-ACPPD) in green [23]. Adapted by permission from Macmillan Publishers Ltd: Nature Biotechnology [23], copyright 2011. C) Improved cancer to background ratio by combining the information of a targeted and an untargeted fluorescent label of a brain cancer in a mouse model: Cancerous and healthy tissue does not show a clear boundary (white arrows) in the white light color image. Both targeted and untargeted fluorescence images do not have good contrast between cancer and background, whereas the image using the combined information of both dyes exhibits best cancer to background ratio [24]. Adapted version reproduced from Kenneth M. Tichauer, Kimberley S. Samkoe, Kristian J. Sexton, Jason R. Gunn, Tayyaba Hasan, Brian W. Pogue, "Improved cancer contrast achieved by single time point dual-reporter fluorescence imaging," Journal of Biomedical Optics 17(6), 066001 (5 June 2012).

First-generation fluorescence imaging devices, used in surgical microscopy or endoscopy, produce either fluorescence or reflectance color images. Also, only one single fluorescent dye is typically imaged. Recent experimental devices allow multispectral fluorescence image acquisition but at the expense of imaging speed and color-imaging capabilities.

These limitations call for novel imaging technologies that combine multispectral fluorescence detection with high-quality color-imaging in real-time.

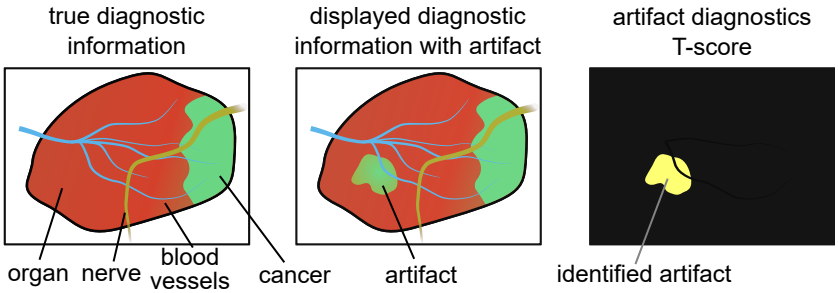

Figure 1.3: Artifact diagnostics: A) Fluorescence guided surgery enhances the color image for example by highlighting cancer tissue, hidden nerves, and blood vessels. B) Perturbations in the fluorescence image data may result in artifacts in the diagnostic information, which is displayed to the surgeon. C) Unmixing artifacts can be identified by the developed T-score metrics.

This thesis describes a novel imaging method and presents a prototype system for real-time multispectral fluorescence and color imaging for surgical applications.

This short introduction to the topic is followed by a review of the state-of-the-art and of the limitations of fluorescence guided surgery in Chapter 2. In addition, it introduces the theoretical basics of color and fluorescence imaging.

The question of *how* the novel system should be designed and *why* it should be designed that way is answered in detail in Chapter 3. As a result, a set of design requirements is fixed. Hereafter, different imaging methods are discussed in detail and a selection for the prototype system is made. Subsequently, Chapter 4 introduces the developed system concept and describes the technical realization of the prototype system.

Chapter 5 investigates *if* each of the design requirements is fulfilled. All in all, the system is analyzed conducting experiments and numerical simulations. The requirements are grouped into four parts. First, numerical simulations analyze the spectral system sensitivity. Second, the ability of the system to reproduce colors is numerically assessed. Third, the capabilities of the system to image and unmix fluorescence are experimentally tested. Finally, the optics of the prototype system

are inspected. Each requirement is analyzed in a separate section that is divided into a methods, results and discussion part.

Owing to the impact of noise in fluorescence imaging, Chapter 6 develops an understanding of noise propagation through unmixing as well as a model to estimate noise based on a single image. As a result, a metric (called T-score) is developed to evaluate unmixing artifacts. Unmixing artifacts pose an obstacle to the clinical introduction of multispectral imaging, since the reliability of the fluorescence information needs to be guaranteed. Figure 1.3 illustrates a hypothetical scenario in which the T-score helps identify unmixing artifacts.

Chapter 7 answers the question of *how* much the system can be improved. The signal to noise ratio of the fluorescence images is optimized by finding the optimal combination of dyes and filter configurations.

The final Chapter 8 discusses whether the design requirements are fulfilled and gives an outlook on future work. Limitations of the system are discussed, and the concept of an ideal device is presented. The system is also compared with related work in retrospect. An outlook summarizes future research directions and shows the next steps towards clinical translation of the system. Finally, conclusions about the impact and the main achievements of the thesis are drawn.

2 RELATED WORK AND THEORY

The use of fluorescence imaging during surgery has first been reported in 1948 to visualize features beyond human color vision [25]. Since then, the field has considerably evolved. In 1958 indocyanine green as first infrared dye was used to study liver perfusion [6]. In 1994 methylene blue has been reported to highlight sentinel lymph nodes during breast cancer resection [26] and in 1998 fluorescence guided surgery for glioblastoma brain cancer resection was introduced and eventually evaluated in a randomized multi-center clinical trial [12, 27, 28]. Since then, the field has experienced a technological boost: surgical microscopes and even endoscopes for fluorescence imaging are commercially available. Fluorescence guided surgery has become clinical practice in several fields.

At the same time, novel staining techniques and modern dyes were developed in biomedical research. These advances have the potential to revolutionize surgical procedures by visualizing features for the surgeon which would otherwise be invisible. However, new instrumentation approaches to complement the biomedical advances are required. As a result, more and more image acquisition techniques emerged and have been published.

This chapter gives an overview of the state-of-the-art in fluorescence guided surgery. First, Section 2.1 gives an overview on clinical applications and recent advances in research. Subsequently, Section 2.2 summarizes the related work on instrumentation. The chapter subsequently introduces the theory of color imaging in Section 2.4 and of fluorescence imaging in Section 2.5. The mathematical description of fluorescence detection and unmixing can be found in Section A.1.

2.1 CURRENT STATE OF FLUORESCENCE IN SURGERY

2.1.1 *Fluorescence guided surgery*

During the last decades, intraoperative fluorescence imaging has been introduced to clinical practice in various disciplines [15, 38, 39]. Neurosurgeons have for example the opportunity to visualize cancer tissue during resection or urologists can also specifically stain bladder cancer tissue for cystoscopic resection [12–14]. Another example for a clinically established procedure is perfusion monitoring for anastomosis of the big bowel or for reconstructive surgery [40, 41].

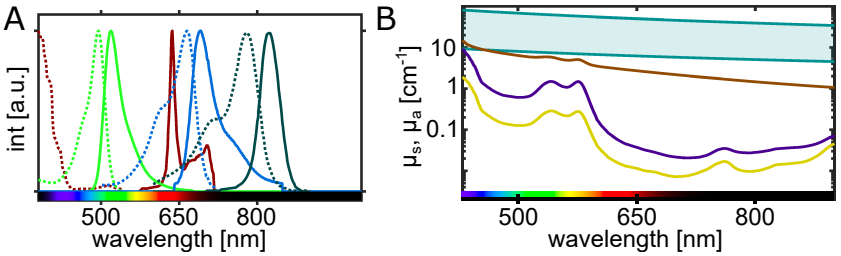

Figure 2.1: A) Excitation (dotted lines) and emission spectra (solid lines) of the clinically relevant fluorescent dyes fluorescein, methylene blue, protoporphyrin IX and indocyanine green. B) Estimated scattering and absorption coefficient in tissue. Range of minimal (lung [29]) and maximum (epidermis [30]) scattering coefficient μ_a at 500 nm for tissue with a simplified model [31]. Absorption coefficient μ_a of breast tissue, abdominal tissue and skin with an simplified model [31]. Breast tissue absorption μ_a is simulated with a hemoglobin concentration of 23.6 µM, oxygen saturation of 67.6%, 14.4% relative water and 65.6% relative fat content [32]. Abdominal tissue absorption μ_a is simulated with a hemoglobin concentration of 12.5 µM, oxygen saturation of 76.0 %, 11.0% relative water and 69.0% relative fat content [33]. Skin tissue absorption μ_a is simulated with a hemoglobin concentration of 9.6 µM, an oxygen saturation of 99.2%, 26.1% relative water, 22.5% relative fat and 1.15% melanin content [34]. Measured absorption spectra of hemoglobin [35], water [36] and fat [37] are used whereas melanin absorption is modeled [31]

Currently, four fluorescent dyes dominate the field of fluorescence guided surgery: fluorescein sodium, protoporphyrin IX (PPIX), methylene blue (MB) and indocyanine green (ICG). The excitation and emission emission spectra of these dyes range from the UV (PPIX excitation) to the near infrared (ICG emission) as shown in Figure 2.1A.

Both, the photons of the excitation light and of the fluorescence emission of a dye interact with the surrounding tissue. Basically, two major types photon tissue interaction are relevant here: elastic scattering and absorption. Both effects strongly depend on the wavelength and on the tissue. Mathematically, both effects can be described by the Beer-Lambert law [31] with the spectrally dependent scattering coefficient μ_s and absorption coefficient μ_a.

Figure 2.1B shows scattering and absorption coefficients for different tissue types. The blue band on the top displays variation of the scattering coefficient μ_s in tissue. Basically, scattering is the dominant effect in tissue. The tissue absorption coefficient μ_a is displayed for the examples of skin, breast and abdominal tissue.

The absorption of photons in tissue is caused by numerous substances with the main contributors being hemoglobin (oxygenated and deoxygenated), water, fat and melanin. Melanin is a very strong absorber and dominates absorption in skin. For other tissue types

which are perfused by blood, hemoglobin typically causes highest absorption in the visible. Around 600 nm, hemoglobin absorption drop exhibits a steep drop. Above 900 nm, the absorption of water increases strongly and restricts light penetration. As a result, a transparent window between 650 nm and 900 nm allows maximum light penetration in tissue. For the displayed Figure 2.1B, μ_a is modeled taking into account the major absorbers at realistic concentrations for skin, breast and abdominal tissue.

Fluorescence guided surgery is mostly a surface based imaging technique with minimal penetration of light into tissue. In contrast, 3D volumetric imaging techniques like US, CT, MRI or PET imaging allow to look into the body. Penetration of light into tissue is below 100 µm in the UV and blue spectral region, between 100 µm and 1 mm in the green and between 1 and 3 mm in the red and NIR [42].

Exciting dyes in the UV region is not only critical because of the high absorption and scattering, but it also tends to excite autofluorescence and the radiation may damage the tissue. Dyes working in the NIR have a higher penetration depth and thus fluorescence from deeper tissue layers can still be seen. Also, autofluorescence is typically not excited above 650 nm and tissue damage is not as critical. Therefore, future developments aim at developing dyes for the spectral window between 650 nm and 900 nm.

This section will first give an overview over state-of-the-art clinical practice sectioned by the used dyes protoporphyrin IX, indocyanine green, fluorescein sodium and methylene blue.

Clinical use of protoporphyrin IX

During the 1990s two mayor oncologic treatment cases have been established: fluorescence guided resection of glioblastoma and urothelial carcinoma.

Glioblastoma multiforme is an aggressive form of brain cancer which expresses the fluorescent dye protoporphyrin IX upon oral administration of 5-aminolevulinic acid [43]. This mechanism is used to accumulate an enhanced red fluorescent dye in cancerous cells. The goal of the fluorescence guided resection is to have a better margin delineation helping the surgeon to resect the cancer as good as possible and thus improving the outcome of the treatment [11, 43, 44]. Clinical studies have shown an improved clinical outcome favoring fluorescence guidance for glioblastoma multiforme resection [12].

Still, there is plenty of room to further improve the procedure. So far, the surgeon can either see the fluorescence or the reflectance color image. The emission filters of these systems are designed to leak some of the blue excitation light so that the surgeon can see some of the parts reflectance image in purple, while the fluorescent emission is red. This concept exhibits some disadvantages. First, the amount of leakage of excitation light limits the range of concentrations of PPIX

which can be detected and therefore limits the dynamic range of the system. Additionally, the surgeon will perceive weak signals as a mixture of blue and red. This means, that if a dye emits with the same color, the color perceived by the surgeon may depend on the fluorescence intensity and thus require extensive training for surgical personnel before being able to perform glioblastoma resections [39]. Surgeons suggest that a change in fluorescent color to a slightly different tone of red could be a hint that a different type of tissue is present at the respective site. So far, the situation is not conclusive whether this effect is caused by a different photochemical state of PPIX in the different tissue or if the effect is caused by weaker fluorescence [45]. In any case, the surgeon needs to remember the fluorescent image and switch to reflectance mode to continue surgery. As switching to fluorescence mode also requires switching off all lights in the surgical theater, the effort is rather high.

As previously mentioned, the second oncologic fluorescence guided intervention is the resection of urothelial carcinoma. PPIX accumulates in cells of carcinoma in situ of the bladder upon topical administration of hexaminolevulinate solution [14]. Fluorescence guided cystoscopy can help to detect neoplastic tissue that would otherwise be missed [14, 46]. A first clinical trial by Kriegmair *et al.* in 1996 already suggested improved sensitivity [13]. Up to date, various clinical studies suggest an improved sensitivity to detect carcinoma in situ, but the low specificity is the biggest criticism of the procedure [14]. Also, different studies do not agree whether fluorescence diagnostic helps to improve the recurrence rate. Different instrumentation options are available on the market: rigid or flexible cystoscopes can be used for photodynamic diagnostics (PDD) [47]. But all options on the market have similar drawbacks than the neurosurgical systems. The surgeon can switch between white light mode and fluorescence mode which leaks some of the excitation light, so the conventional color image can be seen in blue while cancers are glowing red. This filter design limits the dynamic range of fluorophore concentration which can be through the camera dynamic range. Recording fluorescence and reflectance simultaneously and overlaying the different images is not yet clinically available.

Clinical use of indocyanine green

The infrared dye indocyanine green is clinically approved by the FDA and EMA [20] and is currently used for various fluorescence guided surgery applications. A good overview can be found in the reviews by Schaafsma *et al.*, Alander *et al.*, Hong *et al.*, Orosco *et al.*, Mondal *et al.*, Majlesara *et al.* and Zhu. [15, 18, 20, 39, 48–50]. Popular applications include visualization of perfusion or finding sentinel lymph nodes during cancer resection.

To find sentinel lymph nodes, ICG is injected subcutaneously [48]. Successful use of ICG to detected sentinel lymph nodes has been demonstrated for various interventions, including breast cancer [51], skin cancer, squamous cell carcinoma, gastrointestinal cancer and gastric cancer [15].

In a different set of clinical experiments, ICG is clinically used to visualize perfusion. A bolus of the dye is intravenously injected to the bloodstream and both the arterial influx of fluorescent dye to the tissue under observation as well as the venal outflux of the fluorescent dye can be investigated to ensure proper perfusion. For healthy patients, ICG is usually excreted via the liver on a timescale of approximately 10 min.

The review articles above draw a more extensive picture of the current use of ICG. Experimental off-label use of the dye has also been reported. For example, experiments showed a delayed clearance of ICG in glioblastomas which could in future improve fluorescence guided surgery [52].

There are different devices on the medical market to image ICG in different situations. For neurosurgical interventions, surgical microscopes such as the Zeiss Pentero or Leica FL800 can be used [48]. Novadaq offers systems for both open and laparoscopic surgery [15, 53, 54].

In conclusion, ICG is currently the workhorse for fluorescence guided surgery but no specificity to bind to a certain tissue is required for most of the current applications.

Clinical use of flurescein sodium

Fluorescein was historically the first dye with intraoperative usage which has been reported in literature in 1948 [15, 25]. Since then, fluorescein sodium has been used for angiography outside the operating theater. Experiments to specifically target cancer tissue with a specific staining technique have been reported [15, 22, 55]. Another potential usage in future could be glioma resection, as fluorescein sodium was shown to have a higher uptake in gliomas [52].

However, fluorescein is optimally excited in the blue spectral range which also excites autofluorescence. Therefore, image analysis must consider background autofluorescence to avoid artifacts. The blue excitation light also has a lower penetration depth in tissue than NIR light and thus only superficial fluorescein accumulation can be imaged in vivo. Likewise, the green spectral range in which the fluorescence is emitted is essential for color imaging. Thus, recording a color image and a fluorescence image at the same time is almost impossible for fluorescein sodium and systems for fluorescence guided surgery are more challenging than for imaging a NIR dye.

Overall, fluorescein sodium is a clinically well-established dye for the visible range which is mostly used for unspecific imaging.

Clinical use of methylene blue

Methylene blue is a dark blue dye which has been introduced to clinical practice before an approval by the FDA or EMA was required [5, 18]. It is also a fluorescent dye for the NIR range with excitation and emission maximums between 650 nm and 700 nm. Methylene blue is mostly non-specific to target tissue [18] upon injection.

It has recently been used in preclinical and clinical experiments for cardiovascular and lymphatic imaging as well as imaging of the bile duct and gastrointestinal tract or to visualize the ureter [5, 18, 56]. Additionally, experiments in the field of fluorescence guided cancer resection have been reported [5, 18].

2.1.2 *Molecular targeting approaches*

Some medical applications like angiography, visualization of perfusion or detection of sentinel lymph nodes can be achieved by injecting a fluorescent dye into the blood stream or into lymphatic channels. In this case the fluorescent dye is used as a non-specific contrast agent.

However, fluorescence guided surgery can deliver its full potential only in combination with specific targeting. This means that the fluorescent agent targets cells of a specific tissue type like cancers, metastasis, blood vessels or nerves. This section gives a very short overview of state-of-the-art targeting techniques and their potential future use for clinical fluorescence guided surgery.

Antibody targeting

Antibodies are an essential part of the immune system. They bind specifically to antigens which are for example located on the surface of cells. Combining fluorescent contrast agents with antibodies which are known to stick to specific cells allows a specific staining.

Antibody staining has been established as a gold standard in fluorescence microscopy. Novel clinical agents for chemotherapy combine antibody specificity with cytotoxins. In preclinical experiments, various cancers have been successfully targeted by antibodies. The next step requires to translate these results to clinical practice in trials.

Activatable cell penetrating peptides

Cell penetrating peptides (CPP) can penetrate the cell membrane and thus enter cells. These peptides can be combined with small molecules such as fluorescent dyes, quantum dots, gadolinium or other drugs to be delivered into the cell.

When injecting the activatable CCP to a patient, it is deactivated and cannot stick or penetrate cells. In presence of the specific cancer the CPP is activated by a protease reaction and can then stick to

cells and penetrate those. The specificity is obtained by the chemical reaction of the activation process.

This technique has first been presented in 2009 [57] and was designed for medical applications. Since then, numerous promising preclinical experiments have been published [7, 21, 23, 58, 59]. Its chances to be established as a key staining tool for fluorescence guided surgery are good, but clinical trials and regulatory approval are pending.

Fluorescent proteins

Fluorescent proteins are encoded in the DNA of a cell and thus produced by the cell itself. In biological research, the genetic information can be artificially added to the DNA or RNA in a process called transfection. Various transfection methods depending on the application have been established.

Historically, the green fluorescent protein (GFP) has been found in the jellyfish aquorea victoria. The work of Douglas Prasher on the genetics of GFP allowed biologists to use the GFP as a tool [60]. Subsequently, the community continued to modify GFP to improve it and also to develop other fluorescent proteins [61, 62]. Today, fluorescent proteins in various colors can be specifically transfected.

The method has the possibility to target cells with very high specificity which means that for example only cancer or nerve cells show fluorescence, whereas there is no fluorescence in surrounding tissue. But the DNA of these cells is modified. The risk which is associated with modifying cells of a patient is too high to use this method in clinical practice in close future.

Specific accumulation of PPIX

Protoporphyrin IX (PPIX) is a fluorescent dye which is produced in the mitochondria of cells in low doses. Some cancers accumulate high doses of PPIX upon administration of 5-aminolevulinic acid (5-ALA) which is metabolized to PPIX. This technique has been established as a clinical standard fluorescence guided surgery for bladder carcinoma in situ and glioblastoma multiforme [15, 21, 51].

2.1.3 *Clinical advantages of multispectral fluorescence imaging*

There are numerous advantages of imaging multiple fluorophores. For example, different anatomical or functional structures can be imaged or the information of multiple fluorophores targeting the same structure can be combined for better results. Herein, some promising example techniques are presented.

Multiple staining

The most intuitive option to use multiple fluorophores is to stain different structures with different fluorescent dyes. One impressive application has been published by Whitney *et al.* targeting nerves with one fluorescent dye and cancer with a second fluorescent dye [23]. Both dyes could be imaged and overlaid in pseudocolors on the reflectance image.

During cancer resection, the malignant tissue must be completely removed but in contrast nerves must not be transected accidentally. In many surgical scenarios, an optical distinction based on the human vision is challenging. In such cases fluorescence guidance can improve the outcome and potentially also speed up the intervention.

Another scenario would be to target cancer and metastasis or sentinel lymph nodes with different dyes. All in all, any application using a single dye can in principle be combined with another using multispectral fluorescence detection.

Multispectral detection of PPIX

As described earlier, fluorescence guided glioma resection using PPIX fluorescence is a clinically established technique. Though the weak emission has been reported to be a key issue of the procedure. Surgeons need to decide whether fluorescence signal is caused by the cancer or not, based on their experience and visual perception.

To tackle this approach, the PPIX fluorescence can be detected quantitatively using multispectral image acquisition and advanced normalization approaches [63–67]. This approach has been shown to detect residual cancer tissue which would was not seen by conventional fluorescence detection in a clinical experiment. Though, the device is not able to run at video rate and the findings would require to be validated in a larger study.

The fluorescence of PPIX has shown to change its spectrum depending on the chemical environment and the current photochemical state of PPIX. Three distinct spectra of PPIX were found and biopsy findings suggest that the different spectra allow distinction between solid cancer and the infiltration zone [45, 68]. This finding is undermined by surgeons' experience that the PPIX fluorescence shows different tones of red. Further clinical experiments resulting in multispectral fluorescence data are required, but the initial findings suggest a huge potential for improvement.

Improved specificity

Any fluorescent dye which is injected to the blood stream has some affinity to any type of tissue. If targeting a specific cancer, the affinity for this cancer tissue is supposed to be very high, whereas for other tissue types it is as low as possible. Knowing the affinity for a tissue

of interest of various dyes allows to combine the information of all these dyes.

A study by Tichauer *et al.* has demonstrated that the specificity and sensitivity of cancer detection can be improved by injecting one targeted and one untargeted dye and combining the information [24]. The publication demonstrates the improved contrast to noise ratio for four different cancer types. This approach can be directly translated to clinical applications combining any novel targeted agent with an untargeted dye like ICG or FITC.

One future example application might be fluorescence guided glioma resection using PPIX. It is clinically established, but both sensitivity and specificity can still be improved. Clinical experiments using ICG showed increased uptake and slower excretion and thus cancers could be made visible [52]. Fluorescein sodium signal has shown to increase in glioblastomas, most likely due to increased vascularization [52]. Combining this information may improve cancer resection in future, but in return requires multispectral fluorescence detection.

Autofluorescence

Autofluorescence of intrinsic fluorophores like NADH can be used for diagnostic purposes. This requires multispectral detection as autofluorescent agents can be found in many tissue types and thus typically no strong contrast in bare fluorescence intensity allow simple distinction. But relative intensity changes and spectral variations can be observed and exploit for diagnostic purposes. The big advantage is that no agents need to be injected and thus no agent requires pharmaceutical approval.

One example for using autofluorescence is the diagnosis of cervical neoplasia. Spectroscopic measurements of tissue autoflourescence have been conducted to find a way to separate malignant and healthy tissue [69]. Subsequently, systems relying on excitation scanning [70] or emission scanning [71] to differentiate between the different tissue types have been developed and tested.

2.2 RELATED WORK

This section will summarize the related work and recent developments on instrumentation for fluorescence guided surgery. First, approaches to combine reflectance and fluorescence imaging for clinical applications are introduced. Subsequently, an overview over different published technologies to record multispectral image data is presented.

A more complete overview of the field of hyperspectral imaging can be found for example in the following review papers [72, 73]. The following sections are partially based on these reviews.

2.2.1 *Combining color and fluorescence imaging*

Intraoperative fluorescence imaging has first been reported by Moore *et al.* in 1948 [3, 15, 25]. Since then, technological advances have driven progress of the used imaging devices. Combining fluorescence and color imaging continues to pose a challenge on the design of any system.

Two major categories of solutions have been established: In the first option, fluorescence and color image detection are temporarily split. This means that either fluorescence or color images are recorded. The second category splits the spectral range into two parts: One for fluorescence imaging and one for color imaging. This is usually chosen if IR fluorescent dyes are used and the full visible spectral range does not affect fluorescence detection.

Accordingly, this section reviews the related work grouped in these two categories.

2.2.1.1 *Spectral splitting*

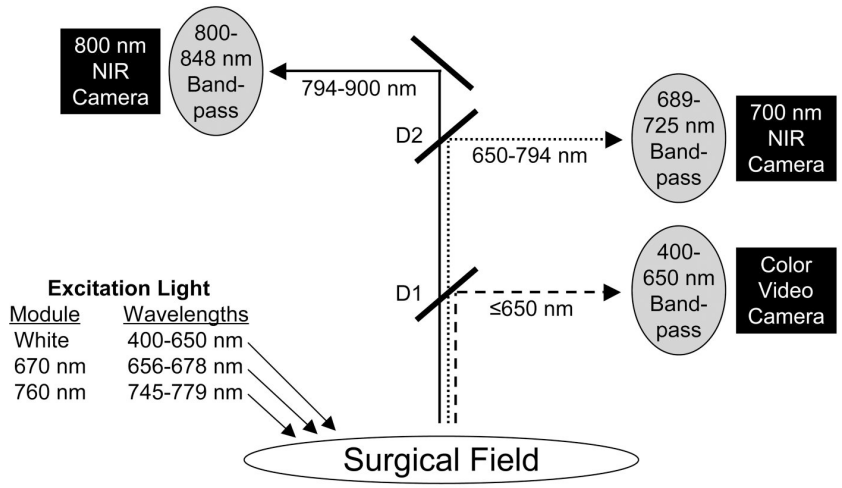

Figure 2.2: Combining fluorescence and color imaging using different spectral domains: Schematic spectral illustration of the spectral splitting concept using dichroic mirrors [51]. Reflectance color images can be recorded from from the blue throughout the red spectral range. Fluorescence is recorded in two NIR channels. Adapted by permission from Springer Customer Service Centre GmbH: Springer Nature, Annals of Surgical Oncology, The FLARE™ Intraoperative Near-Infrared Fluorescence Imaging System: A First-in-Human Clinical Trial in Breast Cancer Sentinel Lymph Node Mapping, Susan L. Troyan, Vida Kianzad, Summer L. Gibbs-Strauss, Sylvain Gioux, Aya Matsui, Rafiou Oketokoun, Long Ngo, Ali Khamene, Fred Azar, and John V. Frangioni, coyright 2009.

Splitting the spectrum into a part for fluorescence detection and one for color imaging is particularly appealing if the fluorescence emission is outside the visible range. One such example system is presented in Figure 2.2 and Figure 2.3.

Typical clinical scenarios falling into this category involve the dye ICG, which has an emission maximum around 800 nm. The available systems for clinical and preclinical use with ICG have been compared in various reviews [5, 48, 74, 75]. Some of the devices offer fluorescence imaging only, whereas others additionally offer a color view. But only few devices allow a real-time overlay of fluorescence and color images.

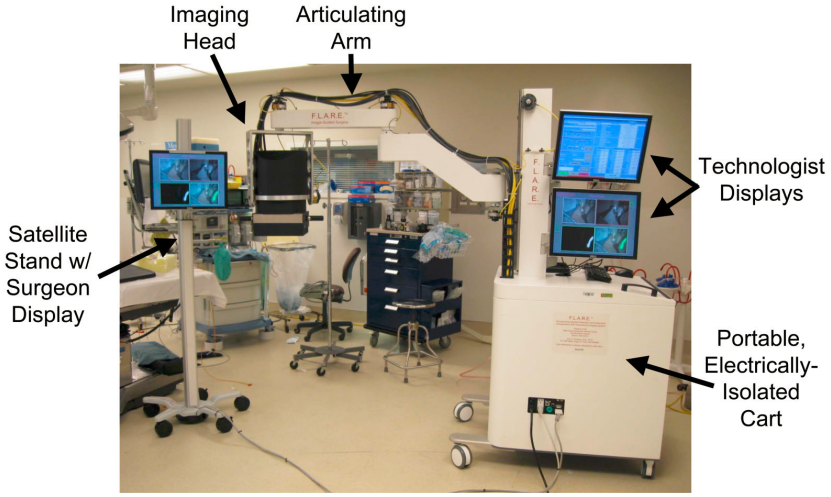

Figure 2.3: Image of the entire surgical imaging system in the operating room [51]. The imaging head is placed close to the patient. It contains the optical assembly. Adapted by permission from Springer Customer Service Centre GmbH: Springer Nature, Annals of Surgical Oncology, The FLARE™ Intraoperative Near-Infrared Fluorescence Imaging System: A First-in-Human Clinical Trial in Breast Cancer Sentinel Lymph Node Mapping, Susan L. Troyan, Vida Kianzad, Summer L. Gibbs-Strauss, Sylvain Gioux, Aya Matsui, Rafiou Oketokoun, Long Ngo, Ali Khamene, Fred Azar, and John V. Frangioni, coyright 2009.

The fluorescence information can be projected into the field of view of the surgeon using goggles in case of open surgery [76–78]. If using a surgical microscope, the fluorescence image information can be injected in the optical path of the microscope [79].

Vargas *et al.* present a system featuring two IR channels and thus being able to image fluorescence multispectrally [80]. Similarly, the commercial system *Curadel Lab-Flare R1* and the *Quest Spectrum* can both image one dye around 700 nm and a second dye at approx. 800 nm. Using a separate sensor for color imaging and for each fluorescent dye allows to adjust imaging parameters like integration time independently.

The laboratory of Frangioni at the Massachusetts General Hospital developed the experimental FLARE system in 2002 [81]. It has been used in many preclinical and clinical studies including sentinel lymph node detection in case of breast cancer [51], cervical cancer or vulvar cancer [82].

Another experimental device which uses spectral beam splitting with dichroic mirrors has been presented by Themelis *et al.* [83] and subsequently been used in clinical experiments to identify ovarian cancer by a targeted contrast agent [22].

Undoubtedly, many systems to image ICG have been developed and some are even commercially available for clinical use. Each of these systems is tailored for a specific scenario. The disadvantage of these systems it that they split the spectral range into one for fluorescence and one for color imaging. This restricts the use of these devices to IR dyes.

2.2.1.2 *Temporal splitting*

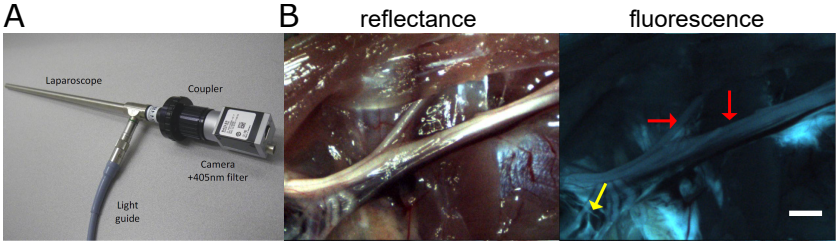

Figure 2.4: Combination of fluorescence and color imaging using temporal multiplexing. The same color sensor records fluorescence and color images in an alternating sequence. A) Photography of an exemplary setup for a rigid laparoscope showing the light guide, the coupling element, the optical filter and the digital camera. Adapted with permission from ref [84], OSA. B) Intraoperative reflectance color image and corresponding fluorescence images showing nerves of a rodent. The red arrow points at the brachial nerve, the yellow arrow points at the phrenic nerve. The bar on the right side corresponds to 1 mm. Adapted with permission from ref [84], OSA.

Recording fluorescence and reflectance images at the same wavelengths is not feasible at the same time. Thus, they are often recorded at different time points. For example, the fluorescent dye PPIX emits in the red spectral region between 600 nm and 700 nm. Classical surgical microscopes which are dedicated to PPIX imaging can be switched manually between a fluorescent mode and a color reflectance mode.

Gray *et al.* present a laparoscopic system which is able to record fluorescence and reflectance images with a single camera in the visible range at 15 fps [84]. The system switches the broadband color illumination and the laser fluorescence excitation on and off every second

frame. A photograph of the laparoscope and example images from preclinical experiments are shown in Figure 2.4.

Novadaq has filed a patent application with an approach in which the fluorescence excitation and only the red color illumination are switched on and off in every second image to record reflectance and fluorescence images with only one sensor [85]. The red and green illumination are constantly kept on. This results in a higher framerate for the color information of the blue and green channel than for the red one.

In open surgery, the fluorescence images may be contaminated by ambient light and the surgical illumination, unless that light is also triggered. Time multiplexing can help in this scenario to correct the fluorescence images for signal from ambient light. Sexton *et al.* present a system with modulated excitation light and a modulated gain an intensified CCD (ICCD) to eliminate ambient light for detection of PPIX [66]. Similarly, Zhu *et al.* also use modulated excitation and an ICCD to detect red fluorescent protein in preclinical experiments [86].

A very compact sensor design to detect ICG has been presented by Chen *et al.* [87]. The prototype system uses acquisition in multiple phases combined with a sensor with 4 different pixels: red, green, blue and IR to record color images, fluorescence of ICG and allow continuous surgical illumination. On the one hand, this allows to combine fluorescence and color imaging in one single sensor. But the sensitivity of the system is limited compared to monochrome fluorescence imaging systems. Additionally, fluorescence excitation is only used when recording every second frame to be able to eliminate the effect of surgical illumination.

All in all, temporal multiplexing allows to combine fluorescence and color imaging in the same spectral region. The presented systems show the high potential of this technique. But the emission filters need to be placed in the optical path and thus the fluorescent dye needs to be fixed in advance. Also, either expensive ICCDs are necessary or the framerate is reduced by temporal multiplexing.

2.2.2 *Multispectral imaging in medicine*

Numerous efforts to combine multispectral imaging with biomedical applications have been published. In comparison with the previous chapter, which focused on progress to combine intra-operative fluorescence and color imaging, this section is dedicated to progress in the filed of multispectral imaging.

This chapter selects the most relevant references and summarizes the related work structured by technology.

For each technology, the publication which covers best multispectral fluorescence and reflectance imaging is selected with highest

priority. Publications presenting multispectral fluorescence imaging have second priority and publications which only refer to multispectral reflectance imaging have lower priority in this section.

First, snapshot systems which record a complete multispectral image in one single acquisition are presented. Second, technologies are presented recording a complete spatial image at a time and sequentially recording the spectral information. Third, approaches to record the entire spectral information of a location simultaneously and to scan spatially are summarized.

A review of the current state of the art has been published in literature, for example by Lu *et al.* or Calin *et al.* [73, 88].

2.2.2.1 *Snapshot hyperspectral imaging systems*

During the last decade, snapshot hyperspectral imaging systems (HSI) which allow to record a complete hyperspectral data cube in one single acquisition became increasingly popular.

Numerous techniques to record the data have been established and will be discussed in detail in literature [72]. Here, an overview over realized setups in biomedical applications is given. The different approaches are grouped by acquisition technique.

Image mapping spectrometer

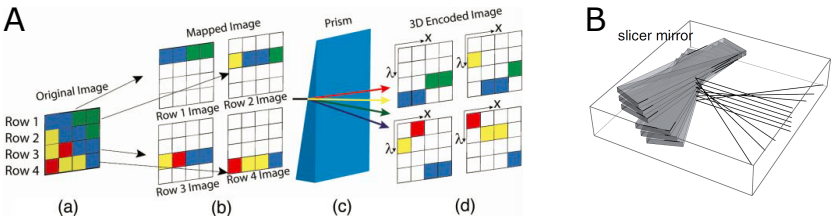

Figure 2.5: Schematic drawing explaining the functionality of an image mapping spectrometer. A) The original image is split on a pixel level and rearranged on the sensor. In the illustration, the individual parts correspond to one pixel row in x direction. The pixel order is maintained in x direction, whereas the different rows are rearranged in y direction to make space to obtain spectral information. The light of each row is into its spectral components using a dispersive element. The image needs to be mapped electronically to its original composition. Adapted version reproduced from Robert T. Kester, Noah Bedard, Liang S. Gao, Tomasz S. Tkaczyk, "Real-time snapshot hyperspectral imaging endoscope," Journal of Biomedical Optics 16(5), (2011). B) One possible element to split the image is a slicer mirror in an image plane splitting the different rows. Adapted version reproduced from Nathan Hagen and Michael W. Kudenov. "Review of snapshot spectral imaging technologies". Optical Engineering 52.9 (2013).

One variant of snapshot HSI devices are image mapping spectrometers, which typically record data sets with 10 to 40 spectral bands.

In this technique, the image is split for example by placing a micro-structured mirror in the image plane which relocates the location of the pixels on the sensor as illustrated in Figure 2.5. An additional dispersive element reveals the spectral components.

One example setup has been implemented by Gao *et al.* and Kester *et al.* for fluorescence microscopy with a data cube size $(x \times y \times \lambda)$ of $285 \cdot 285 \cdot 60 \approx 5MP$ [89, 90]. But the fluorescence images were integrated for 1 s, which would be too long for intraoperative applications. Subsequently, the same technology was adapted to a fiberscope [91], recording images at 5.1fps with a data cube size $(x \times y \times \lambda)$ of $350 \times 350 \times 29 \approx 3.5MP$.

Lavagnio *et al.* also present an IMS adapted to a fluorescent microscope [92]. The device records with a data cube size of $(x \times y \times \lambda)$ of $320 \times 210 \times 60 \approx 4MP$.

All in all, IMS offers a high transmission efficiency and is therefore suitable for fluorescence detection. Spectral and spatial resolution can be selected as needed. However, the systems exhibit a big form factor which is hard be miniaturize and the fabrication of micro-structured elements poses a challenge.

Integral field spectroscopy

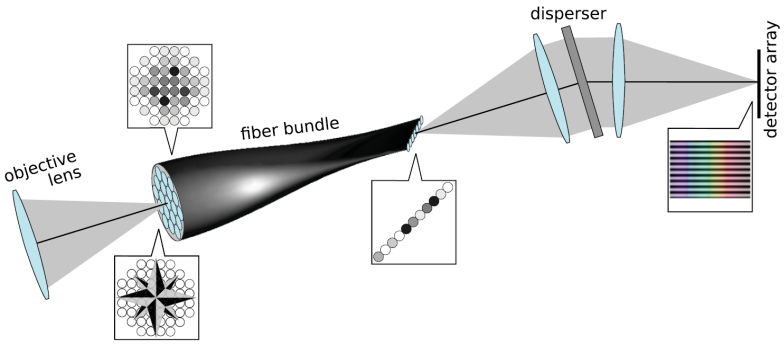

Figure 2.6: Schematic illustration of integral field spectroscopy. The object is imaged using an objective lens onto an optical fiber bundle. Each fiber corresponds to one single pixel in the final image. The fibers are rearranged on the other side in a linear manner. This means that the complete xy plane is stretched out in one dimension. The light is spectrally split in the other spatial dimension and imaged using a monochromatic 2D detector array. Reprinted from Nathan Hagen and Michael W. Kudenov. "Review of snapshot spectral imaging technologies". Optical Engineering 52.9 (2013).

Integral field spectroscopy (IFS) uses different techniques to rearrange the pixels in the image and to obtain the spectral information, for example fibers (IFS-F, illustrated in Figure 2.6), microlens arrays (IMS-L) or micro-structured mirrors (IMS-M) [90].

A multispectral snapshot fiberscope (IFS-F) was presented by Lim *et al.* [93] for fluorescence and reflectance spectroscopy. The system trades high spectral resolution for spatial resolution. The presented spatial resolution is restricted by 100 pixels in total ($10 \cdot 10$), limited through the number of fibers in the bundle. Accordingly, the spectral data is recorded in 756 spectral channels (from 400 nm to 1000 nm).

An IFS-L device adapted to a fluorescence microscope was presented by Dwight *et al.* [94]. It records hyperspectral images at a data cube size of $(x \times y \times \lambda)$ of $88 \times 88 \times 46 \approx 0.35MP$ or $200 \times 200 \times 27 \approx 1MP$ at framerates above 1 fps.

My conclusion is that IFS is a promising technology which combines high spectral resolution with good detection efficiency and is therefore used for fluorescence detection. But spatial resolution is not high enough for surgical microscopy or endoscopy.

Computed tomography imaging spectrometer

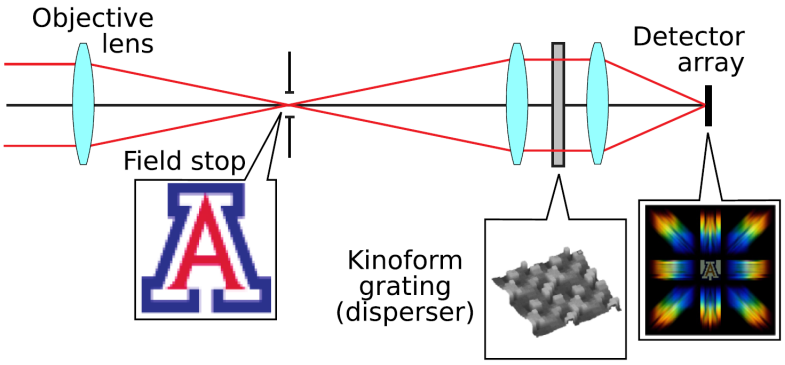

Figure 2.7: In computed tomography imaging spectroscopy, a Kinoform grating is placed in an conjugated imaging space as key element as depicted in the schematic. The resulting image, which is recorded on the detector array consists of a superposition of spectral and spatial information. The mathematical treatment which is necessary untangle the combined information is equivalent to the mathematical treatment of computed tomography. Reprinted from Nathan Hagen and Michael W. Kudenov. "Review of snapshot spectral imaging technologies". Optical Engineering 52.9 (2013).

Computed Tomography Imaging Spectrometers (CTIS) have a Kinoform grating dispenser placed in the aperture. It causes a mixed detection of spatial and spectral information on the sensor as illustrated in Figure 2.7. The hyperspectral data cube needs to be reconstructed with algorithms known from computer tomography.

Jonson *et al.* describe a fundus camera to determine oxygen saturation by reflectance imaging [95]. A full hyperspectral data cube with a size $(x \times y \times \lambda)$ of $208 \times 208 \times 50 \approx 0.35MP$ is recorded in ≈ 3 ms.

In general, CTIS systems can be realized in a very compact form which is ideal for surgical applications in which confined space is a fundamental limitation. But they require complicated design and fabrication of the dispenser element as well as complex image reconstruction which potentially introduces artifacts.

Coded aperture snapshot imager

Coded Aperture Snapshot Imagers (CASSI) work like slit spectrometers where the slit is replaced by a binary mask in the image aperture. Subsequently, the image data needs to be reconstructed to obtain the HSI data cube [72].

A CASSI system adapted to a fluorescent microscope was realized by Cull *et al.* showing fluorescence detection in 31 bands ranging from 450 nm to 750 nm at a framerate of 15 fps [96].

The computational burden of reconstruction remains extensive which poses a fundamental challenge on real-time systems.

Spectrally resolving detector arrays

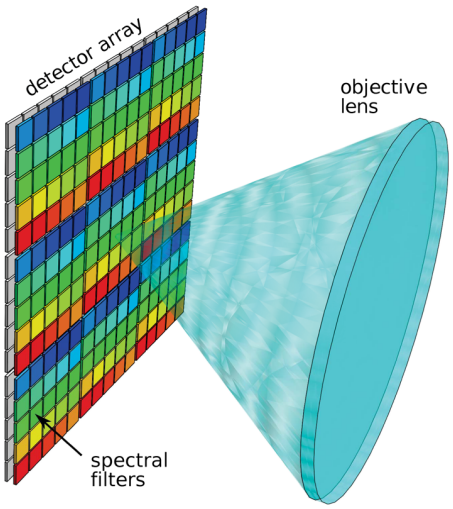

Figure 2.8: Spectrally resolving detector arrays are the most common kind of hyperspectral snapshot imaging as they are used in most conventional RGB sensors on the market. In this technique, a spectral filter is placed on each pixels. The set of spectral filters are usually arranged in a repeating pattern. Depending on the application, the number of filters in the pattern can be adjusted. Processing is required to interpolate for the missing spatio-spectral information. Reprinted from Nathan Hagen and Michael W. Kudenov. "Review of snapshot spectral imaging technologies". Optical Engineering 52.9 (2013).

Spectrally Resolving Detector Arrays (SRDA) are well-known from color imaging, in which a periodic pattern of red, green and blue filters is placed on top of the individual sensor pixels. This concept

can be generalized for a higher number of freely chosen filters as displayed in Figure 2.8.

According to Kaluzny *et al.*, a system to image the retina with a set of 16 filters arranged in a periodic 4×4 grid has been realized [97, 98]. The system records a hyperspectral video stream at ≈ 20 fps with a data cube size ($x \times y \times \lambda$) of $512 \times 256 \times 16 \approx 2MP$.

Chen *et al.* present a system with only four spectral channels to combine color and IR fluorescence imaging: red, green, blue and IR. The setup combines high-quality color imaging with IR fluorescence detection in a very compact way. But the spectral resolution and the fluorescence detection efficiency are compromised in return [87].

In short, SRDA is very potent technology because the systems are very compact and can be combined with any optical system. By contrast, the systems are very complicated to fabricate, favoring mass production. The technique is also not very suitable for fluorescence imaging because most of the light is blocked and the light does not pass the filter perpendicularly. In any case, the recorded information is spread over the hyperspectral space in a way which requires interpolation and thus may cause artifacts.

Multiaperture filter camera

Multiaperture field cameras use microlens arrays which each forms an image. Each lens has its individual aperture with a filter placed in front of it. An ultra-compact system to record 18 bands ranging from the visible to NIR at an image size around 0.5 MP has been presented [99] . The system was used to diagnose wound healing by multispectral reflectance imaging [100]. It was subsequently adapted to a fundus camera to determine the oxygen saturation of blood vessels in the retina [101].

In my opinion, the compactness of the camera is impressive. But the entrance aperture is divided between 18 individual imaging lenses, which reduces the photon collection efficiency. Therefore, the reduced sensitivity might be an obstacle for fluorescence imaging. Moreover, the different images are not formed by a single imaging path. Specular reflections and scenarios in which the light intensity has a strong dependence will cause artifacts.

Summary

Snapshot hyperspectral imaging is a very potent technology, which will become more powerful in the future. The drawbacks are the optically complicated and bulky setups, and the data handling. Still, due to the high data rates, most setups do not run at 30 fps and so far the concepts do not allow to simultaneously record fluorescence and reflectance out of the box, but they can be used for either. If the spectral bands are fine enough, a color image can be reconstructed.

These systems have superior spectral resolution compared to micro-filter Bayer sensors, but still lack of spatial and temporal resolution and additionally struggle to unify color and fluorescence.

2.2.2.2 *Spectral scanning systems*

Recording a multispectral image data set sequentially by acquiring one spectral channel at a time is the most widely used technique in fluorescence microscopy. Consequently, such systems have also been translated to clinical applications. This section is structured by scanning techniques.

Filter wheels

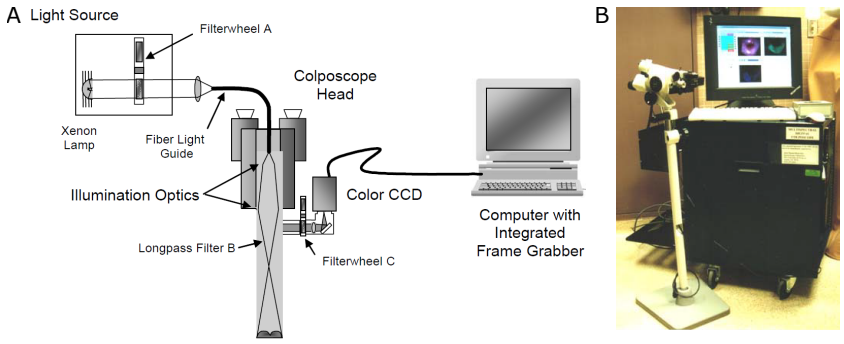

Figure 2.9: Filter wheels are the most popular in fluorescence microscopy as size (and often speed) are not the primary concern. Different spectral filters can be mechanically switched into the imaging path to obtain spectrally distinct images. A) Schematic illustration and B) photography of the multispectral fluorescence colposcope presented by Benavides *et al.*. The presented version use one filter wheel to filter the excitation light as well as another filter wheel to filter the emission. Adapted with permission from ref [70], OSA.

The most simple and straightforward technique to sequentially record images with varying spectral information is to place different filters in front of the sensor using a filter wheel.

A series of papers using filters wheels for is published by a group from Arizona centered around Rebecca Richards-Kortum [69–71, 102, 103]. filter wheels to scan both, excitation and emission wavelengths for fluorescence imaging have been implemented and clinically tested.

A cost effective multispectral colposcope was developed to identify cervical neoplasia by autofluorescence diagnostics. Initial experiments recorded the EEM of diseased and healthy tissue [69, 102]. Subsequent publications focus on minimizing the necessary spectral information and on faster recording. Benavides *et al.* present a system, displayed in Figure 2.9, which uses two different excitation lights and a color sensor to record the emission at 2 fps [70]. Renkoski *et al.* excite autofluorescence at one wavelength and record fluorescence at 8

different bands by switching filters in a clinical study with 50 patients [71]. Color reflectance images are recorded using a red, green, blue and IR filters. The system does not report a framerate but suggests framerates around 1 fps.

The series of publications is very interesting for this work in two perspectives: On the one hand, it demonstrates the path from initial experiments in which the entire autofluorescence EEM is recorded to identifying the important spectral bands for distinction between benign and malignant tissue.

To summarize, all the approaches using filter wheels are far from recording a complete multispectral image data set in video rate. Additionally, the setups are bulky and not suitable for miniaturization.

Besides, the work on cervical neoplasia demonstrates how to find the relevant wavelength bands for discrimination based on reduced acquisition.

Liquid crystal tunable filters

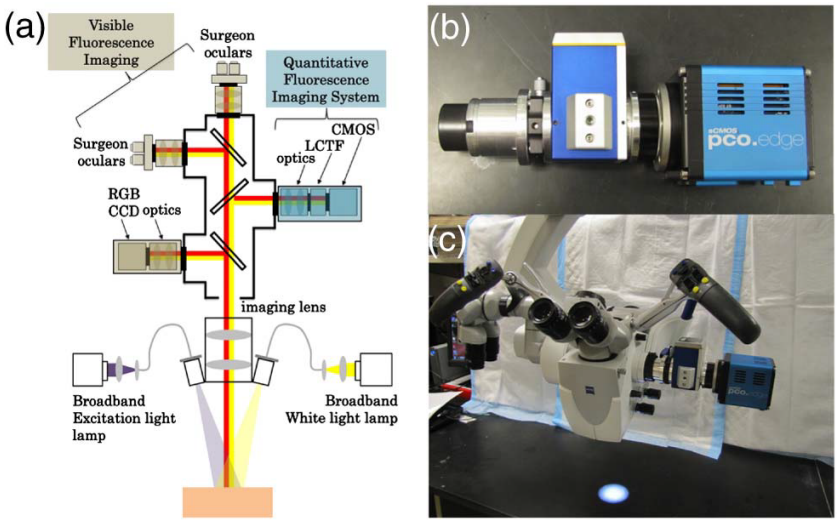

Figure 2.10: Liquid cristal tunable filters (LCTF) are used to spectrally scan the fluorescence emission light. A) Schematic illustration of a modified surgical microscope. The modification of this microscope is shown on the top right part of the schematic. An additional sensor in combination with an liquid crystal tunable filter is used to capture multispectral fluorescence images. B) Hyperspectral fluorescence imaging element consisting of an imaging lens, the LCTF and the sensor (left to right). C) Photography of the hyperspectral surgical microscope. The modified elements are shown on the right side. Reprinted with permission from ref [64], OSA.

Liquid crystal tunable filters allow to spectrally filter light and control the band structure of the filter electronically. The disadvantage of effect LCTF over interference bandpass filters is that they do not have

a strong off band rejection ratio and the edges are not as steep. Moreover, the maximum transmission ratio of LCTSs is typically around 50% and they are sensitive to polarization. The advantage is the option to change the filter characteristics fast and electronically.

Multiple preclinical and experimental clinical devices have been published [63, 104–106]. The resolution of the images depends on the respective sensor placed behind the filter. Gebhart *et al.* present a system for brain cancer identification. It records fluorescence and reflectance multispectrally from 400 nm to 720 nm in steps of 5 nm. Recording of an image requires 2 minutes. Another system to visualize cancer vascularization has been presented by Sorg *et al.*. It also allows to multispectrally detect reflectance and fluorescence images.

The system of Mitra *et al.* records multispectral fluorescence from 650 nm to 750 nm in 2 nm intervals. It is used for ICG fluorescence imaging of the bile duct of a porcine model.

A group from Dartmouth College in Hannover has built a system shown in Figure 2.10 to spectrally resolve intra-operative fluorescence images for neurosurgical glioblastoma resections. The combination of a liquid crystal tunable filter with a monochrome camera was used to sequentially record the entire fluorescence emission spectrum of PPIX intraoperatively with a spectral resolution of 3 nm in 2 to 8 seconds [64, 107]. Additionally, the group has empirically developed a method to convert the raw fluorescence intensity data to be more quantitative and remove the dependence of absorption and scattering of the brain tissue [107–109]. Fitting the spectral signature of PPIX to the data has proven to show better results than conventional imaging and was able to detect cancer tissue that would have been undetected in a clinical scenario [107]. For spectral fitting, the quality of the results depends on the model used for the fit. Using a χ^2 goodness of fit test can help to verify the quality of the fit and therefore make the method more robust [110].

Overall, the presented systems and results are very promising. The big advantage of the LCTF systems is the flexibility to select the needed multiband filter structure. Compared to switching interference filters these systems are a lot faster but do not yet allow to record in real time.

Acousto optical tunable filters

Acousto optical tunable filters (AOTF) use acoustic ultrasound waves in an optical crystal to realize wavelength dependent filters. As AOTFs allow to switch wavelengths very quickly, numerous setups with such devices have been implemented for clinical experiments [111–114].

Arnold *et al.* and Leitner *et al.* introduced an endoscopy system for hyperspectral color reflectance imaging with fast switching rates. The system shown in Figure 2.11 can either record a multispectral data cube with a spatial size of 1MP and with 8 spectral bands at 5 fps or

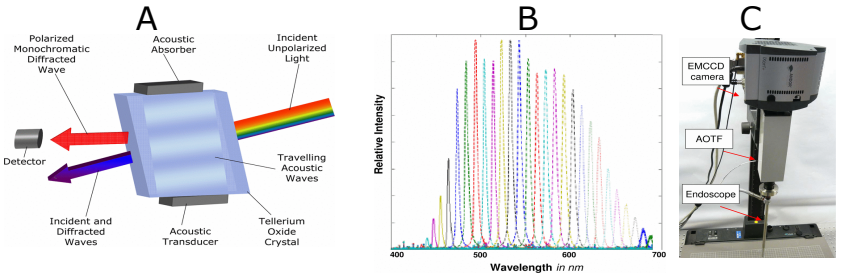

Figure 2.11: Acousto optical filters can be used to filter fluorescent light. A) Acoustical actuators produce waves in an optical crystal. As an effect, the density waves inside the crystal function as a grating for incoming light. The light of a selected wavelength can be split from the other wavelengths. Using this effect, the AOTF can work as a filter. Reprinted from [111], © 2010 IEEE. B) Spectral transmission curves for different acoustical waves. Reprinted from [111], © 2010 IEEE. C) Photography of a setup for hyperspectral fluorescence imaging with a surgical endoscope. Reprinted from [111], © 2010 IEEE.

with 51 spectral bands at 0.8 fps. The system performance is demonstrated imaging clinical biopsies ex situ [111, 114].

Kong *et al.* and Martin *et al.* present a fiberscope system which records multispectral fluorescence and color images. The system is demonstrated in preclinical experiments identifying skin cancer [112] and muscle cancer [113]. The spectrum is recorded from 440 nm to 640 nm in steps of 10 nm and results are displayed at 1 fps.

Both presented systems are the fastest of the spectral scanning systems. But still video-rate imaging has not been successfully realized to my knowledge.

2.2.2.3 *Spatial scanning systems*

In contrary to spectral scanning systems, the spatial scanning systems record all spectral data simultaneously, but they form an image by sequentially assessing different parts of the field of view. One big advantage of this technique is that motion artifacts do not result in spectral artifacts. First, a point scanning macroscopic imaging system is introduced. Subsequently, parallelization approaches, named line scanning are summarized. Finally, efforts to miniaturize a point scanning device into an fiber endoscope are presented.

Point scanning

Constantinou *et al.* have presented the fourth generation of an advanced macroscopic imaging device using galvanometric mirrors to scan medical samples point by point [115]. The device may record fluorescence images, reflection images, transmission images, differential phase contrast images and hyperspectral images. All images can be

recorded at resolutions as high as 385 MP for a field of view of 2.2 cm $\times$ 7.0 cm (pixel width of 2 µm/pixel). In this view, recording an image of an area of 1 cm cm with an integration time per pixel of 5 µs for fluorescence images leads to a total recording time of 8 min and for hyperspectral images with 200 µs/pixel to a appox. 80 min recording time. The system is indeed a striking example for the versatility and flexibility of point scanning systems. But the major drawback of the system also becomes clear: the times are far off video rate.

Multispectral line scanning in medicine

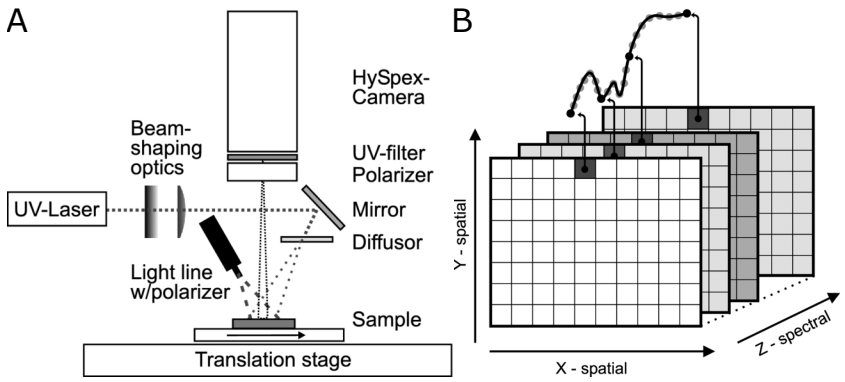

Figure 2.12: Hyperspectral imaging using line scanning: A) Schematic illustration of a line scanning system. The sample is placed on a translation stage. At each point in time, a hyperspectral image of a line perpendicular to the translation movement is recoded by the system. B) Hyperspectral data cube of a sample showing the extracted spectrum of one single pixel. Reprint acknowledgment for both subfigures: Adapted version reproduced from Eivind L. P. Larsen, Lise L. Randeberg, Elisabeth Olstad, Olav A. Haugen, Astrid Aksnes, and Lars O. Svaasand. "Hyperspectral imaging of atherosclerotic plaques in vitro". Journal of Biomedical Optics 16.2 (2011).

To overcome the obstacle of low framerates, one option is to parallelize the recording in one spatial direction and always record all the spectral data of one line at a time. The second spatial dimension which is perpendicular to the recorded line needs to be scanned. This technique, often referred to as push broom or line scanning, is widely used in applications where a linear movement is anyways present. Intuitive examples are satellite observations of the earth or imaging objects on a conveyor belt like diary products [116].

Larsen *et al.* presented a medical system scanning reflectance and autofluorescence from 410 nm to 1000 nm in steps of 3.7 nm to characterize arteriosclerotic lesions [117]. The system which is displayed in Figure 2.12 may acquire up to 160 spectral bands at HD resolution, but it requires as long as 30 s to record one complete data set. The

investigated biopsy samples are placed on a translation stage and moved under the system.

Khoobehi *et al.* introduced a system to image multispectral reflectance images on a fundus camera [118, 119]. The multispectral camera is mounted on a linear translation stage and moved to scan the field of view. The covered spectral range covers 410 nm to 950 nm in steps of 2.5 nm. But recording of 1024 px $\times$ 256$\Delta\lambda$ $\times$ 100 lines requires 8 s.

Most line scanning systems use an entrance slit and a grating or prism to split the light into its individual spectral contributions. In contrast a system presented by Luthmann *et al.* uses a special 2D sensor [120]. Numerous stripes of different bandpass filters are placed on top of the sensor. Each line images a different location and a different spectral band. A complete image is created by moving either the object or the camera in one direction. The system was able to unmix phantoms containing 7 fluorescent dyes with emission in the red and near infrared spectral range. Preclinical experiments allowed to discriminate between 4 different fluorescent dyes (ranging from the red to near infrared) in vivo. But the system is reported to require 4 minutes to record a complete multispectral image. Thus, the technology is not suitable for video-rate fluorescence imaging. Each of the bandpass filters rejects the majority of the incident photons. Motion during integration will lead to both, spectral and spatial artifacts. My conclusion is that the results and experiments look very promising, but the technology is unfortunately not fast and efficient enough for video-rate fluorescence imaging. Additionally, the detection principle has a very low detection photon collection efficiency.

The presented publications show the potential of line scanning devices. They may record multispectral data cubes at high spatial and spectral resolution and superb accuracy. But at the same time, they also show the major drawback: the integration time for one single image is in the order of seconds to minutes and thus far too long.

Rotating fiber endoscopy

Lee *et al.* present a point scanning endoscope with only 1 mm diameter which runs at 30 fps video-rate [121]. Piezo actuators move the single illumination fiber at high frequency so that it illuminates the object field in a spiral pattern as illustrated in Figure 2.13. The light to be detected is either collected by the same fiber or from a bundle of fibers which are placed around the central illumination fiber. Therefore, detection aperture of these devices is very small, particularly if the object is far away from the fiber tip. The resolution is still below 1 MP, but the technology has shown primosing results especially for applications with require ultra-small endoscopes. Example images are displayed in Figure 2.14.

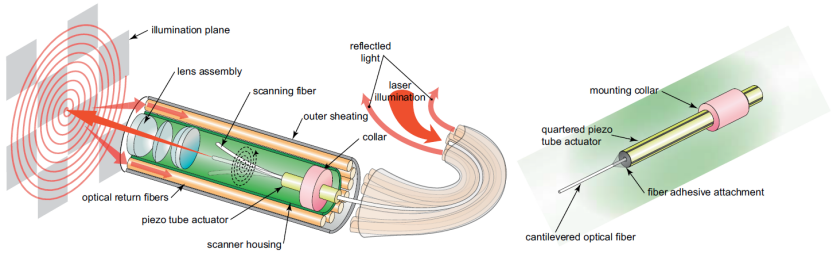

Figure 2.13: Rotating fiber endoscopy technology: The endoscope records all the spectral information of one single pixel at the same time using a rotating fiber. The fiber is spatially translated by piezo actuators located at the tip of the endoscope to sequentially scan the field of view in a spiral pattern. The right side magnifies the key elements: the mounting collar with the piezo actuators and the illumination optical fiber. The technique allows to produce very compact endoscopes. Figure reproduced from [121]: Cameron M. Lee, Christoph J. Engelbrecht, Timothy D. Soper, Fritjof Helmchen, and Eric J. Seibel: Scanning fiber endoscopy with highly flexible, 1 mm catheterscopes for wide-field, full-color imaging. Journal of Biophotonics. 2010. 3. 385-407. Copyright Wiley-VCH Verlag GmbH & Co. KGaA. Reproduced with permission.

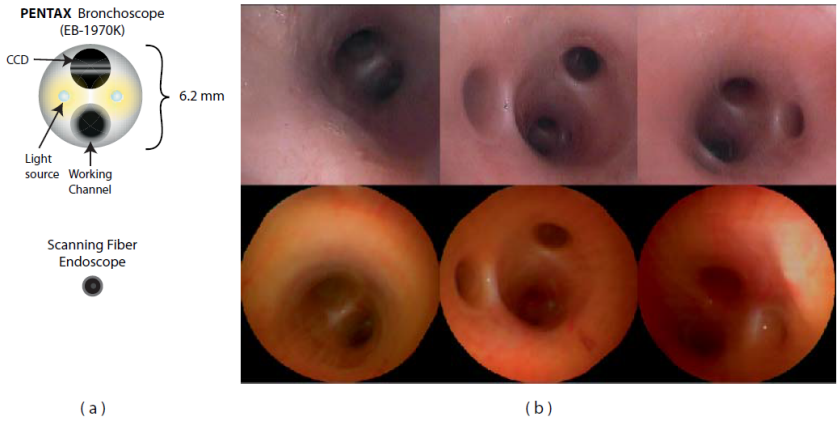

Figure 2.14: Rotating scanning fiber endoscopy (SFE): Comparison between the scanning fiber endoscope and a conventional bronchoscope. The left part compares the size of the convetional brochoscope with 6 mm diameter with the novel SFE. The images on the right showcase porcine airways and compare images recorded with the conventional broonchoscope (top) and the SFE (bottom). Figure reproduced from [121]: Cameron M. Lee, Christoph J. Engelbrecht, Timothy D. Soper, Fritjof Helmchen, and Eric J. Seibel: Scanning fiber endoscopy with highly flexible, 1 mm catheterscopes for wide-field, full-color imaging. Journal of Biophotonics. 2010. 3. 385-407. Copyright Wiley-VCH Verlag GmbH & Co. KGaA. Reproduced with permission.

2.2.3 *Limitations of current technologies*

All technologies which are known so far struggle to combine all three aspects which are crucial for fluorescence guided surgery:

1. Simultaneous acquisition of fluorescence and reflectance images over the entire visible and near infrared range.
2. Multispectral acquisition of the fluorescence data to be able to image multiple dyes.
3. Video-rate acquisition to allow a fluent perception for the surgeon and a seamless integration in the medical work-flow.

In the previous section various devices and technologies have been presented. Here, the shortcomings of these devices are shortly summarized.

Combined fluorescence and reflectance imaging

First-generation fluorescence surgery systems showed a very poor combination of fluorescence and color imaging. The surgeon needed to switch between the two modes pushing a pedal and memorizing the information visible in the other mode.

More recent advances allow to record both, fluorescence and reflectance to combine the information. But this is usually achieved by dividing the spectral range into one part for fluorescence and another part for color imaging.

Other systems record fluorescence and reflectance in the two subsequent temporal phases using alternating illumination. But in this case, there is usually a lack of multispectral image acquisition limiting separation between different dyes.

Multispectral acquisition

Current clinically used systems are restricted to image one fluorescent dye at a time, as multi-dye applications are to be translated to clinical practice. But using multiple dyes at the same time promises a better outcome.

Prototype systems for clinical research with the ability to record multiple dyes and to differentiate between them have been presented. But these systems usually do not run at video-rate and also lack of the ability to combine fluorescence and color imaging.

Video rate imaging

The clear majority of devices in the field recording multispectral fluorescence images cannot run at video rate. But the possibility to visualize and record at video rate is crucial for intraoperative applications and an easy integration into the clinical work-flow. Therefore, this point is emphasized here as it limits the applicability for some of the available technologies. For example, endoscopic setups running at video rate are unlikely to be realized by switching filters with mechanical filter wheels. In contrast, novel sensors with faster readout

may easily allow video-rate acquisition for snapshot hyperspectral imaging in future. Still those technologies do not fulfill all other requirements.

Therefore, a novel imaging method for fluorescence guided surgery running at video-rate is developed in this thesis. The method is introduced in Chapter 4 after analyzing the requirements in Chapter 3.

2.3 RELEVANCE OF THE FIELD

Cancer is the worldwide dominant cause of death among noncommunicable diseases with estimated 8 million deaths in 2012 and around 14 million new cancer cases [1]. This means that worldwide about 2 out of 1000 people were affected per year by a new cancer (world population 2012 estimated to be 7.06 billion).

Treating and potentially curing cancer can be done by surgery, radiotherapy and chemotherapy or a combination of these means. Generally, accurate cancer margin delineation is beneficial for the outcome of surgical cancer resection.

Fluorescence guided surgery has the potential to provide the surgeons with a tool which may help to differentiate cancer tissue from other tissue even if distinction with conventional color vision was normally impossible. Therefore, it is important to establish fluorescence guided surgery as a standard tool for improved cancer resection. A novel imaging method may directly improve many different types of surgery as it can be adapted to the respective needs.

For this reason alone, it is worth to develop novel imaging methods for fluorescence guided surgery. Ongoing developments in the field of fluorescent contrast agents which exploit specific targeting strategies underline this urge.

But fluorescence guided surgery can also provide diagnostic information for other types of surgeries. It can for example be used for retinal or cardiovascular angiography or simply to check the perfusion of tissue during surgery.

This need for research on novel methods is also reflected by the increase in number of publications containing the key words 'fluorescence guided surgery' (search in PubMed central) during the last decades. The number of publications increased from a few annually until the year 2000 up to 165 publications in 2016 (time line shown in Figure 2.15A).

2.4 THEORY OF COLOR VISION AND IMAGING

Color vision and perception

For human vision, the image is captured by light sensitive cells in the retina. Two different types of neural cells are known to convert

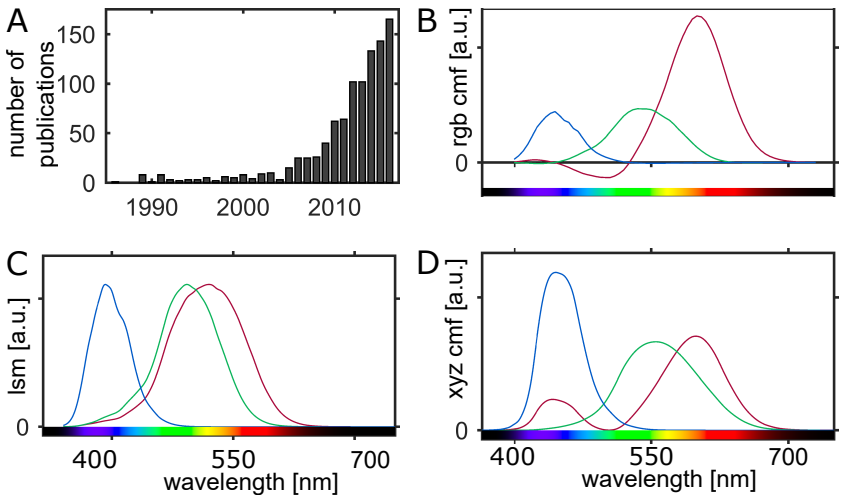

Figure 2.15: Publication trend and sensitivities of the human eye: A) Number of publications for the search term 'fluorescence guided surgery' on PubMed. B) CIE 2 degree rgb color matching functions resemble the spectral perception of the primary colors ■ red, ■ green and ■ blue. C) Stockman and Sharpe 2 degree cone fundamentals reflect the wavelength dependent sensitivity of the ■ long, ■ medium and ■ short cones in the retina (data by the University College London). D) CIE 2 degree xyz color matching functions with the ■ x, ■ y and ■ z chromaticity coordinates (data provided by the University College London).

photons in neuronal output: rods and cones. The rods are more sensitive than cones but cannot resolve color. In contrast, cones exist with three different spectral sensitivities and can therefore capture spectral differences of the incoming light. Figure 2.15C shows the spectral sensitivities of the small, medium and long cones. The neuronal signals are already being processed in the retina. The final visual perception is formed in the visual cortex of the brain. Thus, color perception depends strongly on the processing which takes place after the sensation by photo receptors.

To create a mathematical model for color representation, the theory of three primary colors was created. Accordingly, all colors can be represented as a mixture of red, green and blue light. To determine the relative contribution of the red, green and blue light to match a color of monochromatic light, experiments have been conducted. In these experiments monochromatic light was shine onto a screen. Next to the monochromatic spot a spot of three mixed monochrome lights (red, green and blue) is placed and observers are asked to adjust the relative intensity of the red, green and blue light to match the color the monochromatic beam. This was done for different wavelengths of the monochrome light. The resulting relative intensities $\bar{r}$, $\bar{g}$ and $\bar{b}$ are shown in Figure 2.15B. Between 450 nm and 550 nm the intensity of the red color is negative. This means that some intensity of the red light needs to be shined to the monochrome spot to make it possible

to match the color of the two spots. The $\overline{r}$, $\overline{g}$ and $\overline{b}$ curves represent the relative perceptual spectral sensitivity of the three channels in the trichromatic model. But a sensor with a negative sensitivity is very hard to realize.

To solve this issue, the CIE proposed in 1931 so-called 2 degree color matching functions $\overline{x}$, $\overline{y}$ and $\overline{z}$. These color matching functions are linear combinations of the functions $\overline{r}$, $\overline{g}$ and $\overline{b}$ and are positive for all wavelengths. The associated color space CIEXYZ has proven to be a versatile standard for color imaging. If the color sensitivities of current sensors are linear combinations of the color matching functions $\overline{x}$, $\overline{y}$ and $\overline{z}$, the measured signals can also be transformed linearly into the CIEXYZ color space. From there, transformations into various available color spaces are defined and implemented.

Color spaces

All in all, numerous color spaces are used and have been historically developed. The scientifically most basic color space is the CIEXYZ color space based on the color matching functions $\overline{x}$, $\overline{y}$ and $\overline{z}$. Most modern color spaces have been developed for a specific application. They represent a specific color in a different coordinate system. But some colors may only be present in some color spaces which means that they may just partially overlap. For example, the standard RGB (sRGB) color space is optimized to represent signals for projection on a screen, the CMYK color space is designed for printing and the YCbCr color space is commonly used for digital imaging.

One color space which plays a special role for the color imaging in this work is the CIE L*a*b* color space which was developed to reflect human color perception homogeneously. This means that a distance in color space should be proportional to the perceived color distance. Therefore, most metrics to quantify color differences have been developed in the CIE L*a*b* color space.

Quantifying color differences

In order to quantify the difference between two colors, different formulas evolved historically. The most easy and straight forward method is to simply calculate the Euclidean distance between the two colors in an RGB space. But unfortunately, the metric does not quantify the perceived color differences very well. The same color difference between two green tones might be perceived very differently compared to the difference between two blue color tones.

This was first discussed by MacAdams in 1948 introducing the so-called McAdams ellipses [122]. These ellipses characterize just perceivable color differences at different locations in color space. In an

ideally uniform color space these ellipses should be circles of the same size, but in the real color spaces like CIE XYZ they are not.

Even though the CIE L*a*b* color space has been developed to be uniform for human color perception the Euclidean distance $\Delta E_{a^*b^*}$ does not perfectly predict the perceived color differences. Thus, in CIE L*a*b* color space, the MacAdams ellipses are not circles.

In order to overcome this issue more experimental datasets have been produced and evaluated. The developments eventually resulted in the proposal of a improved color difference formula in 1995 by the CIE: the CIEDE94 formula ΔE_{94}. But research showed that the formula could still be improved. Combining experimental data from many experiments finally resulted in the currently recommended formula CIEDE2000 ΔE_{00}.

Also, the developed formula ΔE_{00} will not be the final answer to quantify color differences as already several critical points have been made in literature [123, pp. 52]. For example, the shape of curves with constant ΔE_{00} is supposed to match the shape of MacAdams ellipses. But for blue colors, the shape of the curves is not completely convex. Another critical point is that ΔE_{00} was developed by combining many different experimental data sets. The different experimental data sets were not acquired under completely standardized conditions. And color perception depends for example on the size of the color target, the colors of the surrounding environment and on previous visual stimuli.

Overall, CIEDE2000 is currently the most widespread metric in the field and therefore used in this work.

2.5 THEORY OF FLUORESCENCE IMAGING

Quantum mechanical description

Fluorescence describes a phenomenon in which a dye, typically a molecule, absorbs light and subsequently emits light at a higher wavelength. The Jablonski diagram shown in Figure 2.16A illustrates the different electronic states of a molecule as well as the transition processes excitation and emission.

For the theory of fluorescence excitation, the molecule is expected to be in the electronic ground state S_0. During excitation, the molecule absorbs a photon and undergoes a transition from the electronic ground state S_0 an the excited state of S_1. Usually, the initially excited state is a higher vibrational state of the electronic state S_1. From the higher vibrational state, the molecule undergoes a transition (approximately 10^{-11} to 10^{-14} s) into the vibrational ground state of S_1 by thermal interaction with the environment. Alternatively, the molecule may transit into a triplet state (not shown in Figure 2.16A), in which it can undergo reactions causing to the destruction of the fluorescent

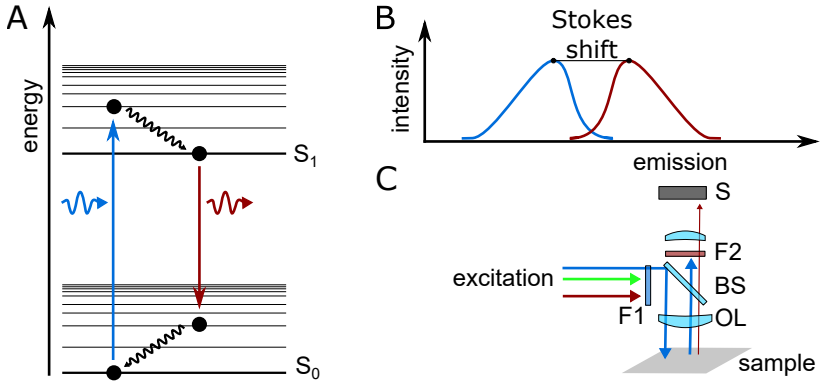

Figure 2.16: A) Jablonski diagram of a fluorescent dye showing the energy levels of the ground state S_0 and the excited state S_1 as well as different vibrational states of S_0 and S_1. The transition between S_0 and a vibrational state of S_1 (■ excitation) is caused by absorption of a photon. The transition between S_1 and a vibrational state of S_0 (■ emission) is characterized by the emission of a photon. B) Example fluorescence excitation and emission spectra of a fluorophore. C) Basic fluorescence imaging setup, including excitation light, excitation filter (F1), objective lens (OL), object (sample), dichroic mirror (BS), emission filter (F2) and a sensor (S).

molecule. Therefore, the probability for transition into a triplet state should be minimal for the stability of a fluorescent dye.

During fluorescence emission, the dye undergoes a transition from the excited electronic state S_1 to the electronic ground state S_0 and emits a photon.

Due to the existence of higher vibrational states, the energy of the absorbed photon is usually higher than the energy of the emitted photon. Consequently, the spectrum of the emission light is shifted towards higher wavelengths compared to the excitation light.

Fluorescent dyes can be characterized by their absorption spectrum, excitation spectrum and emission spectrum.

The absorption spectrum measures the relative absorption of light depending on the wavelength when shined onto the dye. In contrast the excitation spectrum measures how much fluorescence is emitted depending on the wavelength of the excitation light. These two quantities are related but not equal, as the dye may for example be more efficient to convert in emitting fluorescent light for some wavelengths of excitation light than for others.

The emission spectrum quantifies the intensity of emitted fluorescent light depending on the wavelength of the light. To measure the emission spectrum, the dye is usually excited at the excitation maximum.

In fluorescence spectroscopy, excitation and emission of a fluorescent dye are described by so-called excitation-emission matrices (EEM). An EEM quantifies the relative intensity of the emitted light of a flu-

orescent dye depending on both the excitation and emission wavelength.

Fluorescence imaging

Fluorescence imaging is widely used for biomedical applications. The biggest advantage of fluorescence imaging is that a fluorescent dye emits light at a different wavelength region than the wavelength region of the excitation light. Thus, the excitation light can be blocked by filters and only emission light remains to be imaged. This effect results in images where the fluorescent objects appear glowing on black background. The images effectively represent the bio distribution of dye molecules.

The full potential of fluorescence imaging can be exploited combining the fluorescent dyes with biological targeting strategies. Various staining techniques exist to make structural or functional characteristics visible. For example, the cell nucleus can be stained by one dye, whereas the actin filaments and the micro-tubules of the cells can be stained with other dyes. Undoubtedly, the ability to image the bio distribution of molecules combined with the potency of staining techniques which allow to bring the molecules to specific locations have made fluorescence imaging a workhorse in biomedical research.

However, fluorescence imaging also comes along with some disadvantages. The most prominent disadvantage is the low light intensity of the fluorescence emission compared to the excitation. Typical emission intensities are 4 to 6 orders of magnitude smaller than the respective excitation intensities. This requires expensive optical imaging systems which capture as many photons as possible. Accordingly, low SNR is often a limiting factor for fluorescence imaging applications.

Interaction of light with tissue can alter biomedical fluorescence imaging. Typically, two dominant effects are regarded: absorption and elastic scattering.

Various substances in tissue absorb light with different absorption spectra. One of the most prominent examples is the absorption of light by hemoglobin, which depends on the oxygenation state of the hemoglobin. As a result, the spectrum of the excitation or emission depend on the depth of the dye in tissue and the type of tissue. Absorption also limits the imaging depth in tissue typically to below 1 mm for UV light and to several mm for NIR light. Since absorption changes the spectral shape of the excitation and the emission, it may cause artifacts when separating different dyes or when quantifying the signal.

Elastic scattering does not absorb energy of a photon but changes the direction of propagation. For this reason, scattering in combination with tissue absorption influences the overall photon spectrum for example in different tissue layers. Thus, the deeper a stained structure

is in tissue, the more scattering events a photon will undergo on its way to the sensor. Hence, the structures appear smoothened and the light intensity in deeper layers is reduced, and the spectrum might be shifted. In tissue, a scattering event is typically more likely than an absorption event to take place.

Some molecules which are naturally present in tissue also fluoresce. This type of fluorescence is called autofluorescence. In some imaging applications autofluorescence plays and important role and the autofluorescent dyes must be considered in the imaging scenario to avoid unmixing artifacts. Though, in most applications autofluorescence is weaker than the fluorescence of specifically stained structures with modern synthetic dyes.

Image processing

The recorded multispectral fluorescence images need to be processed and statistically evaluated. In this work, linear unmixing is used to convert the multispectral fluorescence data sets into fluorescent component images reflecting the individual dye contributions. This requires knowledge of the spectral signatures of the fluorescent dyes, which are obtained by spectral fitting of image data of phantoms containing pure dyes.

A detailed mathematical description of the mixing, unmixing, parameter estimation, fitting of spectral signatures and a theory of image noise can be found in Section A.1.

3

DESIGN REQUIREMENTS AND TECHNOLOGY CONSIDERATIONS

This chapter is dedicated to answer the question *what* would be the ideal imaging system for fluorescence guided surgery. The title "Real-time multispectral fluorescence and reflectance imaging for intraoperative applications" suggests that the system must fulfill four basic criteria: First, it must be *real-time* with respect to human perception so that the surgeon can use it for the surgical procedure. Second, it is required to image *fluorescence* multispectrally so that multiple dyes can be imaged simultaneously. Third, accurate *color* images must be recorded in parallel to the fluorescence images. And fourth, the system is required to integrate well within the *clinical* routines so that it supports the surgeon and does not hinder him.

The previous Chapter 2 has summarized recent technological developments for multispectral fluorescence acquisition with a focus on related work in the field of fluorescence guided surgery in Section 2.2. The review of related work revealed that none of the devices is suitable to match all the requirements listed above. Consequently, a new system is derived in Chapter 3 and Chapter 4 to match all requirements.

This chapter first analyzes all the requirements which are put on the system to be developed and translates the requirements into technical specifications in Section 3.1. Subsequently, in Section 3.2, different available multispectral imaging technologies are evaluated in detail and considered to be incorporated in the system. The most suitable combination of technologies is selected in Section 3.3 to subsequently develop a system concept in Chapter 4.

3.1 DESIGN REQUIREMENTS

This section analyses the performance requirements of the system regarding fluorescence detection, color imaging quality, framerate, optical aspects like resolution and finally clinical considerations such as available space and compatibility with room lights.

3.1.1 *Fluorescence imaging*

This section reasons in detail why specific requirements are put on the system with respect to fluorescence imaging. These are split into a part discussing the spectral detection range to be covered, the ne-

cessity to detect multiple fluorophores in parallel, the required sensitivity and finally aspects related to quantification.

Spectral detection range

The key feature of the system is multispectral fluorescence detection over the entire visible and near infrared range from 400 nm to 900 nm.

Four fluorescent dyes are currently in clinical use: Protoporphyrin IX (PPIX), fluorescein, methylene blue (MB) and indocyanine green (ICG) [18, 74]. A more detailed discussion on their clinical usage can be found in Section 2.1.1. Their emission spans over the entire visible and near infrared range. Fluorescein emits in the green around 500 nm, PPIX and MB emit between 600 nm and 700 nm, whereas ICG emits in the IR above 800 nm. Alternatively, endogenous fluorescent dyes, produced by the cells, can be imaged. Some of the most prominent autoflurescent dyes are Melanin (emission 500 nm – 700 nm) and NADH (emission 400 nm – 600 nm).

Imaging in the IR offers higher penetration depth because of less tissue absorption and thus better diagnostic opportunities. In the blue visible range, 1 mm of blood or tissue is sufficient to block all fluorescence. The literature envisions additional IR windows for intraoperative fluorescence imaging in future: the first emits closest to the visible between 650 nm and 800 nm, the second dye, for example ICG emits between 800 nm and 900 nm while a third dye emits further in the IR above 1000 nm [18, 31, 124].

All in all, the system is required to image any of the currently clinically available dyes emitting in between 400 nm and 900 nm. As dyes for the proposed second IR window between 1000 nm and 1400 nm are not close to any clinical application, this window will not be considered for imaging in this project [18, 124].

Multispectral detection

One of the key features of the system is to image multiple fluorescent dyes simultaneously. The benefit of imaging multiple dyes has been shown in various clinical and preclinical studies.

One of the most intuitive applications labels different tissue types with different agents to distinguish for example between nerve tissue and cancerous tissue [21, 23].

Alternatively, the diagnostic information for a single tissue type can be improved combining the information of multiple dyes. In medical applications, the targeted agents also show a non-cancer specific uptake. Tichauer *et al.* developed a method to improve the signal to background ratio combining the information of a targeted agent with an untargeted agent [24, 125].

Valdes *et al.* developed a method to quantify PPIX fluorescence during glioblastoma resection and presented a clinical example in

which residual cancer could not be seen with conventional fluorescence imaging, but it was identified by multispectral imaging separating the cancer PPIX fluorescence signal from autofluorescence [107]. Montcel *et al.* even suggest that different photochemical states of PPIX and autofluorescence can be detected individually by multispectral imaging. The different photochemical states may allow to draw diagnostic conclusions about the status of the cancer cells [45].

Most of the listed examples image two dyes only. Though, it is very likely that in future more dyes will be used in clinical scenarios. Therefore, the minimum number of fluorophores that the system needs to image and unmix simultaneously is set to three for this work.

Unmixing artifacts

To convert the recorded multispectral fluorescence images into fluorescent component images corresponding to relevant clinical information, a mathematical calculation is necessary. In this work linear unmixing as the most wide-spread algorithm is used. Though, it requires to calibrate the spectral signatures of the individual fluorescent component signatures. In biomedical imaging scenarios the recorded multispectral signal of a pure dye may deviate from the calibrated signal due to ambient light, tissue absorption or molecular interactions of the dye. Such a change in the detected signal leads to unmixing artifacts. The algorithm will always provide unmixed component images, but the contained information may be falsified by the artifacts.

In the field of fluorescence microscopy, this problem is often approached by finding the spectral signatures from the recorded information of the image itself. Such approaches include non-negative matrix factorization NMF [126], spectral phasor analysis [127], parallel factorization PARAFAC [128] or independent component analysis ICA [129]. Most of these approaches put prerequisites like knowledge about pure dye signal for some pixels on the imaging scenario. However, the biggest issue for intraoperative applications is that the algorithms may produce wrong results. So, it cannot be guaranteed that the algorithm always detects for example nerve and tissue and classifies it correctly. Thus, these techniques were not considered in this work. Instead, the spectral signatures of the individual components are pre-calibrated.

As unmixing artifacts may well be present in the images which are to be presented to the surgeon, a diagnostic method needs to be developed to judge on the quality of the unmixed information. This diagnostic is best calculated on basis of a single image and does not require extensive statistical evaluation of multiple images so that the diagnostics can also run at video rate.

Number of detection channels

Unmixing multiple fluorescent dyes requires multispectral or hyperspectral detection. In order to unmix three fluorescent dyes, at least three channels are mathematically necessary if no further assumptions are available. Additional detection channels can improve the separation between different dyes in channel space and therefore improve the SNR after unmixing. Also, additional channels can make the imaging scenario more robust against numerous inferring signals which are often present in biomedical scenarios. Neher *et al.* have shown for a few examples that the SNR of the unmixed fluorescent components improves when increasing number of well-chosen channels [130]. However, for their example of three dyes, the improvement was well observable up to 6 or 8 channels, but additional channels then only caused minimal improvement. Even though their work just treats some special cases it makes an important point: unmixing three fluorescent dyes does not necessarily require recording a high number of channels ranging over the entire spectrum.

Detection limit

The detection limit is the lowest concentration of a fluorescent dye which can be imaged with a system. However, the limit depends on many factors besides concentration. The excitation and emission spectra of the dye need to match with the spectral shape of the excitation light and the spectral system sensitivity. Additionally, the quantum yield influences the emission intensity. However, the detection limit is also influenced by tissue optical properties. Absorption and scattering of light in tissue reduces the number of photons and thus the lowest detection limit is higher for a labeled structure which is deeper inside tissue.

Overall, a typical dye concentration for a clinical scenario is fixed here as design requirement so that the system can reasonably perform in medical experiments.

Molecular concentrations of fluorescent dyes differ over orders of magnitude for different clinical applications. The highest concentrations in a clinical application can be found for ICG bolus injections which are as high as 1 mM [74]. For targeted molecular fluorescence imaging scenarios, concentrations are lowest, because the dye is left in the body to circulate and bind to the tissue of interest whereas it is washed out from the surrounding tissue. Therefore, the concentrations for tracer applications are supposed to range roughly between 1 nM and 1 µM [74].

Typical concentrations for current clinical applications range in between these two extreme scenarios. For example, concentrations of the clinically used fluorescent dye PPIX in cancer tissue for neurolog-

ical glioma resection are reported to range between approx. 350 nM and 10 µM [107].

The requirements for the system are set to detect realistic intraoperative concentrations which is in the center of the clinically available concentration range. It is not necessary to tune the system directly for maximum sensitivity and thus for very low concentrations. Thus, the system is required to image multiple dyes each with a concentration below 10 µM. As a result, the final system will be evaluated using phantoms with fluorescent dye concentrations in the range of 1 µM to 10 µM. Future developments can further improve system sensitivity, for example by modifying the filter bandpass structure, the optical efficiency or increasing the excitation intensity.

Spatial resolution

In clinical practice, volumetric 3D imaging techniques such as magnetic resonance imaging or computed tomography are well-established. Alternatively, surface based video-rate 2D imaging is used for example in endoscopy or surgical microscopy. This work aims to enhance 2D surface image data with fluorescence information but not to open an additional imaging dimension.

Fluorescence microscopy allows 3 dimensional imaging of microscopic or even small macroscopic structures with an extend in the range of mm [131]. However, recording 3D fluorescence images at video rate for objects with the dimension of several cm as required for intraoperative imaging is not possible. Therefore, fluorescence images are only used as 2D surface images in this work.

However, light is not completely reflected from the first layer of tissue and thus the surface images contain also some information from deeper tissue layers. The behavior of light in tissue mainly depends on the scattering and absorption properties of the tissue. In general, the intensity drops to $1/\exp$ (approx. 37%) after 50 µm to 100 µm for UV light, after 100 µm to 500 µm for green light and after 1 mm to 3 µm for IR light [42]. This results in an roughly estimated imaging depth of 1 mm for blue light, 1.5 mm for green light, 3 mm for red light and up to 1 cm for IR light [132]. Fluorescence of a dye in the NIR can be imaged deeper in tissue than a dye in the blue. One of the main causes for this effect is the absorption of hemoglobin.

Scattering of light penetrating into tissue also influences the spatial resolution at which different objects can be resolved. In the VIS/NIR range, the scattering coefficient of tissue is generally higher than the absorption coefficient. If a photon is scattered it changes the direction resulting in diffuse images of a sharp object under a scattering layer. The deeper an object is placed in tissue, the more scattering events the light undergoes on its way and thus the more the image will be blurred.

Sub-millimeter resolution is desirable for fluorescence imaging to distinguish between different structures. Optical resolutions in the scale of micrometers is not necessary for fluorescence diagnosis because the detected fluorescence information is blurred by scattering of light in tissue. The extend of blurring depends on the wavelength and the tissue. For the system, the optical resolution required by reflectance color imaging is higher than the resolution needed for fluorescence imaging and will be presented in Section 3.1.5.

Quantification

The ability to absolutely quantify fluorescent dye concentrations in situ adds diagnostic information as the field moves to specific molecular staining [74, 132]. Therefore, future systems are required to provide some sort of specific measure to quantify in situ.

Absolute quantification is based on many factors: excitation illumination, optical detection efficiency, geometrical arrangement of the tissue relative to the imaging device, object distance from the imaging device, wavelength dependent tissue scattering and absorption properties, wavelength dependent sensitivity of the sensor and optical system and the depth of the fluorescent tissue in other surrounding tissue just to name the most important factors. Therefore, it is extremely complicated to report absolute fluorescent dye concentrations in situ. Current commercial systems do not yet provide this ability, but different approaches have been published: Multiple tracers can be used for quantification using the relative intensities and pharmacokinetical models [74, 125, 133]. An alternative approach uses multispectral detection and corrects for tissue absorption and scattering of brain tissue in PPIX guided glioblastoma resection [107].

These approaches require and extensive effort to report absolute concentrations or intensities instead of relative ones for a specified device and application. Substantial research is required to develop and validate quantification concepts.

In this work, the focus was not put onto the ability to absolutely quantify fluorescence concentrations, even though it is an important aspect. No quantification concept is yet available to cover all the potential usages of the system. However, future research to develop quantification concepts with the system for specific applications is of high clinical relevance.

3.1.2 *Color imaging*

The perceived color of an object mainly depends on the reflectivity spectrum of the object and the illuminant spectrum. Additionally, psycho-physiological effects which depend on the observer influence color perception in human vision.

Intraoperative imaging systems are required to accurately represent colors as they appear to the surgeon under normal lighting conditions. As additional psycho-physiological effects depend on the individual observer, they are not considered in this work. To match the colors closely, first the normal lightning conditions need to be specified and second a metric to quantify color differences needs to be selected.

Daylight is the most basic illumination at which colors are usually observed. The quality of artificial white light sources is evaluated with the color rendering index which measures how well the color reproduction of a set of colors matches the impression under daylight. Therefore, the color reproduction of the system needs to match colors under CIE D65 daylight as well as possible.

Various metrics have been developed during the last decade to quantify the difference between two colors. In this work the color difference metric CIEDE2000 ΔE_{00} is selected as it quantifies perceptual differences well. Color differences smaller than $\Delta E_{00} = 0.5$ are hardly perceivable, up to $\Delta E_{00} = 1.5$, the differences are slightly perceivable. Above $\Delta E_{00} = 1.5$, the color differences are noticeable [134]. As color differences should not be noticeable for a surgical system, the average ΔE_{00} is required to be smaller than $\Delta E_{00} = 1.5$.

3.1.3 *Framerate and delay*

This section summarizes the established knowledge about timing for the interaction between humans and video input and specifies requirements for an intra-operative system.

The title of this thesis names the *real-time* aspect and puts emphasis on its importance. Usually, real-time is defined in the context of a closed loop system. In this work, the multispectral imaging system and the surgeon together form the closed loop.

Digital imaging systems have two different timing aspects which influence the performance: framerate f_{system} and delay time t_{delay}. The framerate describes how many images are recorded per second while the delay time (also called latency) characterizes how much time passes between an event and the display of that event on the screen. Both are equally important for the overall system performance.

The framerate is fundamentally limited by the integration time of the system, while the delay time is limited by the framerate, but can also be higher:

$$t_{integration} \leq \frac{1}{f_{system}} \leq t_{delay}$$

Various studies investigated the effect of framerate and latency on the user perception and the performance to work with the system [135–144].

The first question to ask is at what framerate a video stream of images is perceived to be satisfyingly fluent. The answer depends on the scene to be recorded.

Claypool *et al.* tested both, performance and perception of players in video games for different framerates [140]. Perception clearly improved with increasing framerate up to 30 frames per second. Accordingly, the performance also improved with higher framerates, even when increasing the framerate from 30 fps to 60 fps. So between 30 fps and 60 fps the improvement in perception is not as big as the improvement in performance. This means that even though a video stream appears fluent, higher framerates supposedly help to further improve the resulting performance. The study also showed that tasks which require rapid and accurate response are more sensitive to framerate compared to tasks that require less precision and slower responses. Similarly, medical experiments revealed that tasks like suturing or knot tying are more sensitive towards timing than others.

This finding is undermined by a study asking about what is the minimum time for human vision to perceive a very quickly showed image. Potter et al. [144] have shown that human vision can identify images displayed for only 13 ms in a stream of 12 images. So, humans are able to perceive image information from such small integration times. Frame rates up to $f_{\text{system}} = 77$ fps can thus be beneficial even though the stream of images might be perceived fluent at lower framerates.

The second question to answer is in what way system latency influences the perception of the surgeons and also their performance. This is particularly important because the doctors are actively involved in a surgical setup and not only passive observers. Therefore, various authors have been investigating how system latency influences the outcome of laparoscopic surgery or telesurgery. A good summary of studies can be found in the study of Kamucu *et al.* [136]. Most of these studies agree that high latency dramatically increases the time needed for the intervention [136]. Additionally, more complicated tasks like suturing could not be performed at higher latency times.

The time these studies report vary between a total delay of 60 ms and several hundred milliseconds, depending on the setup and the investigated tasks. The tested latency in these studies range from typically 100 ms up to around 1 s. Most studies agree that the lowest delays with less than 100 ms allow to perform the tasks comparably well while delays as high as 1 s are reported to be dangerous and inefficient to perform surgery. However, the studies do report different thresholds in between, because the studies have been designed differently. One recent study even reports advantages for latencies as low as 60 ms in combination with haptic feedback [143]. Additionally, several papers report that doctors switch to a »move–and–wait« approach from a certain delay on, depending on the task itself.

Further research with more carefully designed studies taking into account framerate, latency and training status of the test persons are needed for conclusive results on the combined effect of latency and framerate on surgical outcome.

In conclusion, an effective framerate of at least 30 fps and a total latency of no more than time 160 ms ($t_{delay} \leq 160$ ms) are important for fluent perception. Optimally, the system should run with more than 77 fps and a latency below 60 ms. But since the best available research is still fragmented and inconclusive, it is quite possible that future research will show that even higher standards would be beneficial for surgical scenarios, especially as most studies did not focus their investigation on short times.

For this work, it is important to ensure that the developed *concept* can fulfill even the optimal demands ($f_{\text{system}} \geq 77$ fps; $t_{\text{delay}} \leq 60$ ms). However, for the technical realization of a *prototype system* in this work aims at fulfilling state-of-the-art requirements ($f_{\text{system}} \geq 30$ fps; $t_{\text{delay}} \leq 160$ ms).

3.1.4 *Clinical requirements*

The intended use for the developed system concept is intra-operative imaging and thus this work must also consider clinical aspects.

State-of-the-art operating theaters are equipped with a high number of devices mounted to carts on the floor or hanging from the ceiling. Additionally, surgeons, assistants and nurses gather around the patient. This leaves little space for additional clinical equipment. Hanna *et al.* have reported that the placement of the monitor is relevant for performance and required time for endoscopic surgeries [145]. Therefore, it is important to make the imaging device small to leave sufficient space to the surgeon and to allow flexible placement of equipment such as monitors.

All in all, a small form factor is required for a final device. The prototype must not yet fulfill this criterion, but the concept must allow for miniaturization.

For intraoperative imaging in applications like glioblastoma resection the surgeon is working with surgical tools between the microscope objective lens and the patient. Thus, a larger working distance improves the usability of the system. Current state of the art surgical microscopes allow a minimal working distance of 20 cm which can be extended up to 60 cm [146, 147]. Modern clinical and preclinical ICG imaging systems provide a working distance of 10 cm to 75 cm [74]. Thus, the required minimal working distance for the system is set to 10 cm, it should be 20 cm and can optimally be increased up to 75 cm.

The system must not only add medical benefit to the surgical outcome but also integrate well into the clinical work-flow to succeed. Every minute of surgery is estimated to cost between 40–50 Euro

[148]. One publication by Busse claims a higher variation of reported costs from 10 Euro – 120 Euro per minute [149] depending on author motivation and calculation schematics. In any case, every minute of surgery is extremely expensive and adding time must be reasoned well also in terms of the economical perspective. Good clinical device integration allows to speed up surgeries and therefore allows hospitals to operate more economically. This would help to introduce a novel concept into the market, additionally to the diagnostic benefit.

One of the major obstacles for a seamless integration of fluorescence imaging devices into the surgical procedure is the requirement to switch off the room lights when imaging fluorescence to avoid leakage of the room lights into the fluorescence detection [66, 74]. For systems which only detect fluorescence in the IR, the spectrum can be divided into the visible for color imaging and the IR for fluorescence imaging [74]. If the application requires fluorescence imaging in the visible, such as PPIX guided resection of glioblastoma or bladder cell carcinomas, the spectrum cannot be split. Published concepts to unify fluorescence and color imaging include pulsed illumination with gated sensors or modulated sensors with a lock-in detection concept [66, 86]. For this work it is important that the system concept can be combined with surgical illumination.

3.1.5 *Optical requirements*

The first prototype system aims at macroscopic surgical imaging, which is comparable to surgical microscopy. It should also be usable for small animal imaging. Therefore, a the field of view (FOV) of at least $5\,\mathrm{cm} \times 5\,\mathrm{cm}$ and sub-millimeter resolution is required. Endoscopic surgeons are accustomed to strong vignetting on the edges of the images in exchange for a larger field of view. Therefore, the field of view is defined in this work as the area within 50% vignetting.

A major application of fluorescence guided imaging is cancer resection, in which it is essential for the surgeon to be able to see small cancers and the cancer boundaries [15]. The optical resolution of the imaging system is required to be at least as good as the visual resolution of a surgeon.

The optical performance of human vision at $\mathrm{MTF} = 0.5$ is determined to be less than $10\,\mathrm{lp/deg}$ [150, 151]. This means that with human vision a maximum of 10 line pairs can be resolved within one angular degree of the visual field of view (at reduced contrast of 0.5 reflected by the condition $\mathrm{MTF} = 0.5$). With an estimated distance of 50 cm between the eye of the surgeon and the patient, this translates into $1.15\,\mathrm{lp/mm}$ which is set as lower limit for the optical performance of the system. A higher resolution would be desirable, but as the focus of this work is on a proof of concept to unify multispectral fluorescence imaging with color imaging, the requirements are kept

reasonable at this point. In future, the optical system can be improved independent of the detection concept.

A sensor size with high definition standard has been established with 10^6 pixels (1 MP) as state-of-the-art for neurosurgical imaging [146, 152, 153]. Thus, the minimum required sensor size for the system is 1MP. Novel clinical systems even in endoscopic applications allow to record video streams at 4K resolution (3840 px × 2160 px or 4096 px × 2160 px corresponding to more than 8 MP) [154, 155].

The technology will be translated to endoscopy in a second step. Because miniaturization technically more challenging and not as flexible during the development process, this task is left for a follow up project and this work focuses on the method development.

Fluorescence detection calls for high photon collection efficiencies to allow detection of small fluorescence signals. This translates into a numerical aperture on the object side.

To summarize, the system requires a $FOV \geq 5\,\text{cm} \times 5\,\text{cm}$, an optical imaging resolution higher than 1.15 lp/mm at MTF $= 0.5$ and a sensor pixel resolution of at least 1 MP.

3.1.6 *Summary of the design requirements*

The derived design requirements for an intra-operative imaging system are summarized here:

FLUORESCENCE Multispectral fluorescence detection from 400 nm to 900 nm, unmixing of at least three fluorescence dyes at typical clinical concentrations ranging between 1 µM and 10 µM.

Develop a diagnostic method which allows to judge on the quality of the unmixed fluorescence information on basis of an individual image.

COLOR IMAGING Good color reproduction, average difference between reproduced system colors after correction better than $\Delta E_{00} \leq 1.5$ compared to the colors as perceived at CIE D65 daylight.

TIMING Imaging minimally at 30 fps, better at 60 fps with delays below 160 ms, best less than 60 ms.

OPTICS Field of view of $FOV \geq 5\,\text{cm} \times 5\,\text{cm}$ (at 50% intensity drop due to vignetting).

Submillimeter resolution with spatial frequencies ≥ 1.15 lp/mm at MTF $= 0.5$; Sensor pixel resolution must be at least 1MP, optimal resolution of 4K.

The numerical aperture should be as high as possible for high photon collection efficiency of the system and thus good SNR.

CLINICAL ASPECTS The developed method aims at intraoperative imaging, but the prototype is not dedicated to laboratory and

preclinical experiments. Therefore, only the concept is required to fulfill the clinical requirements.

Adaptability to clinical devices and procedures like surgical microscopes and endoscopes. Potential for miniaturization for chip on the tip endoscopes. Overlay of fluorescence and reflectance images must be possible.

Concept must allow to integrate with room lights.

Free working distance must be at least 10 cm, should be 20 cm and can optimally be extended up to 75 cm.

3.2 TECHNOLOGY CONSIDERATIONS: MULTISPECTRAL IMAGING APPROACHES

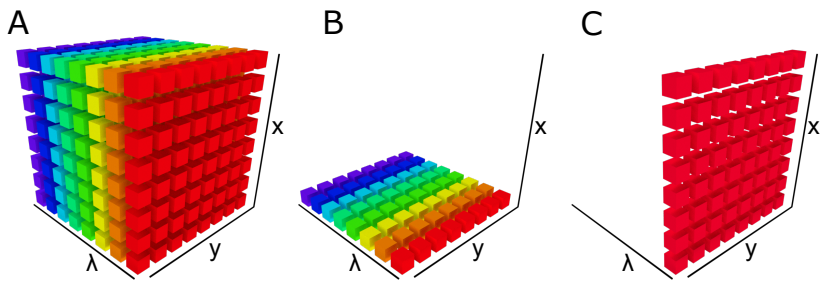

Figure 3.1: Comparison of how different multispectral image acquisition methods fill the hyperspectral image data cube. A) Snapshot hyperspectral imaging fills the entire cube in one acquisition. B) Spatial scanning records all spectral channels in one acquisition but needs to scan over the spatial coordinates (here a push broom acquisition in x direction is shown) C) Emission spectral scanning records the entire spatial image for one spectral band at a time (here the acqusition of the red channel is displayed).

This section compares different approaches to record multispectral fluorescence data. The core capacities of the system is to image multiple fluorescent dyes simultaneously (see Section 3.1.1). This requires multispectral imaging.

In hyperspectral imaging, the data recorded for each frame consists of a complete three-dimensional data cube as shown in Figure 3.1A. To combine fluorescence and reflectance imaging, each single frame of the video stream needs to record a complete three-dimensional hyperspectral data cube for color and fluorescence images separately.

In contrast, conventional camera sensors based on silicon detectors can only detect light on a two-dimensional pixel array and thus spectral information is lost in the recording.

Various suitable acquisition strategies can be found in literature to record hyperspectral data cubes, each making compromises specific to the technology. An overview of experimental systems based on

these technologies is presented in Section 2.2. Five established methods are selected for further comparison compared:

1. spectral emission scanning
2. spatial scanning
3. snapshot hyperspectral imaging
4. excitation scanning
5. micro-structured color sensors.

Each of these five different methods is evaluated regarding color imaging capabilities, real-time performance, multispectral acquisition quality, detection efficiency, potential for miniaturization and robustness to be used in a clinical scenario.

3.2.1 *Spectral emission scanning*

Spectral emission scanning records images of spectrally filtered light while changing the filters over time. It is the most intuitive and widely used method of hyperspectral imaging. To fill the hyperspectral data cube, multiple acquisitions with different filters are necessary (see Figure 3.1). Most commonly, this is technically implemented using filter wheels with bandpass filters, liquid crystal tunable filters (LCTF) or acousto optical tunable filters (AOTF) [70, 104, 107, 111, 112, 114]. Bandpass filters have the advantage that it is very easy to customize the filter shapes, but the setup is very slow, bulky and impossible to miniaturize. In contrast LCTF and ATOF systems can be controlled electronically and are more suitable for intraoperative applications. Still, all spectral images need to be recorded sequentially resulting in a low framerate. If only 20 spectral bands are recorded for each hyperspectral frame, this leaves 1.7 ms on average only for each individual frame and requires the sensor to record at 600 fps. In practice, these systems do not run at high framerates.

Movement will result in spectral unmixing artifacts because objects will be misplaced in different spectral channels of the same image.

The overall detection efficiency decreases linearly with the number of recorded bands, because on average most of the light is being blocked and only a little proportion can reach the sensor. Thus, this technique is not suitable for fluorescence imaging.

Color imaging with good color reproduction can be achieved either by specific color filters causing the recording sensitivity to match that of the human tristimulus values or alternatively by recording a complete spectral reflectance data cube and computing the intensity in the different color channels.

Overall, spectral scanning is a very powerful and versatile technique if intensity and time are no constraints. However, for real-time

fluorescence imaging applications, the sensitivity and speed are not sufficient.

3.2.2 *Spatial scanning*

Spatial scanning fills the 3D data cube by sequentially recording the full set of spectral information from individual locations. In such a setup, as the detector arrangement can be sophisticated and flexible because no spatial image needs to be maintained in the optical detection path.

For example, confocal laser scanning microscopes scan each pixel individually using galvanometric mirrors to direct the laser spot across the sample. Industrial and airspace hyperspectral imaging applications often use push broom techniques, parallelizing the spatial recording in one dimension (see Figure 3.1).

The biggest challenge for spatial scanning is the available recording time per pixel: recording for example sequentially 10^6 pixels per frame at 30 fps, the resulting overall integration time per pixel is 34 ns to record both fluorescence and reflectance spectral data. Such short integration times are very challenging for state-of-the-art photo detectors. Avalanche photo diodes can count up to 10^{10} photons per second, resulting in a maximum of approximately 300 photons per pixel for homogeneous images.

The illumination can be increased compared to widefield techniques as only the recorded spot or line needs to be illuminated and thus the recorded light intensity can be increased. However, in medical imaging when living tissue is illuminated, the intensity must be limited for patient safety.

Object motion results in spatial artifacts which can become visible in combination with the scanning pattern, but it does not cause spectral artifacts. If data is only processed in the spectral dimension, this is very favorable for the algorithm. Obviously, the spatial artifacts will remain after processing, but users will be able to recognize artifacts up to a certain extend.

Devices with galvanometric scanners have a big form factor and it does not seem possible to miniaturize them to endoscopic systems. Recently introduced micromechanical mirror scanning devices (MEMS) could replace galvanometric scanners in future [156] with small form factors. Another approach tailored for endoscopy uses piezo actuators to move the illumination fiber end and thereby scanning the field of view [40, 157].

Reflectance color imaging does not come with spatial scanning, but it can be included for example by illuminating with spectrally shaped light.

All in all, spatial scanning offers good spectral resolution and a high detection efficiency, but it is not suitable if high framerates and high-resolution is not possible.

3.2.3 *Snapshot hyperspectral imaging*

Snapshot hyperspectral imaging technologies record an entire hyperspectral data cube at the same time. Various methods have been developed to optically split the three-dimensional information so it can be recorded by two-dimensional sensor arrays.

Some examples among the popular methods are integral field spectrometry (IFS), multispectral beam splitting (MSBS), computed tomography image spectroscopy (CTIS) and image mapping spectrometry (IMS) [72]. IFS and IMS use various assemblies like fiber guides, micro structured mirrors and lenslet arrays to redistribute the 3D hyperspectral data cube on a 2D silicon detector for recording. In contrast, CTIS uses a dispenser element in the aperture causing the light to spread in a mixed spectral and spatial form onto the 2D sensor plane. The necessary computational reconstruction is based on algorithms originally developed for computed tomography. A method to record less than 10 spectral bands is MSBS, in which the imaging path is split depending on the wavelength of light. This results in multiple images representing the respective spectral regions. Strictly speaking, color sensor arrays also belong to the category of HSI, but this technology is listed separately in Section 3.2.5.

All snapshot hyperspectral imaging techniques share the advantage, that object motion does not cause any artifacts due to image acquisition. Though, some techniques show artifacts, due to the recording itself, but not linked to object motion. For example, CTIS can produce artifacts [72].

Thus, the sensor generally needs a high number of pixels which is directly linked to high data rates. To avoid this difficulty, most realized technologies compromise either the spatial or spectral resolution. As an example, to record hyperspectral images at 1MP spatially and in 20 spectral bands (resolution of 20 nm from 400 nm to 800 nm), the total number of pixels required are $x \cdot y \cdot \lambda = 1000 \cdot 1000 \cdot 20 = 20MP$. Transferring and processing image data of $20MP \cdot 16$ bit in real-time at framerates of 30 fps results in a data stream of 1.2 GB/s. Increasing the optical resolution to 4K (4096 × 2160 px) results in approximately 10.6 GB/s which is above the capability of standard computers to be transferred, processed and recorded.

Still, there are interesting approaches becoming increasingly appealing in future due to new developments in the sensor technology and FPGAs based image processing directly in the camera.

As the field of snapshot technologies is very wide, the robustness and form factor vary widely. While MSBS and CTIS setups can be

built very compact, some IMS setups are very bulky and cannot be miniaturized sufficiently. In the same manner, the detection efficiency varies among the techniques. While all photons of well implemented MSBS, IFS and IMS setups are directed to the sensor, CTIS only has an optical efficiency below on third. Detection of colors is not intrinsically included in the setup, but if enough spectral bands are acquired, the reflectance color images can be calculated computationally.

To summarize, snapshot hyperspectral imaging techniques are powerful but also difficult to implement. The systems require precise optical and advanced mechanical designs as well as high data transfer. Unfortunately, current systems make some trade-off regarding either framerate or spatial resolution and thus do not fulfill the requirements. Though, it is a very potent technique that will come up in future.

3.2.4 *Excitation scanning with monochrome sensors*

Widefield fluorescence imaging systems are in most cases equipped with monochrome sensors, as they show the highest available quantum efficiency. To record multiple fluorescent components, the emission is recorded for different excitation lights. The 3D data cube consists in the spectral dimension of different illumination wavelengths, not of different emission wavelengths. This is a fundamental difference between excitation and emission scanning in the type of data.

The excitation needs to be selected so that different fluorophores ca be separated well.

As excitation scanning generally separates fluorescence quite well, a rather low number of channels is necessary. For example, to record six fluorescence channels, six sequential acquisitions are necessary to record 6 fluorescence channels. Running a system with the clinically required 30 fps results in an overall framerate of 180 fps. Transferring the required resolution of 1 MP with such a framerate is technically hardly feasible. Also, the fluorescence integration time $\tau < 6\,\text{ms}$ resulting in rather noisy images. Moreover, the different excitation lights need to be blocked in the detection path which complicates the optical design.

Color imaging can also be facilitated by sequentially illuminating with different lights to record the red, green and blue color channels. The missing spectral sensitivity of the sensor would need to be encoded in the respective illumination spectra. This requires spectral shaping of the different color channel illumination lights, which need to be strong for medical applications.

Object motion will result in spectral artifacts as all channels are recorded at different time points. A big advantage of the concept is, that the excitation light can be merged into a fiber and subsequently directed to the setup. Thus, the bulkiest part can be easily kept out-

side the medical setup. Various manufacturers offer high-resolution monochrome sensors on the tip of an endoscope. Thus, the concept is suitable for the medical environment in terms of robustness.

To summarize, excitation scanning requires sequential recording, leading to high framerates, short integration times and potentially causes spectral artifacts. Therefore, the concept was only partially selected to be realized in the system.

3.2.5 *Color sensors*

Micro structured mosaic filter patterns such as the RGB Bayer filter pattern are commonly used in consumer imaging sensors but are not widespread in scientific applications. The 3D multispectral data cube is only partially recorded (see Figure 3.1). Each pixel only has one spectral information, while the neighboring pixels have different spectral information. However, the spectral cube is filled homogeneously (having double the number of green pixels than red and blue). The missing fields are spatially interpolated using various techniques. The most well-known is bilinear interpolation, but more sophisticated algorithms show improved performance for example at sharp edges [158].

The spectral sensitivity of the combination of filters and sensors corresponds to the human tristimulus curves $\overline{x}, \overline{y}$ and $\overline{z}$ as well as possible. The individual color filters reject photons resulting in roughly 50% detection sensitivity compared to the respective monochrome sensor.

Motion does not result in major artifacts because all spectral information is acquired at the same time. Though, sharp edges cause spectral and spatial artifacts during interpolation. Potential consequences of this effect need to be investigated for the application of fluorescence unmixing.

Color sensors using a Bayer pattern are mechanically robust and can be miniaturized into chip on the tip endoscopes with diameters around 1 mm. High resolution images (4k imaging standard) can be transferred with more than 30 fps with the data transfer speed being the limiting factor for higher framerates.

Advanced patterns with a higher number of micro-structured filters than the RGB Bayer pattern have been developed. For example, 16 different filters can be arranged in a 4×4 pixel pattern or 25 filters can be realized on a 5×5 pixel pattern. This method increases the number of spectral channels on the cost of spatial resolution and usually also on cost of detection efficiency. As the filters need to be fabricated on the sensor, the initial production cost is rather high, and the filter design cannot be flexibly changed afterwards. Overall, the concept offers very compact and robust sensors which are suitable for various applications [51, 97].

First developments to construct sensor arrays in which a single pixel can detect multispectrally started even before the Bayer pattern was developed [159]. Usually these pixels consist of a wavelength dependent sensitivity in depth that is resolved. Different approaches, also for the IR range, have been made, but no more than 3 spectral channels were successfully realized. So far, these technologies are still waiting for their breakthrough [51, 160–165].

3.3 TECHNOLOGY SELECTION

This short section collects the condensed technological evaluation of different technologies regarding the required usage of multispectral imaging technologies.

Table 3.1: Comparison of different imaging methods to acquire a multispectral fluorescence and color image data cube regarding aspects which are relevant in the design requirement: color imaging capability, real time performance, spatial resolution, quality of the multispectral image data, fluorescence detection efficiency, form factor reflecting the miniaturization potential, robustness for usage and the impact of artifacts. Ratings (+/○/−) are reasoned in the text in detail.

Aspect	Bayer Pattern Sensors	Excitation scanning	Spectral Scanning	Spatial Scanning	Snapshot
color	+	○	○	○	○
real-time	+	○	−	−	−
resolution	+	+	○	−	−
multispectral	○	+	+	+	+
efficiency	○	+	−	+	−
form factor	+	+	−	+	−
robustness	+	+	○	+	○
artifacts	○	−	−	−	+

The detailed evaluation of the different multispectral acquisition technologies is summarized in Table 3.1. The different aspects are ordered by importance for the described intra-operative application. The compared technologies are also ranked in the table starting with the technology that has best performance in the most important aspects.

The scope of this work is to bring multispectral imaging into the operating room. Though, clinical usability is the key factor translating the technology to clinical practice.

Therefore, color and real-time imaging capabilities at high-resolution are even more essential than advanced multispectral performance and ranked first in the table. Third important is the multispectral performance, which is the key aspect of this work. This means that multispectral detection is to be added to current technology while real-time color imaging must be maintained and cannot be compromised. Otherwise the technology would face obstacles when translating to the clinics.

A high quantum efficiency of the technology to detect photons is also important because high signal levels lead to a good signal to noise ratio. A small form factor with the ability to miniaturize would be favorable, but technology evolves rapidly. Even if the system is not yet miniaturized it is more important that future developments have the option for miniaturization.

Another important factor to consider between different technologies is the potential for artifacts, mostly caused by motion. Motion can be limited in scenarios such as brain surgeries, but in endoscopy the image moves very rapidly (change of entire field of view only in several images).

Micro-structured sensors with RGB Bayer pattern on the chip are developed for color imaging and thus record quality color images in high resolution at real-time. Therefore, it is ranked first in the technology comparison and excitation scanning as second.

In Chapter 4, a novel system concept is described based on these two technologies. The combination of excitation scanning in two phases with two micro-structured RGB sensors allows both fluorescence and reflectance imaging.

Spectral scanning or spatial scanning both exhibit very good multispectral performance but the recess in color imaging at high-resolution in real time is too big to be acceptable for surgical applications. Snapshot hyperspectral imaging has a big potential, but technical limitations are still too big to be overcome, especially for high resolution real-time imaging.

4 SYSTEM DESIGN AND REALIZATION

The goal of this thesis is to advance the field of fluorescence guided surgery by developing an improved imaging system. This chapter presents the key elements of the thesis: the developed system concept and the technical implementation of the realized prototype system.

The previous chapters revealed that systems used in clinical practice for fluorescence guided surgery suffer from technical limitations. As an example, numerous state-of-the-art systems either record fluorescence or reflectance color images but not both at the same time. A detailed review of related work is presented in Section 2.2.

Hence, this thesis focuses on harmonizing multispectral fluorescence detection and high quality color imaging at video-rate.

The requirements analysis in Chapter 3 revealed that fluorescence and color images need to be recorded over the visible (and NIR) spectral range. However, recording fluorescence and reflectance color images of a wavelength cannot be done simultaneously. To fulfill the requirements, a combination of spectral and temporal multiplexing is developed. Section 3.3 has identified that a combination of RGB color sensors with multiple illumination lights is most suitable to realize a system in the context of this work.

This chapter consists of two major parts: in Section 4.1 a system concept is developed and in Section 4.2 the technical realization of the prototype system is described.

Following this chapter, the system performance is evaulated experimentally and theoretically in Chapter 5. Subsequently, a metric (named T-score), is developed in Chapter 6 to predict the quality of unmixed fluorescence information to ensure diagnostic reliability. Besides, Chapter 7 presents system optimization approaches to determine which system parameters can be varied to further improve fluorescence detection.

The system concept and variations of it have been published in peer-reviewed publications and patent applications [166–169].

4.1 SYSTEM CONCEPT

The following section introduces the spectral system concept step by step. First, in Section 4.1.1 a conventional color imaging scenario and single band fluorescence imaging scenario are presented. These help to emphasize the differences between conventional imaging and the developed system. Subsequently, the concept of multiband fluorescence imaging and multiband color imaging using a single sensor are

introduced. The possibility to record these two distinct images at the same time by adding a second sensor is shown.

Section 4.1.2 works out the combination of *spectral* and *temporal* multiplexing and how the information of different phases complements each other. Subsequently, Section 4.1.3, focuses on the image processing which takes the series of images as an input and produces a fused image to be presented to the surgeon. However, the system concept also comes with limitations which are shortly discussed in Section 4.1.4. Finally, the concept and the major implications are summarized in Section 4.1.5.

4.1.1 *Spectral multiplexing concept*

This section will introduce the spectral multiplexing concept step by step. It starts by presenting a conventional color imaging setup and a conventional single band fluorescence imaging setup. Subsequently, multiband filters are introduced to image multiple fluorophores at the same time. To allow high performance fluorescence and color imaging, a second sensor and a second phase are introduced. The figures in this section will use the schematic illustration of Figure 4.1 displaying an organ containing an invisible cancer boundary, nerves and blood vessels.

Reflectance color imaging

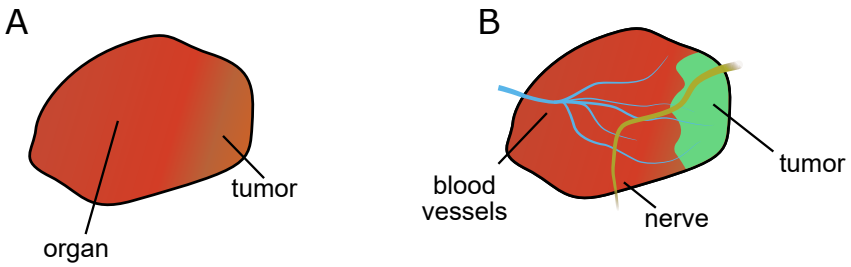

Figure 4.1: Schematic illustration of the imaged object to introduce the system concept: A) Organ as seen by the human eye. Visual perception allows to identify a cancer on the right side, but accurate cancer boundary delineation remains challenging. B) The cancerous area, a hidden nerve and hidden blood vessels are artificially highlighted, which can be achieved by fluorescence guided surgery.

Reflectance color imaging records pictures which correspond to the image information seen by the human eye. A schematic illustration of a typical scenario is shown in Figure 4.2. The object, an organ in the illustration, is illuminated with white light. The light interacts with the matter of the object and is reflected off the surface. The spectral reflective properties of the object determine the color of the object.

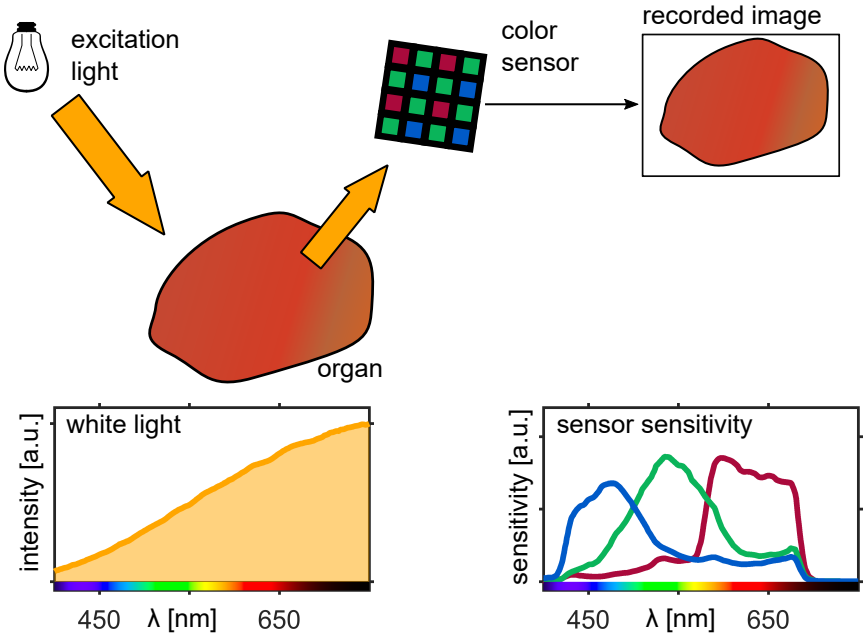

Figure 4.2: Schematic illustration of the color imaging scenario. The object, here an organ, is illuminated by a light source and the reflected light is detected using a silicon color sensor. On the planar sensor S, pixels with ■ red, ■ green and ■ blue sensitivity are arranged in a periodic 2×2 pattern. Exemplary illumination spectra and sensor sensitivity spectra are displayed in the lower part.

As a result, the spectral intensity of the detected light depends on the illumination spectrum and the object reflectivity. To detect the object color, the reflected light is detected by sensor with multiple channels, mimicking the spectral sensitivity of the human eye. More precisely, the spectral sensitivity of the sensor ought to be a linear transformation of the eye sensitivities.

The vast majority of commercially available silicon color sensors use microsctructed pixel detectors. Red, green and blue pixels with distinct spectral sensitivities are arranged in periodic mosaic pattern on the sensor. As a consequence, only one of the three color signals is recorded per pixel. The neighboring pixels record different spectral channels. To obtain full resolution for all channels, the missing information is obtained by an interpolation process, named demosaicing.

Before presenting the recorded signal to the user, it is usually further processed to improve color representation, brightness and contrast.

Singleband fluorescence imaging

Fluorescence imaging has been established as a standard tool in biomedical research as it allows to record the bio distribution of fluorescent dye molecules. Anatomical, functional or pathological structures

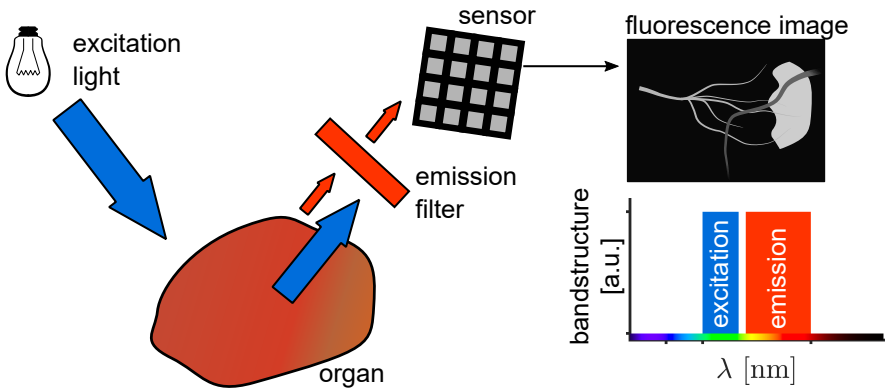

Figure 4.3: Schematic illustration of singleband fluorescence imaging. For fluorescence imaging, the spectral illumination band must be of lower wavelength than the detection band. The illumination is partially reflected by the organ and partially absorbed by fluorescent dyes in the organ. The emitted fluorescent light is orders of magnitude weaker than the excitation light. To detect only fluorescence, an emission filter is placed in front of the sensor.

can be stained with a fluorescent dye which is then visualized. The recorded images show the dye signal on dark background. A detailed description of fluorescence is presented in Section 2.5.

Figure 4.3 shows how a fluorescent dye is excited by illuminating the sample with spectrally confined light at a suitable wavelength. The excited dye molecules spontaneously emit photons (emission) at a higher wavelength. The emission light mixes with the excitation light. To detect only the emitted photons, the shorter wavelength excitation light is blocked by an optical filter. As a consequence, the sensor records pure excitation light. To ensure high detection efficiency, monochromatic sensors are often chosen to detect fluorescence.

Provided that multiple distinct dyes need to be imaged in a sample, multiple images can be acquired by switching excitation lights and emission filters. Alternatively, multiband filters can be employed for rapid acquisition.

Multiband fluorescence imaging

Multiband fluorescence imaging allows to record multiple fluorescent dyes simultaneously for applications in which integration time is sparse. For multiband imaging, both the excitation light as well as the emission filter require multiple spectral bands which must not overlap to prevent any leakage of excitation light into the emission path. Such a scenario is illustrated in Figure 4.4. In the most simple scenario, the excitation spectrum of each dye matches to one of the excitation bands and the emission matches to one of the emission filter bands. The monochrome sensor needs to be replaced by a multi channel sensor to allow spectral separation of the dyes.

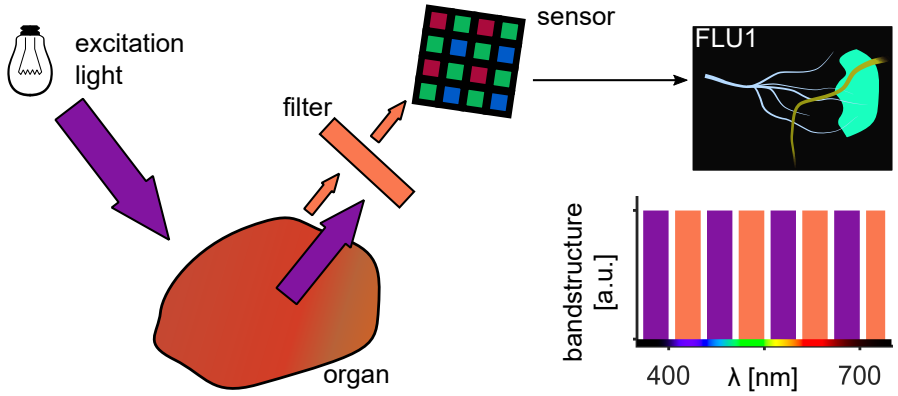

Figure 4.4: Multiband illumination and detection allows to detect multiple fluorescent dyes simultaneously. The illumination light source and the emission filter need to have complementary blocking and transmission bands (schematic illustration on the right). In this case, various fluorescent dyes which emit at different colors, can be detected at the same time using a color sensor. Consequently, the individual fluorescent dyes may be separated by color.

Essentially, a combination of multiband illumination, multiband emission filters and color sensors is used as system concept for this work.

Multiband color imaging

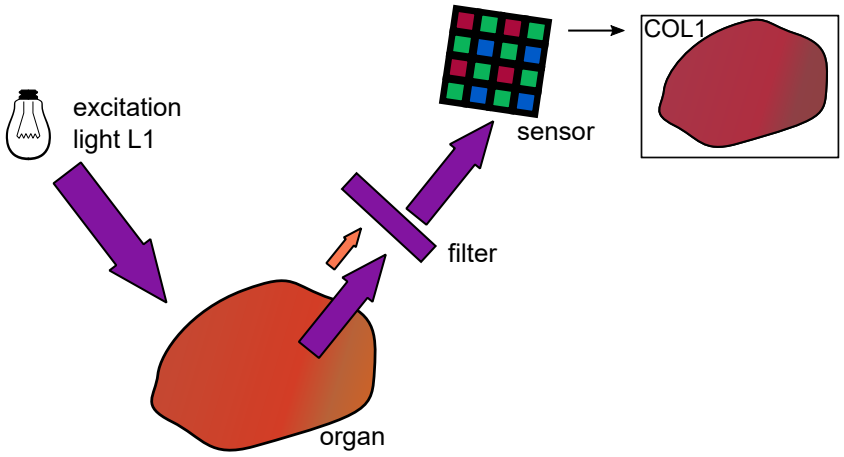

Figure 4.5: Color imaging scenario using multiband illumination and detection. The object is illuminated with multiband light and the reflected light can pass an emission filter and reach the sensor, where it is detected. Fluorescence emission may be spread over the entire spectral range. Usually it is partially blocked and partially be transmitted to the sensor. Because it is orders of magnitude weaker than the reflected excitation light, its contribution to the color image is minimal and can usually not be observed.

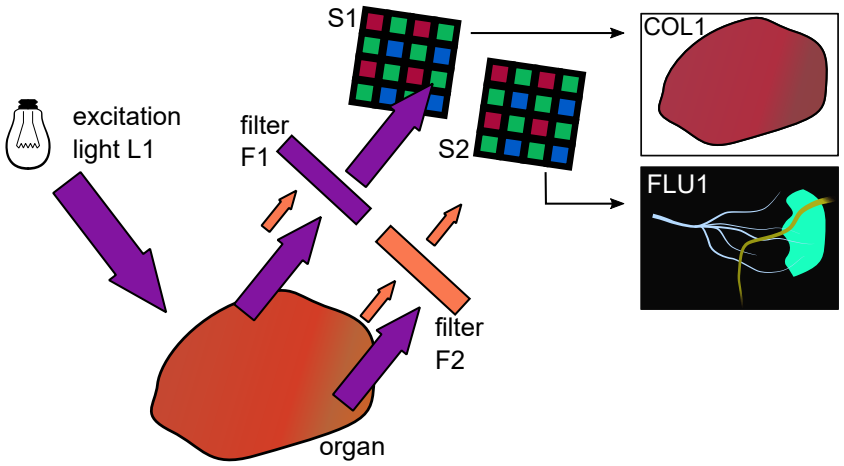

Figure 4.6: Combining fluorescence and color image acquisition: To record multiple fluorescent dyes and reflectance images at the same time, two color sensors are used. The fluorescent light can pass the multiband filter F2 whereas the excitation light L1 is blocked and is detected by sensor S2. A second sensor S1 with a filter F1 is used to record the reflectance light. As the transmission bands of F1 are complementary to F2, the excitation light can pass to S1 and a reflectance color image is recorded. Light from multiple spectral regions contribute to the formation of the reflectance color image, but approximately half of the spectrum is blocked. This may impeach the color perception. As a solution, the missing spectral bands can be recoded in a second phase.

For fast image acquisition, color reflectance images and fluorescence images are ideally acquired simultaneously. Since the fluorescence sensor is required to record only fluorescence, a second sensor is used.

This sensor is identical to the sensor detecting fluorescence, but no emission filter is required in front of the sensor as shown in Figure 4.5. The object is illuminated with multiband excitation light to match the requirements of fluorescence imaging. The photons of the reflected excitation light are detected for color reflectance imaging. The recorded color image from spectrally restricted bands may look reasonable after applying color correction algorithms.

However, the object is not illuminated with light covering the entire visible range. Consequently, information on the object reflectivity in spectral regions which are not illuminated can not be contained in the recorded image data. Therefore, color images with reasonable appearance cannot be guaranteed to exhibit high color reproduction accuracy. For example, if the recorded signal of two pixels is identical, the object reflectivity may be very different in the visible spectral regions which are not recorded. From a medical perspective, this restricts the usability of a single sensor for diagnostic purposes.

Figure 4.6 illustrates the parallel recording of fluorescence and color images using the same illumination. The color sensor is equipped

with a filter that matches the illumination spectrum. It allows the illumination light to pass and is not vital for this phase, but is essential for further development of the system concept.

The subsequent section shows how the concept can be further extended to record fluorescence and color reflectance images of the entire spectral region using a second phase.

Dual-phase multiband fluorescence imaging

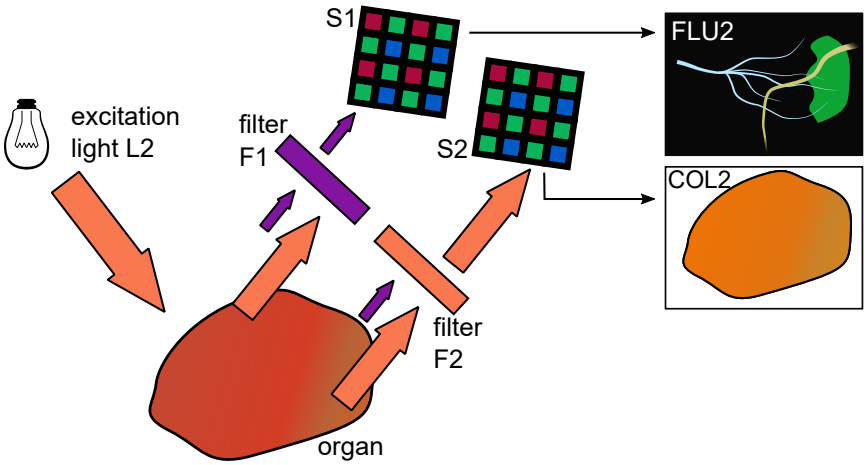

Figure 4.7: A second temporal phase is introduced to record the spectrally complementary part of the fluorescence and reflectance color images. The object is illuminated with light L2 that is spectrally complementary to L1. Both sensors and filters are identical as in phase 1. Sensor S2 records a reflectance color image because the illumination light L2 can pass filter F2. In contrast, sensor S1 records fluorescence because the filter F1 blocks the illumination light L2. The recorded color and fluorescence information is spectrally complementary to the information recorded in phase 1.

A second temporal phase is introduced to record the missing fluorescence and color information.

In this phase, the object is illuminated with spectrally complementary light compared to the first phase. However, the sensors and filters remain as illustrated in Figure 4.7. The reflected light L2 can pass through filter F2 because the spectral bands match. Consequently, sensor S2 records a reflectance color image in this phase. In contrast, the reflected light cannot pass though filter F1 and only fluorescent light is recorded by sensor S1.

4.1.2 *Spectral and temporal multiplexing*

The spectral and temporal multiplexing concept is illustrated in Figure 4.8. It allows to record fluorescence and reflectance color images

over the entire spectral range. The system runs in two alternating phases with two sensors and records two color and two fluorescence images in each cycle. To record information at video rate, the acquisition of the set of images must be repeated at video rate.

When illuminating in phase 1 with light in the spectral bands of L1, a reflectance color image is recorded by S1. Sensor S2 detects fluorescence because filter F2 is placed in front of the sensor and the excitation light cannot pass to the sensor.

When illuminating in phase 2 with light in the spectral bands of L2, a color reflectance image is recorded by sensor S2 in the bands of F2, whereas fluorescence is recorded with sensor S1 in the spectral transmission bands of F1.

Combining the information of the two phases results in image information from the bandpass regions of F1 and F2. Ideally, these add up to cover the complete spectral range detected with the red, green and blue sensitivities.

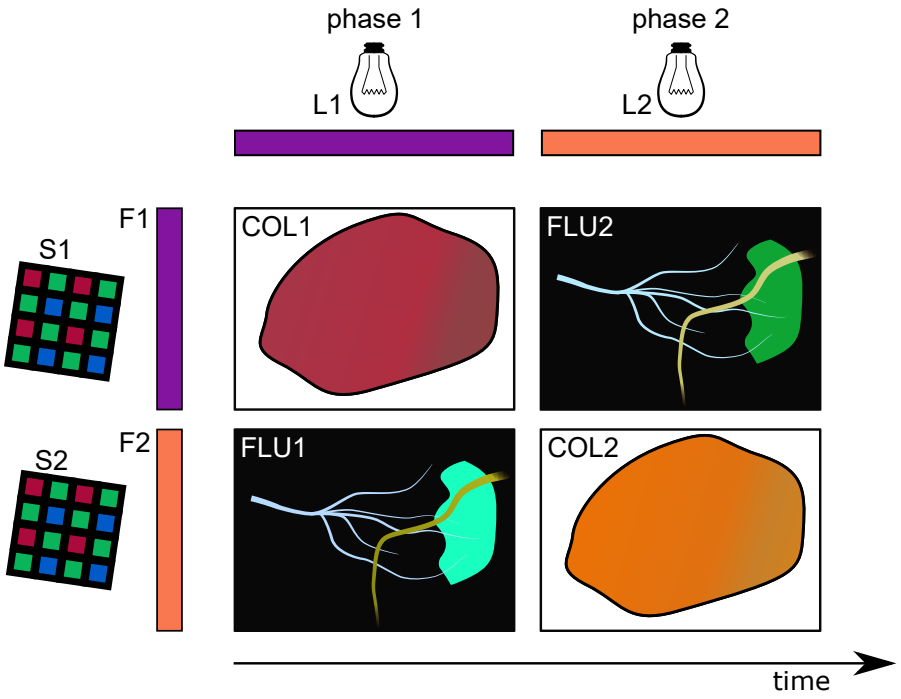

Figure 4.8: Schematic illustration of the combined spectral and and temporal multiplexing concept. Each of the four displayed images contains different information, which is recorded by the two sensors in the two phases. The upper row shows images, which are recorded by S1, the lower row images which recorded by S2. During phase 1, the object is illuminated with light L1. Consequently, sensor S1 records a reflectance color image, whereas sensor S2 records a fluorescence image. During the next phase, phase 2, the object is illuminated with light L2, which is spectrally complementary to L1. Consequently, S1 records fluorescence during phase 2 as the illumination light is blocked by the filter in front of S1. Accordingly, sensor S2 records reflectance color images during phase 2.

Fluorescence coverage

To analyze the spectral coverage for fluorescence detection, the detection range for the phases is marked in an excitation-emission-matrix (EEM) plot in Figure 4.9. When combining the two sensitivities, the EEM plot shows that half of the plot is not covered. This is not a big issue if gaps are not bigger than the width of excitation and emission bands.

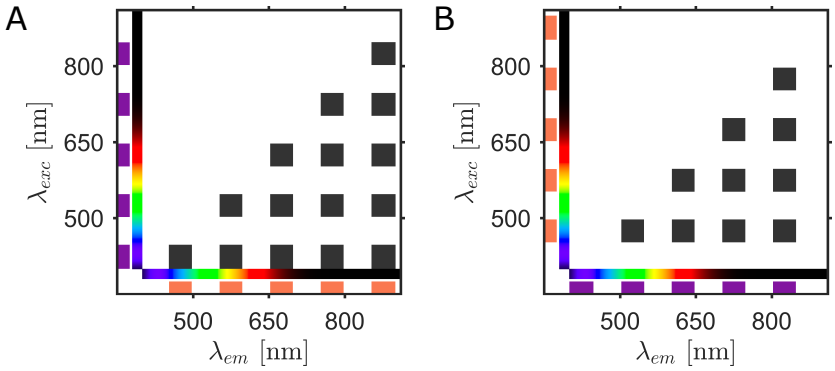

Figure 4.9: Illustration of the system sensitivity for fluorescence detection of S1 and S2 in the form of an excitation-emission-matrix. The range of detectable fl uorescence is restricted by the filters ■ F1 and ■ F2 as defined in Figure 4.14B. Colored bars on the outer side of the plot mark the respective transmission regions of the filters, black boxes mark the spectral window in the EEM plot at which fluorescence can be detected with the filter configuration. A) Fluorescence detection of sensor S2 when using ■ F1 as excitation filter and ■ F2 as emission filter B) Fluorescence detection of sensor S1 when using ■ F2 as excitation filter and ■ F1 as emission filter.

4.1.3 *Image processing*

The previous section describes in detail how color and fluorescence images can be recorded over the entire spectral range using two sensors and two phases in which a spectrally complementary illumination is applied. The acquired four images need to be processed to obtain both high quality color images and fluorescence component images. Finally, a fused image needs to be created from the color and the fluorescence images visualizing the combined information. This section presents an overview on the image processing.

Fluorescence image processing

One of the two sensors records a fluorescence image in each phase. Figure 4.10 schematically illustrates how the images are combined in a six channel fluorescence image after background correction, registration and normalization.

Since the signals of different fluorescent components add linearly, a linear transformation is required to separate the components. This transformation, usually refered to as linear unmixing, is well established in fluorescence image processing. Here, the transformation is represented by the unmixing matrix $\boldsymbol{u}$.

Various methods to obtain the parameters of the unmixing matrix have been published for fluorescence imaging applications. These include fitting techniques from calibration data sets or blind techniques.

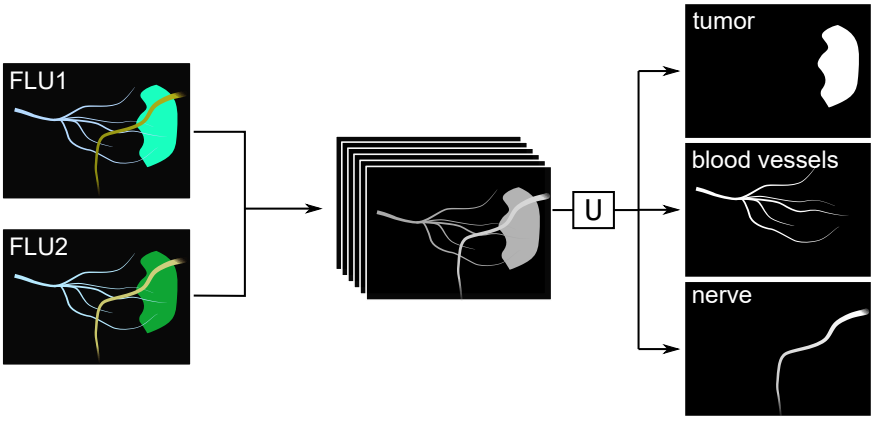

Figure 4.10: Fluorescence images F1 and F2 recorded by sensor S1 and sensor S2 in subsequent phases have 3 channels each (R, G and B). The images are pre-processed to combine all channels into a single six channel image (in the center). The pre-processing includes background subtraction, intensity correction and registration. Subsequently, the six channel image is unmixed using the unmixing matrix $\boldsymbol{u}$ into the individual components. In this example, the components reflect cancer tissue, blood vessels and nerves.

Algorithms of the category of blind unmixing techniques such as non negative matrix factorization or independent component analysis only rely on the fluorescence images.

Section 5.3 is dedicated to evaluate the fluorescence imaging capacity of the system. In this section, fluorescence image processing is described in more detail.

Color image processing

During the two phases, two spectrally complementary color images are recorded. Each image consists of three channels, an R, G and B channel. To combine the images as illustrated in Figure 4.11 in one single six channel image, the images need to be preprocessed to remove variations between the two different sensors and to spatially register the images. A linear transformation $\boldsymbol{m}_M$ between sensor color space and CIE XYZ color space is used for color correction. The parameters of this transformation can be chosen for optimal color representation of the final image.

A detailed analysis on accuracy of the final color images and optimization strategies to find the best possible color correction matrix $\boldsymbol{m}_M$ are presented in Section 5.2.

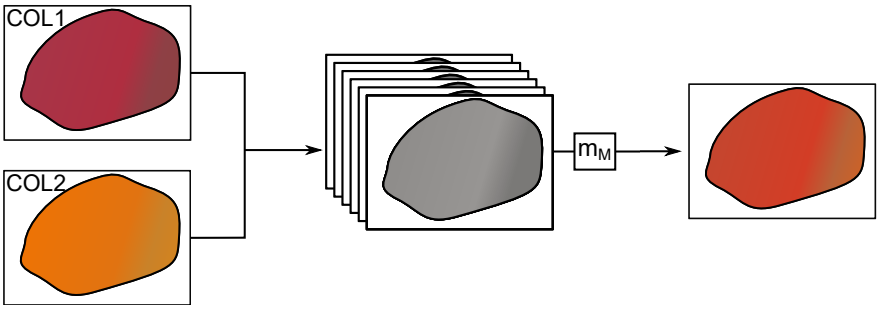

Figure 4.11: Color image processing: the images recorded in phase 1 and phase 2 contain spectrally complementary information. The images are pre-processed and combined into one single six channel image (illustrated in the center by six stacked grayscale images). The six channel image is processed using a linear transformation matrix $\boldsymbol{m}_M$ to obtain a three channel color image which corresponds to the visual perception of the surgeon as close as possible.

Fusing fluorescence and color images

The key advantage of the system is its ability to enhance high quality color images with functional, structural or pathological information which is gained by fluorescence imaging. In the series of illustrations, this corresponds to combining image information of the cancer, the blood vessels and nerves with the color image.

Various methods can be imagined to fuse the different images together. In Figure 4.12, the different fluorescence components are combined into one pseudocolor image which is overlaid on top of the color image. The processing may require to choose pseudocolor maps and transparency functions to obtain appropriately fused images [170]. The final video stream, formed by processed image data streams from sensors S1 and S2, is displayed in Figure 4.13.

All fusing methods need to enrich the color image with fluorescence information while avoiding loss of information in the color image. Generally, overlay techniques tend to hide parts of the color images at the risk of missing essential information. Thus, more sophisticated image fusion techniques could only modify the color appearance of regions while maintaining features of the background color image. One example would be to convert the background color image into a grayscale image and then only colorize the fluorescent regions with pseudo color tones. Alternatively, brightness and saturation of the background color can be maintained whereas the hue channel is modified to indicate fluorescence. This is an ongoing field of research which is not the focus of this thesis.

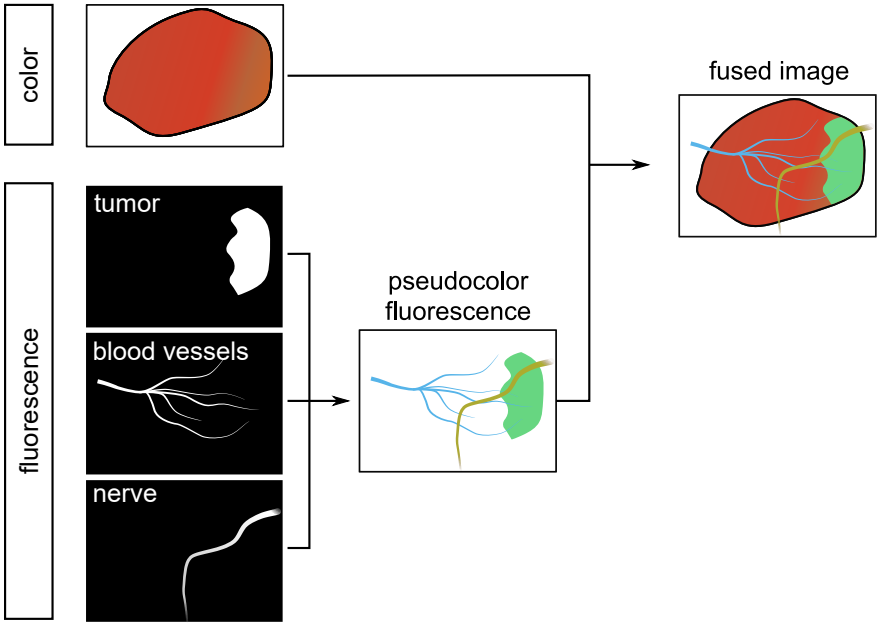

Figure 4.12: Combining color and fluorescence image information: The color image, which corresponds to the view of the surgeon, needs to be fused with the diagnostic fluorescence information. Each of the three fluorescence component images may reflect to the bio distribution of a fluorescent marker in tissue. In the example shown here, fluorescence intensity of the first component can be translated into prescence of cancer cells, the second fluorescence component indicates blood vessels and the third component nerve tissue. Various methods exist to fuse the fluorescence images. Here, the most simple way is illustrated: The three fluorescence components are combined into a single pseudocolor fluorescence image which is overlaid to top of the color image.

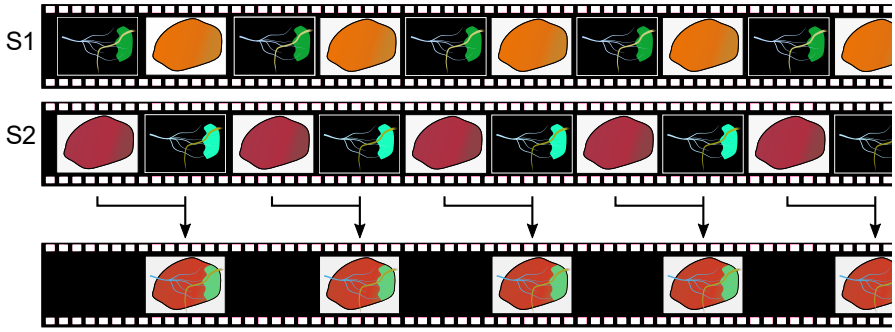

Figure 4.13: Illustration of the final video stream (lower image series) which is presented to the surgeon. It is composed of processed image data acquired by S1 and S2. The final stream has half the frame of the sensors S1 and S2.

4.1.4 *Concept limitations*

The presented concept also comes with some limitations. These will be shortly presented here. A more detailed discussion which also considers the experimental results of the realized system is presented in the final discussion in Section 8.1:

1. The overall sensitivity of RGB color sensors is lower than the sensitivity of the respective monochrome sensors (loss in efficiency of approx. 50%). This is the tradeoff which is made to record spectral information.
2. Fast object movement may results in spectral artifacts because the spectral information of color and fluorescence imaging is recorded in two subsequent phases.
3. In case of open surgery, temporal multiplexing with different illumination of the surgical field causes flickering. For low imaging framerates, this may be disturbing for the surgeon.
4. As a result of the mosaic pattern, the spectral information of the different channels at a pixel location is partially reconstructed from neighboring pixels. This may cause artifacts if the reconstruction is not optimal, for example at steep intensity boundaries.
5. Fluorescence images are recorded in total with six spectral channels. Theoretically, this may be sufficient to unmix up to 6 different fluorescent dyes. Further analysis is required to show how well fluorescence can be unmixed in reality. Section 5.1 theoretically investigates the sensitivity of the system, Section 5.3 experimentally investigates unmixing and Chapter 7 shows optimization approaches to investigate the boundaries of detectable dye combinations.

Even though these limitations exist, they are expected to have a minor impact as the concept is tailored for fluorescence guided surgery. The capabilities of a realized prototype system will be investigated experimentally and theoretically in the subsequent chapters of this thesis.

4.1.5 *Summary*

The purpose of the system is to record both fluorescence and reflectance color images with sensitivity over the entire visible and near infrared range. This is realized using a concept of spectral and temporal multiplexing:

SPECTRAL MULTIPLEXING: Fluorescence imaging requires to eliminate any excitation light from the emission wavelength region,

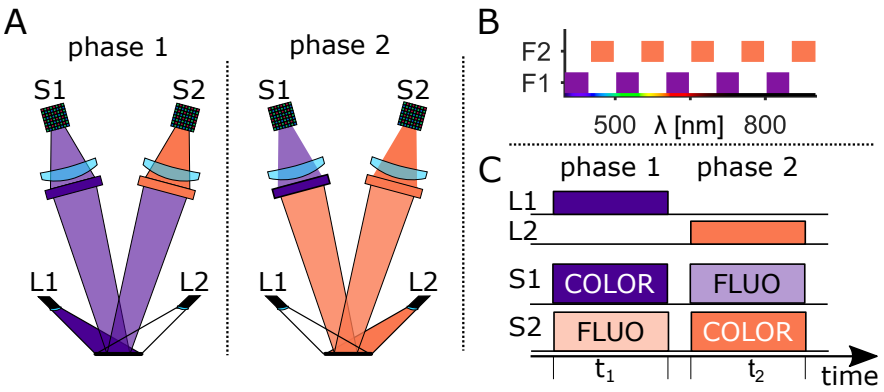

Figure 4.14: A) Schematic illustration of the imaging concept during the two phases. Simplified setup with two lights L1 and L2 and the two sensors S1 and S2, both equipped with the complementary bandpass filters F1 and F2. B) Transmission bands of two exemplary complementary filters F1 and F2 with 5 bands each. C) Timing concept of the light sources L1 and L2 and the two sensors S1 and S2. During each phase, one sensor records fluorescence and one sensor records reflectance color images.

because the fluorescent light is orders of magnitude weaker than the excitation. Thus, the spectral region must be split into at least two complementary multiband regions.

TEMPORAL MULTIPLEXING: Two temporal phases are used to record fluorescence and color images for each of the spectral multiband regions using two spectrally complementary illumination lights.

In order to unify fluorescence and color imaging over the entire spectral range with no moving parts, two temporal phases and two sensors are needed.

In the presented approach, the VIS/NIR spectrum is split into two complementary regions using multi-bandpass filters F1 and F2. One of the sensors, sensor S1 is equipped with an emission filter F1. In contrast, the other sensor S2 is equipped with a filter F2 transmitting light in the complementary bands as illustrated in Figure 4.14.

Fluorescence can be observed in all parts of the visible and near infrared spectrum with only minor gaps.

The major advantage of this method is that in each phase fluorescence and color is recorded by using the fluorescence excitation light also for reflectance imaging. The approach will therefore provide rapid image acquisition. In both phases, each of the sensors records relevant information for the imaging scenario. Thus, the technique is very efficient to record a maximum of information during the available time.

In the following Section 4.2, each of the different system components is discussed and a solution for the prototype is presented. Sub-

sequently, in Chapter 5, the system is evaluated regarding the design requirements which are put on it in Section 3.1.

4.2 TECHNICAL REALIZATION

So far, the theoretical concept was introduced and reasoned, but no specific parts for the realization were selected. This section describes the technical realization and explains in detail the sensor, filters, imaging lens light source and optical design choices.

The realized prototype system has been published by Dimitriadis *et al.* [167].

4.2.1 *Sensor selection*

Table 4.1: Comparison of selected sensor models regarding technology, resolutions (res) in pixel, maximum quantum efficiency (qe) in %, readout noise (noise) in e^- and framerate (fps) at maximum resolution in s^{-1}. Values are obtained from camera manufacturer specifications sheets [171, 172]. The reported framerate corresponds to the respective camera model for each of the sensors as reported in the references. The sensor as is may allow different framerates with a different readout electronic.

MODEL	TYPE	RES [px]	QE [%]	NOISE [e^-]	FPS [s^{-1}]
CIS2521	sCMOS	2560×2160	45	1.67	100
ICX674	CCD	1440×900	53	8.85	35
CMV4000	CMOS	2048×2048	45	17.25	90
EV76C570	CMOS	1600×1200	40	6.69	47
IMX265	CMOS	2048×1536	66	2.22	55

The selected concept puts very high requirement on the sensor, as it needs to be suitable for both, high sensitivity fluorescence imaging as well as accurate color reproduction.

For fluorescence imaging, the sensor needs to detect low light intensities. Therefore, it needs to be as sensitive as possible. This is achieved by a sensor with high quantum efficiency that adds as little noise as possible in the detection process to the image.

For color imaging, the sensor is usually read out at higher light intensity levels than for fluorescence imaging. In this case, a the high sensitivity and low noise are also beneficial, but not as essential as for fluorescence imaging. To obtain a good color reproduction, an RGB microfilter Bayer pattern with spectral filter transmission curves matching the tristimulus values of the human eye are used [123, 173, 174].

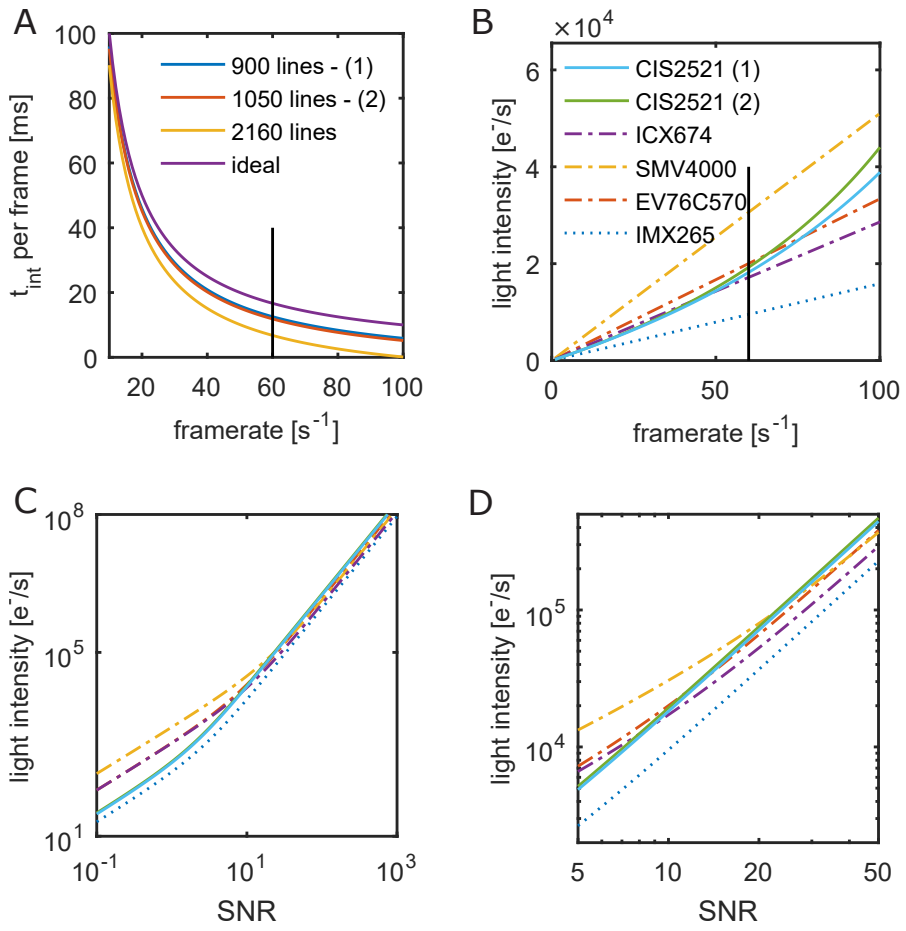

Figure 4.15: Comparison of the application specific performance of the sensors CIS2521 (Fairchild), ICX674 (Sony), SMV4000 (CMOSIS), EV76C570 (e2V) and IMX265 (Sony). A) Effective integration time t_{int} per frame depending on framerate for CIS2521 for different region of interest (1440 px × 900 px - (1); SXGA+ 1400 px × 1050 px - (2); full size 2650 px × 2160 px). The line at 60 fps marks the framerate required for fluent visual perception. B) Light intensity required on a sensor pixel to trigger enough electrons in order to obtain a SNR of 10 for each frame at the maximum quantum efficiency wavelength depending on the framerate. C) Dependency of the required photon flux on the image SNR for a fixed framerate of 60 fps. D) Magnification of C) for better visibility of the SNR between 5 and 50.

The sensor market is constantly evolving with options ranging from charge-coupled device (CCD) sensors, complementary metal-oxide semiconductor (CMOS) sensors, scientific CMOS (sCMOS) sensors to electron-multiplying CCD (EMCCD) sensors. The following overview of sensors compares selected model as representatives for a closer evaluation regarding their performance in combination with the concept:

CIS2521 The sensor CIS2521 (Fairchild) belongs to a class of so-called scientific CMOS (sCMOS) sensors. It combines high-resolution, good timing, 16bit A/D conversion and high framerates with very low readout noise. Additionally, it is available as color and monochrome sensor.

ICX674 The ICX674 (Sony) sensor is a typical CCD sensor. It combines high quantum efficiency with reasonable noise performance, but is rather slow in the readout process and thus is hardly able to run at high framerates.

CMV4000 CMV4000 (CMOSIS) is a fast CMOS sensor with high readout noise and a rather low quantum efficiency.

EV76C570 EV76C570 (e2v) combines low readout noise with a decent quantum efficiency and good sensor readout speed.

IMX265 IMX265 represents a state-of-the-art CMOS sensor which became available in 2016. It combines high-resolution, high framerates, versatile triggering options using a global shutter mode, very low readout noise and good color reproduction. This sensor was released to the market after the system was built, but it is considered here to show what novel sensor technology could add.

EMCCD EMCCD sensors are able to capture images at very low light intensities by amplifying the signal before sensor readout. Unfortunately, they have typically low resolution of 128x128 pixels and only exist in a monochrome version.

IIT Image intensifiers tubes (IIT) are very useful for low light applications, but they also suffer from low resolution and only exist as monochrome versions. Additionally, they are very fragile and expensive.

EMCCD sensors and IIT play a significant role in fluorescence imaging due to their high SNR at low light intensities. Recent publications have suggested higher detection sensitivity for intraoperative fluorescence imaging using an EMCCD instead of a state of the art monochrome CMOS camera [67]. However, both EMCCD and IIT are not available as color sensors and are therefore excluded from further considerations.

Table 4.1 compares the introduced models in terms of resolution, quantum efficiency, readout noise and framerate at full resolution. As all the selected sensors exhibit a microfilter Bayer pattern with spectral filter characteristics closely matching the human tristimulus curves, color imaging with adequate color reproduction is expected for all models.

For a fluent intraoperative perception, the system needs to run at 30 Hz so the sensor needs to be able to deliver images at 60 Hz (detailed

considerations regarding framerate and perception can be found in Section 3.1.3). To compare the performance of the different sensors at this speed, Figure 4.15 displays the performance of the cameras depending on framerate and the resulting SNR.

Further sensor selection is done by comparing the capability of the sensors to record fluorescence images at 60 fps.

The CIS2521 is a sCMOS sensor running in rolling shutter mode and thus requires time to read out each frame depending on the number of lines used to record before the next frame can be recorded. Thus, less integration time is available per frame (Figure 4.15A). At 60 fps, the 16:9 format resolution of 1440 px × 900 px requires to read-out 900 lines and thus only 12.5 ms instead of ideally 16.7 ms (corresponding to approx. 75%) are available to integrate photons. For the higher resolution of 1400 px × 1050 px the integration time is further reduced to 11.9 ms per frame and for full sensor size of 2560 px × 2160 px only 6.8 ms are available for integration of the light.

Figure 4.15 relates the SNR for a certain pixel with the photon flux and framerate with given parameters for quantum efficiency, sensor readout times and readout noise from Table 4.1. According to Section A.1.3, the SNR for a photon count number Y is related with the sensor readout noise according to by the following equation:

$$SNR = \frac{Y}{\sqrt{\mathrm{var}\left[Y\right]}} = \frac{Y}{\sqrt{Y + \sigma^2_{readout} + \sigma^2_{dark}}}.$$

As the used integration times are below 1 second, the dark current noise is neglected because $\sigma_{readout} \gg \sigma_{dark}$. Replacing the number of detected photons in one pixel during integration of one frame with the $Y = q.e. \cdot t_{\mathrm{int}} \cdot \Phi_{Phot}$ allows to calculate the SNR depending on the photon flux arriving at the sensor per pixel for sensor comparison.

The necessary light intensity to detect signals at fixed SNR of 10 is shown in Figure 4.15B for the different sensor models depending on the framerate. The sensor IMX265 is the best choice at any condition, but it was just released by Sony in 2016. Therefore, it will be excluded from the discussion here.

For the realized setup, the pco.edge 5.5 color (PCO AG, Kehlheim, Germany) sCMOS camera incorporating the CIS2521 sensor was selected since it performs best at low light conditions. The camera combines high framerates with high sensitivity and low readout noise.

4.2.2 *Filter selection*

The system concept requires to select a multiband filter pair splitting the spectrum in two complementary parts. This section is dedicated to considering different approaches and to select the filter of choice.

Filter sets for fluorescence imaging require good blocking characteristics which are at least 4 – 6 OD, because the intensity of fluores-

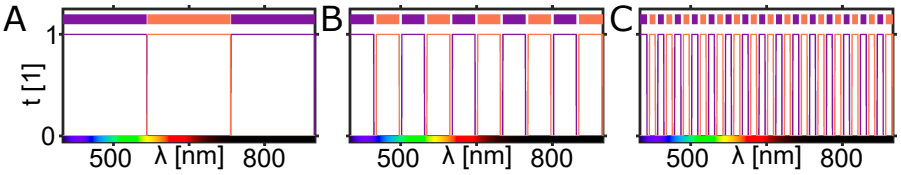

Figure 4.16: Illustration of different filter concepts for splitting the spectral range with a multiband filter pair with the individual filter transmission plotted as ■ and ■ into a total number of A) 3 bands, B) 10 bands and C) 30 bands.

cent light is orders of magnitude smaller than the excitation. Leakage of excitation or ambient light into the fluorescence detection channel will pose a limit on the detection sensitivity and cause unmixing artifacts. The clinical dye PPIX has a Stokes shift of more 200 nm, so the transition between excitation and emission is not very challenging. However, other dyes like ICG or FITC have a Stokes shift of less than 30 nm and thus sharp edges in the band structure are required [74].

It is necessary to find a filter pair, splitting the wavelength region from 380 nm to 900 nm into two complementary multiband regions. Three different hypothetical scenarios are shown in Figure 4.16. In Figure 4.16A, the spectrum is split into 3 bands. The bandpass filter pair for this concept can be relatively easily produced and the reflectance color image suffers only from minor spectral gaps. However, the fluorescence imaging capabilities are severely compromised. Any fluorophore can be excited, but the chance that the emission falls onto a band of the other filter is not very high, because there are only two band transitions present in the concept. Though, a concept with few bands may work if the edge wavelengths are tailored for a specific scenario.

In other extreme would be to split the spectrum into as many parts as possible. In Figure 4.16C, a total number of 30 bands is displayed. However, the concept can be increased to even more bands. As reflectance spectra are quite smooth over the spectral range, both sensors will detect effectively the same color information. The information carried by light which passes through one band will be almost identical to the information of light carried by light passing through the neighboring band. So, the bands themselves do not add any information, though information can be added by illuminating with different lights in the two phases. Fluorescence of any dye can be detected with the setup because the band spacing is closer than a typical emission width. Unless different excitation schematics are used, the two sensors will provide the same signal. Overall, only half of the emitted fluorescence intensity is transmitted to the sensor, so the efficiency of the filter is equally bad for all dyes.

The optimum is achieved somewhere in between. The neighboring filter bands should be spaced such that the fluorescence can be ex-

cited in one band and detected in the next band. This is achieved if the band widths correspond approximately to the excitation width, the emission width and the Stokes shift. In such a case if the bands match well, the fluorescence can be efficiently excited and most of the emitted photons are detected. The multispectral signal of two fluorophores whose spectra differ by around the bandwidth are very different. Unmixing a set of dyes emitting for example at 530 nm, at 565 nm and at 610 nm (as shown in Section 5.3.1) is only possible because the multispectral imaging uses differentiation by excitation and emission. So, a combination of excitation and emission unmixing is employed and makes the system very powerful separating dyes with spectral differences in the magnitude of the bandwidths. Separating dyes whose emission is spectrally far apart can be done using the information of the RGB color sensor.

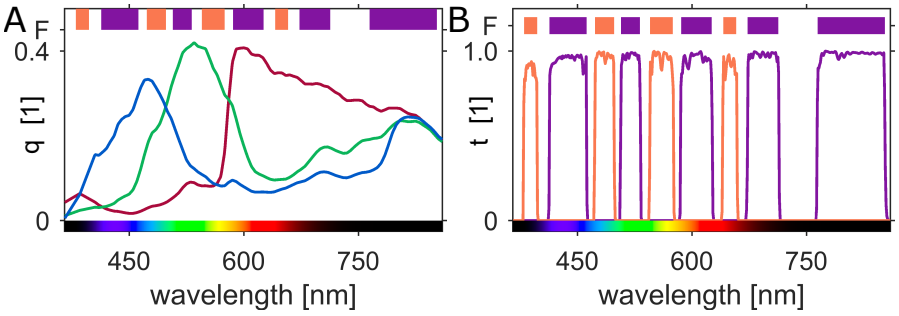

Figure 4.17: A) Quantum efficiency curves $q(\lambda)$ for the red, green and blue channel of the sensor CIS2521 IR; B) Filter transmission of the two Semrock interference filters FF01-387-485-559-649 and FF01-440-521-607-694-809. Adapted with with permission from ref [167], OSA.

Generally, the higher the number of bands, the lower the average transmission of the filter pair. This is caused by gaps in between to neighboring bands in which both filters must completely block the light. Such gaps, which are in reality as wide as 10 nm are required to avoid leakage. In both imaging setups photons do not pass the filter necessarily perpendicular, but in a slight variation of angles. Interference filters are sensitive to the angle of incidence [74]. Different angles result in a slight shift of the bandpass structure (also depending on polarization). Therefore, spectral security gaps are required to allow some angular variation in the optical path. The optical setup is designed for minimal angular variation of all image rays as described in Section 4.2.3.

For the realized setup, a commercially available filter set with a bandpass width of approx. 25 nm to 60 nm covering the VIS/NIR spectral range is selected. The best match and spectral coverage was found for FF01-387-485-559-649 and FF01-440-521-607-694-809 (Semrock Inc., Rochester, USA). The transmission spectra of these filters are shown in Figure 4.17B.

It is obvious, that the choice contains many compromises which were necessary to realize the setup: the bands neither optimized for the used LEDs, for the sensor sensitivity curves nor for a dye of interest. However, they satisfy the basic conditions quite well.

Though, the spectra reveal two minor problems of the choice. First, the IR band of F2 between 700 nm and 760 nm is blocked. Thus, no emission or reflectance information can be detected in that wavelength range. Such an additional IR band would be suitable to image IR dyes. The separation between the different IR dyes would also be very powerful, because each of the IR dyes would be mainly detected on one of the different sensors.

The complementary bandpass set is designed for excitation with the band structure of F2 and detection with the band structure of F1. Therefore, the individual bands of F2 are quite narrow compared to the bands of F1. This will result in lower signal strength on S2. These shortcomings can be fixed by designing and manufacturing a custom bandpass pair optimized for a specified application as introduced in Section 7.2.

4.2.3 *Lens selection*

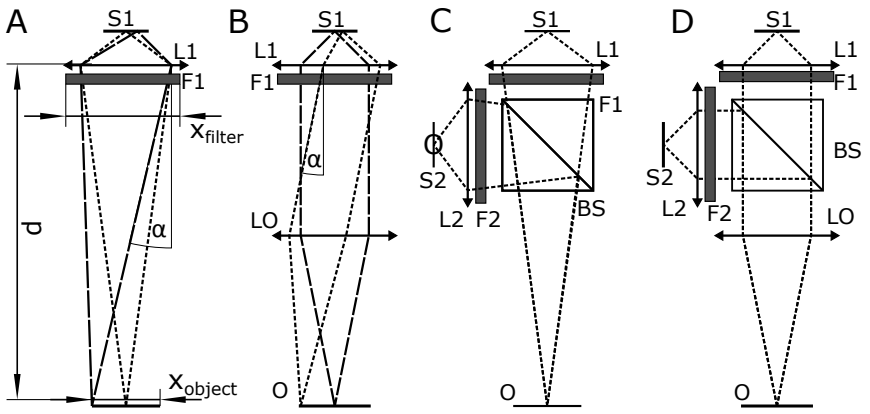

Figure 4.18: Schematic illustration of the optical path of different lens arrangements. Possible filter placement and maximum angle of incidence on the filter for a single imaging lens (A) and two imaging lenses in 4f configuration (B), both drawn for one sensor only. Corresponding setup with the two sensor approach for a single imaging lens per path (C) and the 4f imaging approach with two lenses per path. Labels: x_{object}: object size; x_{filter}: filter diameter; d: object distance; S1, S2: sensor 1,2; F1,F2: filter 1,2; LO: objective lens; L1,L2: imaging lens for path 1,2; BS: beam splitter cube.

Different imaging lens assembly options are discussed here for the selection of a suitable commercially available system. For the concept,

lenses are considered to be ideal lenses. Though, in reality single ideal lenses are realized by an assembly of lenses to minimize aberrations.

First, a conventional single imaging lens system as shown in Figure 4.18A is considered. It is small, compact, low cost and offers good imaging performance. As it is essential to place the emission filter in the optical path at a position with minimal angle of incidence to ensure blocking of excitation light. As the sensor size ($x_{\text{sensor}} = 10.4\,\text{mm}$) is smaller than the object size ($x_{\text{object}} = 50\,\text{mm}$), the total magnification $m = \frac{10.4\,\text{mm}}{50\,\text{mm}} \approx 0.2 \gg 1$ resulting in a higher numerical aperture on the image side than on the object side of the lens. In this case, the filter is placed directly in front of the lens with the same aperture as the lens to save space. Figure 4.18A shows schematically how the maximum angle α in which light can pass the filter can be estimated as

$$\alpha \approx \arctan\left(\frac{x_{\text{object}} + x_{\text{filter}}}{2 \cdot d}\right), \tag{4.1}$$

where $x_{\text{object}} \approx 50\,\text{mm}$, $x_{\text{filter}} \approx 25\,\text{mm}$ and the working distance $d \approx 200\,\text{mm}$ resulting in $\alpha \approx 10.6°$.

An alternative approach is to build a 4f imaging setup with two lenses, an objective lens Lo and an camera lens L1 as shown in Figure Figure 4.18B. In this case, the filter is placed between the lenses in an infinity corrected space. The maximal angle for the light to pass through the imaging system can be calculated as

$$\alpha \approx \arctan\left(\frac{x_{\text{obj}}}{2 \cdot d}\right). \tag{4.2}$$

For the same constrains, the maximum transmission angle $\alpha \approx 7.1°$. Therefore, it is better to place the filter in infinity corrected space. The maximum transmission angle is then determined by the field of view and does not additionally depend on the focusing aperture.

To realize a dual sensor system with spectrally complementary paths, the imaging path needs to be split and the two sensors with complementary multi-bandpass filters need to be placed in the path after it is split. In Figure 4.18C and D the two possible scenarios are compared. Figure 4.18C shows the option of an individual objective lens for each sensor. In this case, the two individual objective lenses need to be aligned and focused separately. In contrast, the concept visualized in Figure 4.18D splits the path in the infinity corrected optical part. In this case, the tolerances of the alignment towards lateral and angular misalignment of the individual camera objective lenses is much higher. Also, the two lenses L1 and L2 only once need to be focused individually. Distance variations between camera and object do not cause different magnification, as an axial displacement in infinity corrected space does not cause any magnification. Additionally, for the beam splitting device the angles of incidence are smaller which is desirable for the performance.

In conclusion, various reasons, summarized in Table 4.2, show a preference to use a 4f lens arrangement in which the beam is split and filtered in infinity corrected space. The only drawback of a 4f imaging assembly is that with the given constrains the photon collection efficiency on the object side tends to be low and the size tends to be big. A detailed evaluation of the photon collection efficiency is presented in Section 5.4.4.

To realize such a setup, the Leica Z6 (Leica Microsystems, Heerbrug, Switzerland) imaging system is selected. The modular system is equipped with an objective lens, a zoom lens part and camera objective lens.

Table 4.2: Comparison between a single lens and a 4f lens arrangement as optical concept regarding numerical aperture, registration robustness, astigmatism, filter transmission angle, zoom option and form factor. Ratings (+/−) are reasoned in the text in detail.

	SINGLE LENS	4F ARRANGEMENT
numerical aperture	+	−
registration robustness	−	+
astigmatism (with BS plate)	−	+
filter angle	−	+
zoom option	−	+
form factor	+	−

4.2.4 *Optomechanical system*

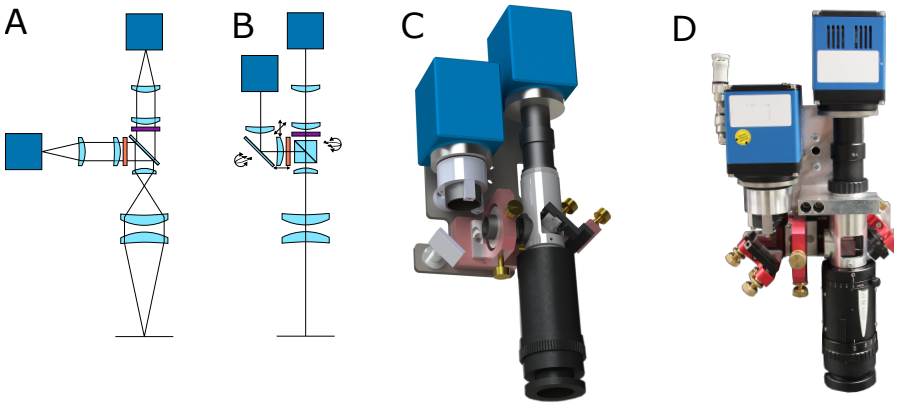

Figure 4.19: Optomechanical design: A) Optical concept where the optical arms for the sensors are orthogonally aligned. Elements include the objective lens, the zoom system Z6, the beam splitter, the filters, the camera lenses and the sensors. B) Optical path where the second path is mirrored by 90 degrees to align the sensors in parallel. C) CAD rendered planning of the optomechanical elements. D) Photography of the realized system setup.

In this section, the development and realization of the optomechanical system is described. This section is specific to the realized prototype system for this work whereas most of the considerations in the previous chapters can be generalized for any system aiming at combined color and fluorescence imaging.

Development, realization and evaluation of the optomechanics was performed in collaboration with Tobias Behr. His work is published in the form of his master's thesis [175].

As described in Section 4.2.3, the favored optical concept uses a 4f lens assembly as shown in Figure 4.18 with the Z6 system. The object is imaged in an infinity corrected part of the image path using an objective lens, a zoom lens and two camera objective lenses. There, the path is split to obtain two paths, where the light is spectrally filtered and then focused individually onto the sensors.

Figure 4.19A shows the finalized optomechanical design of the imaging system which is based on the design concept displayed in Figure 4.18D. Such an assembly would result in a very bulky setup, as the path of sensor S2 horizontally sticks out of the vertical path. Such a setup would not fulfill the requirements to integrate easily into a surgical scenario. Additionally, the heavy camera on that optical arm has a strong torque due to the long arm in combination with the weight of the camera. This requires a stable and thus heavy mount and makes the optical alignment challenging.

To circumvent both of these issues, the imaging path to sensor S2 is folded by 90° using a mirror. This moves the two sensors S1 and S2 close together and allows easier mounting. The optical elements like beam splitter, lenses and mirror can be aligned independently of the cameras and do not need to carry the weight of the sensors. This makes the system more robust and the alignment less fragile. In order to realize this setup, the individual lenses of L2 need to be split and mounted individually. A detailed description of the optomechanical design concept and adjustment can be found in [175].

Some of the mounting elements of the presented work in T. Behr's thesis [175] were manufactured using 3D printing from plastic materials. These turned out not to be robust enough to maintain the adjustment and calibration of the setup reliably over days of use. To compensate for this, these parts were redesigned and manufactured from metals, favorably from aluminum.

4.2.5 *Illumination light source*

The light source for the system is used for both color reflectance imaging and fluorescence imaging. This section discusses different illumination options and chooses the most suitable light source.

Classical lights

Most surgical microscopes being able to image color and fluorescence use classical light sources such as incandescent, halogen, or Xenon lights up to date [74]. These light sources have a very wide spectrum and high intensity illumination can be generated. Though, the light emanates in the source from a rather big area in high angles. Such a light distribution is very hard to collimate due to the Abbe sine condition. Thus, filtering with multiband interference filters with small spectra gaps between excitation and emission bands is very challenging and will most likely result in leakage of excitation light in the fluorescence emission path. As these sources have a very wide light spectrum, a lot of light is blocked at the emission filters with results in a high amount of heat dissipation. It is usually not possible to switch incandescent and Halogen light sources on and off in time intervals in the order of 10 µs. Though, flashlight Xenon light sources can be triggered at 100 Hz but have a rather low lifetime of around 300 h [176, 177].

White LEDs

White LED sources continue to be integrated into medical equipment because they combine several advantages: small size, high intensity output, fast trigger options and comparably low heat dissipation. The spectrum of a white LED is confined between 400 nm and 700 nm with two major intensity peaks. The first peak is usually sharp at around 450 nm whereas the second peak is wider around 550 nm. An example for a white LED spectrum is shown in Figure 5.8. If the excitation wavelength fits to one of the two intensity peaks, the result might be acceptable, but for example FITC is excited at 490 nm where white LEDs usually show an intensity minimum. Thus, the resulting filtered excitation light intensity would be a small fraction of the total light intensity.

Generally, white LEDs with different light temperature are available and allow good color reproduction.

To obtain high light intensities for excitation, the area of the LED must be large. Additionally, the radiation angle of high power LEDs is wide and therefore the light cannot be collimated well. Consequently, white LEDs are hard to filter using dielectric filters and are therefore not suitable for fluorescence excitation.

Lasers

Lasers are commonly used for fluorescence excitation in research laboratories as they show various advantages for fluorescence imaging. A single mode beam can be filtered very well. Many lasers such as diode lasers can also be easily triggered. The intensity can be confined at a specific wavelength to be selected for fluorescence exci-

tation. However, regulatory safety issues regarding power limits require to diffuse the beam reliably and thus pose an obstacle on the usability. Some imaging devices for clinical ICG fluorescence imaging such as Fluobeam (Fluoptics), Spy (Novadaq), LAB-Flare (Curadel) and the Iridium (VisionSens) use a laser for excitation [74]. These devices usually split the illumination for color imaging in the visible range and fluorescence excitation in the NIR. Lasers usually emit at a single wavelength, and thus reflectivity information is only measured at those wavelengths. Further research is required to evaluate if this information is adequate for good color reproduction in clinical applications.

Multiple narrowband LEDs

Narrowband LEDs emit the lion's share of the light intensity in a confined spectral region of approximately 15 nm to 50 nm. Thus, for an illumination solution different modules must be combined. These LED modules can be triggered independently and at sufficiently high frequencies. The light of the modules can be collimated acceptably to be filtered by individual bandpass filters and thus offers flexibility in filtering. High output intensities can be obtained combining the individual modules using dichroic mirrors. Additionally, the intensity of the individual LED modules is independently adjustable allowing to extend the dynamic range for fluorescence imaging.

System light sources

Considering all these options (summarized in Table 4.3), a set multiple narrowband LEDs which can be individually filtered, is selected as illumination device for the system. The light of the individual LEDs is merged into a common path using dichroic mirrors. The set of the commercially available light sources pE-4000 (CoolLED Ltd. ,Andover, UK) and LEDHub (Omicron-Laserage Laserprodukte GmbH, Rodgau-Dudenhofen, Germany) are used with the system. The white LED light source ZLED CLS 9000 MVW (WILD GmbH, Völkermarkt, Germany) can be used for dedicated color imaging in one phase as described in [166].

Table 4.3: Performance comparison between the different light source technologies multi LED, white LED, laser, halogen or Xenon regarding suitability for fluorescence imaging, color imaging and triggering. Ratings (✚/○/━) are reasoned in the text in detail.

ILLUMINATION	FLUORESCENCE	COLOR	TRIGGER
multi LED	✚	✚	✚
white LED	━	✚	✚
laser	✚	━	✚
halogen	━	✚	○
Xenon	○	✚	○

Illumination power

The following part will estimate the maximum and realistic light flux in the field of view. Currently available narrowband LEDs with a spectral width of typically 10 nm - 50 nm are commercially available in multi LED light sources for the entire VIS/NIR spectral range with output powers ranging from 50 mW up to 1000 mW. The field of view is specified to be at least 5cm × 5cm, which requires to illuminate at least 25 cm^2 [178–180]. The final system will have around 10 spectral bands at which the sample can be illuminated. Thus, the maximum light flux Φ_{max} is estimated as

$$\Phi_{max} = \frac{10 \cdot 1000\,\mathrm{mW}}{25\,\mathrm{cm}^2} = 400\,\mathrm{mW\,cm^{-2}}. \tag{4.3}$$

This is still well below the maximum permissible exposure of 2000 $mW\,cm^{-2}$ for human tissue [42].

For a more realistic scenario, light is lost before being delivered to the object area inside the field of view by many factors: excitation filters require to spectrally cut off the illumination for fluorescence imaging, light guides absorb or reflect some light and usually light is distributed over a larger area than the field of view to avoid vignetting of color artifacts on the edges of the image. Combining all factors together results in a realistic light flux per band of 100 $\mu W\,cm^{-2}$ [166] on the lower end and up to 10 $mW\,cm^{-2}$ for stronger light sources and optimized optical illumination. This implies that illumination can be further increased up to 100 times by choosing stronger light sources. This would allow fluorescence imaging at lower concentrations or increasing the SNR at the same dye concentration.

DSouza *et al.* published an optical irradiance ranging from 4 $mW\,cm^{-2}$ up to 31 $mW\,cm^{-2}$ in an review comparing different clinical fluorescence imaging systems for ICG [74]. The overall irradiance of the system presented here is at the same order of magnitude than other imaging systems.

5 SYSTEM CHARACTERIZATION

Recent developments in molecular imaging allow to specifically target various tissue types with different fluorescent dyes. During surgery, these can be visualized to the surgeon, even though their visual appearance would not allow distinction. Overall, surgical imaging can be enriched by the capacities of molecular imaging which is already clinically established for example for PET imaging.

This thesis focuses on developing a system for next generation fluorescence guided surgery. The requirements for the system are based on the intended use as described in Chapter 2. Subsequently the design requirements were translated in detailed technical specifications in Chapter 3. Moreover, Chapter 4 presents a novel system which combines *real-time* high-quality *color* imaging with *multispectral fluorescence* detection. The system is based on a combined spectral and temporal multiplexing approach using a complementary multiband filter pair and two color sensors.

This chapter is dedicated to evaluating the performance of the realized system. First, the spectral sensitivity of the system is analyzed and the ability to detect any dye throughout the visible and near infrared region is demonstrated in Section 5.1. In Section 5.2, the capacity of the system to accurately image and reproduce colors is numerically tested. In Section 5.3, the fluorescence imaging capacity is experimentally tested. Finally, in Section 5.4, the optical performance of the system is evaluated.

All in all, the system fulfills the design requirements and the novel imaging method is found to be suitable for fluorescence guided surgery.

The system has been published by Dimitriadis *et al.* and consequently experiments, data and concepts from the publications in ref [166, 167] are reused in this chapter.

5.1 SYSTEM SENSITIVITY

This section analyzes the spectral sensitivity of the designed system. First, the overall quantum efficiency of the system is calculated. Second, the efficiency to detect dyes over the entire visible and near infrared range is analyzed.

Some of the concepts, simulations and results which are presented in this section have been published in the peer reviewed publications [166, 167] by Dimitriadis *et al.*.

5.1.1 *Spectral quantum efficiency*

In this section first the spectral quantum efficiency curves of the individual channels are computed and compared with the respective efficiency of a monochrome sensor. Second, the section will display the quantum efficiency in terms of an excitation-emission-matrix as it is common for dyes in fluorescence spectroscopy.

5.1.1.1 *Methods*

The quantum efficiency of a system sensor channel cf is computed as the product of spectral sensor quantum efficiency $q_c(\lambda)$ and spectral filter transmission $t_f(\lambda)$.

$$q_{cf}(\lambda) = q_c(\lambda) \cdot t_f(\lambda) \tag{5.1}$$

for all combinations of filter bands $f \in \{1, 2\}$ and $c \in \{R, G, B\}$, so $cf \in \{R1, G1, B1, R2, B2, G2\}$. The averaged sensor quantum efficiencies q_{S1} and q_{S2} are calculated as

$$q_{S_1}(\lambda) = \frac{1}{4} \cdot q_{R_1}(\lambda) + \frac{1}{2} \cdot q_{G_1}(\lambda) + \frac{1}{4} \cdot q_{B_1}(\lambda) \tag{5.2}$$

and

$$q_{S_2}(\lambda) = \frac{1}{4} \cdot q_{R_2}(\lambda) + \frac{1}{2} \cdot q_{G_2}(\lambda) + \frac{1}{4} \cdot q_{B_2}(\lambda). \tag{5.3}$$

The overall quantum efficiency is defined by

$$q_S(\lambda) = q_{S_1}(\lambda) + q_{S_2}(\lambda). \tag{5.4}$$

Accordingly, the quantum efficiency of a monochrome system is computed for the two sensors as

$$q_{M1}(\lambda) = q_M(\lambda) \cdot t_1(\lambda), \qquad q_{M2}(\lambda) = q_M(\lambda) \cdot t_2(\lambda) \tag{5.5}$$

and

$$q_M(\lambda) = q_{M_1}(\lambda) + q_{M_2}(\lambda). \tag{5.6}$$

The filter transmission spectra of the filters FF01-440-521-607-694-809 and FF01-387-485-559-649 (both from Semrock, see Section 4.2.2) are obtained from the manufacturer website [181] and data is interpolated for the numerical calculation on a grid ranging form 365 nm to 900 nm in steps of 0.1 nm. Relative sensor spectra had previously been recorded in the laboratory by illuminating the sensor with monochromatic light and measuring the power of the monochrome light (not part of this thesis) [167]. The wavelength of the light was scanned at 365 nm, 385 nm and from 405 nm to 900 nm in steps of 5 nm using a monochromator. At each wavelength the power was measured with a calibrated power meter. The sensor sensitivity is converted

from power spectral density (electron counts per illumination power) to electron counts per photon. The sensitivity is scaled so that the curves match the maximum quantum efficiency as specified by the manufacturer [171]. For the numerical calculations here, the data is interpolated on the same grid as the filter transmission spectra from 365 nm to 900 nm in steps of 0.1 nm.

For the excitation-emission-matrix (EEM) sensitivity plots, the emission sensitivity is multiplied with an excitation intensity. Here, a constant excitation of 1 in a. u. is assumed for wavelengths which are complementary to the emission. An additional gap of 5 nm between all excitation and the complementary emission bands is chosen for illustration because it would be necessary in a real system to avoid leakage of excitation light to the emission channels.

5.1.1.2 *Results*

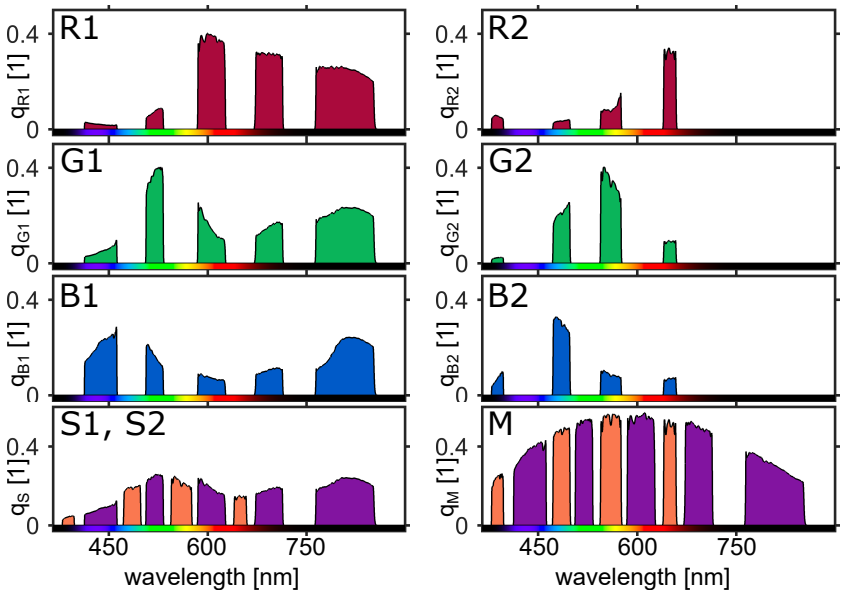

Figure 5.1: Spectral quantum efficiency q of the system channels R1, G1, B1, R2, G2 and B2, for the sensor S1 and S2 (averaged over channels) and for a system with monochrome sensors M1 and M2. Curves are calculated by multiplying the sensor quantum efficiency curves with the respective filter transmission spectrum at each wavelength. Adapted with with permission from ref [167], OSA.

Calculated quantum efficiency spectra q_{cf} displayed in Figure 5.1 include the effect of the multiband emission filters, the color filters of the sensor pixels mask as well as the monochrome quantum efficiency of the silicon sensor.

The curves resemble the complementary multiband structure of the emission filters with strong separation between different bands as well as the wide sensitivity curves of the color channels. The sen-

sitivity ranges from around 380 nm up to around 855 nm. Quantum efficiency curves of the sensors show only minimal gaps between the detection channels which are between 5 nm and 10 nm wide. One band around 750 nm is missing on both sensors, so the system has no sensitivity at these wavelengths.

Maximum quantum efficiency is very similar for both sensors. For sensor S1 the maximum q. e. is found to be 40% for the green channel at approximately 528 nm, for S2 the maximum is 40% also for the green channel around 550 nm.

The average quantum efficiency of the system ($\text{mean}_\lambda \left[q_S(\lambda)\right] \approx 11\%$) is approximately 2.4 times higher than the sensitivity of the monochrome system ($\text{mean}_\lambda[q_M(\lambda)] \approx 27\%$) .

No error could be estimated for maximum and average quantum efficiencies of the sensor because no error is provided with the quantities on which the calculation relies. More precisely, the calculation requires knowledge of the emission filter spectra, the relative sensor sensitivity curves as well as the maximum quantum efficiency. Both emission filter spectra and maximum quantum efficiency are provided by the manufacturer without error. The measured relative sensitivities appear reasonable in comparison with the manufacturer specified sensitivities in the visible range. But for these spectra, also no error estimation is available. Consequently, the presented data is not presented with errors.

Visualizing the quantum efficiency of the channels in the form of an EEM plot in Figure 5.2 shows that the system channels cover a wide range of dyes with different sensitivities. A detailed analysis on the sensitivity towards different dyes is presented in Section 5.1.2.

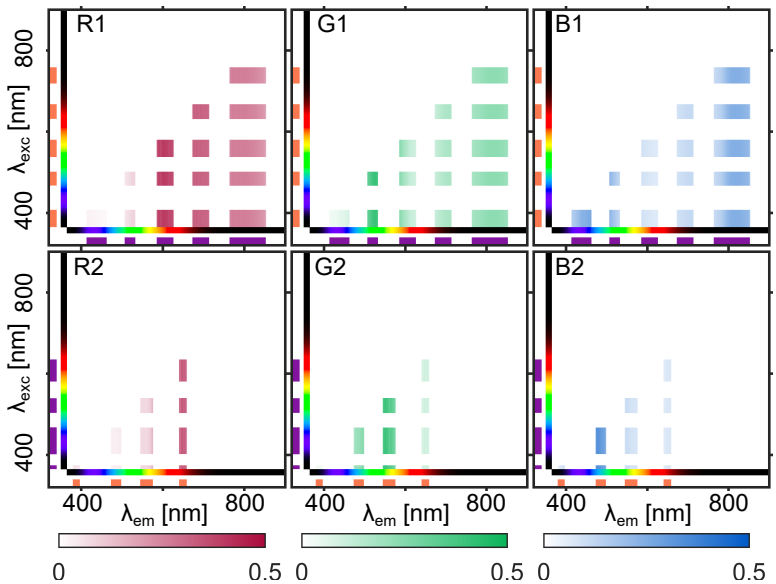

Figure 5.2: System efficiency visualized as excitation-emission matrix.

5.1.1.3 *Discussion*

The sensitivity of the system ranges over the VIS/NIR which is required for both fluorescence and color reflectance imaging as defined in Section 3.1.6. Thus, the overall sensitivity range is sufficient. The gaps between the complementary bands will not affect fluorescence imaging but may alter color reproduction. This issue will be analyzed in detail in Section 5.2.2. The missing band around 700 nm does not affect color imaging at all as color imaging is restricted to the visible range. However, it limits the versatility for NIR fluorescence imaging. If that band was instead available, fluorescence imaging with three dyes in the deep red and NIR would be feasible: one dye emitting at 650 nm, a second dye emitting around 730 nm and a third dye emission above 750 nm should be easy to unmix due to the complementary structure of the bands. In a future version of the system a novel set of bandpass filters can easily improve this aspect.

The detection efficiency of the color system compared to a monochrome system is a factor of 2.4 lower. This loss in efficiency which is attributed to the RGB Bayer pattern is the price tag for color imaging and multispectral fluorescence detection. The monochrome system would just have 2 channels instead of 6. For this analysis, the sensitivities of the two channels have been added. As the sensitivities are spectrally complementary this is feasible. However, during image acquisition as intended for the system, the images of the sensors are recorded at different time points and thus the quantum efficiency would need to be divided by two to correspond to a temporal average efficiency.

The measured transmission spectra of the filters F1 and F2 are specified for orthogonal light incidence. If the light transmits the filter in another angle, the blocking- and pass-bands shift in wavelength. This shift also depends on polarization of the incident light, potentially changing the polarization of light when passing one of the filters.

The light passes the optical filters in infinity corrected space, so the spatial information of the object is encoded in the angle of light to the optical axis. Thus, light being detected at different pixel locations may show slightly different spectral sensitivity due to filtering. In the setup used here, no strong spectral artifacts with a fixed spatial pattern are observed. This is most likely due to low light propagation angles which are below 10° in the setup but such artifacts may occur.

Overall, the spectral quantum efficiency is sufficient for the system, but it is reduced due to the color imaging ability.

5.1.2 *Fluorescence detection efficiency*

The system is required to detect dyes over the entire visible and near infrared range from 400 nm to 900 nm. This section investigates how efficient a fluorescent dye can be detected by the system.

First, the dye emission spectrum is modeled by a Gaussian shaped profile with the center being shifted. This allows to estimate the detection efficiency of an arbitrary dye in the VIS/NIR range.

Subsequently, the system detection efficiency is calculated for dyes whose emission spectra are obtained from a library and compared with the Gaussian emission spectra.

Methods

Measured fluorescent dye emission spectra usually report the relative energy per wavelength $E_{\text{psd}}(\lambda)$ in units of power spectral density as $\left[\frac{W}{\text{nm}}\right]$. Sensor quantum efficiency curves determine the probability of that an incoming photon hitting the sensor triggers an electron on the sensor and thus results into a count. Therefore, the power spectral density emission spectrum needs to be converted to an emission spectrum $E_{\text{photon}}(\lambda)$ in units of photons numbers per wavelength $\left[\frac{\text{Photons}}{\text{nm}}\right]$ to simulate the response of the sensor channels to emitted light:

$$E_{\text{psd}}(\lambda) = E_{\text{photon}}(\lambda) \cdot \frac{h \cdot c}{\lambda} \tag{5.7}$$

where h is the Planck constant and c the speed of light.

For the simulation, the response of the sensor to a certain dye emission intensity is desired. Therefore, all spectra are normalized so that the spectra show the spectral emission profile of a single photon:

$$e(\lambda) = \frac{E_{\text{photon}}(\lambda)}{\int E_{\text{photon}}(\lambda) d\lambda} \tag{5.8}$$

The detection efficiency of a sensor channel $c \in \{R1, G1, B1, R2, G2, B2\}$ for a fluorescent dye with emission spectrum $e(\lambda)$ is calculated as

$$\eta(c, \lambda) = \int e(\lambda) \cdot q(c, \lambda)\, d\lambda. \tag{5.9}$$

For the numerical implementation, all dye emission spectra $E_{\text{psd}}(\lambda)$ are interpolated to a finite set of bins ranging from 365 nm to 900 nm in steps of 0.1 nm. In the next steps, the dye intensity is converted to photon counts and normalized. The sensor quantum efficiency is interpolated onto the bin centers from 365 nm to 900 nm in steps of 0.1 nm. Dye emission intensities which is out of the sampling range of the sensitivity are cropped. The system is calculated according to Equation 5.9 maintaining the numerical quantization. Overall average sensor sensitivities $\eta(\text{S1}, \lambda)$ and $\eta(\text{S2}, \lambda)$ are calculated by averaging the respective set of channels:

$$\eta_{\text{S1}}(\lambda) = \frac{1}{4} \cdot \eta_{\text{R1}}, (\lambda) + \frac{1}{2} \cdot \eta_{\text{G1}}(\lambda) + \frac{1}{4} \cdot \eta_{\text{B1}}(\lambda) \tag{5.10}$$

and accordingly

$$\eta_{\text{S2}}(\lambda) = \frac{1}{4} \cdot \eta_{\text{R2}}(\lambda) + \frac{1}{2} \cdot \eta_{\text{G2}}(\lambda) + \frac{1}{4} \cdot \eta_{\text{B2}}(\lambda). \tag{5.11}$$

Gaussian emission spectra with width σ and center emission wavelength λ_c are defined as

$$E_{\text{photon}}(\lambda|\lambda_c,\sigma) = \frac{1}{\sigma\sqrt{2\pi}} \exp^{-\frac{(\lambda-\lambda_c)^2}{2\sigma^2}} . \tag{5.12}$$

The Bayer micropattern of the sensors is of the form »RGGB«. For the numerical calculation the numbers are created using the Matlab pre-implemented function `normpdf`. Fluorescent dye emission is simulated for dyes with a center wavelength of $\lambda_c = 395\,\text{nm} \ldots 870\,\text{nm}$ in steps of 1 nm for a emission width $\sigma = 20\,\text{nm}$, $\sigma = 30\,\text{nm}$ and $\sigma = 40\,\text{nm}$.

A selection of 701 dyes with emission maxima above 400 nm from a library of existing fluorescent dyes with emission and excitation spectra provided by the TU Graz are used to calculate the detection efficiency of the system for real dyes [182]. The names of all used dyes are listed in Section A.3. As the dye emission was interpolated on a grid ranging from 390 nm to 900 nm, the emission maxima inside this range are determined.

Results

Numerical results of a selection of the simulated detection efficiencies of the dyes are displayed together with the efficiency curves of the parametrized Gaussian emission in Figure 5.3.

The statistical properties mean, median, minimum and maximum of the numerical results regarding emission curves and emission efficiency for the real dyes obtained from the library are provided in tabular format in Section A.2 together with the individual values for a selection of dyes.

The efficiencies η of the Gaussian emission curves oscillate with the filter bands characteristics. If the center emission wavelength matches the centers of a filter band, η has a local maximum. In contrast η is minimal if the center wavelength falls within a filter gap. Among the different emission widths, oscillations are strongest for $\sigma = 20\,\text{nm}$, smaller for $\sigma = 30\,\text{nm}$ and quite small for $\sigma = 40\,\text{nm}$.

Most of the values which are plotted as points in Figure 5.3 of library dyes scatter around the three Gaussian curves. For regions of high curve slopes, the points representing real dyes tend to lie at lower wavelength regions compared to the respective Gaussian shaped dye.

Both Gaussian shaped and real dye transmission efficiencies are overall higher for sensor S1 than for S2. Highest detection efficiencies can be found in the NIR above 700 nm.

The overall detection efficiency η_{S1+S2} is obtained by summing up the two efficiencies η_{S1} and η_{S2}. In Figure 5.3, the oscillations of η_S are minimal over VIS compared to the plot of η_{S1} and η_{S2}. However, in the NIR spectral range, the intensities oscillate.

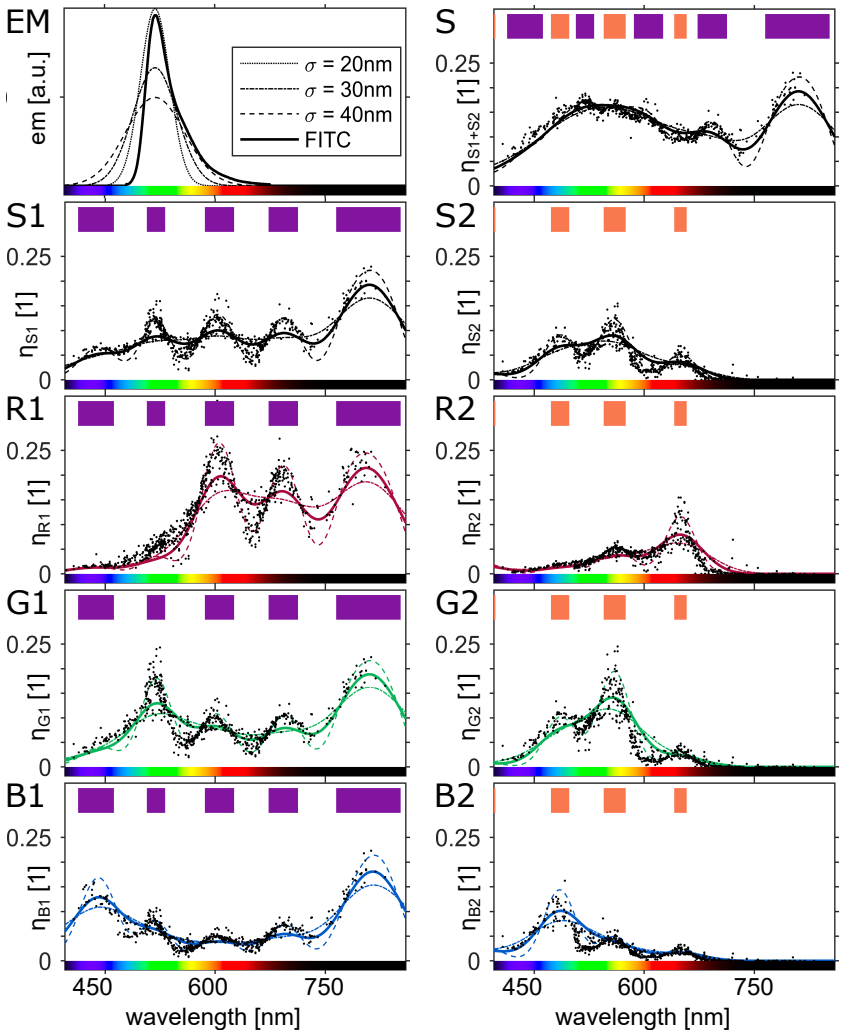

Figure 5.3: Detection efficiency η for a set of 701 measured fluorescence emission spectra and for parametrized Gaussian shaped emission with varying center wavelength λ_c and widths of $\sigma = 20\,\text{nm}$ (dashed line), $\sigma = 30\,\text{nm}$ (bold line) and $\sigma = 40\,\text{nm}$ (dotted line). Efficiencies of the existing dye spectra are plotted depending on the respective emission maxima. Filter transmission bands of filter ■ F1 and ■ F2 are plotted on top of the plots. Plots are extended from a respective plot in [167]. Adapted with with permission from ref [167], OSA.

No errors are provided for the calculation because all results rely on the sensor quantum efficiency which is specified by the manufacturer without specifying its error. Also the relative sensor sensitivity curves, the filter transmission and the dye emission spectra do not provide errors.

Discussion

The data shows that the detection efficiency of real dye spectra is slightly distinct from the parametrization model, but most dyes are

very close to one of the models. This allows to conclude that the model to parameterize the fluorescence emission with a Gaussian emission curve with σ between 20 nm and 40 nm is suitable. Though, it is important to keep in mind that real dyes have distinct spectra and thus show a different spectral behavior.

One shortcoming of the model is that Gaussian spectra are symmetric whereas real fluorophore spectra are skewed. This explains the lower shift of slopes for real dyes to lower wavelengths.

The parametric model shows that different σ values result in similar overall η_{S1+S2} efficiencies, but the oscillations between S1 and S2 are much higher for smaller σ. Thus, the overall number of detected photons of a dye with spectrally narrow emission will be the same as with wide emission given both emit the same number of photons. However, the variation of the spectral signatures for small changes in wavelength will be stronger for narrow emission profiles. Thus, it is easier to unmix two dyes which are spectrally close if they have narrow emission spectra ($\sigma = 20$ nm) compared to wide emission spectra ($\sigma = 40$ nm).

Computing η_{S1+S2} can be misleading, as it assumes that the fluorescence emission is equal in both phases for all dyes. This is hardly ever the case. Depending on the integration time in both phases and the excitation lights, the sensor efficiencies need to be weighted for each dye individually. The dyes can thus also be separated by the excitation, leading to even stronger unmixing of spectrally close dyes.

The quadband emission filter F2 is missing a spectral band in the NIR around 750 nm. This leads to low detection efficiencies at that wavelength and fluctuations of the efficiencies. The easiest solution to circumvent this issue would be to use a custom designed filter with an additional band at 750 nm. If modifying the filter, the transmission bands of S2 could be made broader and the bands of S1 could be made smaller in return so that the widths are equal for both filters. This would result in more similar detection efficiencies for the two sensors.

Generally, the system is very sensitive in the NIR because neither of the three microfilters in the RGB Bayer pattern blocks the light. Thus, the sensor quantum efficiency in the NIR is close to the quantum efficiency of a monochrome sensor. For intraoperative fluorescence imaging, the wavelength region between 650 nm and 850 nm is very attractive because tissue absorption is minimal.

Conclusion

The simulation using a set of real dyes and additionally a parametrization model has shown that model can reasonably replace real spectra with some limitations. This parametric model will be used in Chapter 7 to optimize the system.

The simulation proofs that the system can detect any dye over the visible and near infrared range and thus fulfills this design requirement.

5.2 COLOR CORRECTION

This section investigates the capacity of the developed multispectral imaging system to accurately reproduce colors. It is split into three parts. First, the capacity of Luther-Ives criterion, as a well-established method to correct colors in imaging is applied to the system. Second, a linear correction algorithm is developed resulting in minimal perceptual color deviation between ideal and corrected colors. It's performance is compared with the Luther correction. Third, the linear color correction is evaluated for different illumination scenarios that are relevant for the clinical application.

Color sensors typically record reflectance images in a red, green and blue channel. Ideally, these signals should correspond to the red, green and blue visual perception of the human eye represented by the color matching functions $\overline{x}$, $\overline{y}$ and $\overline{z}$. However, deviations of the camera sensitivity spectra to the color matching functions require to correct the signals before displaying. Additionally, color perception involves neural processing steps which include for example brightness and color adaption depending on many factors such as the surrounding scene, the immediate history of visual impressions and many more.

The developed multispectral imaging system does not have three color channels with close spectral response to the color matching functions. Instead, it has six channels which exhibit a multiband structure with steep spectral edges. Therefore, a transformation from sensor channel space to a normed color space corresponding to human perception is required. The CIE XYZ color space corresponds to human perceptual sensation and is therefore selected here as target color space for color correction.

Various different approaches to transform the signal from sensor space to CIE XYZ space have been published. Among these approaches are lookup tables, polynomial or neural network based algorithms [183]. For algorithms with a higher number of parameters improved correction results are expected. Hong *et al.* presented higher order polynomial methods with superior performance compared to linear transformation [184]. Adding an offset term and a term proportional to the product of all three camera channels caused strongest improvements. Cheung *et al.* compared polynomial based transformations with neural networks [185]. Both approaches result in similar performance, though neural networks require tedious training. Therefore, the publication favors polynomial based approaches over neural networks. One of the most important prerequisites is that a correction algorithm

needs to be computationally light because the calculation needs to be executed for each image in video refresh rate [183]. Lookup tables measure the entire color space and linearly interpolate in between the measurements. On the one hand, the method only relies on the measurement which can capture all sort of effects. Accordingly, errors in some measurements will lead to errors in the correction. Also, interpolation for values in between the lookup table may influence the result. Lookup tables need to be calibrated once and cannot be updated in real-time [183]. As the illumination of the imaging may change to adapt for better fluorescence unmixing, lookup tables are not used here.

In this work, all color correction approaches use a linear transformation between camera signal space and CIE XYZ color space. Linear transformations are computationally easy to implement and can be modified quickly if necessary.

Different methods to find the best estimate for the parameters of the linear correction algorithm will be investigated here. First, the Luther-Ives condition is applied, which tries to spectrally match the spectral sensor sensitivity curves to the color matching functions in Section 5.2.1. As the spectral matching does not work well for sensitivities with sharp edges, a perceptual performance based method is used to estimate the best set of correction coefficients. It minimizes the deviation between the ideally perceived colors by the human eye and the corrected color values for a set of colors. This method is supposed to have superior performance compared to the spectral based method, but the illumination needs to be fixed as presented in Section 5.2.2. The last part (Section 5.2.3) investigates whether for all illumination scenarios a good estimate for the parameters of the linear correction algorithm can be found.

Some of the concepts, simulations and results which are presented in this section have been published in the peer reviewed publications [166, 167] by Dimitriadis *et al.*.

5.2.1 *Color image correction by Luther criterion*

According to the Luther-Ives criterion, a linear transformation between the sensor sensitivity curves and the color matching functions $\overline{x}$, $\overline{y}$ and $\overline{z}$ should exist for good color reproduction [123, 173, 174]. In this section, the closest estimate for the linear transformation, the Luther matrix $\boldsymbol{m}_L$, is obtained for some sensor configurations. The Luther error, corresponding to the root mean square deviation between the color matching functions and the linearly transformed sensor sensitivities is minimized.

The biggest advantage of the Luther criterion is that it does not depend on illumination. Accordingly, sensors and systems can be compared independent of the illumination light source they are used

with. However, the result does not consider the actual visual impression. This section investigates whether the Luther-Ives criterion and the associated Luther error is a good measure to evaluate the color reproduction of the system.

Additionally, different sensor configurations are compared with the system. The standard CIS2521 sensor is compared as it is the normal color imaging sensor. Additionally, the impact of extending the sensitivity to the IR, of adding multiband filters with sharp spectral edges or of using only one single sensor of the system on color reproduction is investigated.

5.2.1.1 *Methods*

The measured quantum efficiency curves of the sensor CIS2521 (see Section 5.1.1) are converted from spectral quantum efficiency $q_c(\lambda)$ to spectral response in units of power spectral density:

$$s(c,\lambda) \sim q_c(\lambda) \cdot \frac{\lambda}{h \cdot c_0} \tag{5.13}$$

and the sensitivity $s(c,\lambda)$ is normalized for each channel c to be maximally one.

For the numerical calculations, a fixed wavelength grid with 5 nm wide bins and bin centers from 380 nm to 780 nm is used. The sensitivity spectra on the grid are computed as the average over the respective bins using linear interpolation if necessary.

The CIE published in 1931 sensitivity curves for a linear photo detector, displayed in Figure 5.5, which represents the sensation of the eye, called the CIE 2 degree color matching functions [186–188]:

$$s_{eye}(c,\lambda) = \left[\overline{x}(\lambda), \overline{y}(\lambda), \overline{z}(\lambda)\right]. \tag{5.14}$$

Here, the matrix $\boldsymbol{m}_L$ is calculated so that the spectral sensitivity curves of the sensor match the color matching functions as close as possible:

$$\arg\min_{\boldsymbol{m}_L} \left[\frac{1}{n_\lambda} \sum_{\lambda}^{n_\lambda} \Big(s_S(c_{eye},\lambda) - \underbrace{\sum_{c_S} m_L(c_{eye},c_S) \cdot s_S(c_S,\lambda)}_{s_{L,S}(c_{eye},\lambda)} \Big)^2 \right] \tag{5.15}$$

This ensures good color reproduction as stated by the Luther-Ives condition [123, 173, 174].

The Luther matrix is calculated using the Matlab pre-implemented function `mrdivide`. It minimizes the Luther error δ_S for a sensor S, defined as

$$\delta_S = \sqrt{\frac{1}{3 \cdot n_\lambda} \sum_{c_{eye}} \sum_{\lambda}^{n_\lambda} \Big(s_S(c_{eye},\lambda) - s_{L,S}(c_{eye},\lambda) \Big)^2}. \tag{5.16}$$

Table 5.1: Overview of the Luther error δ_S for the selected sensor configurations.

	CIS2521	CIS2521 IR	System	S1+S2	S1	S2
δ	0.1892	0.2505	0.2519	0.2845	0.3324	0.4374

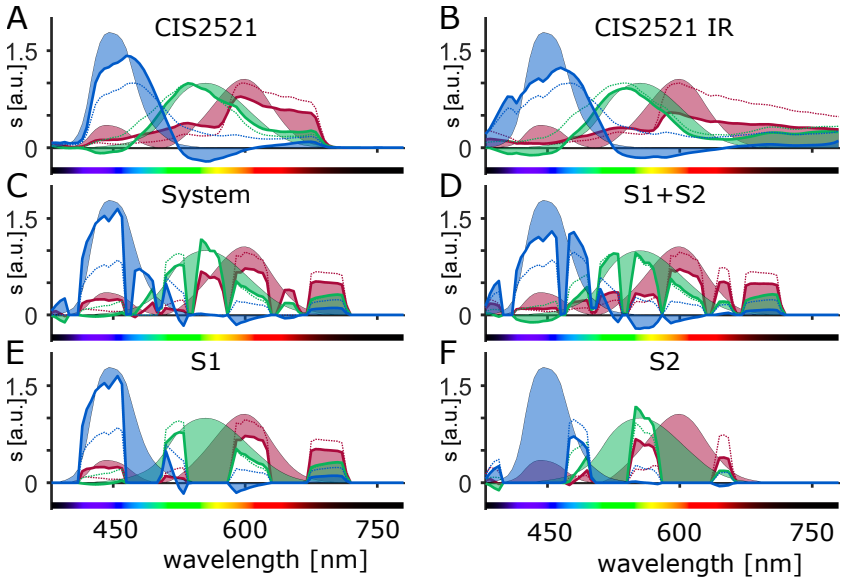

Figure 5.4: Luther plots of the sensor sensitivity spectra of A) the sensor CIS2521, B) CIS2521 IR (no cutoff filter), C) the dual sensor system with S1 and S2, D) the system adding the sensor sensitivities S1+S2 and the two individual sensors E) S1 and F) S2. For each sensor, normalized raw channel sensitivities are plotted as dotted lines in ■ red, ■ green and ■ blue for the respective channels. Sensor sensitivity $s_{L,S}(c_{eye}, \lambda)$ after correction with the Luther matrix are plotted as solid lines. The area between the Luther sensitivity and the respective color matching function is filled. The reported rms error in Table 5.1 corresponds to the sum of the rms of the marked areas.

5.2.1.2 *Results*

Figure 5.4 shows Luther sensitivities $s_{L,S}(c_{eye}, \lambda)$ for six different sensor configurations which are related to the developed system: the basic sensor CIS2521 in the most common configuration with an IR blocking filter, the sensor CIS2521 IR with sensitivity in the IR region, the dual sensor system with both sensors S1 and S2, the individual sensor sensitivities S1 and S2 and finally the addition of the two sensors S1 + S2.

All results need be put into perspective with the sensor CIS2521 ($\delta_{CIS2521} = 0.1892$) because the other systems are based on it. Adding IR sensitivity to the system by removing the IR cutoff filter results in an increase in δ of approximately 32%. As the color matching functions do not have any sensitivity in the IR, sensitivity of a sensor

channel results in too low sensitivity of the corrected curve in the visible. This increases the Luther error.

The dual sensor system has almost the same Luther error ($\delta_{\text{system}} = 0.2519$) as the CIS2521 IR sensor, but different areas in the Luther plot accumulate the error: the dual sensor system shows that the curves follow the color matching functions well, but the sharp edges of the multiband filters cause a high Luther error. In contrast, CIS2521 IR accumulates δ in the IR, which is blocked by the specific multi-bandpass filter pair used in the system.

Adding the sensitivity of the two individual sensors results in a sensitivity corresponding to the CIS2521 IR with additional bandgaps due to the emission filter. It shows Luther sensitivity curves corresponding to the CIS2521 IR, but has additional errors due to the filter bands. Thus, the higher error ($\delta_{S1+S2} = 0.2845$) is expected.

Both individual sensors S1 ($\delta_{S1} = 0.3324$) and S2 ($\delta_{S1} = 0.4374$) have very high Luther errors. The intensities match in some band regions, but for most of the spectrum the curves cannot match because of the multiband structure of the sensitivities.

No error is specified for the presented Luther error results δ, because no error is available for the basic quantities required for the calculations. The absolute quantum efficiency scaling of the sensor sensitivity spectra is not important for the color representation, as color is not defined by the absolute channel sensitivities but rather by the relative response of the different color channels. The color matching functions are taken as a defined standard and thus no error is provided. The remaining source of error are the sensor sensitivity spectra, for which no error is specified (see Section 5.1.1). All systems (but CIS2521) rely on the same sensitivity measurement. Thus, any error would be introduced in all remaining 5 calculations, but it would be weighted differently and thus contribute differently to the result. In short, the number of digits of the results is not associated with an error calculation.

5.2.1.3 *Discussion*

The dual sensor system has only a slightly higher Luther error than the sensor CIS2521 IR alone, but it consists of different contributions: the basic sensor CIS2521 IR has big contributions in the IR and in the visible range due to too low sensitivity. In contrast, most of the error of the system is based on the filter gaps.

For conventional consumer color cameras, Luther errors between 0.12 and 0.26 have been reported [189]. So, the basic sensor CIS2521 has a rather high Luther error but is still inside the range for color sensors. The IR version of the sensor and the dual sensor system are at the upper end of the range of Luther errors of normal color sensors. All other configurations have higher Luther errors than conventional color sensors.

Sensitivity in the IR is generally problematic for color reproduction, because the color matching functions do not have any sensitivity in the IR. However, it is necessary for many fluorescence imaging applications. The Luther-Ives condition does not handle this aspect very well, because it deforms the curves in the visible part to compensate for the IR sensitivity.

Adding multiband filters to the sensor causes additional errors. The sharp gaps between filters and the blocking regions with no sensitivity in any of the channels result in a higher Luther error. As the rms error is minimized, the Luther sensitivity is matched as close as possible to the color matching functions. The algorithm cannot compensate for small wavelength gaps in the sensitivity for example by increasing the sensitivity in the vicinity. Such a strategy is supposed to perform well because reflectivity spectra of colors are spectrally smooth and are not sensitive to small spectral gaps.

A thought experiment demonstrates the issue: Assuming that a sensor would have sensitivity curves corresponding exactly to the color matching functions but at every second nm the sensitivity is zero. So, approximately half of the light is transmitted, but the color response of the sensor is supposed to match to the response of the color matching functions because reflectivities are usually very wide compared to 1 nm. On the contrary, the Luther error would be big, because every second wavelength value matches perfect or completely deviates. Multiband filters with sharp edges face this problem.

Therefore, I would like to conclude that the Luther-Ives condition, which is a widespread criterion to evaluate the quality of color sensors, is not sufficient to describe the performance of systems with sharp edges of the spectral sensitivity.

To get a more realistic evaluation of the color imaging performance of the system, the system is evaluated regarding perceptual differences instead of sensitivity differences in the next section. For this analysis, the illumination needs to be specified and is therefore no more a pure evaluation of the sensitivity itself.

The Luther-Ives analysis showed that the error of the system is at the higher end compared to commercial sensors, but still acceptable. As a big part of the error originates from sharp wavelength drops, results will be perceived better than expected from the following analysis.

5.2.2 *Color imaging quality with Munsell colors*

This section develops a linear correction approach by optimizing the color representation as perceived by the human eye for a fixed set of colors.

So far, color correction was performed by minimizing at spectral sensitivity deviations as proposed by Luther and Ives [123, 173, 174].

However, the Luther error δ is not suitable to characterize color imaging systems with sharp spectral edges in the sensitivity curves as discussed in Section 5.2.1.3.

Alternatively, the parameters for the linear transformation can be estimated to obtain best perceptual performance. Therefore, the set of parameters is chosen so that the corrected colors of the system are perceived as similar as possible to the colors as perceived by the human eye under D65 illumination as similar as possible.

This requires specifying a metric measuring color differences. In this work the elaborate and complex metric CIEDE2000 ΔE_{00} is used. It aims at reporting small color differences as perceived by the eye and has been sequentially developed from CIEDE74 and CIEDE96 [190]. CIEDE2000 was also chosen because it has been extensively validated and is used widely in the scientific community. Even though some issues remain, an overall acceptable performance is guaranteed.

The hypothesis is that the perceived color difference is not as big as with the Luther-Ives condition, because the sharp spectral edges in the system sensitivity do not cause strong perceptual effects due to smooth reflectance spectra. The Luther-Ives criterion does not require any knowledge for the illumination light source and is therefore universal.

In contrast, the illuminant spectra of medical imaging systems are well-known as it is defined by the manufacturer supplied light source. Therefore, the flexibility to account for unknown light sources is not necessary. The known light spectra are required to ensure knowledge of the white point for color transformations.

For the analysis, the color signal of the used sensor and configurations of it are simulated for standardized daylight illumination CIE D65 and a set of reflectivity spectra representing 1269 Munsell colors.

5.2.2.1 *Methods*

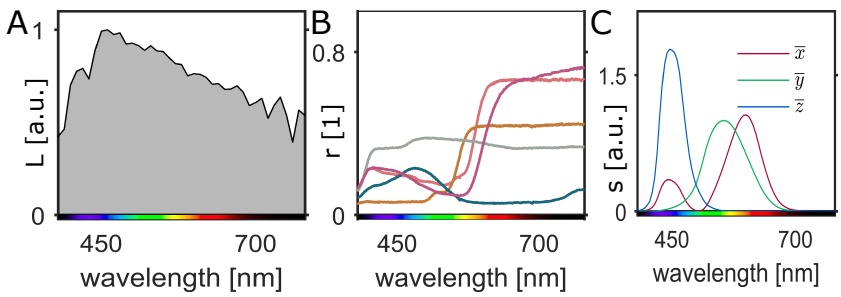

Figure 5.5: Illumination and reflectivity and color matching function spectra. A) Spectral power distribution of D65 daylight. B) Reflectivity spectra of the Munsell colors ■ 2.5R 6/10; ■ 5YR 6/10; ■ 5B 4/6; ■ 10GY 7/1; ■ 5RP 5/12. C) Color matching functions $\bar{x}$, $\bar{y}$ and $\bar{z}$.

Measured reflectivity spectra $r(t,\lambda)$ of the 1269 matt Munsell colors t with $t = 1,\ldots,1269$ are obtained from the "Color Research Laboratory of the University of Eastern Finland" [191] from 380 nm to 780 nm with a spacing of 1 nm. If necessary, reflectivity spectra $r(t,\lambda)$ are extrapolated using the respective nearest neighbor assuming smooth reflectivity curves.

The reflectivities are averaged over the numerical bins ranging from 380 nm to 780 nm with a spacing of 5 nm in the same way as the sensitivities (see Section 5.2.1.1 for a detailed description).

Illuminant l spectra $L(l,\lambda)$ for D65 daylight and equal energy illuminant A are provided by the CIE [192]. The spectrum of the halogen light source was obtained from the Rochester Institute of Technology [193].

The color matching functions $s_{\text{eye}}(c,\lambda)$ are described in Equation 5.14 and Figure 5.5C.

The response $B_{\text{eye}}(l,t,c)$ of the human eye in CIE XZY color space with $c \in \{\overline{x},\overline{y},\overline{z}\}$ for Munsell colors t with reflectivities $r(t,\lambda)$ illuminated by $L(\,l,\lambda)$ is calculated as

$$B_{\text{eye}}(l,t,c) = k \cdot \int_{\lambda=377.5\,\text{nm}}^{782.5\,\text{nm}} L(\,l,\lambda) \cdot r(t,\lambda) \cdot s_{\text{eye}}(c,\lambda)\,d\lambda \tag{5.17}$$

with

$$k = \int_{\lambda=377.5\,\text{nm}}^{782.5\,\text{nm}} L(\,l,\lambda) \cdot s_{\text{eye}}(2,\lambda)\,d\lambda. \tag{5.18}$$

The sensor response $A_S(l,t,c)$ to the Munsell colors t illuminated with light l is computed as

$$A_S(l,t,c) = k \cdot \int_{\lambda=377.5\,\text{nm}}^{782.5\,\text{nm}} L(l,\lambda) \cdot r(t,\lambda) \cdot s_S(c,\lambda)\,d\lambda. \tag{5.19}$$

This sensor signal is transformed from sensor color space to XYZ color space using the color correction matrix $\boldsymbol{m}_M$

$$B_S(l,t,c) = \sum_{c_S} m_M(c,c_S) \cdot A_S(l,t,c_S). \tag{5.20}$$

Each illumination spectrum may require a different color correction matrix $\boldsymbol{m}_M$ for optimal performance. Consequently, the matrix $\boldsymbol{m}_M$ may depend on the illumination.

The signal of the color tiles is then transformed to L*a*b* color space with $c \in \{L^*,a^*,b^*\}$ as

$$B_{\text{eye}}(l,t,c) \xrightarrow{\text{D65}} C_{\text{eye}}(l,t,c). \tag{5.21}$$

using D65 illumination as the white point. This transformation from XYZ to L*a*b* color space was done using the `xyz2lab` Matlab function [174, 188][p. 13, pp. 209–210]. The series of transformations can be schematically written as

$$A_S(l,t,c_S) \xrightarrow{\boldsymbol{m}_M} B_S(l,t,c) \xrightarrow{\text{D65}} C_S(l,t,c). \tag{5.22}$$

The best correction matrix $\boldsymbol{m}_M$ is estimated by minimizing the average error $\overline{\Delta E_{00}}$ for each detection scenario.

The average color difference for n_t Munsell colors between the corrected colors obtained by the camera and the color seen by the human eye (under D65 illumination) is calculated as

$$\overline{\Delta E_{00}} = \frac{1}{n_t} \cdot \sum_{t=1}^{n_t} \Delta E_{00}\Big(C_S(l,t,c), C_{eye}(D65,t,c)\Big). \tag{5.23}$$

The best color correction matrix $\boldsymbol{m}_M$ for all Munsell color targets is calculated by minimizing the average color difference

$$\arg\min_{\boldsymbol{m}_M} \left[\frac{1}{n_t} \cdot \sum_{t=1}^{n_t} \Delta E_{00}\Big(A_S(c,t) \xrightarrow{\boldsymbol{m}_M, D65} C_S(c,t), C_{eye}(c,t)\Big)\right]. \tag{5.24}$$

The optimization is implemented using the Matlab predefined `fminunc` function.

The starting value of $\boldsymbol{m}_M$ for the local optimization is taken as

$$\boldsymbol{m}_{M0} = \begin{pmatrix} 1 & 0 & 0 & 1 & 0 & 0 \\ 0 & 1 & 0 & 0 & 1 & 0 \\ 0 & 0 & 1 & 0 & 0 & 1 \end{pmatrix} \tag{5.25}$$

in case of six sensor channels and

$$\boldsymbol{m}_{M0} = \begin{pmatrix} 1 & 0 & 0 \\ 0 & 1 & 0 \\ 0 & 0 & 1 \end{pmatrix} \tag{5.26}$$

in case of 3 sensor channels.

The Matlab optimization function `fminunc` with standard parameters is used because of the unconstrained and multivariable nature of optimization problem. As no Hessian matrix of the fitness function is directly supplied to the algorithm, the `quasi-newton` algorithm with standard parameters is used.

The sensitivity of a sensor being corrected with the optimized matrix m_t on basis of the Munsell tiles is calculated as

$$s_{t,s}(c_{eye}, \lambda) = \sum_{c_s} \boldsymbol{m}_M(c_{eye}, c_s) \cdot s_s(c_s, \lambda). \tag{5.27}$$

5.2.2.2 *Results*

The error ΔE_{00} for each of the Munsell colors is calculated using the optimized correction matrix $\boldsymbol{m}_M$ for each of the systems. The boxplot for all Munsell colors in Figure 5.7 shows a statistical analysis of the error ΔE_{00} and Table 5.2 reports the statistical properties mean, median, minimum, maximum, 5% and 95% quantile. Additionally, the exit flag of the optimization algorithm `fminunc` is provided.

Table 5.2: Statistical analysis reporting the mean, median, minimum, maximum, 5% quantile and 95% quantile of the color error ΔE_{00} for the 1269 Munsell colors for the different imaging systems using CIE D65 illumination after optimization. Exit reasons for the optimization: 0: number of function evaluations or iterations exceeded a threshold; 1: gradient was smaller than a threshold; 5: predicted change of the fitness function is smaller than a threshold.

	MEAN	MEDIAN	MIN	MAX	5% Q.	95% Q.	EXIT
CIS2521	1.20	0.84	0.03	6.61	0.20	3.69	5
CIS2521 IR	1.61	1.10	0.06	19.32	0.35	4.52	5
System	0.75	0.47	0.02	11.82	0.15	2.43	0
S1+S2	2.15	1.30	0.06	16.23	0.38	7.06	1
S1	4.05	3.31	0.12	18.80	0.89	9.48	5
S2	1.28	0.92	0.09	12.94	0.31	3.52	0

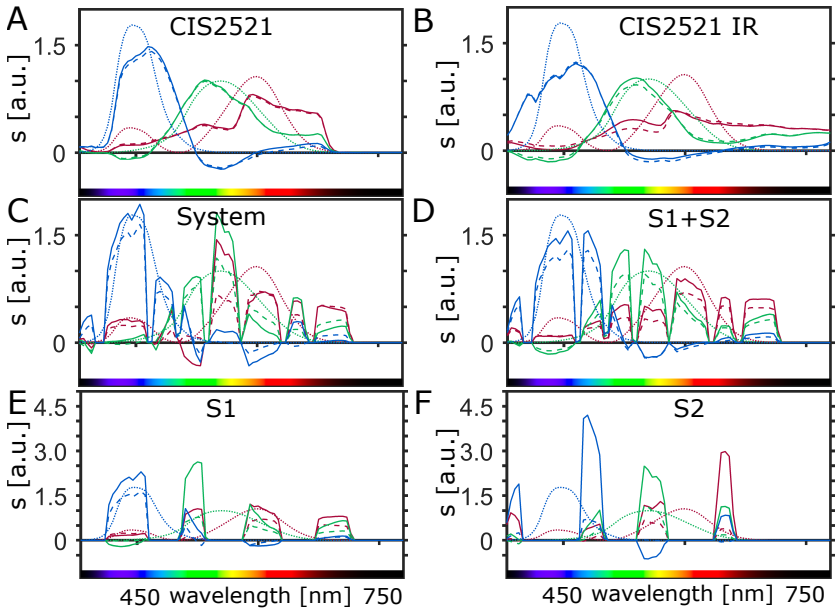

Figure 5.6: Reporting of optimized $\boldsymbol{m}_M$ as Munsell corrected sensitivity spectra $s_M(c_{\text{eye}}, \lambda)$ for the CIS2521, CIS2521 IR sensor, the dual sensor system, S1+S2 and the individual sensors S1 and S2 displayed as solid lines. The corresponding ideal color matching function $\bar{x}$, $\bar{y}$ and $\bar{z}$ are displayed as dotted lines, the corrected Luther spectra $s_{\text{L,S}}(c_{\text{eye}}, \lambda)$ are displayed as dashed lines. Channels: red, green and blue.

For all system configurations, the error ΔE_{00} of the optimized correction matrix is smaller than the error ΔE_{00} of the Luther corrected colors (see Figure 5.7). The system performs best in terms of mean and median error even though it has sensitivity in the IR and spectral gaps. The conventional sensor CIS2521 performs better than the sensor with IR sensitivity CIS2521 IR, because signal in the IR can only lead to altered color signals. The combined sensitivity S1+S2

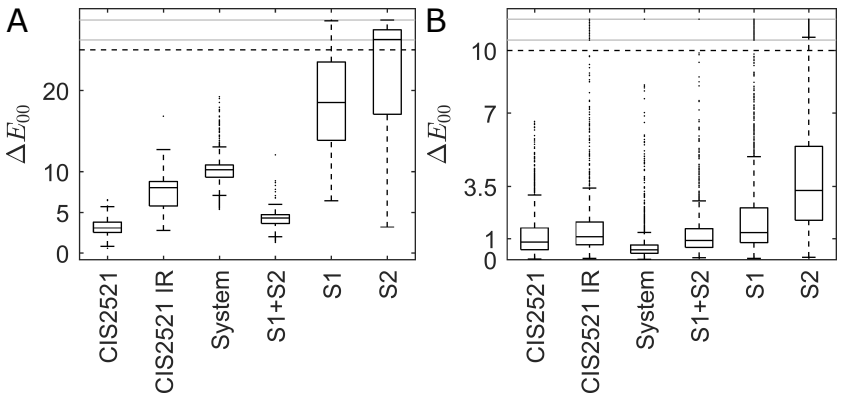

Figure 5.7: Boxplot of ΔE_{00} for a set of Munsell colors of different sensor configurations and correcting A) by using the Luther-Ives criterion or B) by optimizing $\overline{\Delta E_{00}}$. The different sensor configurations are the pure sensor CIS2521, the IR extended version CIS2521 IR, the realized six channels system, the addition of the channels of S1 and S2 sensitivity per channel and the two individual sensitivities of S1 and S2 with the emission filters.

has on average a higher error than the sensor itself and than the IR extended version. This sensor demonstrates that IR sensitivity and a band structure with only three channels does not result in a good color reproduction. Both sensors of the system S1 and S2 individually perform very poor compared to the other configurations.

Munsell sensitivities are shown in Figure 5.6 to represent the best estimated color correction matrices $\boldsymbol{m}_M$. These Munsell sensitivities $s_{t,s}(c_{\text{eye}}, \lambda)$ in general follow the color matching functions better than the curves corrected with the Luther-Ives criterion. For the sensors CIS2521 and CIS2521 IR the differences are minor. For the system and scenario S1+S2, the Munsell sensitivities are higher if spectral gaps are close and compensate for the gaps in the vicinity. Both single sensor systems S1 and S2 compensate the big spectral gaps with zero sensitivity by increasing the sensitivity in the close by bands so that the brightness matches.

No errors are specified for the CIEDE2000 results, because neither sensor sensitivity spectra nor illumination spectra or Munsell colors are provided with an error. The presented accuracy of the results is chosen to allow identification of differences between the scenarios, but is not associated with an error calculation.

5.2.2.3 *Discussion*

For all the investigated sensor systems, the color correction using the estimated Munsell matrix $\boldsymbol{m}_M$ results on average in a perceived smaller color deviation than correcting using the Luther matrix $\boldsymbol{m}_L$.

As the illuminant has been fixed to D65 daylight, the correction matrix only holds for this illuminant. In contrast, the Luther matrix

$\boldsymbol{m}_L$ is independent of the used illuminant but the error ΔE_{00} depends on the used illuminant. For intraoperative imaging the illuminant is well-known so this restriction is not relevant, but each illumination requires its own Munsell matrix $\boldsymbol{m}_M$.

The good match of Munsell spectra and Luther spectra for CIS2521 and CIS2521 IR shows that for smooth reflectivity spectra, the Luther-Ives criterion and estimated optimal correction matrices for visual perception of Munsell tiles both perform well. However, the analysis also shows that the system performs way better estimating the Munsell matrix $\boldsymbol{m}_M$ because the band structure with sharp edges is not handled well by the Luther-Ives criterion.

Jiang *et al.* report the color correction error CIE $\overline{\Delta E_{00}}$ for 28 commercially available digital color camera sensors correcting with the Luther-Ives criterion ranging between approximately $\overline{\Delta E_{00}} \approx 1.5$ and $\overline{\Delta E_{00}} \approx 15$ [189]. Valazques-Corral *et al.* present two different color correction algorithms to find the best correction matrix for a set of 37 sensors relying on least squares optimization or alternatively on a spherical sampling technique. The reported error CIE ΔE_{00} ranges between $\Delta E_{00} \approx 1.1$ and $\Delta E_{00} \approx 7.3$ [194]. Thus, our imaging system is on average better than any of the presented sensors with $\overline{\Delta E_{00}} = 0.75$. However, all of the presented results by Valazques-Corral *et al.* and Jiang *et al.* do not fix the illumination as done in this work. Also, all the presented commercially available sensors only have 3 channels whereas the dual sensor system has 6 channels resulting in 18 parameters to be estimated instead of 9. More parameters in a model usually lead to better results.

The dataset of 1269 Munsell color reflectivity spectra was used for both, optimization to obtain the best $\boldsymbol{m}_M$ and also for the evaluation of ΔE_{00}. In general, this can be problematic as the correction might just be good for the sample it is optimized for but not for other colors. As the number of samples (1269 Munsell colors) exceeds the number of parameters (max. 18 matrix entries) by far and because the Munsell colors are distributed equally over the entire color space, this is not expected to have a strong influence.

The color correction can be further specialized for medical applications by selecting a set of medically relevant reflectivity spectra for the optimization, for example of human organs and tissue. Alternatively, the medically relevant colors in the set of Munsell colors can be given a higher weight in the optimization.

The method matches colors detected by the system as close as possible to the perceived colors by the human eye under D65 daylight, because this is the illumination under which humans are used to perceive and interpret colors. Alternatively, the detected color values could be matched to the perceived value under a different illumination, for example surgical light illumination. It can be argued that surgeons are not used to seeing organs under daylight, because sur-

gical theaters often do not have windows but are instead equipped with strong artificial illumination. Alternatively, the color difference between certain tissue types can be maximized by finding a specific illumination scenario [195–197]. Though, this alters the known natural color perception which is a big obstacle for the clinical introduction. Olympus introduced narrow band imaging, which modifies the color appearance to highlight superficial versus deeper blood vessels for example in bladder cystoscopy [198]. In this work, the color reproduction is tried to be as close as possible to the human perception. Future work can investigate the possibility to highlight certain structures using a modified algorithm.

The result of the local optimization algorithm `fminunc` generally depends on the starting point. Choosing an (extended) unity matrix is intuitive, but different starting values may lead to better results. The algorithm terminated for various reasons (see Table 5.2). For the system, a computational limit was exceeded. This means that no local minima was reached yet and it is very likely that more computational time would lead to a better result. All the reported results show that the systems are at least that good, but better color correction with another Munsell matrix $\boldsymbol{m}_M$ might as well be possible.

The sensor signals are transformed into CIE XYZ color space using a linear matrix transformation. Alternatively, a nonlinear transformation could be used for better results [184, 185]. However, the linear approach used here still remains very popular also because the transformation must be applied to every image in the video stream and linear transformations can be easily implemented.

The CIE ΔE_{00} formula is an elaborate measure for color differences. However, it was derived from multiple sets of experimentally determined perceived color differences. As such experiments depend on the subjective perception of the set of test persons, there have been scientific arguments about the exact conditions for which this data can be used [123, p. 53]. Additionally, some effects were observed which have not been considered in the development of ΔE_{00} [123, 188]. Thus, novel developments of improved color spaces and color differences formulas are an ongoing area of research [188, pp. 66] and can be used in future to further improve the calculation of ΔE_{00}.

The average difference of the corrected system is below $\overline{\Delta E_{00}} = 1.5$, which is reported as the limit for a slightly perceivable color difference. Thus, the average color reproduction of the system can be valued as very good.

To summarize, the above analysis has shown that a linear color correction matrix which is found by minimizing the perceived color difference error ΔE_{00} produces superior results compared to finding the matrix using the Luther-Ives criterion for the developed dual sensor system. The proposed correction algorithm matches the corrected colors as close as possible to the perceptual appearance for the hu-

man eye under D65 daylight because this is the way humans identify colors.

5.2.3 *Color correction for variable illumination*

So far, the performance of the system to reproduce colors accurately was done using the Luther-Ives criterion to match sensitivity curves and alternatively simulated for a set of Munsell colors. To simulate the response of the system for Munsell colors, the illumination is specified as the standardized CIE D65 daylight spectrum [123, 199, p. 34]. This section will investigate the system's ability to record and accurately render colors for illumination scenarios other than CIE D65. This is necessary because the illumination in surgical applications will be different from daylight. The selected illumination scenarios are an incandescent lamp (CIE A), a white LED light and a set of multiband illuminations. For all scenarios, the colors are corrected to ideally match the impression of human eye under normal daylight (CIE D65), because all people are accustomed to the impression of colors under daylight.

First, the color rendering of the system with respect to an incandescent lamp (CIE A) and to a white LED are simulated and the best color correction matrix with minimal $\overline{\Delta E_{00}}$ is calculated for each of the two scenarios. This evaluates the usability of the designed system with two common types of light sources: halogen lights and more modern white LED illumination systems.

Though, for fluorescence imaging the imaging system combines best with multiband LED sources because excitation of different fluorophores can be balanced. This leads to improved SNR of the individual fluorescence components. However, it requires a different color correction matrix with good color reproduction for each individual combination of LED light intensities. To investigate the dependency from the imaging setup, a set of different multiband illumination spectra is created. For each illumination, an estimate for the correction matrix is computed and evaluated regarding performance.

5.2.3.1 *Methods*

The mathematical calculations of the color signals of the system and the eye, the correction algorithm and the perceived color difference ΔE_{00} are described in detail in Section 5.2.2.1.

The spectra of CIE D65 and CIE A light are obtained from the CIE [192] and the illumination spectrum of the white LED source CLS9000 MV-W (ZETT OPTICS GmbH, Braunschweig, Germany) is obtained from the manufacturer. For the optimization, the spectra are interpolated on a finite grid with 5 nm bins ranging from 377.5 nm to 782.5 nm.

The transmission spectra of the multiband filter pair of the system as described in Section 4.2.2 is used to create a set of multi band illuminants. The band edge wavelengths are fixed to the 10% transmission limit of the filter bands. The last excitation band has no transmission in any of the two filters, therefore it is not considered. The light will never fall into any of the sensors. The highest wavelength emission band is not required to excite fluorescent dyes and is therefore not used for further analysis. In the remaining 8 bands, a flat illumination power spectral density was assumed. All 6561 combinations of 3 relative power levels at $\frac{1}{3}$,$\frac{2}{3}$ or 1 per band are taken into account as displayed in Figure 5.8C. For each illuminant an estimate for the color correction matrix is obtained by minimizing $\overline{\Delta E_{00}}$. For the first illuminant, the maximum number of function evaluations of the `fminunc` algorithm is set to 2000 and starting with the matrix shown in Equation 5.25. For each of the other illuminants, the best estimation of the Munsell matrix of the previous illuminant is used as starting parameter. The maximum number of function evaluations is set to 1000 for each optimization.

5.2.3.2 *Results*

Halogen and white-LED illumination

Statistical parameters for the best estimated Munsell matrix are listed in Table 5.3. The optimization terminated in all three scenarios because the number of function evaluations or iterations exceeded the standard threshold. For all three illuminants the average color difference ΔE_{00} is below one and the 95% quantile is below 3. For the white LED illumination, the 95% quantile is even below 1. The boxplot in Figure 5.8B displays that the error ΔE_{00} for the best estimated color correction is better for LED illumination than for CIE D65 illumination. In contrast, CIE A illumination does not perform not as good as CIE D65 illumination.

As reasoned before, no errors can be specified for the CIEDE2000 results, because neither sensor sensitivity spectra nor illumination spectra or Munsell colors are provided with an error. The presented accuracy of the results is chosen to allow identification of differences between the scenarios, but is not associated with an error calculation.

Multi-LED illumination

For the multi-LED scenario, the algorithm terminated for all approaches because the maximum number of iterations or the maximum number of function evaluations was exceeded. The average error $\overline{\Delta E_{00}}$ ranges from $\overline{\Delta E_{00}} = 0.575$ to $\overline{\Delta E_{00}} = 1.782$. Figure 5.8 shows a histogram of all $\overline{\Delta E_{00}}$ for the 6561 illuminants.

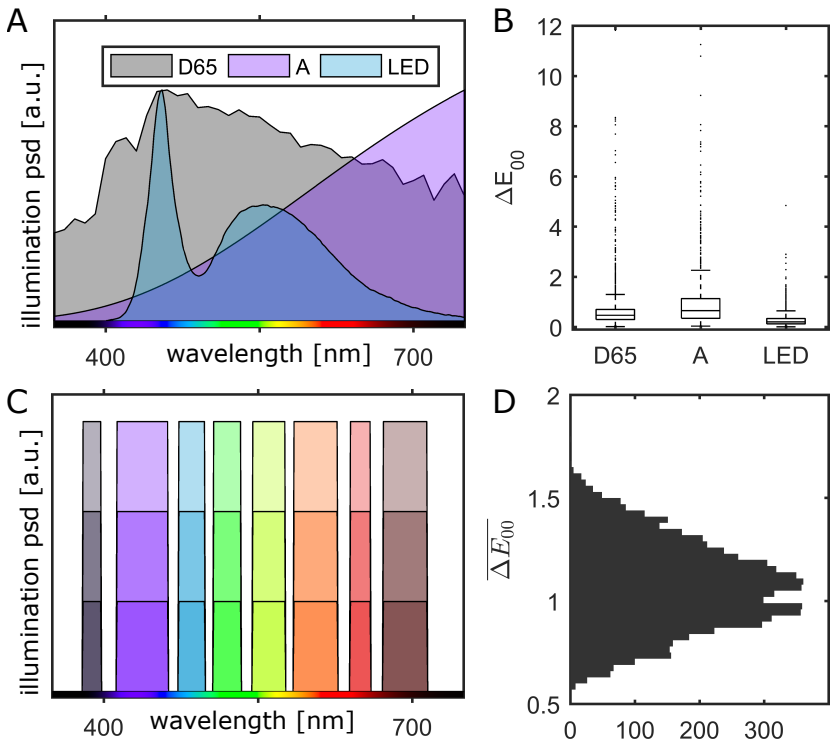

Figure 5.8: Optimizing color correction for Munsell colors with variable illumination. A) Normalized illumination spectra of CIE D65 (average daylight), CIE A (incandescent lamp as blackbody radiator at 2856K) and of a white LED lamp. Spectra are in units of power spectral density. B) Boxplot of the color reproduction error CIE ΔE_{00} for the set of Munsell colors for illumination with CIE D65, CIE A and LED light. C) Illumination spectra when illuminating with multiband light matching the band structure of the emission filters. All possible combinations of the 8 individual band intensities at 1/3, 2/3 or 1 are schematically illustrated. D) Histogram of the best optimization results for each of the 6561 multiband illumination scenarios.

Table 5.3: Statistical evaluation of the mean, median, minimum, maximum, 5% quantile and 95% quantile of ΔE_{00} of the Munsell colors after optimization for the different illumination scenarios. The mean is used as Figure of Merit for the optimization. Exit reasons for the optimization algorithm: 0 number of function evaluations or iterations exceeded the standard threshold.

ILLUMINATION	MEAN	MEDIAN	MIN	MAX	5% Q.	95% Q.	EXIT
CIE D65	0.75	0.47	0.02	11.82	0.15	2.43	0
CIE A	0.96	0.66	0.04	11.26	0.17	2.70	0
LED	0.29	0.21	0.01	4.85	0.06	0.74	0

5.2.3.3 *Discussion*

Halogen and white-LED illumination

For CIE D65 illumination and CIE A illumination the color correction is on average good, because for most colors a difference $\Delta E_{00} < 1$

is observed. In the worst case for the LED illumination $\Delta E_{00} = 4.85$, so the deviation for this color is between noticeable and appreciable [134]. The worst corrected color for CIE D65 and CIE A is above $\Delta E_{00} = 10$, so the perception of the color difference for that color is between appreciable and much [134]. Such interpretations must be taken with caution because color perception depends on the individual observer.

Section 5.2.2 shows that detecting light in the IR is always problematic for color imaging in the visible range. The detected light alters color perception because the color matching functions $\bar{x}$, $\bar{y}$ and $\bar{z}$ have almost no sensitivity in the IR above 700 nm. This may explain the good color reproduction performance of the LED illumination which has hardly any intensity above 700 nm. In this case the highest wavelength detection band of sensor S1 will not receive any light. In contrast, the highest band detects a relatively big amount of light for CIE D65 and CIE A illumination as shown in Figure 5.8. The white LED has a color temperature of approx. 6200K, whereas medically used LED lights tend to have lower color temperature around 4500K. The difference in color temperature is usually achieved by balancing the two peak intensities of the LED illumination shown in Figure 5.8 differently. For lower color temperature the spectrum of LEDs has typically the same spectral range and thus also only little intensity above 700 nm.

The CIE A illuminant represents an incandescent lamp which can be close to the illumination of a halogen light source. Commercial light sources often contain additional elements causing strong spectral lines. These may add a high amount of light intensity at a single wavelength and seriously deteriorate the color reproduction.

As discussed before, the optimization algorithm `fminunc` is looking for the closest local minimum. It is therefore always possible that the extended unity matrix as starting point leads to a better minimum for the LED illumination than for the D65 or the A illumination.

Multi-LED illumination

The previous chapter has shown that applying the Luther-Ives criterion to the designed multispectral imaging system does not lead to satisfying results. It is better to calculate the color correction matrix for each illuminant individually on basis of perceptual color differences, but this requires specifying the illumination. In contrast, fluorescence imaging performs best with multiband illumination for which the individual light intensities can be freely adjusted. Therefore, the set of 6561 illumination scenarios was successfully tested.

The obtained results for any of the tested illuminations are in lower range for published commercial color sensors, but these use different correction approaches [189, 194].

The permutations of multiband light intensities are very coarse and can be made finer on the cost of computational power. It is beneficial that all the bands have at least some reasonable light intensity. This ensures that no channel is required to be extremely amplified in the transformation and thus noisy color images after color correction are avoided. However, it restricts the flexibility needed for certain fluorescence imaging scenarios. Very low light intensities of the illumination in a band may lead to noisy images after color correction. Thus, the evaluation performed here gives an idea about the potential of color correction for reasonable scenarios, for extreme scenarios color correction might be deteriorated or noisy. However, if such scenarios are needed by all means for fluorescence imaging, a third phase can be introduced dedicated only to color imaging. For such a phase, the light intensity of the individual bands can be optimized for best color reproduction.

In reality, bigger spectral security gaps are required, and each LED has its specific spectral profile. Thus, the results give an estimate of the possible color reproduction of the system. For clinical systems and use-cases, the specific estimate of $\boldsymbol{m}_M$ must be computed and $\overline{\Delta E_{00}}$ must be evaluated.

Moreover, the same aspects as previously discussed in Section 5.2.2.3 apply for the optimization itself. As all optimization scenarios in this section terminated because of a threshold in the number of iterations and function evaluations, higher thresholds promise to result in better correction matrices. However, this demands more computational power. In general, `fminunc` is a local optimization algorithm and it is possible that the algorithm is running into a local minimum and misses the absolute minimum. However, as the results are superior compared to the Luther correction, the optimization improved the color correction and can be used in a real scenario. Though, a better color correction matrix may exist.

Conclusion

All in all, this section has demonstrated that color correction for the novel dual sensor imaging system performs well with light sources which are commonly used for medical illumination: CIE A illumination and LED illumination. Additionally, it is implied by varying the multiband illumination intensities that the system can reproduce colors independent of the multiband illumination, as long as it is within boundaries and each band has at least some minimal intensity.

5.3 FLUORESCENCE IMAGING

This section analyzes the system performance regarding fluorescence imaging of up to three fluorescent dyes as specified in the design requirements.

First, phantom experiments of the dyes Atto532, Atto565 and Atto610 with strong overlap of the emission spectra are presented. These experiments demonstrate the strong separation power in unmixing dyes.

Second, the performance of single sensor systems is evaluated. For medical applications like endoscopy, available space to fit the sensor is restricted and thus using a single sensor might be desirable. In this part, the same phantom scenario as before is analyzed on basis of a single sensor system. Additionally, phantoms containing the dyes Atto488, Atto655 and Atto740 are imaged. These experiments show that propagation of noise in unmixing can deteriorate the image quality.

Concepts, experiments, the underlying data set and results which are presented in this section have been published in the peer reviewed publications [166, 167] by Dimitriadis *et al.*.

5.3.1 *Fluorescence imaging and unmixing*

This section describes imaging experiments to evaluate the fluorescence imaging performance of the developed dual sensor approach. Fluorescent phantoms with strongly overlapping spectra are prepared and imaged. The data is successfully unmixed into the individual fluorescent dye components.

5.3.1.1 *Methods*

Phantom preparation

Table 5.4: Peak absorption (λ_{abs}), peak fluorescence (λ_{fl}) and dye concentrations, intralipid and agar content in vials I to VI. Adapted with with permission from ref [167], OSA.

	λ_{abs} nm	λ_{fl} nm	I μM	II μM	III μM	IV μM	V μM	VI μM
Atto532	532	552	2.5	2.5	-	-	-	2.5
Atto565	565	590	-	2.5	2.5	2.5	-	-
Atto610	610	633	-	-	-	2.5	2.5	2.5
intralipid [%]			0.93	0.90	0.93	0.90	0.93	0.90
agar [mg]			5.6	5.4	5.6	5.4	5.6	5.4

Phantoms containing the fluorescent dyes Atto532, Atto565, Atto610 (all Atto-Tec GmbH, Siegen, Germany) are prepared. The peak emis-

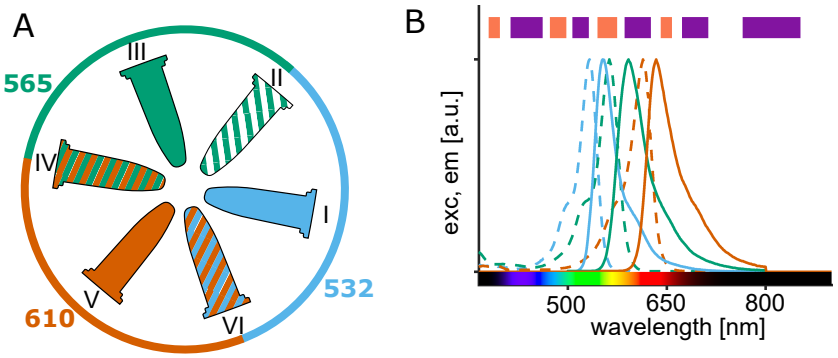

Figure 5.9: A) Arrangement of the phantoms containing the fluorescent dyes ■ Atto532, ■ Atto565 and ■ Atto610. Solid vials contain only one dye, the hatched vials contain two dyes each. B) Excitation spectra (dashed lines) and emission spectra (solid lines) of the dyes show strong overlap. Colored boxes on top indicate the filter bands of ■ F1 and ■ F2. Adapted with with permission from ref [167], OSA.

sion wavelengths of the three dyes lie within less than 85 nm. Excitation and emission spectra are displayed in Figure 5.9B. Six vials (I to VI) each with a total volume of 500 µl containing different mixtures of the dyes with Intralipid as scatterer and agar are prepared. The agar (Sigma Aldrich, Germany) is dissolved in pure water and boiled. When cooling down, Intralipid (Sigma Aldrich, Germany) and fluorescent dye solutions are added. To homogenize the solution, the final content is mixed and vortexed while cooling down. Table 5.4 provides a detailed description of the final concentrations for each of the phantom vials.

Imaging

Images of the phantom are recorded with the presented imaging system as described in Section 4.2. The vials are arranged in a circular holder as displayed in Figure 5.9A. Fluorescence is excited in two phases using two multispectral LED light sources (LedHub, Omicron-Laserage Laserprodukte GmbH, Germany). In phase one, LED modules with peak wavelengths at 455 nm, 550 nm and 625 nm illuminate the sample, while in phase two LED modules with peak wavelengths at 470 nm, 550 nm and 655 nm illuminate the sample. The excitation light of each module is spectrally filtered so that the light cannot pass to the sensor imaging fluorescence light in that phase.

For each of the two excitation scenarios, 100 consecutive images $\boldsymbol{Y}(\xi)$ with an integration time of 50 ms are recorded.

Image processing

The raw images are (1) background subtracted, (2) demosaiced, (3) intensity corrected with an electron conversion factor and (4) registered to obtain an image $\boldsymbol{Y}(\xi)$ for further processing:

1. Background subtraction: the mean over 100 dark camera images is subtracted from all the recorded images.

2. Debayering: images are debayered here by collapsing the four neighboring pixels with the spectral RGGB filters into one pixel with four spectral channels. The spatial resolution is reduced by a factor of two in each dimension and no spatial averaging is done.

3. Conversion factor: the intensity of the digital raw image is proportional to the number of electrons measured by A/D converter of the sensor. The number of electrons is the Poisson distributed quantum mechanical property which determines the shot noise [15, 200]. The conversion factor is obtained from the camera manufacturer.

4. Registration: test images with geometrical markers are recorded with both cameras and an affine transformation matrix is computed. Nearest neighbor image classification is used to maintain pixel intensities and to avoid spatial smoothing.

Averaging in the debayering process and registration is avoided for this analysis to ensure that the noise characteristics of the images are not altered.

Spectral signatures $\boldsymbol{\kappa}$ are obtained by fitting recorded averaged fluorescence data $\boldsymbol{Y}(\xi)$ of pure emission signal as described in Section A.1.2. Images $\boldsymbol{Y}_i(\xi)$ are unmixed to fluorescence component images $\boldsymbol{X}_i(\xi)$ as described in Section A.1.

5.3.1.2 *Results*

Fit results for the signatures of the dyes Atto532, Atto565 and Atto610 are presented in Table 5.5. The splitting ratio of the signatures shows that Atto565 is mainly detected by sensor S1 while Atto532 and Atto610 are detected mainly by sensor S2. The signature values for G1 and G1* as well as for G2 and G2* are supposed to be identical. However, the deviation between these channels is one order 1 for signatures normalized to 100. To estimate the error of the measurement, bootstrapping for 95% confidence bounds obtained by 1000 repetitions was used. The estimated errors were below 0.1 for the individual components. This shows that the statistical bootstrapping error is too small to describe the actual error of the measurement.

The »monochrome« fluorescence image $\boldsymbol{Y}_i(\xi)$ which is presented in Figure 5.10A displays the sum of the electrons which have been

Table 5.5: Estimates of the spectral signatures of the dyes Atto532, Atto565 and Atto610 normalized to 100.

CHANNEL	κ_{Atto532}	κ_{Atto565}	κ_{Atto610}
R1	2.6	38.6	7.9
G1	1.3	14.4	2.6
G1*	1.2	14.4	2.8
B1	0.7	8.2	2.2
R2	8.7	7.1	49.1
G2	38.3	7.5	12.7
G2*	38.8	7.6	13.5
B2	8.4	2.3	9.3

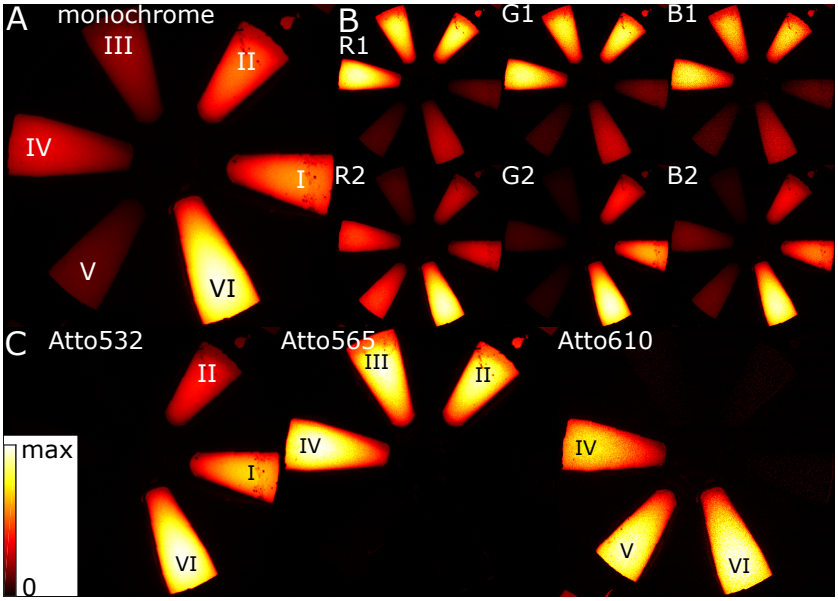

Figure 5.10: Raw fluorescence image of the phantom containing mixtures of the dyes Atto532, Atto565 and Atto610. A) Monochrome image as sum over all spectral channels, B) individual channel intensities $Y(c, \xi)$; channels G1* and G2* are not shown as they correspond to G1 and G2. C) Unmixed fluorescence component intensities $X(c, \xi)$. All images are scaled from zero to the 0.9999 quantile of the data: A) monochrome: 5597; B) R1: 572; G1: 224; B1: 145; R2: 846; G2: 2001; B2: 507; C) Atto532: 4780; Atto565: 1257; Atto610: 807. All subplots are based on the same underlying data set as the respective plots in [167]. Adapted with with permission from ref [167], OSA.

triggered per pixel in all spectral channels. It shows strongest intensity for vial VI containing the dyes Atto532 and Atto610, the vial V containing only Atto532 appears weakest. Images of the individual channels confirm that most of the intensity of Atto565 is detected by sensor S1, whereas most of the intensity of Atto532 and Atto610 is detected by sensor S2.

Unmixed fluorescent component images (Figure 5.10C) for each fluorescent dye shows strong signal at the position of vials containing that dye, while no intensity is visible at positions where the respective dye is not contained in the vial. Thus, no crosstalk is visible. Each dye is present in three phantom vials in the same concentration. Though, the unmixed component intensities of the same dye vary.

5.3.1.3 *Discussion*

The deviation of the spectral signature channels G1 and G1* as well as G2 and G2* must be due to systematic errors, because the statistical error is approximately one order of magnitude smaller. The systematic difference between the channels G and G* can be attributed to the fact that the channels G and G* record signal at different locations. So, if the sample signal shows some spatial intensity gradient over the selected data, one of the channels will always record smaller signals than the other. That intensity gradient might be due to a dye concentration gradient, an intensity gradient in the excitation light, an intensity gradient in the filter transmission, an optical transmission gradient due to vignetting or due to the relative imaging angle with the object surface. Strong gradient effect could be reduced by interpolating the signal when debayering. Alternatively, different transmission characteristics of the microfilter pattern for different locations on the sensor are possible. Overall, the systematic error between the G and the G* channels is around 1%, which proves to be sufficiently small not to cause observable unmixing artifacts. To obtain more robust dye signatures, images of different scenarios (different phantoms, different location, etc.) can be recorded.

The fluorescence images are unmixed successfully as no artifacts or intensity crosstalk is visible. The difference in intensity between different vials containing the same dye concentration in the mixture can be explained by the positioning of the individual vials. Neither the illumination nor the surface of the vials is orthogonal to the image plane. Thus, different vials will be illuminated and imaged at a different angle explain variations of the recorded intensity. This effect does not interfere with the unmixing, but it shows that detected fluorescence intensities must not be translated directly to dye phantom concentrations.

5.3.1.4 *Conclusion*

The experiments of recorded phantoms containing dye mixtures demonstrate that the system can unmix data of three fluorescent dyes with strongly overlapping spectra without artifacts or crosstalk.

As expected, unmixed component images also reveal that detected intensity does not directly correspond to dye concentrations. Recent advances allow to report dye concentrations in the field of view for

neurosurgical applications [107]. Future work is needed to translate the published normalization concepts to the system presented here.

5.3.2 *Fluorescence unmixing with a single sensor systems*

Detecting fluorescence with only one single sensor of the system has advantages over using both sensors: miniaturized endoscopic systems can be implemented in confined space. Alternatively, the dual sensor system can run with one phase only to avoid flickering and movement artifacts.

Single sensor systems require the excitation and emission spectra of the dyes to match the band structure of the filters. Also, separating different dyes by unmixing relies only on the emission.

To experimentally investigate the effect of restricting the fluorescence recording to one single sensor, two experiments are performed. First, the data recorded in Section 5.3 is evaluated using only the information of one of the sensors at a time. Second, experiments with dyes whose emission spans over the VIS/NIR range are performed. Both experiments have been published [166, 167].

5.3.2.1 *Methods*

The fluorescent data recorded in Section 5.3.1 with two sensors in two phases is analyzed per sensor. The fluorescence image channels R1, G1, G1* and B1 of sensor S1 are unmixed using these channels of the spectral signatures. Analogously, fluorescence information of sensor S2 is unmixed using only data and signature channels R2, G2, G2* and B2. The data is otherwise handled as described in Section 5.3. Angles between the spectral signatures $\boldsymbol{\kappa}_1$ and $\boldsymbol{\kappa}_2$ are defined by the inner product $\langle \cdot, \cdot \rangle$:

$$\cos(\alpha) = \frac{\langle \boldsymbol{\kappa}_1, \boldsymbol{\kappa}_2 \rangle}{\langle \boldsymbol{\kappa}_1, \boldsymbol{\kappa}_1 \rangle \cdot \langle \boldsymbol{\kappa}_2, \boldsymbol{\kappa}_2 \rangle}. \tag{5.28}$$

Transmission efficiencies η for a set of channels $\mathcal{C}$ are calculated on basis of the spectral signatures (for the dual sensor system):

$$\eta(\mathcal{C}) = \frac{1}{\sum_{c=1}^{N_c} \kappa(c)} \cdot \sum_{\mathcal{C}} \kappa(c). \tag{5.29}$$

Fluorescent phantoms of the dyes Atto488, Atto655 and Atto740 are prepared diluting stock solutions of the respective dyes down (using ethanol and/or water depending on the dye solubility) to a final concentration of 5 µM and 500 nM. The final solutions are filled into vials VII, VIII and IX each with a volume of 500 ul and placed in the imaging system as shown in Figure 5.11A. Dye concentrations and fluorescence properties are summarized in Table 5.6. Fluorescence images are recorded with sensor S1. The dyes are excited by two filtered

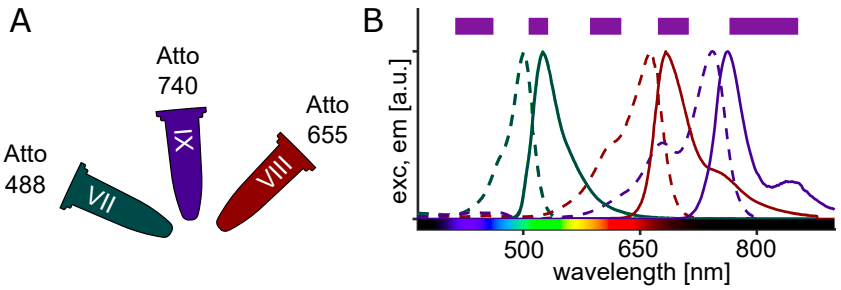

Figure 5.11: A) Arrangement of the phantoms containing the fluorescent dyes ■ Atto488, ■ Atto655 and ■ Atto740. B) Excitation spectra (dashed lines) and emission spectra (solid lines) of the dyes ranging over the VIS/NIR spectral range. Bars on top indicate the filter bands used for detection. Adapted with with permission from ref [166], OSA.

multi LED light sources (pE-4000, CoolLED Ltd. , Andover, UK) with peak emission at 490 nm, 550 nm, 660 nm and 740 nm.

The fluorescent images are background subtracted and debayered. To obtain the spectral signatures of each dye, regions containing a pure dye are manually selected in the intensity images $\boldsymbol{Y}(\xi)$. The selected data of phantoms with a dye concentration of 5 uM and 500 nM (not shown) is used to compute the spectral signature $\boldsymbol{\kappa}$ of each dye as described in Section A.1.2. Subsequently, the raw fluorescence images $\boldsymbol{Y}(\xi)$ are unmixed to fluorescence component images $\boldsymbol{X}(\xi)$ using the spectral signatures as described in Section A.1. Gaussian image filtering is performed with the MATLAB pre-implemented function `imgaussfilt`.

Table 5.6: Peak absorption (λ_{abs}), peak fluorescence (λ_{fl}) and dye concentrations of Atto488, Atto655 and Atto740 in vials VII, VIII and IX.

	λ_{abs} nm	λ_{fl} nm	VII μM	VIII μM	IX μM
Atto488	500	520	5	-	-
Atto655	663	680	-	5	-
Atto740	743	763	-	-	5

5.3.2.2 *Results*

Fluorescence intensity images of Atto532, Atto565 and Atto610 as if recorded with a single sensor are presented in Figure 5.12. All images appear very noisy in both dark and bright fluorescence intensity regions. It also seems that unmixing fails because all vials are visible in all component images, even in the ones that should not show any signal appearing as a salt and pepper noise. The line profiles in Figure 5.12 C, D and E show that intensity fluctuations in the component

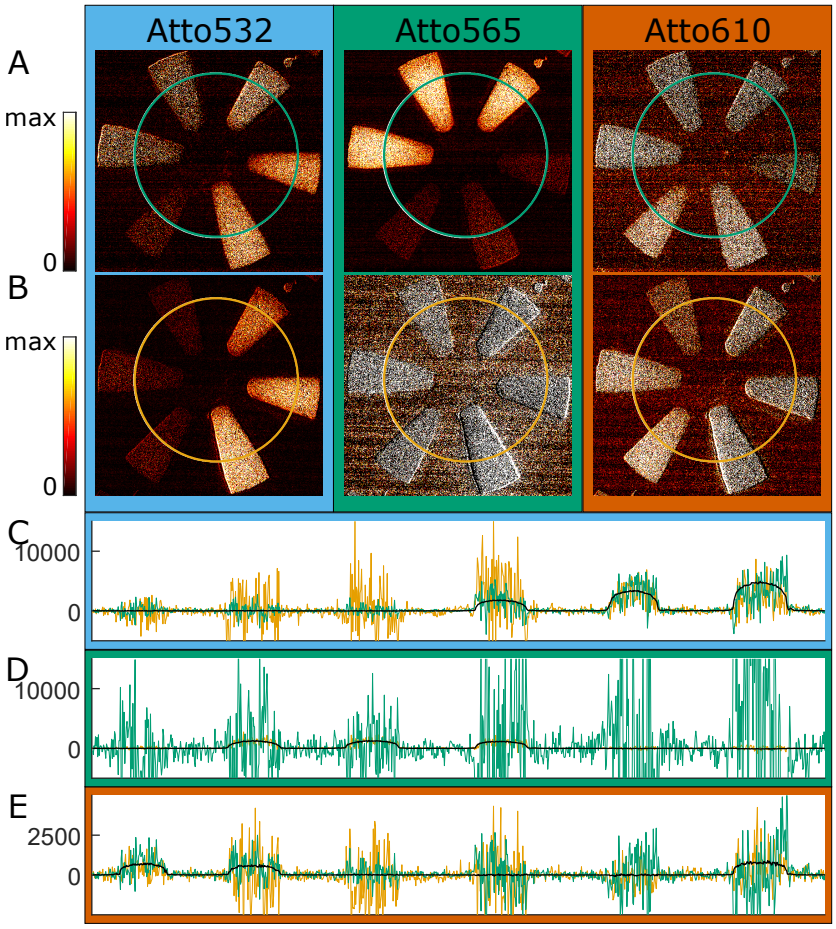

Figure 5.12: Unmixed fluorescence intensity of Atto532, Atto565 and Atto610 using only A) sensor S1 or B) sensor S2. All graphs are scaled identically to Figure 5.10C. C), D) and E) show intensity profiles of Atto532, Atto565 and Atto610 along the white circular profile of S1 as in A (green), of S2 as in B (yellow) and S1+S2 (black) as in Figure 5.10C. Subfigures A) and B) are based on the same underlying data set as the respective plots in [167]. Adapted with with permission from ref [167], OSA.

images are higher if fluorescence intensity is present in any component compared to dark regions with low intensity for all components. For several of the component intensities, the noise exceeds the amplitude of the fluorescence intensity. Also, the noise from high intensity regions of one component is spilled to the other components at that region. This effect leads to ghost images which appear as unmixing artifacts. Overall, the SNR is dramatically decreased by unmixing with signatures which are very close together in channel space.

Comparing the transmission efficiencies in Table 5.7 shows that most photons emitted by Atto565 are detected by sensor S1, whereas most photons originating from Atto532 and Atto610 are detected by sensor S2. Thus, Atto565 can be unmixed from the other dyes based on information gained in the two phases. Atto532 and Atto610 are

Table 5.7: Comparison of single and dual sensor system: detection efficiency and separation angles in channel space. Upper part: efficiency to detect a photon in the respective system. Lower part: separation angle between spectral signatures of the dyes in the dual sensor system (S1 and S2) and the two single sensor systems (sensor S1 or sensor S2). Values are calculated from the spectral signatures in Table 5.5. Adapted with with permission from ref [167], OSA.

	S1 + S2	S1	S2
η(Atto532)	100%	6%	94%
η(Atto565)	100%	76%	24%
η(Atto610)	100%	15%	85%
$\measuredangle$(Atto532, Atto565)	71°	6°	24°
$\measuredangle$(Atto532, Atto610)	59°	8°	59°
$\measuredangle$(Atto565, Atto610)	67°	4°	35°

both mainly detected by sensor S2 and good unmixing of these two dyes is based on spectral emission information of sensor S2.

The angles in channels space between the three dyes recorded with the two-sensor system are big enough to allow for good unmixing. Comparing the angles with both single sensor systems shows that the spectral emission information on sensor S1 results in very small angles between the dye signatures. Sensor S2 shows that the angle between Atto532 and Atto610 is sufficiently high to unmix these two dyes on basis of the emission information. Angles between Atto532 and Atto610 for sensor S2 are smaller.

Raw fluorescence images of phantoms containing Atto488, Atto655 and Atto740 are shown in Figure 5.13A. Raw images of one single acquisition can be successfully unmixed as shown in Figure 5.13B. In each of the images, only one of the vials is supposed to show intensity. Though, noisy ghost images of the vials containing another fluorescent dye are visible. These vanish after smoothing the images with a 4×4 pixel Gaussian filter (see Figure 5.13C). Intensity profiles along the white curve of the unmixed signal and the respective Gaussian smoothed signal are plotted in Figure 5.13D, E and F. As expected, unmixed signal shows little noise in dark regions on the background. Locations with high intensity show higher noise in all components. However, locations with low intensity in one channel and high intensity in other channels also show high noise in the channel with low intensity. At these locations, the noise is centered around zero resulting in negative values for some pixels. In the intensity images displayed in Figure 5.13C, the negative values are set to zero whereas the positive values are displayed. This effect results in the noisy ghost images appearing as unmixing artifacts. After applying the Gaussian filter the effect of ghost images is reduced. The Gaussian filtered im-

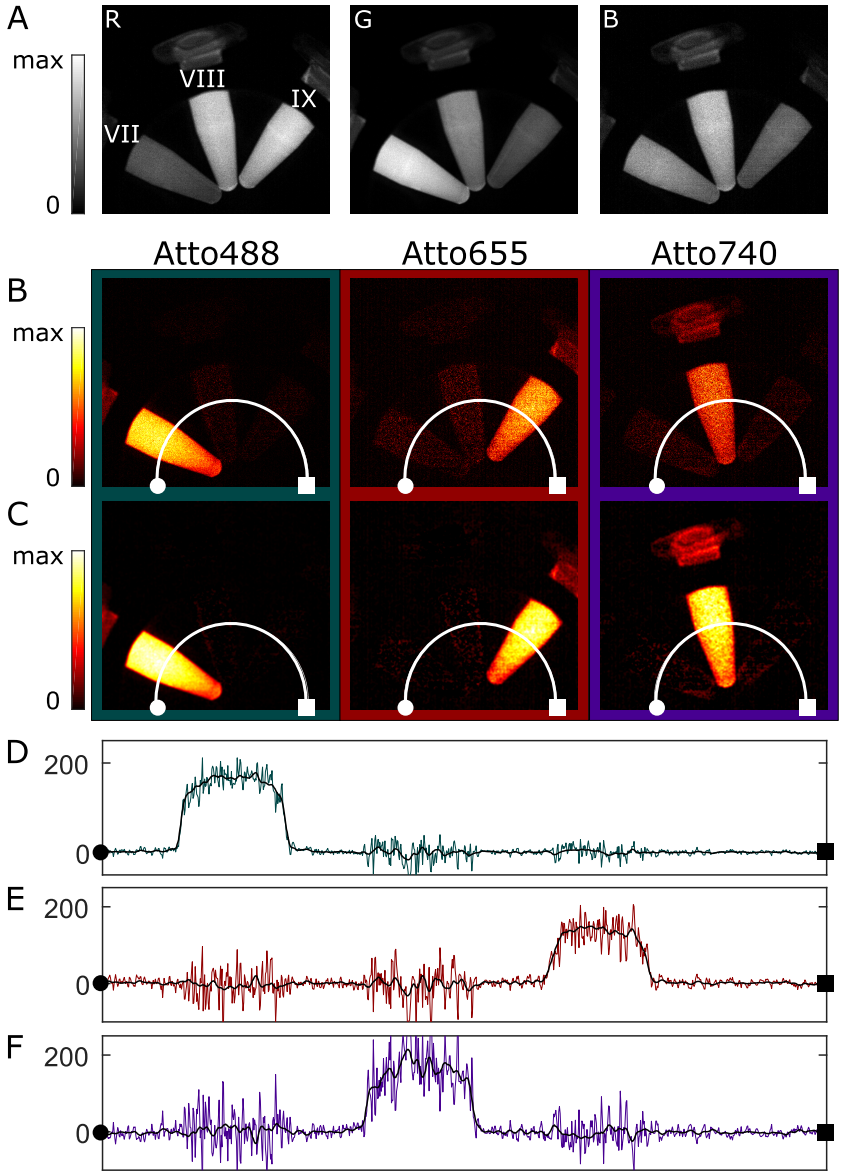

Figure 5.13: Unmixing of Atto488, Atto655 and Atto740. A) Raw images of the sensor channels R, B and G. B) Unmixed intensity of the three dyes Atto488, Atto655 and Attto740. C) Gaussian 4×4 filtered unmixed intensity. Adapted with permission from ref [166], OSA. Intensity profile $Y(\xi)$ of the dyes D) Atto488, E) Atto655 and F) Atto740 along the white curve plotted in color for the unmixed component intensities as in B) and plotted as black curve for the Gaussian filtered curve as in C). Scaling: images are scaled between 0 and max, which is individually specified per image. Max values: A) R: 153, G: 172, B: 89; B) Atto488: 225, Atto655: 237, Atto740: 360; C) Atto488: 185, Atto655: 175, Atto740: 206. Subfigures A) - C) are based on the same underlying image data set as the corresponding plots in [166]. Adapted with permission from ref [166], OSA.

age and the respective line profiles hardly show ghost images or unmixing artifacts.

5.3.2.3 *Discussion*

The presented experimental results show that unmixing fluorescence recorded with a single sensor works if the filter bands match the dye emission and if the spectral signatures are separated well enough. This is mostly guaranteed by selecting dyes with non-overlapping emissions profiles.

Evaluating the dual sensor phantom experiments shows that if the dye emission does not match the filter bands, as it is the case for single sensor systems, the dyes cannot be successfully unmixed. Atto532 has the lowest photon detection ratio on sensor S1 which results in an expected decrease in the SNR by a factor of 5 (due to 6% photon detection ratio). However, the experimentally measured decrease in SNR is orders of magnitude higher. Analyzing the angles between the dyes for the different sensor systems shows that the two single sensor systems have higher angles between the dyes and thus unmixing does not amplify the noise as much. Comparing angles for the dual sensor system versus the single sensor systems translates in comparing angles between 4D channel space and 8D channel space. Here, it is also assumed that all sensors integrate for the same time. Strictly speaking, the single sensor systems may integrate longer as no fluorescence needs to be recorded in the second phase and thus collect up to twice the number of photons. For a direct comparison this is not feasible, but it allows a maximum increase in SNR of $\sqrt{2}$, which is not a significant contribution in this analysis.

To summarize, the analysis shows in detail that the dual sensor system does not only collect additional photons, but also increases the separation between spectral signatures using the combination of excitation and emission multiplexing.

The phantom experiments using Atto488, Atto655 and Atto740 show that fluorescence data recorded with a single sensor can successfully be unmixed. The dye emission is distributed over the entire VIS/NIR range, but the dyes are chosen to match the filter bands. Noise is spilled in the unmixing process between components. Applying a Gaussian filter reduces ghost images of the unmixed images. The sacrifice in spatial resolution appears acceptable as intra-operative fluorescence data in biomedical applications usually does not exhibit sharp edges due to tissue scattering, though it is visible in the images.

5.3.2.4 *Conclusion*

In this section, an imaging scenario using single sensor data is presented. Experimental data of three dyes (Atto488, Atto655 and Atto740) is unmixed successfully. Unmixing artifacts originating from noise ap-

pear as ghost images and can be eliminated to some extend by spatial smoothing of the final unmixed images. In this scenario, the dye emission spectra range over the VIS/NIR, but they match the emission filter bands.

In contrast, the dyes Atto532, Atto565 and Atto610 in the second imaging scenario do not match the filter bands of neither of the two single sensor systems. The overlapping emission profiles result in similar spectral signatures. A detailed analysis comparing spectral signatures between single and dual sensor systems reveals that the dual sensor system using a combination of excitation and emission multiplexing is more flexible and has higher separation power.

Both scenarios show that noise in the unmixed fluorescence component images may deteriorate the image quality. In extreme cases the noise makes images useless, even though the raw fluorescence images show sufficient fluorescence intensity. To further investigate this effect, noise propagation in unmixing is investigated in detail in Section 6.1.

All in all, single sensor systems show inferior unmixing performance compared to dual sensor systems. However, if the spectral characteristics of the dyes and the system match, the performance of a single sensor system is acceptable. This is appealing for devices such as chip on the tip endoscopes with constrained space available for sensors.

5.4 OPTICAL PERFORMANCE ANALYSIS

The realized optical system which is described in detail in Section 4.2 is tested in this section whether it fulfills the requirements of Section 3.1.6. First, the requirements regarding field of view (FOV) and vignetting are checked. Second, the optical resolution and the connected modulation transfer function of the optics are tested and compared with the requirements. Both sections use raw data and results published by Tobias Behr [175]. Finally, the free working distance and the available numerical aperture are analyzed and discussed. This analysis is purely based on specifications and theoretical considerations.

5.4.1 *Field of view and vignetting*

The requirements for the imaging system are specified in Section 3.1.6 are set to have a FOV with a diameter of at least 5 cm and a resolution of at least 1 MP. This section analyzes if these two conditions are fulfilled by both sensors of the developed system. For unmixing and color reproduction, homogeneous detection sensitivity is important.

5.4.1.1 *Methods*

White raw reflectance image data for both imaging paths is reused from the thesis of Tobias Behr [175]. The thesis contains further details about the optical system, image acquisition and image processing. After image acquisition, the raw images are debayered and a grayscale image is computed by averaging the channels.

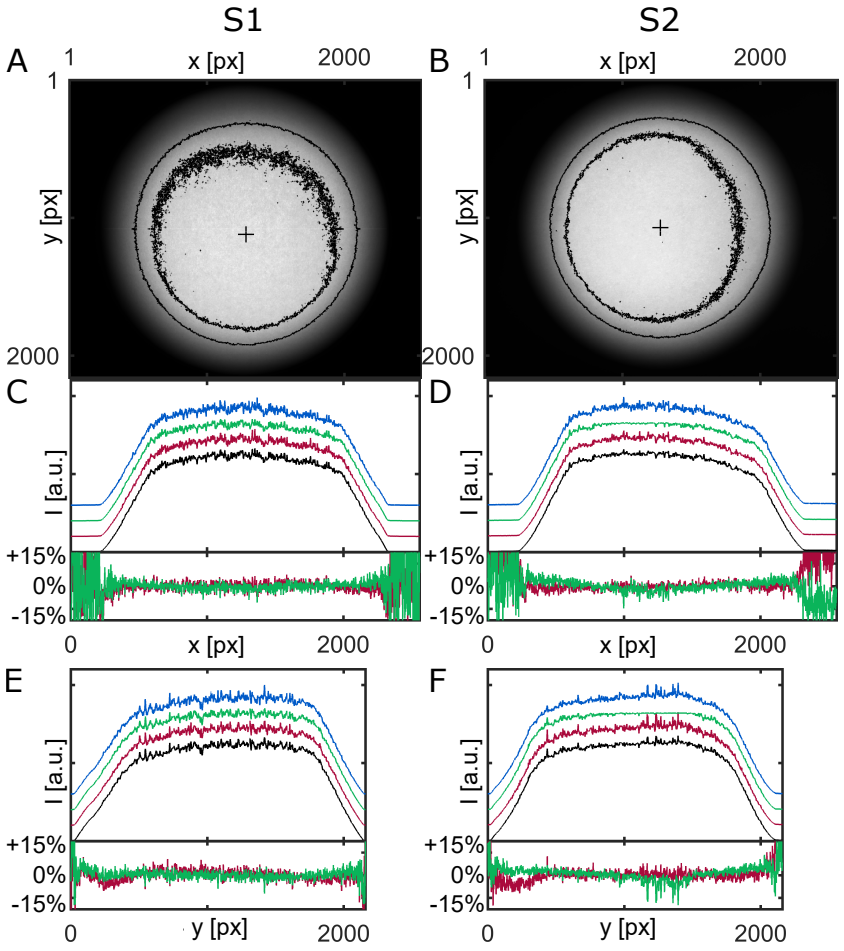

Figure 5.14: Vignetting of the imaging system for sensor S1 (left side) and sensor S2 (right side). Grayscale images of sensors A) S1 and B) S2 scaled from zero (black) to the maximum value (white). The drawn black contour lines indicate the 75% and 50% intensity levels. The cross in the image center indicates the location of the line profiles. C), D) Horizontal intensity line profile across the FOV. E), F) Vertical line profile across the FOV. The upper plots of C),D),E) and F) show the individually normalized intensity profiles of the ■ blue, ■ green, ■ red channel and the ■ combined average in arbitrary units. The individual profiles of the different channels are vertically shifted. Below each intensity plot, the relative ratio between the ■ red and the blue channel and the relative ratio between the ■ green and blue channel are displayed.

The center of the FOV is determined finding the most inner 50% intensity barriers on the line horizontal and vertical profiles at the image center. The pixel line which is closest to the center of the two 50% barriers is selected for the line profiles.

The relative response of the red channel is computed dividing the normalized intensities of the line profile of the red channel by the blue channel per pixel. Analogously, the green channel intensity is divided by the blue intensity per pixel.

Minimum and maximum pixels of the field of view are reported for an intensity drop in the grayscale image to 75% and 50%. The reported pixels correspond to the first pixel at which the intensity drops below the limit. The determined FOV in pixels (px) is converted to mm in the object plane using the minimal magnification of the imaging lens assembly and the pixel size of 6.5 µm for both sensors. The total magnification is calculated as the product of the individual magnification factors

$$m_{system} = m_{\text{objective}} \cdot m_{\text{zoom}} \cdot m_{\text{sensor}} \tag{5.30}$$

with $m_{\text{objective}} = 0.5$, $m_{\text{sensor}} = 0.63$ and with variable magnification of the zoom element $m_{\text{zoom}} = 0.57 \ldots 3.6$ the resulting magnification is

$$m_{\text{eff,min}} = 0.5 \cdot 0.57 \cdot 0.63 \approx 0.18 \tag{5.31}$$

$$m_{\text{eff,max}} = 0.5 \cdot 3.6 \cdot 0.63 \approx 1.13. \tag{5.32}$$

The individual magnification values are obtained from the manufacturer manual without error specification [201].

5.4.1.2 *Results*

Both grayscale images in Figure 5.14 A) and B) show a bright center followed by a region which shows vignetting and is surrounded by dark pixels because the sensor is bigger than the size of the image. Besides, the contour lines of S1 at 75% of the maximum intensity are blurred at the right top and the contour line does not form a circle. Instead, it shows stronger vignetting at the upper right part of the FOV. Similarly, the image on sensor S2 shows vignetting at the 75% intensity contour on the right side.

Though, both images show patches with varying intensity in the bright part of the image which is due to a structure in the imaged object. Besides, the image of S1 shows a small horizontal stripe close to the the center which can be observed if zooming in closely. However, that stripe can most likely be attributed to some artifact and can be neglected because its intensity change is below 10%.

To evaluate the color constancy of the system, the horizontal and vertical channel ratios show deviations of less than ±15% for both images inside the 50% vignetting region. Nevertheless, the intensity profiles of S1 and S2 show slightly different tendencies. Providing

Table 5.8: Field of view for the imaging paths of sensors S1 and S2 for relative vignetting limits of 75% and 50% of the maximum intensity. Lowest and highest horizontal (x) and vertical (y) pixels and the differences are reported. The distance in pixels is converted to FOV in mm using the minimum magnification of the system and a pixel size of 6.5 µm. The number of pixels in megapixels (MP) in the area A is computed using the reported coordinates as the corners of a tetragon.

		S1		S2	
		0.50	0.75	0.50	0.75
y_{min}	[px]	303 ± 20	485 ± 75	267 ± 20	386 ± 75
y_{max}	[px]	1932 ± 20	1834 ± 75	1874 ± 20	1758 ± 75
Δy	[px]	1629 ± 40	1349 ± 150	1607 ± 40	1372 ± 150
Δy_{max}	[mm]	58.8 ± 1.4	48.7 ± 5.4	58.0 ± 1.4	49.5 ± 5.4
x_{min}	[px]	473 ± 20	615 ± 75	459 ± 20	568 ± 75
x_{max}	[px]	2107 ± 20	1993 ± 75	2083 ± 20	1935 ± 75
Δx	[px]	1634 ± 40	1378 ± 150	1624 ± 40	1367 ± 150
Δx_{max}	[mm]	59.0 ± 1.4	49.8 ± 5.4	58.6 ± 1.4	49.4 ± 5.4
A	[MP]	1.33 ± 0.05	0.93 ± 0.14	1.30 ± 0.05	0.94 ± 0.15

that information of both sensors is used for unmixing or color correction, this may lead to some unmixing artifacts and deviations in color correction.

Specifying an intensity drop of 50% as acceptable vignetting results in a roughly circular field of view with a horizontal spread of (5.88 ± 0.14) cm for S1 and (5.80 ± 0.14) cm for S2. The vertical spread is (5.90 ± 1.40) cm for S1 and (5.86 ± 0.14) cm for S2 (see Table 5.8). The available sensor size corresponds to (1.33 ± 0.05) MP for S1 and (1.30 ± 0.05) MP for S2.

Errors are estimated by considering $(\pm 1\%)$ intensity variation at the 50% intensity level and at the 75% intensity level. For the 50% level, the measurements variations are estimated to be below 20 px, for the 75% intensity level, the variations are estimated to be below 75 px. These are thus estimated to be the errors of the determined pixel locations. Errors of calculated quantities are propagated accordingly.

The errors describe the uncertainty to determine the position at respective intensity levels. Additionally, systematic errors relating to the setup may be contained in the results. For example, inhomogeneous illumination and an inhomogeneous white background may contribute to systematic errors. However, inhomogeneous illumination effects would also be present during intraoperative imaging.

5.4.1.3 *Discussion and conclusion*

Both the minimal resolution and the minimal FOV are fulfilled if accepting vignetting up to 50%. The non-circular shapes of the vignetting contour lines originate most likely from inaccurate lens alignment in the two imaging paths and calls for a more robust and better aligned optomechanical system.

One option to improve the vignetting performance is to close the aperture. In this case the light intensity is reduced resulting in more noisy fluorescence images.

For this FOV, the ratio between the different color channels of each sensor seems to be acceptable as it is lower than $\pm 15\%$ for both sensors. For this reason, color correction and spectral unmixing are considered to be spatially invariant.

Inhomogeneities of images may originate from inhomogeneous illumination, an inhomogeneous diffuse white reflectance object or sensor field gain inhomogeneities.

Additionally, an extensive study combining all channels would give a more conclusive picture of the relative channel intensities. However, six channel unmixing experiments presented in Section 5.3 suggest that the detection is constant enough to unmix different dyes which are spectrally very close.

To summarize, the field of view and the resolution slightly exceed the minimum requirements. However, vignetting is present and leads to dark edges which are well-known from imaging systems with a large FOV. For example, endoscopic surgeons prefer a large field of view and in return accept strong vignetting on the edges of the images.

5.4.2 *Spatial resolution and modulation transfer function*

This section determines the spatial resolution, characterized by the modulation transfer function (MTF) of the imaging system and checks whether it fulfills the requirements put on the system in Section 3.1.6. The results of the analysis are reused from the experimental data of the Master's thesis of Tobias Behr [175]. Thus, the methods and results are shortly summarized in this section. However, a more complete and extensive analysis can be found in the original thesis.

5.4.2.1 *Methods*

The MTF of digital imaging systems can be determined using the slanted edge method [202]. Images of both optical paths of the well-adjusted system are recorded. The object is a target with a sharp edge which is placed in different parts of the object plane. The slanted edge allows to compute an oversampled edge spread function which is converted to a line spread function and subsequently to the MTF.

The MTF is analyzed at five different locations, the image center, top, right, bottom and left side. At each location the meridional and sagittal MTF are measured and the spatial frequency at $\mathrm{MTF} = 0.1$ and $\mathrm{MTF} = 0.5$ are reported for grayscale images. Mean and standard deviations of the outer image locations are calculated for meridional and sagittal $\mathrm{MTF} = 0.5$ and $\mathrm{MTF} = 0.1$. The results as presented in Table 5.10.

Table 5.9: Spatial frequencies in lp/mm for meridional (mer.) and sagittal (sag.) $\mathrm{MTF} = 0.1$ and $\mathrm{MTF} = 0.5$ at the object locations center, right, bottom, left and top and for both sensors. The overview is compiled from the experimental data published in [175].

	S2				S1			
	SAG.		MER.		SAG.		MER.	
$MTF =$	0.5	0.1	0.5	0.1	0.5	0.1	0.5	0.1
center	3.2	9.4	3.1	10.5	3.3	9.1	3.3	9.0
right	3.1	9.5	2.7	6.1	3.1	8.8	2.3	5.1
bottom	3.1	8.6	2.2	5.0	3.0	8.3	2.0	5.0
left	3.5	10.3	2.2	4.8	3.1	8.6	2.3	5.4
top	3.1	8.7	2.7	5.5	3.0	8.0	2.3	5.2

5.4.2.2 *Results*

The spatial frequencies of the corresponding measured MTF curves are reported in Table 5.9 in lp/mm. The spatial frequencies at $\mathrm{MTF} = 0.1$ range between 4.8 lp/mm and 10.5 lp/mm for the different locations and sensors. The sagittal frequencies of $\mathrm{MTF} = 0.1$ performs better than the meridional MTF with between 8.0 lp/mm and 10.3 lp/mm. However, the meridional $\mathrm{MTF} = 0.1$ at outer locations has lower spatial frequencies of 4.8 lp/mm to 6.1 lp/mm. The frequencies at $\mathrm{MTF} = 0.5$, which is relevant for the system specifications, are spatially more homogeneous. The respective spatial frequencies range from 2.0 lp/mm to 3.5 lp/mm (sagittal: 3.0 lp/mm to

Table 5.10: Mean and standard deviation of the MTF results of the outer image positions (center excluded). This evaluation contains statistical as well as some systematic errors caused by different image positions. The condition $MTF = 0.5$ exceeds the required 1.15 lp/mm at all image locations..

$MTF =$	0.5	0.1
SAG.	(3.13 ± 0.16) lp/mm	(8.85 ± 0.73) lp/mm
MER.	(2.34 ± 0.24) lp/mm	(5.26 ± 0.41) lp/mm

3.5 lp/mm; meridional: 2.2 lp/mm to 3.3 lp/mm). There is no clear difference in performance between S1 and S2.

The statistical evaluation in Table 5.10 shows that all spatial frequency mean values exceed the requirements.

5.4.2.3 *Discussion*

All the measured frequencies for MTF = 0.5 are bigger than the required 1.15 lp/mm. Thus, the imaging system with opened aperture and zoomed out has superior optical performance compared to the natural vision of a surgeon looking at the object from a distance of 50 cm. If zooming further in, even finer object structures can be resolved.

Large high-resolution displays could display even more information to the surgeon. The resolution is not limited by the digital resolution of the sensor, but by the optical resolution of the imaging system.

Thus, it might be beneficial for the color imaging performance to design an imaging system with a better resolving power. In contrast, fluorescent objects usually appear rather wide due to scattering in tissue. If the optical resolving power exceeds the digital resolution limit given by the pixels, the lateral displacement between the red, green and blue channels will cause artifacts. Such artifacts have been observed and reported in Section 6.3 and [167]. An optical point spread function which is wider than the distance between pixels will smooth the performance and thus improves unmixing.

In this analysis, only grayscale images are considered. As the sensor has two times more green pixels than red or blue pixels, the spatial MTF of the green channel shows a better performance than the red or blue MTF. A more detailed analysis of this effect can be found in [175].

5.4.3 *Working distance*

Most clinical open field fluorescence imaging systems specified for ICG have a working distance of 10 cm to 30 cm [74]. Thus, a free working distance of at least 10 cm is required, 20 cm are better and 30 cm are best. For the selected lens configuration with an objective lens with magnification of $m_{\text{obj}} = 0.5$, the working distance is 18.7 cm [201]. This distance will be reduced by sterile drapes by a couple of cm. The remaining approx. 15 cm free working distance are more than minimally required. Thus, the minimal condition is fulfilled.

This working distance is necessary for intraoperative imaging as the surgeon is required to handle surgical tools in the remaining space. A higher free working distance would be better and future optical developments should focus on this aspect.

5.4.4 *Numerical aperture*

As fluorescence of tissue samples is usually very weak, a high collection efficiency for light of the imaging lens is desirable. The numerical aperture on the object side is a quantitative measure for the collection efficiency of the lens system:

$$\eta_{\text{lens}} \sim \text{NA}_{\text{obj}}^2. \tag{5.33}$$

The numerical aperture of the system is given by the combination of objective lens and zoom system. The manufacturer only specifies the numerical aperture of the $m = 2\times$ objective lens as $\text{NA}_{\text{obj}} = 0.04$ and for the $m = 1\times$ objective lens as $\text{NA}_{\text{obj}} = 0.02$, but not for the $m = 0.5\times$ objective lens which is used here [201]. Accordingly, the object side numerical aperture of the system is estimated to be $\text{NA}_{\text{obj}} \approx 0.01$.

In fluorescence microscopy objective lenses with no immersion medium have numerical apertures as high as $\text{NA}_{\text{obj}} = 0.95$ (for example CFI Plan Apo Lambda 40X, Nikon Instruments Europe). However, the field of view and working distance of typical microscopy objective lenses with $40\times$ magnification are less than 1 mm. Thus, lenses of that size can be manufactured.

In contrast, for the required working distance of 187 cm, the first objective lens would require a diameter of at least 1.14 m to allow a $\text{NA}_{\text{obj}} = 0.95$. This example illustrates that high numerical apertures as known in microscopy are absolutely unreasonable for macroscopic imaging.

A more reasonable comparison is made with high aperture machine vision objective lenses. If replacing the imaging system with a single objective lens, the corresponding focal length would be $f \approx 28.5$ mm. High numerical aperture lenses for macroscopic imaging which would fit to the imaging scenario are for example Otus 1.4/28 or Distagon 2.0/28 (both Carl Zeiss AG, Oberkochen, Germany). The object side numerical aperture is calculated using the optics tool System PreDesigner (Qioptiq Photonics GmbH & Co. KG, Goettingen, Germany) for a focal length $f = 28$ mm, an object distance as free working distance of 187 mm, a FOV of 54 mm and an f number when focusing at infinity of f/2.0 and f/1.4. The resulting aperture on the object side is $\text{NA}_{\text{obj, f/1.4}} = 0.053$ and $\text{NA}_{\text{obj, f/1.4}} = 0.037$. These numbers are more reasonable than microscopy objectives as estimate of what can be expected as maximum numerical aperture for an imaging system. Still, these objectives are expected to collect between $13\times$ and $28\times$ more light than the used lens configuration.

All in all, the aperture of the designed system is by far not as big as for high end objectives with the same magnification and working distance. However, the lens system was selected because it is suitable for beam splitting and filtering in infinity corrected space. Future improvements of the optical system may include increasing the numer-

ical aperture which can improve optical photon collection efficiency by one order of magnitude.

6

NOISE MODEL AND UNMIXING ARTIFACT DIAGNOSTICS

Fluorescence guided surgery has shown to benefit from simultaneous detection of multiple dyes. This requires multispectral imaging and subsequent unmixing to display multiple fluorescent dye component images. Unmixing comes with two aspects altering the image quality: First, unmixing may amplify noise and cause noise crosstalk between the individual component images. As fluorescent light is usually detected at low intensities, image noise is always an issue to be considered. Second, deviations from the intended imaging scenario in the raw fluorescent images which may be caused by tissue absorption, autofluorescence or ambient light lead to artifacts in the unmixed raw images. These artifacts may potentially result in wrong medical decisions.

This chapter is dedicated to investigating the effects of noise for imaging scenarios and to develop a method which indicates unmixing artifacts.

First, the effects of noise on the unmixing results are demonstrated with an experimental phantom imaging scenario in Section 6.1. Subsequently a noise model of the fluorescence detection to estimate the noise per image and per pixel on basis of an individual image is introduced and established using the experimental data in Section 6.2. The noise estimation is used subsequently to indicate unmixing artifacts and also to optimize the system for minimal noise.

Unmixing artifacts may be caused if the detected raw data does not correspond to the expected scenario with the respective spectral signatures. For clinical scenarios it is essential to spot such artifacts to avoid altered diagnostic information. A novel method to indicate such artifacts is introduced in Section 6.3. The metric, called T-score, puts the unmixing residuals in relation with the expected noise. Its potential is demonstrated unmixing the experimental phantom images with correct and on purpose with wrong spectral signatures.

Concepts, experiments, the underlying data set and results which are presented in this section have been published in the peer reviewed publication [167] by Dimitriadis *et al.*.

6.1 PROPAGATION OF NOISE IN UNMIXING

One of the most important criteria to evaluate image quality is the SNR of the final images. In this work, the unmixed fluorescence component images are to be displayed. Phantom experiments in Section 5.3.1

have shown good signal to noise ratio for the unmixed fluorescence component images, while Section 5.3.2 showed examples with deteriorated SNR. Unmixing with similar signatures in channel space results in amplification of noise.

This section will analyze noise and the resulting SNR of unmixed images in detail.

Methods

Each image of the stream of $i = 1 \dots 100$ of identically acquired images $\boldsymbol{Y}_i(\xi)$ is individually unmixed (same data as in Section 5.3.1):

$$\boldsymbol{X}_i(\xi) = \boldsymbol{u} \cdot \boldsymbol{Y}_i(\xi). \tag{6.1}$$

The mean of the images mean $\left[\boldsymbol{Y}_i(\xi)\right]$ is calculated as

$$\overline{\boldsymbol{X}}(\boldsymbol{\xi}) = \text{mean}\left[\boldsymbol{X}_i(\xi)\right] = \sum_{i=1}^{N_i} \frac{1}{N_i} \cdot \boldsymbol{X}_i(\xi). \tag{6.2}$$

The image noise on each pixel is the empirical standard deviation calculated as

$$\Delta\boldsymbol{X}(\xi) = \text{std}\left[\boldsymbol{X}_i(\xi)\right] = \sqrt{\frac{1}{N_i - 1} \cdot \sum_{i=1}^{N_i} \left(\boldsymbol{X}_i(\xi) - \text{mean}\left[\boldsymbol{X}_i(\xi)\right]\right)^2} \tag{6.3}$$

with $N_i = 100$. The SNR of the image is calculated as

$$SNR_X(f, \xi) = \frac{\overline{X}(f, \xi)}{\Delta X(f, \xi)}. \tag{6.4}$$

Results

Figure 6.1 displays the mean fluorescence intensity, the temporal imaging noise (standard deviation) and the SNR. In the Figure 6.1B we can see that image regions in which no fluorescence intensity is present in any channel have very little noise as these regions are dominated by the low intensity readout noise of the sensor. Though, if high fluorescence intensity is present in any component at a location, all components are contaminated with noise of approximately the same order of magnitude.

So, the signal to noise ratio for a component increases with increasing component intensity (see Figure 6.1C). High fluorescence intensity causes high SNR of a fluorescent component after unmixing. But the noise of other components at this location is also high even though the intensity of that component is low. This effect can best be observed in Figure 6.1D, E and F.

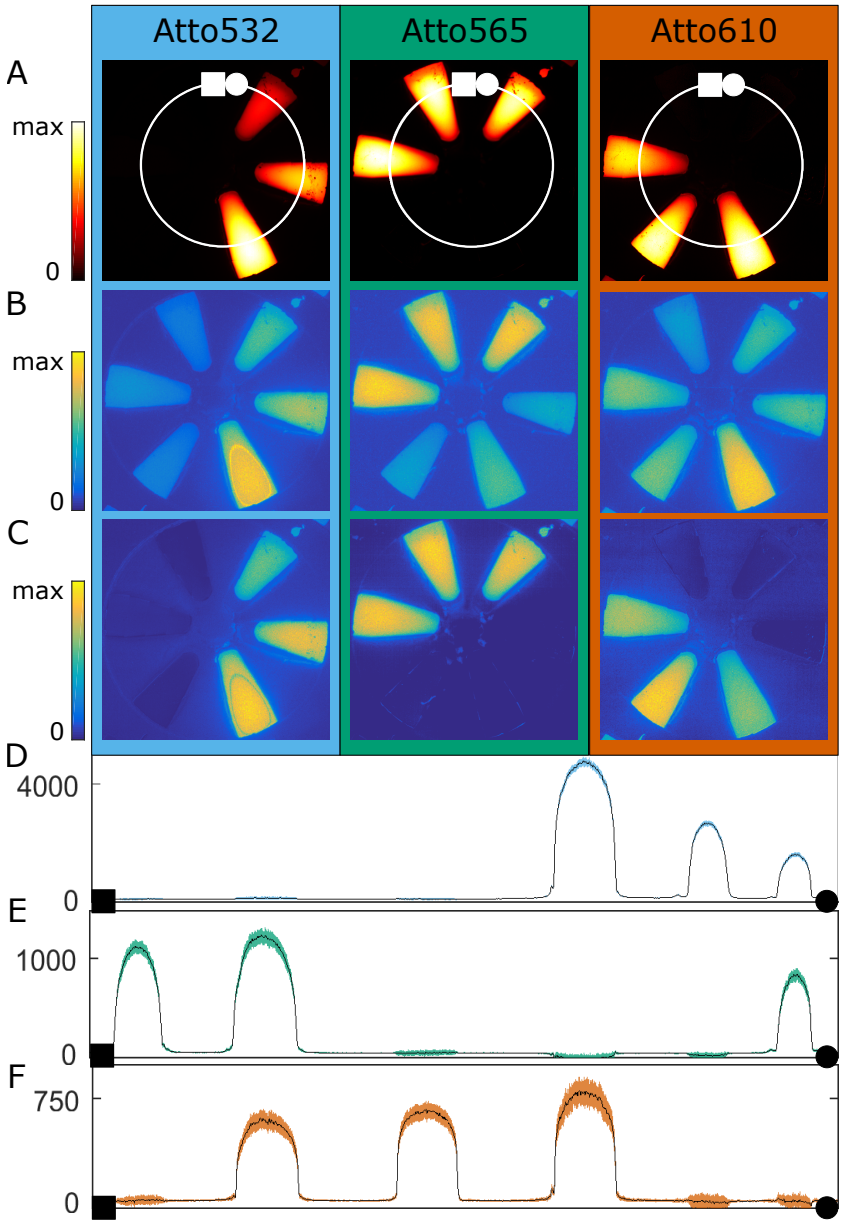

Figure 6.1: Noise propagation in unmixing. A) Unmixed fluorescence intensity $\overline{X}(f,\xi)$ of Atto532, Atto565 and Atto610 (mean over 100 images), scaled between 0 and the maximum (maximum of Atto532: 4780; Atto565: 1257; Atto488: 807). B) Temporal image noise $\Delta X(f,\xi)$ (standard deviation over 100 images) per pixel scaled between 0 and the maximum (maximum of Atto532: 101; Atto565: 55; Atto488: 68) C) $SNR_X(f,\xi)$ per pixel scaled between 0 and the maximum value (maximum of Atto532: 62; Atto565: 30; Atto488: 21). D), E) and F) line profiles of the intensity of Atto532, Atto565 and Atto610 along the white circle shown in A). Intensity mean drawn as black line and [5%, 95%] confidence bounds as colored background. Subfigure B) is based on the same underlying data set as the respective plot in [167]. Adapted with with permission from ref [167], OSA.

Discussion

Image noise is determined as the variation over a stack of identically acquired images. As all images in the stack have been acquired identically, the only variation should be noise. This evaluation could be disturbed by temporal fluctuations of the excitation light intensity or camera readout sensitivity. Both effects are minimized as the sensors are temperature stabilized and the light source output power is stabilized.

Conclusion

The findings show a fundamental limitation of all unmixing scenarios. Intensity in a single channel causes noise in all other channels. If all channels show equal intensity at a specific location, this is of minor importance. But if one channel is strong and others are weak, the signal of the weak channel becomes very noisy. If looking at a video of unmixed images, this will cause noisy signal on pixels with high intensity of another channel.

In the following section a theoretical noise model which allows to estimate the noise per pixel on basis of a single image is developed (see Section 6.1). The model can be used to optimize the system for best unmixing performance (see Chapter 7). Also, a diagnostic measure of the unmixing performance based on the noise model is developed (Equation 6.3).

Developing a theoretical noise model allows to estimate the noise per pixel on basis of a single fluorophore.

6.2 SINGLE FRAME NOISE ESTIMATION

In this section, a method to estimate the noise for each pixel of a fluorescence image after unmixing on basis of single image without knowledge of previous or future images is introduced. The noise estimation is based on the noise model described in the EMVA 1288 standard [200]. The noise model is approximated for the used sensor model and application scenario here. In addition, the noise of the raw images is propagated to the unmixed fluorescence component images.

The noise estimation method of the unmixed component images based on the intensity of these unmixed components can be used to further develop an unmixing artifact diagnostics and to optimize the imaging system for best SNR.

Methods

The EMVA 1288 standard describes a noise model to characterize image noise of modern silicon sensors such as the sensor CIS2521 (Fairchild), which is used in this work [171, 200, 203]. However, the EMVA 1288 noise model describes the image data and the associated noise for a grid of scalar pixel values. In this work, multispectral image data, in which each pixel consists of a vector of multispectral values, is used. Since each data point in the multispectral image data is acquired by one planar silicon pixel, the EMVA 1288 noise model can be applied here for each data point independently (assuming independence of the pixels). For consistency with the multispectral image data, the variance in the noise model is therefore substituted by covariance matrices as described in detail in Section A.1.3.

Here, the individual contributions are listed and approximated for fluorescence guided surgery. The noise of a fluorescence image $Y(c, \xi)$, mathematically described by the covariance matrix $\mathbf{\Sigma}_Y(\xi)$, is composed of the sensor readout noise $\mathbf{\Sigma}_R(\xi)$, the sensor dark current noise $\mathbf{\Sigma}_I(\xi)$, quantization noise $\mathbf{\Sigma}_Q(\xi)$ and photon shot noise $\mathbf{\Sigma}_{Y,S}(\xi)$. The individual contributions, which are described in detail in Section A.1.3, are summed to obtain $\mathbf{\Sigma}_Y(\xi)$:

$$\mathbf{\Sigma}_Y(\xi) = \mathbf{\Sigma}_{Y,\mathrm{P}}(\xi) + \mathbf{\Sigma}_R(\xi) + \mathbf{\Sigma}_I(\xi) + \mathbf{\Sigma}_Q(\xi). \tag{6.5}$$

All covariance matrices of the acquired images $Y(c, \xi)$ are assumed to be diagonal, because the noise of different channels is assumed to be independent.

Readout noise

For the used sensors, the readout noise is specified by the manufacturer as σ_0, which is approximated to be constant for all pixels [171]. This results in diagonal entries of the covariance matrix of

$$\Sigma_R(c, c, \xi) = \sigma_0^2 \approx (1.67\,\mathrm{e}^-)^2. \tag{6.6}$$

This approximation assumes that the readout noise of all pixels and (in the setup used here) all sensors has the same value. As the dominant source of noise for fluorescence guided surgery is the shot noise, this simplified approach is reasonable.

Dark Current Noise

The diagonal entries of the covariance matrix caused by dark current is given by

$$\Sigma_R(c, c, \xi) = I_{dark} \cdot t_{\mathrm{int}}. \tag{6.7}$$

The dark current is specified for the sensor as $3\,e^-/s$, so for frames with a comparably large integration time of 50 ms, the dark current noise [171] is approximated as

$$\Sigma_R(c,c,\xi) \approx 0.15\,e^{-2}. \tag{6.8}$$

which is negligible compared to the readout noise and the photon shot noise [171, 174, 200]. In general, the dark current is strongly temperature dependent. Thus, spatial temperature variations on the sensor may lead to spatially dependent dark current noise contributions.

Quantization noise

The quantization noise is introduced when digitalizing the measured pixel values into a fixed 16 bit representation (for CIS2521) [200, 204]. For an equidistant spacing Δg of gray values g, the diagonal entries of the covariance matrix are given by

$$\Sigma_Q(c,c,\xi) = \frac{1}{K^2}\frac{1}{12}\cdot\Delta g \tag{6.9}$$

Here, with $K = 2.22\,/e^-$ [171] and $\Delta g = 1$, the overall quantization noise added to each frame is in the range of

$$\Sigma_Q(c,c,\xi) \approx 0.017\,e^{-2}. \tag{6.10}$$

The quantization noise itself only depends on the quantization and not on the actual image. But as the noise contributions are analyzed in terms of e^-, the factor K is incorporated in the covariance matrix. In theory, the conversion factor K may slightly vary from sensor to sensor and also from pixel to pixel.

Shot noise

As the intensity image $Y(c,\xi)$ corresponds to the number of Poisson distributed electrons e^-, the diagonal entries of the covariance matrix correspond to the respective image intensities Section A.1.3:

$$\Sigma_{Y,S}(c,c,\xi) \approx Y(c,\xi). \tag{6.11}$$

Both quantum efficiency $q(\lambda)$ and conversion factor K are supposed to be spatially homogeneous. The low photo response non-uniformity ($PRNU \leq 0.5\%$) of the sensor guarantees sufficient signal homogeneity.

Noise estimation

For fluorescence guided surgery, high intensity signals for best SNR have pixel count rates of more than $1000\,e^-$ per pixel and frame. Images with fluorescence signal in the order of $100\,e^-$ allow reasonable

Table 6.1: Overview of different noise contributions in the form of covariance matrices as described by the EMVA 1288 model with an estimate for the used sensor CIS2521 running in global shutter mode with $t_{\text{int}} = 50\,\text{ms}$ [171, 200, 204].

NOISE TYPE	FORMULA	ESTIMATED VALUE $[\text{e}^{-2}]$
shot	$\Sigma_{Y,S}(c,c,\xi)$	$\approx Y(c,\xi)$
readout	$\Sigma_R(c,c,\xi)$	$= \sigma_0^2 \approx 1.67^2$
dark current	$\Sigma_D(c,c,\xi)$	$= I_d \cdot t_{\text{int}} \approx 0.16$, $(t_{\text{int}} = 50\,\text{ms})$
quantization	$\Sigma_Q(c,c,\xi)$	≈ 0.017
approx. image noise	$\Sigma_Y(c,c,\xi)$	$\approx Y(c,\xi) + \sigma_0^2$

imaging quality and signals of at least $10\,\text{e}^-$ are needed for real-time fluorescence guided surgery. This allows to estimate the influence of each individual contribution to the overall noise and only consider the dominant effects as summarized in Table 6.1.

The overall noise covariance matrix is approximated as

$$\Sigma_Y(c,c,\xi) = Y(c,\xi) + \sigma_0^2 \tag{6.12}$$

for all channels c and pixels ξ on basis of a single image $Y(c,\xi)$.

In this formula, all pixels of all sensors are assumed to exhibit identical noise characteristics. This is mathematically expressed by the constants I_{dark}, K and σ_0 which are identical for all pixels and sensors.

To obtain $Y(c,\xi)$, the recorded raw image was background subtracted and converted to e^- using the conversion factor K. The conversion to e^- is necessary to determine the shot noise. The subtracted dark image was obtained by averaging individually acquired dark images.

Noise propagation in unmixing

To calculate the covariance matrix $\mathbf{\Sigma}_X(\xi)$ of the unmixed fluorescence component intensities $X(c,\xi)$, the covariance matrix needs to be transformed from $\mathbf{\Sigma}_Y(\xi)$ by

$$\mathbf{\Sigma}_X(\xi) = \boldsymbol{u}\mathbf{\Sigma}_Y(\xi)\boldsymbol{u}^\mathsf{T}. \tag{6.13}$$

The image noise of the individual fluorescent components f is determined by the diagonal elements of the covariance matrix:

$$\Delta \boldsymbol{X}^2(\xi) = \operatorname{diag} \mathbf{\Sigma}_X(\xi). \tag{6.14}$$

6.2.0.1 *Experimental image processing*

Unmixed noise of the phantoms fluorescence images (see Section 5.3.1) is estimated on basis of a single image using Equation 6.13 and Equation 6.14. Results are compared with the experimentally determined

temporal noise over a stack of 100 sequentially acquired images (as described in Section 6.1).

Results

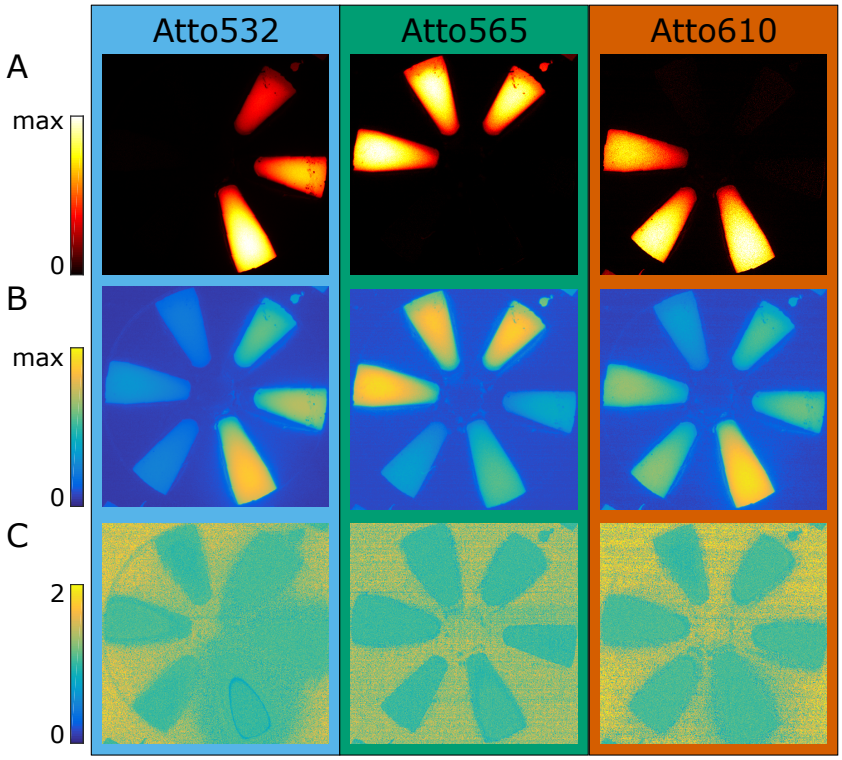

Figure 6.2: Comparison between theoretical predicted noise based on the described model and experimentally determined noise. A) Intensity of a single unmixed fluorescence image. B) Estimated fluorescence noise based on the model and the intensity information of a single image. C) Ratio between predicted noise shown in B) and experimental noise (see Figure 6.1B). Noise estimate on basis of the individual image shown in A). Scaling maxima of A) Atto532: 4780; Atto565: 1257; Atto488: 807; of B) Atto532: 101; Atto565: 55; Atto488: 68. Subfigure A) is based on the same underlying data set as the respective plot in [167]. Adapted with with permission from ref [167], OSA.

Figure 6.2 shows the comparison between experimentally determined temporal noise of the unmixed data and the estimated noise on basis of the pure intensity of a single image. For all three dyes, experimentally measured and theoretically estimated noise are in good agreement. Figure 6.2C shows that the ratio between theoretical and experimental noise is close to one for regions with fluorescence intensity of any dye present. In dark image regions where no fluorescence is captured, the theoretically estimated noise is bigger than the experimentally determined noise.

Discussion

These results support the noise model, considering both sensor readout and shot noise to be appropriate for the intended use. Also, the noise propagation in the unmixing process (as derived in Equation A.1.1) allows to estimate the noise per pixel on basis of a single unmixed frame.

The deviation between estimated noise and the measured noise is only high at pixels with very low light intensity, whose noise behavior is of minor importance. Though, future work also considering the complex noise behavior of the readout electronics may further improve the prediction for areas with low light intensity. In this work, estimating the noise in regions with fluorescence intensity is sufficient.

The noise per pixel has been measured in literature by sequentially recording a stack of images and calculating the standard deviation over the stack.

Estimating the image noise of each component by recording only a single image is advantageous for real-time applications. It allows to evaluate the unmixing quality (see Equation 6.3) for a fluent video stream and does not require to record and process multiple identical images.

Additionally, the analytical noise calculation is used to optimize the SNR varying system parameters. For the user, the SNR of the final unmixed fluorescent component images is important and thus an analytical calculation of noise allows a computationally efficient implementation of the fitness function.

6.3 UNMIXING ARTIFACT DIAGNOSTICS

Fluorescence unmixing may produce artifacts in the unmixed fluorescence component images due to tissue absorption, autofluorescence or the presence of dyes which are not expected and thus not considered. In this section a metric named T-score is developed to indicate unmixing artifacts. In a second step, the performance and statistical significance of the T-score are investigated using experimental phantom image data. Finally, the sensitivity of the T-score for bad unmixing scenarios with missing signatures is demonstrated.

Methods

In this section, the standardized vectorial residual $\boldsymbol{\varepsilon}(\xi)$ and the $T(\xi)$-score as the corresponding scalar measure are introduced to evaluate the unmixing performance. The measured fluorescence intensity $\boldsymbol{Y}(\xi)$ is unmixed using the spectral signatures $\boldsymbol{\kappa}_1, ..., \boldsymbol{\kappa}_N$. If the number of spectral channels is higher than the number of dyes, some of

the measured fluorescence data points are expected to be outside the subspace spanned by $\boldsymbol{\kappa}_1, ..., \boldsymbol{\kappa}_N$ due to noise.

An example unmixing for two dyes is presented in Figure 6.3A. The vectorial residual $\boldsymbol{R}_Y(\xi)$ of an observation $\boldsymbol{Y}(\xi)$ is defined as the difference between the measured data point $\boldsymbol{Y}(\xi)$ and the corresponding closest point $\boldsymbol{muY}(\xi)$ in the subspace spanned by the dyes:

$$\boldsymbol{R}_Y(\xi) = \boldsymbol{Y}(\xi) - \boldsymbol{muY}(\xi). \tag{6.15}$$

The standardized residual $\varepsilon_Y(c, \xi)$ is defined as the ratio between the residual components $R_Y(c, \xi)$ and the expected noise covariance components $\Sigma_R(c, c, \xi)^{\frac{1}{2}}$:

$$\varepsilon_Y(c, \xi) = \frac{R_Y(c, \xi)}{\Sigma_R(c, c, \xi)^{\frac{1}{2}}} \tag{6.16}$$

with the covariance matrix of the residual given as

$$\begin{aligned} \Sigma_R(\xi) &= \operatorname{cov}\left[\boldsymbol{R}_Y(\xi), \boldsymbol{R}_Y(\xi)\right] \\ &= \operatorname{cov}\left[\boldsymbol{Y}(\xi) - \boldsymbol{muY}(\xi), \boldsymbol{Y}(\xi) - \boldsymbol{muY}(\xi)\right] \\ &= \boldsymbol{\Sigma}_Y(\xi) + \boldsymbol{mu}\boldsymbol{\Sigma}_Y(\xi)\boldsymbol{u}^\intercal\boldsymbol{m}^\intercal - \boldsymbol{mu}\boldsymbol{\Sigma}_Y(\xi) - \boldsymbol{\Sigma}_Y(\xi)\boldsymbol{u}^\intercal\boldsymbol{m}^\intercal. \end{aligned} \tag{6.17}$$

The scalar $T_Y(\xi)$ score is obtained by summing over the squared vectorial components of $\boldsymbol{\varepsilon}_Y(c, \xi)$:

$$T_Y(\xi) = \sum_{c=1}^{N_c} \varepsilon_Y(c, \xi)^2. \tag{6.18}$$

Assuming the statistical variation of the detected fluorescence signal is normal distributed

$$Y(c, \xi) \sim \mathcal{N}\Big(\mu_Y(c, \xi), \Sigma_Y(c, c, \xi)\Big) \tag{6.19}$$

then the channel components of the residual vector are also normal distributed

$$R_Y(c, \xi) \sim \mathcal{N}\Big(0, \Sigma_R(c, c, \xi)\Big) \tag{6.20}$$

leading to

$$\varepsilon_Y(c, \xi) \sim \mathcal{N}\Big(0, 1\Big) \tag{6.21}$$

for all c and thus

$$T_Y(\xi) \sim \sum_{c=1}^{N_c} \mathcal{N}\Big(0, 1\Big)^2 = \chi^2(k), \tag{6.22}$$

where $k = N_c - N_f$ are the degrees of freedom [205]. So, the standardized residuals are χ^2 distributed if the observations of the random

variable are normal distributed. If the random variables are not normal distributed in the first place (see Equation 6.19), the normalized residual will not be χ^2 distributed.

For real-time video-rate imaging applications, the $T_Y(\xi)$-score needs to be calculated for each frame individually. Thus, an estimation of the covariance $\Sigma_R(c, c, \xi)$ matrix of $\boldsymbol{R}_Y(\xi)$ on basis of the image information of the single frame is required. Using the noise estimation on basis of a single frame described in Section A.1.3 combined with Equation 6.17 allows to estimate the covariance of the residual on basis of a single image.

The standardized residuals $\boldsymbol{R}_Y(\xi)$ and the $T_Y(\xi)$-score are calculated using Matlab and the pre-implemented `multiprod` function [206] for one individually recorded image as described in Section 5.3.1. To display the unmixed fluorescence signal in a compact way, the unmixed component images of Atto532, Atto565 and Atto610 are individually scaled from zero to the 0.9999 quantile of the data and subsequently fused as R, G and B channels of an RGB image.

Visible yellow patches or structures in the T-score plot mean that for those regions the residual is higher than expected by the estimated noise. In the same way, dark blue regions mean that the noise estimation is too small, while brighter blue regions with noise appear as well unmixed.

In order to demonstrate the effect of wrongful unmixing, the dyes are unmixed with an unmixing matrix that is missing at least one of the dye signatures on purpose. So, the data is unmixed with an unmixing matrix created on basis of only one or two of the spectral signatures, whereas all three spectral signatures of Atto532, Atto565 and Atto610 are needed for correct unmixing. Unmixed images and the T-score is calculated for all combinations of unmixing with one or two dyes only.

Results

The unmixed fused RGB fluorescence component image is displayed in Figure 6.3B. This underlying data is the same as in Figure 5.10, so the image shows good unmixing with close to zero crosstalk. The vial containing pure signal of the dye Atto532 is displayed in blue (bottom left), pure signal of Atto565 is displayed in green (top left) and pure signal of Atto610 is displayed in red (right).

The individual standardized residuals are shown in Figure 6.3C for each channel individually. Most channels show a horizontal stripe pattern especially visible in the background. Image regions where vials with high fluorescence intensity show a gradual change from positive to negative values over the vial or from negative to positive, depending on the vial location and channel.

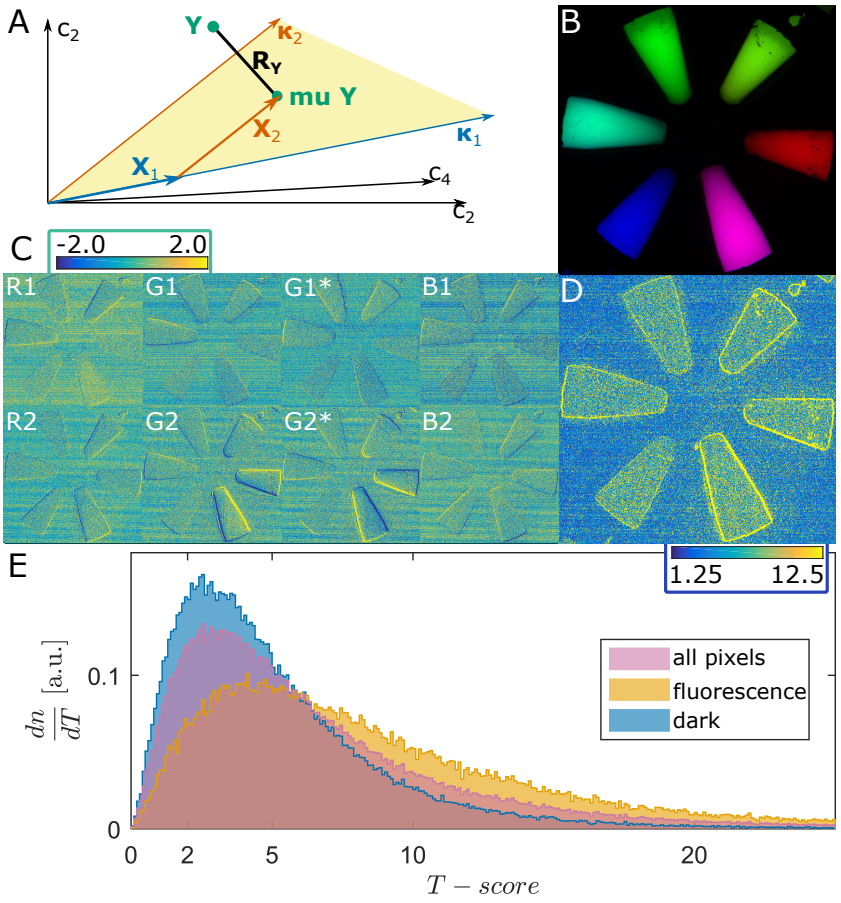

Figure 6.3: Diagnostic T-score for the unmixing procedure. A) Systematic example scatter plot of one measured data point $Y(c,\xi)$ in channel space spanned by $c_1,\ldots,c_N$. The measured data is unmixed with signatures $\boldsymbol{\kappa}_1$ and $\boldsymbol{\kappa}_2$ to component contributions $X(1,\xi)$ and $X(2,\xi)$, which sum up to the closest point in the component subspace (here, the component space is the plane spanned by $\boldsymbol{\kappa}_1$ and $\boldsymbol{\kappa}_2$). Y. The residual vector $R_Y(c,px)$ connects the closest point in the component subspace with the measured data point $Y(c,\xi)$. B) Unmixed fluorescence image with Atto532 intensity as red channel, Atto565 intensity as green channel and Atto610 intensity as blue channel. C) Individual channel contributions of the normalized residual $\boldsymbol{\varepsilon}_Y(c,\xi)$. D) T-score $T_Y(c,\xi)$ characterizing the unmixing quality. E) Histogram of the T-score values for all pixels, high fluorescence intensity values and the dark regions. Subfigure D) is replotted based on the same underlying data set as the respective figure in [167]: Adapted with with permission from ref [167], OSA.

The T-score image is displayed in pseudocolors in Figure 6.3D. The stripes visible in the standardized residuals of the individual channels are not as prominent as in the T-score image. Both fluorescent and dark regions appear in blue, which means that the majority of the pixels is inside the confidence bounds. The T-score of the dark regions appears to be lower compared to the high intensity regions.

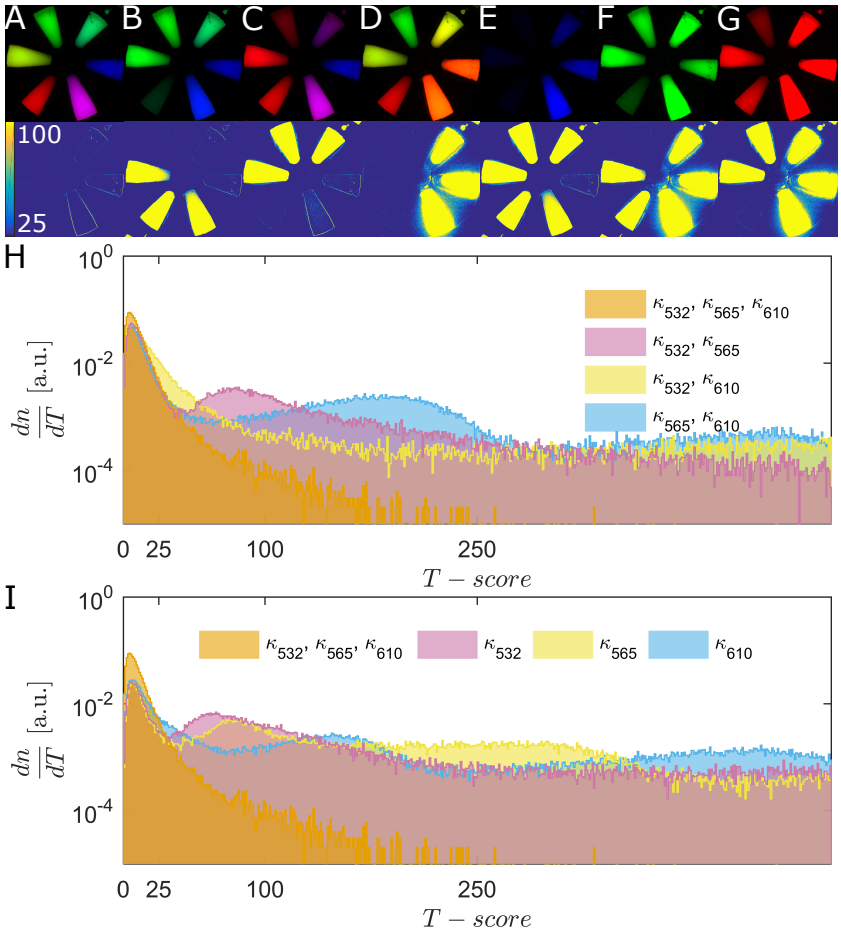

Figure 6.4: Unmixing the raw data presented in Figure 5.10 using mixing matrices for different dye combinations: A) Correct unmixing for all dyes Atto532, Atto565 and Atto610, B) unmixing for Atto532 and Atto565, C) unmixing for Atto532 and Atto610, D) unmixing for Atto565 and Atto610, E) unmixing for Atto532, F) unmixing for Atto565 and G) unmixing for Atto610. Upper images display the three unmixed components as scaled RGB image. Lower images show the T-score value of the unmixed dyes. H) Histogram of the T-score unmixed as in A), B), C) and D). I) Histogram of the T-score unmixed as in A), E), F) and G). Lower part of subfigure A) is replotted based on the same underlying data set as the respective figure in [167]: Adapted with with permission from ref [167], OSA.

The edges of the vials especially on the right side of the image show high T-scores. Figure 6.3E shows a histogram of all the pixels, the dark image regions and the high intensity image regions separately. T-scores of the dark regions are generally lower than the T-scores of the high intensity regions.

Figure 6.4 presents examples for correct and wrong unmixing. All unmixing attempts result in a fluorescence component image and comparison with Figure 6.4A reveals for which vials the unmixing did not work correctly. The corresponding T-score plots of each of

the unmixing scenarios indicates in yellow which of the vials were not unmixed correctly. Histograms of the T-score images are shown in Figure 6.4H and I.

Discussion

Readout noise in CMOS sensors typically causes stripe patterns in the images. The stripes visible in Figure 6.2B can thus most likely be attributed to the readout of the two sensors and in combination with demosaicing and spatial registration.

The gradual slope in the standardized residual images in regions of high fluorescence intensity can be explained by the mosaic pattern on the sensor. If the fluorescence intensity is not constant over a region, the micro-filter pattern will result in a too small or too big intensity value depending on the location of the pixel in the micro-pattern. This theory is undermined by the complementary behavior of the channels G2 and G2* which should show the same spectral behavior. In the T-score image, the gradual slopes of the standardized residuals of the different channels seem to compensate each other and average out.

The high T-score on the edges of some vials appears to be caused by a high intensity gradient of the dyes in combination with the micro-pattern on the sensors and miss-registration between the two sensor.

The lower T-scores in dark image regions compared to the vials can be attributed to non-Gaussian readout noise and thresholding for negative intensities when estimating the noise (see Section 6.2). The gradual slopes in the standardized residual images indicate that the micro-pattern has a relevant contribution to the T-score. This is a systematic error which is not considered in the noise estimation.

The T-scores of both fluorescence and dark regions in the correctly unmixed component images are rather low (up to 20) compared to the T-score of wrongfully unmixed pixels, which goes up to several hundreds.

The statistical interpretation of the T-score as being χ^2 distributed is only applicable if photon shot noise and readout noise are normal distributed and no systematic errors are present. Strictly speaking, the signal in dark regions (readout noise dominant) is not normal distributed. But for high count numbers the noise of the fluorescence signal governs the overall noise and can be well approximated by a normal distribution (see Section 6.1). In case of non-Gaussian statistics of the underlying properties the T-score can still be calculated and can also perform well. In this case the T-score is not χ^2 distributed and thus interpretations containing probabilities and confidence bounds must then be treated with caution.

The T-score is a statistical consistency check of the unmixing. High T-scores indicate that the pixels have most likely not been unmixed well. But low T-scores do not guarantee good unmixing, it just indi-

cates that the residual is comparable or lower than the expected noise. In this analysis the T-score proved to be very sensitive for data points with wrong unmixing. If a measured fluorescent data point is modified inside the subspace spanned by the unmixing signatures, the residual vectors are not changed, because differences inside the subspace spanned by the signatures cannot be measured. The higher the number of fluorescence channels and the lower the number of components to unmix for, the lower the chances that invisible modifications of the spectral signatures occur.

Calculating the T-score for each pixel in real-time is more challenging than unmixing, as the processing involves several steps. The computationally most heavy operation is the calculation of the covariance matrix of the residuals, because it involves several matrix multiplications. But if the computational load is too extensive to be performed in the main processor, it can either be outsourced to a FPGA or the GPU.

Conclusion

Unmixing always results in component images no matter how accurate those results might be. It is up to the user to judge on the quality of the unmixed images without clear indications. The introduced T-score indicates regions for which the data is not unmixed correctly on basis of a single image.

Intraoperative fluorescence imaging is sensitive to various derangements such as ambient light, autofluorescence or tissue absorption in combination with scattering. In contrast, surgeons must rely on the unmixed fluorescence data to take medical decisions based on the data. Thus, the developed T-score may pave the way for video-rate intraoperative fluorescence imaging of multiple components.

Application specific research is needed to evaluate the most common derangements and the sensitivity of the T-score towards these effects.

7 SYSTEM OPTIMIZATION

So far, this thesis has been focusing on developing a system for next generation fluorescence guided surgery. First literature was reviewed in Chapter 2. Subsequently, design requirements were specified in Chapter 3 and a prototype system was realized in Chapter 4. When building the prototype, compromises were made to accommodate technical constrains. Chapter 5 revealed that the system fulfills the specified design requirements even with the technical constrains. However, this chapter aims on estimating how good a system could potentially be neglecting some of the technical constrains.

A noise model which allows to estimate the image noise based on a single image was derived in Chapter 6. This model is used here to optimize the system by minimizing the noise of the final fluorescence component images.

The system is optimized for specific scenarios and leads to an estimation on how much the system can be further improved. In this context, the following questions will be answered:

1. What is the ideal combination of dyes for the system? How well can the system unmix $2, \ldots, 6$ dyes in the best case?
2. For a given set of dyes, what is the ideal multiband filter? How many bands should the two complementary multiband filters have?

These questions are answered in Section Section 7.1 and Section 7.2. Similar optimization approaches with different parameters as employed in this section have been published in [167].

7.1 THE OPTIMAL DYE COMBINATION

Having the system build and tested as described in Chapter 4 and Chapter 5, the question arises what would be the ideal dye or combination of dyes for the system? This section will answer this question.

Optimization methods

To optimize the system, the performance of the system needs to be quantified in the so-called figure of merit. In this section, the overall SNR of the final unmixed images is maximized varying the emission center wavelengths for a fixed number of dyes as illustrated in Figure 7.3. Thus, the noise of unmixed fluorescent components for a given number of emitted photons needs to be expressed.

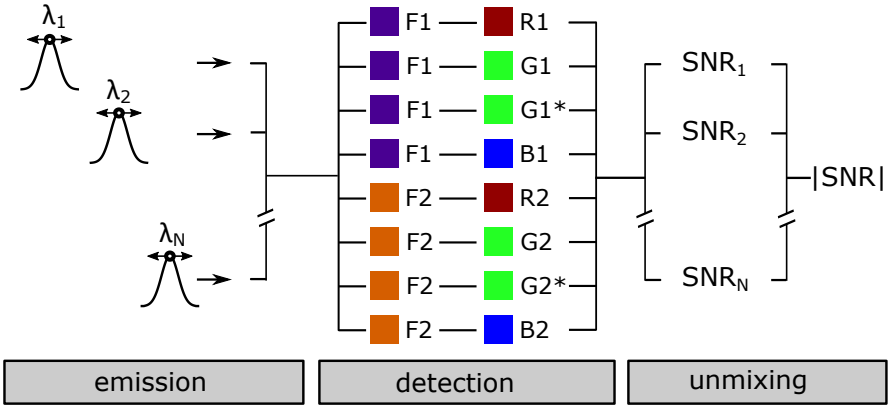

Figure 7.1: Schematic illustration of the numerical optimization flow: Fluorescent dyes f are parameterized as a Gaussian profile with the center wavelength λ_f as optimization parameter. Subsequently, the emission is mixed, split into two paths, filtered by the filters F1 and F2 and detected by the sensors S1 and S2 with a total of eight channels. The green channels are doubled to take care of the effect of the RGGB Bayer pattern on the sensor. The estimated signal to noise after unmixing is computed for each dye and an absolute SNR is calculated as figure of merit.

A detailed description of the mathematical formulation of mixing, unmixing, fitting of spectral signatures and noise theory can be found in Section A.1. An experimentally validated noise model of the system, which is reused here, is described in detail in Section 6.1.

Figure of merit

A set of fluorescent dyes $f = 1 \dots n_d$ each emits N_0 photons, which are all assumed to be imaged onto the sensor. On the sensor S, the number of photons $Y_f(c)$ is detected due to the spectral sensitivity

$$Y_f(c) = \eta(c, f) \cdot N_0 = \kappa(c, f) \cdot \eta_S(f) \cdot N_0 \tag{7.1}$$

Summing over the different fluorescent dye emissions and combining with Equation A.15 leads to the vectorial formulation

$$\boldsymbol{Y} = \boldsymbol{m} \cdot \underbrace{\boldsymbol{\eta}_S \cdot N_0}_{\nu} . \tag{7.2}$$

The number of photons which are detected by the system of a dye f is expressed as ν_f. All formulas here correspond are formulated for one location or intensity value. This means that the location index ξ is not written for all formulas here because the formulas need to be optimized for one intensity value only. The noise $\Delta \boldsymbol{X}^2$ of the unmixed component images $\boldsymbol{X}$ is given by the diagonal elements of

the covariance matrix $\mathbf{\Sigma}_X(\xi)$ according to equations Equation 6.1 to Equation 6.14 as

$$\Delta \boldsymbol{X}^2 = \operatorname{diag} \mathbf{\Sigma}_X = \operatorname{diag} \left[\boldsymbol{u} \cdot \mathbf{\Sigma}_Y \cdot \boldsymbol{u}^\mathsf{T} \right] \tag{7.3}$$

with

$$\Sigma_Y(c,c) = \sum_f m(c,f) \cdot X(f) + \sigma_0^2. \tag{7.4}$$

The signal to noise ratio SNR_f for a fluorescent dye f is defined by

$$SNR_f = \frac{X(f)}{\Delta X(f)}. \tag{7.5}$$

For the optimization the absolute signal to noise ratio is required. Here, the inverted root mean square is used to combine the individual SNR ratios as figure of merit:

$$|SNR| = \left(\frac{1}{n_f} \sum_f SNR_f^{-2} \right)^{-\frac{1}{2}} \tag{7.6}$$

The rms is inverted so that the absolute SNR becomes zero if any of the individual SNR values is zero. Without inversion, one single zero SNR value would still be okay for the overall SNR. However, all dyes must be unmixed well, so a single value with very bad SNR would not be acceptable. The root mean square was chosen over the normal average to favor solutions which are closer together. Thus, similar SNR values for the individual components are favored over some very high and some very low SNR values by this figure of merit.

Reporting SNR values can be rather complicated to understand as SNR values are not intuitive. Thus, the SNR values can be converted into an apparent photon number [130].

If Ξ_f Poisson distributed photons are detected, the statistical variance corresponds to the expectation value if no further sources of noise are present:

$$SNR = \frac{\Xi_f p}{\operatorname{std}[\Xi_f]} = \sqrt{\Xi_f}, \tag{7.7}$$

which can be written as

$$\Xi_f = SNR_f^2. \tag{7.8}$$

In this section, the SNR of individual dyes is reported as an apparent number of photons Ξ_f . Perfect detection of Ξ_f photons results in the same SNR than the real detection process.

In short, theoretically the number N_0 of photons for one dye f could be detected, but due to reduced quantum efficiency only $\nu_f = \eta_S(f) \cdot N_0$ photons are detected. Unmixing further decreases the SNR of the unmixed images as if only Ξ_f had been detected.

System parameterization

The fitness function of the optimization procedure maximizes the root mean square signal to noise ratio by varying the peak emission wavelengths for a fixed number of fluorescent dyes.

All fluorescent dye photon emission spectra are assumed to have a Gaussian emission profile with parameter $\sigma = 32\,\text{nm}$ for all dyes. The fluorescent dye model is described in Section 5.1.2. This corresponds approximately to the median standard deviation of the library of fluorescent dyes shown in Section A.2. The system is parameterized as described in Section 5.1.2.

The spectrum is sampled on a fixed finite grid of spectral intensity bins with equidistant spacing of 0.1 nm from 365 nm to 900 nm. The filter transmission and the sensor sensitivity are both re-sampled on the bin centers and the number of photons emitted by each dye into the detection system is assumed to be $N_0 = 10\,000$. This assumption is rather arbitrary but necessary. This can result in the detection on average of up to 100 photons per channel and per frame which is a realistic number.

In order to calculate the spectral signature of each dye for the given system the fraction of photons reaching the sensor is calculated.

Numerical implementation

The numerical calculations have been implemented in Matlab. For the scenario of two fluorescent dyes ($n_d = 2$), the entire parameter space of $\lambda_1 = 395\,\text{nm} \ldots 870\,\text{nm}$ and $\lambda_2 = 395\,\text{nm} \ldots 870\,\text{nm}$ has been evaluated in steps of 1 nm. The measures Ξ_1, Ξ_2 , and $|\Xi|$ are calculated for each combination of λ_1 and λ_2.

The MATLAB GlobalSearch algorithm with fmincon was used to find an optimal solution.

The boundaries for the fluorescent dye emission center wavelengths were set to be $395\,\text{nm} \leq \lambda_f \leq 870\,\text{nm}$. Additionally, the minimal distance between the center emission wavelength of two dyes is $\lambda_{f+1} - \lambda_f \geq 10nm$ for all fluorophores f to ensure a minimal spacing between two dyes.

Results

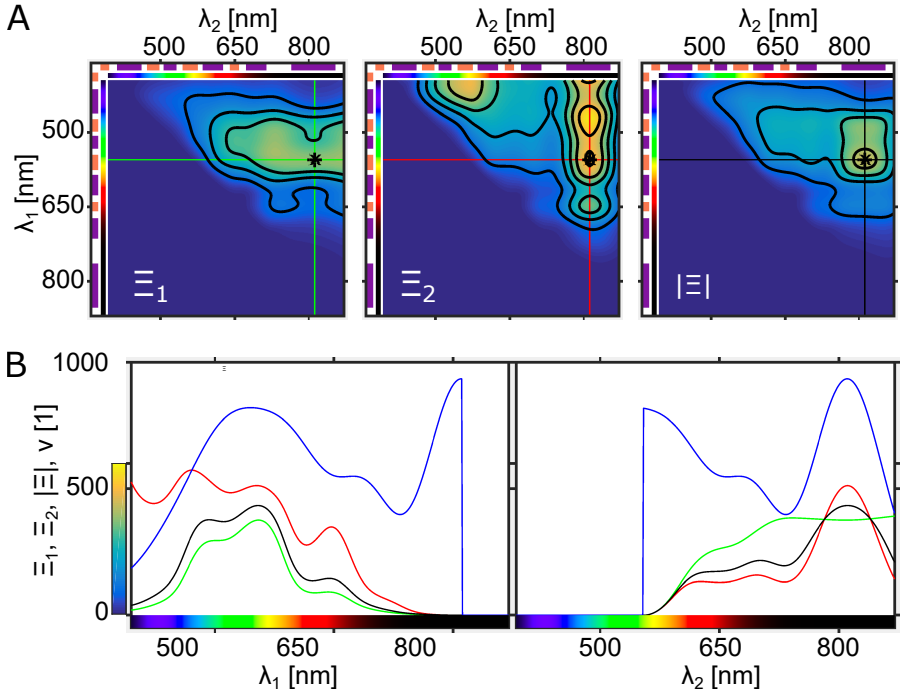

Figure 7.2: Numerical results for Ξ_1 , Ξ_2 , and $|\Xi|$ sampling the entire parameter space of λ_1 and λ_2. A) Ξ_1 , Ξ_2 , and $|\Xi|$ for $N_0 = 10000$ photons. The green, red and black lines mark the position line profiles. Contour lines at 100, 200, 300, 400 and 500 are plotted. B) Line profiles along λ_1 (left) and λ_2 (right) for Ξ_1 , Ξ_2 and $|\Xi|$ cross in the optimum of $|\Xi|$. ■ ν_1 profile on the left and ν_2 profile on the right indicate how many photons have been detected for the respective fluorescent dyes and the apparent number of photons ■ Ξ_1, ■ Ξ_2 and ■ $|\Xi|$. Due to the symmetry of the problem, $\lambda_1 \leq \lambda_2$ is fixed, which results in solutions for the upper right parts in A) and the cutoff in transmission efficiency in B).

Table 7.1: Optimization results to find the optimal combination of emission center wavelengths for Gaussian shaped dye emission spectra. Upper part reports the SNR as apparent photon numbers Ξ and detected photon numbers ν of potentially detectable 10000 photons. Lower part of the table lists the respective emission center wavelengths.

	RMS		DYE 1		DYE 2		DYE 3		DYE 4		DYE 5		DYE 6	
n_d	$\lvert SNR\rvert$	$\lvert\Xi\rvert$	Ξ_1	ν_1	Ξ_2	ν_2	Ξ_3	ν_3	Ξ_4	ν_4	Ξ_5	ν_5	Ξ_6	ν_6
2	21	434	376	818	513	935								
3	12	135	194	644	80	562	218	806						
4	8	66	44	425	129	820	49	553	100	684				
5	6	33	23	340	30	752	32	799	36	551	68	619		
6	4	14	12	311	12	652	12	818	11	768	21	549	38	552

	λ_1	λ_2	λ_3	λ_4	λ_5	λ_6
2	555 nm	811 nm				
3	483 nm	643 nm	835 nm			
4	447 nm	547 nm	649 nm	774 nm		
5	432 nm	505 nm	574 nm	651 nm	768 nm	
6	426 nm	484 nm	535 nm	588 nm	654 nm	762 nm

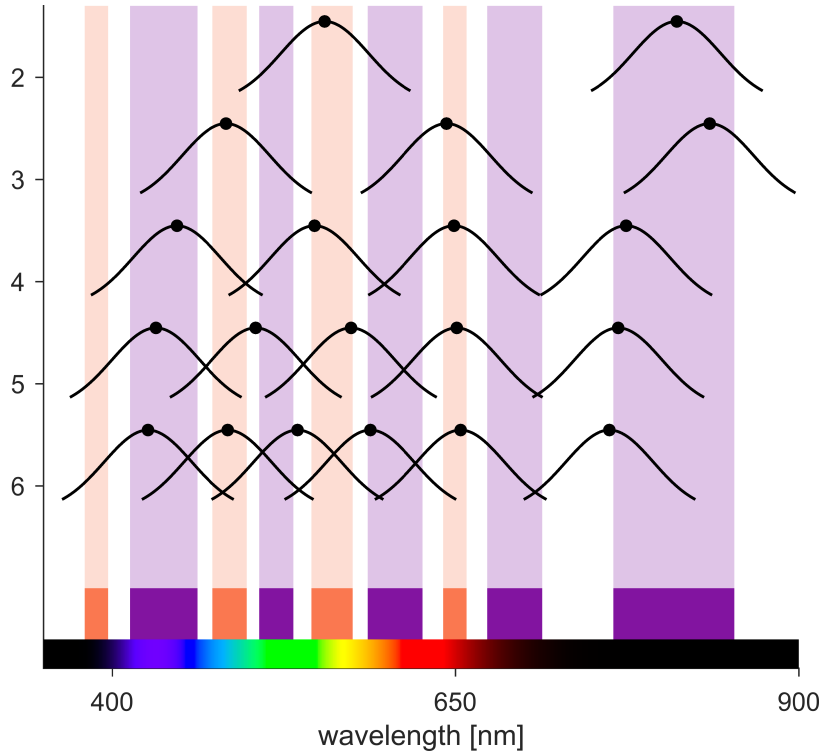

Figure 7.3: Optimal choice of emission center wavelengths for a scenario of $n_f = 2 \ldots 6$ dyes for the imaging system with Gaussian shaped emission spectra.

The numerical results for the evaluation of Ξ_1 , Ξ_2 and $|\Xi|$ for the entire parameter space are shown in Figure 7.2. The maximum $|\Xi|$ matches to the solution found by the optimization algorithm within the numerical limits. The results of the optimization algorithm are shown in detail in Table 7.1 and schematically illustrated in Figure 7.3.

The line profiles in Figure 7.2B illustrate that the figure of merit is continuous and smooth. As expected, the number of photons of the initially 10000 photons which are detected by the sensor range between around 200 and almost 1000, depending on the exact emission center wavelengths. The unmixing reduces the SNR further as if only between 350 and 550 photons would have been detected of the 10000 photons.

The $|\Xi|$ reduces dramatically when increasing the number of dyes. As a rule of thumb in this case, each additional dye reduces the $|\Xi|$ at least by a factor of two.

Discussion and conclusion

In case of $n_d = 2$, the results of the optimization algorithm match to the results of the sampled parameter space. The optimization certainly improved $|\Xi|$ for all $n_d = 2 \ldots 6$ compared to the initial starting

point, though a better solution might exist. This means that the algorithm may converge to a local minimum and not to the global minimum. The sampling intervals of λ_f have been chosen smaller than the width of the emission profiles (1 nm $\leq$ 32 nm). This ensures that no effects are lost in between the sampling points. The used noise model has been validated in Section 6.2.

The performance of the system can be seriously deteriorated if non optimal dye combinations are chosen (see Figure 7.2). Thus, it is essential to check if a combination of dyes is suitable for the system before going to experiments.

For a high number of dyes ($n_f = 4 \ldots 6$), the SNR is increasingly deteriorated by unmixing. Even the optimized scenarios do not show good SNR of the unmixed components. Neher *et al.* showed that it is beneficial for an imaging scenario if the number of detector channels exceeds the number of dyes by a few. This is not the case for $n_f = 4 \ldots 6$, thus increasing the number of channels by a different sensor design may help.

The mixing matrix was based only on the emission of the dyes which means that they are identically excited in both phases. However, in real applications, excitation varies in the two phases and usually adds separation power. This effect can dramatically improve the unmixing performance of the system. Thus, all conclusions drawn here can only apply for continuous excitation which is identical for both phases.

In future, a more complex simulation and improved numerical models may include also the excitation process and use excitation-emission-matrices instead of emission spectra only. This would give a more accurate estimate of how well the system performs for example with multiband excitation. Such a simulation would allow to additionally optimize the excitation bands and excitation power.

The simulation could also be improved replacing the Gaussian dye emission by a more realistic dye model which is for example also skewed and might allow translation to real dyes more easily.

Moreover, the number of photons emitted was set to $N_0 = 10000$ counts per dye. This quantity needs to be fixed and may influence the results. Thus, for other intensity combinations the optimal solutions may vary. Future work could be dedicated to find a figure of merit which is independent of N_0. If optimizing a specific scenario, different emission intensities for the different dyes can be chosen.

Tissue interactions like absorption or scattering can alter the spectral measurements and cause unmixing artifacts in the worst case. It would also be interesting to design a figure of merit favoring robust solutions for spectral artifacts.

All in all, the simulation shows that the concept suits well it's intended use to simultaneously image multiple dyes for fluorescence guided surgery.

7.2 FINDING THE OPTIMAL FILTER CONFIGURATION

For a real imaging scenario with a given dye combination it is of high interest to know what would be the best possible filter combination for the given scenario. The results show how much improvement in imaging SNR can be obtained by replacing the current filter pair by the best possible one. This is quite relevant, because filter companies can produce custom multiband filter sets with specified filter band combinations on demand.

Methods

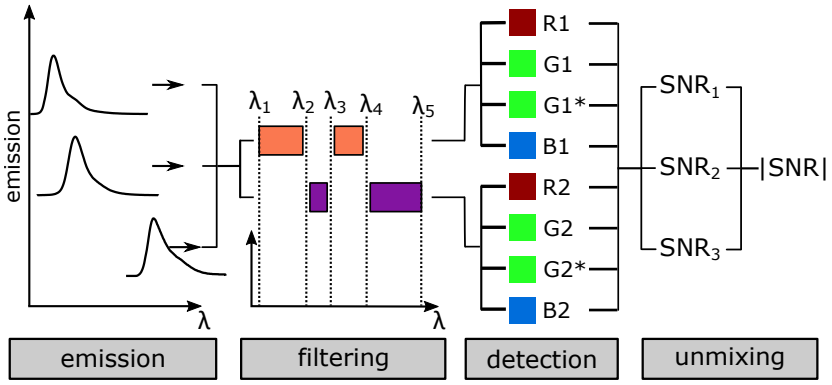

Figure 7.4: Simulation schematic to optimize the multiband structure of the emission filters for the dyes Atto532, Atto565 and Atto610. Each dye emits 10 000 photons during the acquisition of one image on one single pixel. The photons are spectrally distributed according to the respective emission spectrum. All emitted photons are added up in one single beam which is subsequently split by a neutral density beam splitter into two separate paths for the two different sensors. The photons of each path are filtered with one of the complementary multiband filters. The band structure of the filters is parameterized by the wavelengths $\lambda_1 \dots \lambda_{n_b+1}$ which are optimized here. Two identical color sensors detect the photons of the three dyes. Subsequent unmixing of the multispectral signal allows to determine the SNR of the three dyes Atto532, Atto565 and Atto610 and the overall $|SNR|$ which is used as figure of merit for the optimization algorithm.

Figure 7.4 illustrates numerical implementation schematically. The optimization implemented almost identically as in Section 7.1. Here, only the differences are mentioned.

The Gaussian emission spectra are replaced by real photon emission spectra of the dyes Atto532, Atto565 and Atto610. Details on the spectral processing of the dye emissions are specified in Section 5.1.2.

The transmission spectrum of the ideal multiband filter pair is parameterized for the optimization. The bands are assumed to have per-

fect transmission or perfect blocking characteristics. The edge wavelengths between the bands can be varied with fixed number of bands n_b. The multiband filter pairs always need to have a spectral gap in between two neighboring bands which is fixed to $\Delta\lambda = 0.5\,\text{nm}$. The specified edge wavelengths λ_b are the center of the gap, where both filters do not transmit. As an exception, the first and the last edge have coincided with the respective wavelength, because there is no other band to follow. In blocking wavelength regions, the filter has zero transmission, in passing wavelength regions the filters are expected to have complete transmission of 1. If the filter edge falls within a bin and not on the bin edge, the effective transmission of the bin is calculated as the average transmission between 0 and 1 over the respective range. The minimal distance between two subsequent band edges is $\lambda_{b+1} - \lambda_b \geq 3\,\text{nm}$. The bands are restricted to be all between 500 nm and 800 nm.

As starting point, the edge wavelengths are linearly distributed over the available range, leaving space on the outer edges.

Results

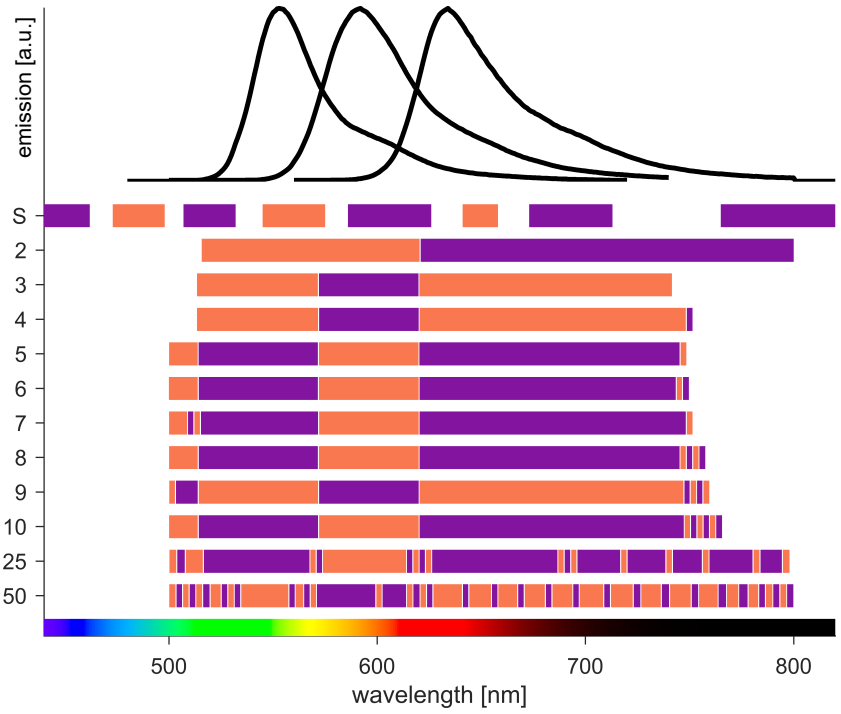

Figure 7.5: Visualization of the optimal filter band structures depending on the number of bands n_b after unmixing based on emission only. The bandpass structure of the multiband filter pair used for the system is illustrated as S. The top part illustrates the emission spectra of the three dyes Atto532, Atto5565 and Atto610 with strong spectral overlap.

Table 7.2: Optimization results of the filter bandpass structure with the fluorescent dyes Atto532, Atto565 and Atto610. The imaging scenario was optimized for each number of filter bands n_b separately for best $|SNR|$ and the respective $|\Xi|$. Additionally, the apparent number of photons of the initial starting filter configuration $|\Xi_0|$ is reported. For each dye, the apparent photon number Ξ and the number of detected photons ν as well as the exit reason for optimization algorithm is listed in the table. Exit reasons for the algorithm: 0: number of iterations or number of function evaluations exceeded standard setting; 1: gradient is smaller than standard tolerance; 2: change in band edge wavelength λ_b was small than the standard step tolerance.

	RMS			Atto532		Atto565		Atto610		
n_b	$\|SNR\|$	$\|\Xi\|$	$\|\Xi_0\|$	Ξ	ν	Ξ	ν	Ξ	ν	EXIT
2	9.7	93	0.4	124	1115	52	980	208	835	1
3	13.9	193	17.7	192	1108	212	961	177	786	1
4	13.9	192	6.0	191	1108	211	965	178	798	1
5	13.9	192	63.6	191	1109	212	965	177	795	1
6	13.9	192	95.2	191	1109	212	965	178	795	1
7	13.9	192	34.3	190	1109	212	966	178	798	1
8	13.9	192	20.7	190	1109	211	968	178	803	2
9	13.9	192	15.2	189	1109	211	968	178	805	1
10	13.8	192	7.1	189	1109	211	970	178	810	1
25	13.3	176	1.1	185	1090	193	952	154	804	0
50	11.3	128	1.1	149	1050	125	928	115	774	0

The optimization results are listed in Table 7.2 and the optimal bandpass configurations are visualized in Figure 7.5. The $|SNR|$ is best for 3 bands, which corresponds to the number of dyes. Most optimal filters cover the majority of the wavelength region, but may block all light on the edges where hardly any emission is present. The solutions between $n_b = 3$ and $n_b = 10$ perform almost equally well with a performance variation below 1%. These band structures are very similar at the region of high emission intensity and will thus result in very similar spectral signatures. The transition edges are aligned with the crossing of the emission profiles. The additional bands are scattered on the edges and seem to be obsolete.

For $n_b = 25$ bands, the rms apparent number of photons $|\Xi|$ is 176 and thus quite close to the best result with 193 photons for 3 bands. Also, long bands can be found at the emission peaks of the dyes. For $n_b = 50$ bands, a rms apparent number of 128 photons is detected.

The performance $|\Xi_0|$ of the starting bandstructure (bands equally distributed) ranges from 0.4 ($n_b = 2$) up to 95.2 ($n_b = 6$). Here, the optimization algorithm improves the SNR of the imaging scenario in all cases at least by a factor of 2 and up to over 200 times for $n_b = 2$.

Discussion

The results show that a band structure which is aligned with the emission spectra will result in an optimal overall SNR of the unmixed images. In effect, one band of the multiband pair is dedicated mainly to one fluorophore. The edges of the bands are at the wavelengths at which the different emission spectra cross each other. This corresponds to an intuitive choice, which would have been made by a scientist who is familiar with the field.

For all number of bands n_b, the optimal solution found by the algorithm improves the unmixing compared to the starting configuration, in which the bands were equally distributed. The performance of the starting configuration appears to be random.

The number of detected photons is almost equally good for all filter choices which means that the changes in SNR are due to modification of the spectral separation in channel space. The filter configurations with many bands (25 and 50) have slightly reduced detection efficiencies compared to the other filter configurations. This is expected as the configuration with $n_b = 50$ has 49 transition gaps between adjacent bands and the configuration with $n_b = 3$ has only 2 gaps where no photons are transmitted. However, this effect plays a minor role as the gaps are chosen to be unrealistically small here.

The unmixing scenario is very challenging due to the spectral overlap of the emission spectra. Consequently, an apparent photon number of around 200 it is reasonable. Though, the algorithm may have found a local optimum only instead of not the global optimum. Also, other solutions which perform close to optimal may exist.

However, the narrow band structures of the scenarios with $n_b = 25$ and $n_b = 50$ somehow reduces the spectral separation between the dyes. This case was already discussed when designing the system in Section 4.2.2. Though, it is very likely that the optimization could not successfully find the global optimum in for these scenarios. Intuitively a scenario with the three bands aligned with the dyes and all other bands squeezed into the edges should have superior performance. The case demonstrates very well that a higher number of band is not always beneficial and that the band structure needs to be designed for each set of dyes.

Relevant aspects regarding sampling, the chosen figure of merit and the used optimization algorithm apply as discussed in Section 7.1.

Further research is required to fully parameterize the imaging scenario and the system. The scenario which is optimized here does not consider the fluorescence excitation. This corresponds to equal excitation during both phases for all dyes. In general, the system can gain separation power between dyes due tailored excitation in each phase.

Overall, this optimization approach has shown that it is important to choose the right filter band structure depending on the used dyes.

8

DISCUSSION, OUTLOOK AND CONCLUSION

This chapter will finalize the thesis by putting the developed imaging method and prototype in perspective with the intended clinical use.

Fluorescence guided surgery supports the surgeon by highlighting anatomical, functional or pathological structures which would otherwise be invisible. Labeling cancer tissue with a certain fluorescent agent while concurrently labeling nerve tissue with a different agent will help surgeons to achieve complete cancer removal while preserving healthy tissue. For this purpose, the utilized imaging device is required to record a video stream of multispectral fluorescence and high-quality color images simultaneously which still poses a challenge to instrumentation.

After a short introduction to the topic in Chapter 1, the state-of-the-art in fluorescence guided surgery and the associated instrumentation is analyzed in Chapter 2. Subsequently, the requirements for such an imaging device are derived in Chapter 3 and a suitable imaging method is developed in Chapter 4. This method is based on a combination of spectral and temporal multiplexing to record multispectral fluorescence and high-quality reflectance images over the entire VIS/NIR in only two alternating phases. Accordingly, the method can run at video-rate – therefore enhancing the color video stream with diagnostic fluorescence information. A prototype system is developed as part of this thesis and systematically investigated in Chapter 5 with experiments and numerical simulations.

One generic issue, common to any multispectral fluorescence imaging devices, is addressed in the thesis: many artifacts in the multispectral raw data lead to altered diagnostic information after unmixing, without the user being aware of this phenomenon. A novel indicator, called T-score, is developed in Chapter 6. It provides a self-consistency check for the unmixed images by relating the unmixing residuals with the expected noise.

The noise model is used to optimize the system performance in Chapter 7 to provide best signal to noise ratio for the unmixed fluorescent dye images. First, the fluorescent dye is parameterized, replacing the emission spectra with Gaussian shaped emission spectra. With this, the optimal combination of dyes is determined and it is shown how well the optimal combinations of $2, 3, \ldots, 6$ dyes performs. The method provides sufficient insight to selecting suitable combinations of dyes for the system. The results also show that more different dyes cause more image noise after unmixing. Thus, imaging more than 3 dyes results in increasingly noisy unmixed images.

As a remedy, additional detection channels can decrease the spectral mixing and thus improve the result. Subsequently, the multiband filter pair of the imaging system is parameterized to vary the spectral design of the bands. With this model, the system is optimized for the detection of the dyes Atto532, Atto565 and Atto610. In this scenario, the optimal bandpass structure aligns with the fluorescence emission of the dyes mentioned above. The edges of the bandpass filter align with the crossing points of the dye emission spectra. In general, the two optimization example scenarios demonstrate the potential of this technique. Not only is a best-case scenario being demonstrated but, more importantly, the amount of improvement which can be expected with this best-case scenario is shown.

In this last chapter, it is firstly discussed to what degree the developed imaging method and the prototype system meet the design requirements. Subsequently, limitations of the system regarding efficiency, unmixing performance, surgical illumination and clinical aspects are discussed. Furthermore, a section of this chapter is dedicated to presenting a vision of an ideal device and discussing the technical limitations which will hinder the realization of such a device. The last part of the discussion puts the system in perspective with the relevant academic and research work in this field.

Next, an outlook points out the steps towards clinical translation and improvements of technical aspects. Finally, conclusions about the major achievements of this work are drawn.

8.1 DESIGN REQUIREMENTS AND SYSTEM PERFORMANCE

This section discusses which of the design requirements have been realized and shows possible directions for future improvements. Table 8.1 compares design requirements with the system performance regarding the aspects of color imaging, fluorescence imaging, timing, optical assembly and clinical aspects. The table references the relevant sections of the thesis.

Color

Recorded reflectance images need to be processed to provide a good color reproduction. Here, colors are corrected with a linear approach to match the color perception of the human eye under sunlight as closely as possible. The system records color information in 6 channels whose combined sensitivity is supposed to correspond to the sensitivity of the human eye. Color differences are quantified using the CIEDE2000 norm which reflects perceptual color differences well. This approach has reached adequate performance levels in numerical simulations for various illumination scenarios (CIE D65, CIE A and white LED illumination). Even flexible multiband illumination seems

to be acceptable. For most colors, the differences are only slightly perceivable. The color imaging performance might be further improved using more complex correction algorithms. Alternative sensor sensitivity curves may additionally improve the color image quality. Experiments using clinical relevant colors are necessary to validate the numerical results. Having color information provided by six different channels may, in future, allow advanced processing to enhance contrast between certain tissue types.

Fluorescence

The system is specified to detect dyes over the entire visible and near infrared range and to successfully unmix three different fluorescent dyes at medically relevant concentrations. Simulations show that practically any fluorescent dye emitting in the VIS/NIR can be detected. Phantom experiments with exemplary sets of three different dyes show good unmixing performance levels. The performance can be further improved by optimizing the selection of filter bands for the system.

A metric, called T-score, has been developed and successfully tested for the ability to indicate unmixing artifacts. It combines unmixing residuals with a noise model of the system to allow calculation of the T-score per frame and per pixel based on a single image. For example, the metric has shown to be very sensitive to detect additional fluorescent dyes which were not regarded for unmixing at relevant concentrations.

All in all, the fluorescence imaging capabilities match the requirements successfully.

Timing

For good human-machine interaction, fluorescence guided surgery systems must perform at high framerates and with short delay times. In other words, it must run in *real-time*.

The selected imaging method requires only two phases to record fluorescence and reflectance images over the VIS/NIR range. In terms of framerate, the chosen method thereby fulfills the design requirements. The delay between the occurrence of an event and the appearance on the screen is only restricted by the recording time of two subsequent frames. Thus, potential delays may be caused by computational processing time. Realizing a system which fulfills the timing requirements calls for extensive efforts in software design and interfacing of high data rates up to 2 GB/s. To ensure that the design requirements are met, it is advisable to implement the processing on FPGAs. Therefore, the prototype system was not tested regarding timing as this aspect was specifically excluded from this work.

Optics

The optical prototype setup exceeds the requirements in terms of FOV, digital resolution and spatial resolution. In future, a costly custom design may further improve the optical performance. Section 8.2.1 discusses in detail how the efficiency of the setup could be further optimized.

Clinical

All in all, the setup can in future be translated to a clinical environment as the design requirements are fulfilled.

The working distance of 18 cm is acceptable for surgeons. The OR room lights can be adapted to the system illumination. However, the flickering at current framerates still poses an issue. Moving towards high frequencies with ultrafast acquisition would eliminate this difficulty. The used illumination intensity is well below clinical limits and can thus even be increased to further improve fluorescence detection.

In future, the system can be miniaturized aiming at implementations as compact as chip-on-the-tip endoscopes.

As the design requirements regarding clinical usability are met, the translation process including certification, clinical experiments and validation, can be initiated.

Table 8.1: Summary of design requirements and system performance.

DESIGN REQUIREMENT	SYSTEM PERFORMANCE
COLOR	
• correction of color images so that displayed colors match the object colors as close as possible as seen under CIE D65 illumination with the human eye. Color deviations should only be slightly perceivable which corresponds to $\overline{\Delta E_{00}} \leq 1.5$	• linear color correction algorithm results in sufficiently good color reproduction for CIE D65 illumination, CIE A illumination and white LED illumination with only slightly perceivable color differences; variable intensity multiband illumination scenarios produce good color correction with $\overline{\Delta E_{00}} \leq 1.5$ for most of the tested scenarios (see Section 5.2)
FLUORESCENCE	
• detect any dye with $400\,\text{nm} \geq \lambda_{em} \geq 900\,\text{nm}$	• numerical calculation of the system detection efficiency for an ideal Gaussian emission profile in Section 5.1.2 and for real dyes in Section A.2

Table 8.1: (continuation)

DESIGN REQUIREMENT	SYSTEM PERFORMANCE
	• experimental detection of Atto488, Atto655 and Atto740 at 5 µM (see Section 5.3.2) and of Atto532, Atto565 and Atto610 at 2.5 µM (see Section 5.3.1)
• detect and successfully unmix three dyes with concentrations of 1 µM to 10 µM	• experimental images of phantoms containing pure dyes and mixtures of Atto532, Atto565 and Atto610 show good unmixing performance in Section 5.3.1 • unmixing amplifies imaging noise according to Section 6.1
• unmixing artifact diagnostics on basis of a single image for live video rate analysis	• developed T-score diagnostics put the unmixing residuals in relation with the expected noise and provide real-time unmixing diagnostics for each pixel on basis of each image itself, details in Section 6.2 and Section 6.3
TIMING	
• recording images minimally at 30 fps, best at 60 fps with delays below 160 ms, best less than 60 ms	• framerate and delays were not investigated with for prototype as these aspects depend on a developed software solution which is not part of this thesis. However, the imaging method and the selected hardware (light sources and cameras) are generally capable to fulfill the requirements. Future technology promises to exceed these requirements (see Section 8.3)
OPTICS	
• $FOV \geq 5.0\,\text{cm} \times 5.0\,\text{cm}$ for each sensor	• requirements are fulfilled with $FOV_{S1} \approx (5.9 \pm 1.0)\,\text{cm} \times (5.9 \pm 1.0)\,\text{cm}$, $FOV_{S2} \approx (5.8 \pm 1.0)\,\text{cm} \times (5.9 \pm 1.0)\,\text{cm}$; see Section 5.4.1
• digital resolution at least 1.0 MP	• requirements are exceeded with a resolution of (1.33 ± 0.05) MP for sensor S1 and (1.30 ± 0.05) MP for sensor S2 as discussed in Section 5.4.1

Table 8.1: (continuation)

DESIGN REQUIREMENT	SYSTEM PERFORMANCE
• spatial resolution at least 1.15 lp/mm at MTF = 0.5 for each sensor	• requirements exceeded with measured spatial resolution ranging between 2.0 lp/mm and 3.3 lp/mm depending on the sensor, location and meridional or sagittal direction (see Section 5.4.2)
CLINICAL ASPECTS	
• free working distance between at minimally 10 cm and 30 cm	• free working distance of the prototype is 18.5 cm, see Section 5.4.3
• concept must allow for miniaturization aiming at chip-on-the-tip endoscopes	• miniaturization requires to modify the sensors and optical setup, but the method is suitable
• flexible multiband illumination light source, power adjustable per band, total intensity must not exceed maximum permissible irradiant of $\Phi_{max} = 2000$ mW cm^{-2}	• multi-LED light source provides an adjustable, filtered multiband illumination which can be triggered and the intensity can be adjusted; estimated maximum irradiant of $\Phi_{max} = 400$ mW cm^{-2} is well below the permissible limit (see Section 4.2.5); power measurements suggest even lower irradiant intensities [166]
• concept must allow to be combined with surgical room lights	• currently possible only with perceivable flickering, future developments for sensors with superfast acquisition promise seamless integration with surgical illumination concepts, for details see Section 8.3

8.2 LIMITATIONS AND POSSIBLE IMPROVEMENTS

It is clear that any prototype system can be further improved as technical choices usually come with a set of limitations. This section discusses the potential for future improvements of the method and the prototype system.

First, the potential for an efficiency improvement is discussed. Subsequently, the limitations of unmixing are debated, followed by a de-

tailed analysis of the impact of surgical illumination. Finally, limitations of clinical usability aspects are examined.

8.2.1 *System efficiency*

The prototype setup was designed to detect multiple fluorescent dyes and reflectance color images. Thus, the focus of this work is on fast multispectral image acquisition and not on detection of the very lowest concentrations as specified in Section 3.1.1. Compromises regarding sensitivity were made on purpose. Therefore, the potential of different endeavors to improve efficiency of the prototype system is summarized in Table 8.2.

The microfilter Bayer pattern on the sensor detects approximately half of the light over the entire spectral detection range that a monochrome sensor would detect. This restriction is directly linked to the need for color sensors. In future, color sensors with stacked detection channels like the Foveon X3 sensor [207] may provide a higher detection efficiency.

Ideally, the sensor can detect photons on any pixel at all times. Unfortunately, the selected sensor CIS2521 causes a fixed dead time during the readout process. This puts a high penalty on higher framerates. Between 20 fps and 40 fps half of the available time is used to read out the sensor (readout time depends on digital resolution). Latest sensor technology such as the one used for example for the Sony IMX265, which was not yet available when realizing the prototype, supports a global shutter without significant dead time for the sensor readout. This sensor outperforms the sensors considered in this work as shown in Figure 4.15. The current rapid progress in sensor technology will most certainly further improve future systems. All in all, the developed concept will benefit from future developments of advanced sensors.

The illumination intensity can be increased by a factor $10\times - 100\times$ before reaching the maximum exposure limits for human tissue. The simplest but not economically feasible solution would be to replicate the light sources as often as needed. LED lights with higher output power or with angularly invariant excitation filters could simplify the illumination and allow high power illumination.

The optical photon-collection efficiency of the system is low compared to state-of-the-art objective lenses with higher numerical aperture as shown in Section 5.4.4. However, these objective lenses do not allow access to the imaging path in infinity corrected space and thus do not allow best filter placement. Additionally, such fast imaging lenses require focusing the image on each sensor individually. Though, a comparison shows that a customized development may improve the detection efficiency by a factor $10\times$ – $30\times$. The developed optical system should allow placing the filters in the optical

path or having the filter directly deposited on the surface of one of the lenses.

A 50:50 beam splitting cube was used in the setup due to its availability as a commercial standard part. Exchanging the beam splitter cube with a specially fabricated optically flat dichroic beam splitter plate to ensure good imaging quality can in principle double the detection efficiency in a final clinical system.

If all the improvements in efficiency are successful, the sensitivity of the system could be improved by a factor as high as 60 000 combining all the discussed effects. This promises sensitivity in the pM range for modern dyes with the same image quality as the phantom images in Section 5.3. The sensitivity would then even be able to compete with state-of-the-art clinical imaging systems which do not offer to image multiple dyes over the VIS/NIR range simultaneously with color images [74].

Table 8.2: Summary of estimated system efficiency improvements and reference to the part of this work where the aspect is discussed in detail.

ELEMENT	FACTOR	REFERENCE
Bayer pattern	2×	Section 3.2.5, Section 4.1
sensor readout	2 × −5×	Section 4.2.1, Table 4.1, Figure 4.15
illumination intensity	10 × −100×	Section 4.2.5
optical photon collection	10 × −30×	Section 5.4.4
optical beam splitter	2×	Section 4.2.3

8.2.2 *Unmixing performance*

In the recorded multispectral raw data, the different components are recorded in a mixed fashion. Unmixing the fluorescence images allows separating different fluorescent components but also comes with its limitations.

The major disadvantage of unmixing is that it can amplify image noise in the final images and noise can also be transferred between different channels. This effect increases if the spectral signatures of the dyes are close. Therefore, it is essential to assess whether the dyes used in a scenario can be unmixed well. For the scenarios tested here, the system was able to unmix all the tested fluorescent dyes at clinically relevant concentrations. As a rule of thumb, the system performed reasonable if the different dye emissions fell into different bands of the multiband filter. It has been designed and been successfully tested to differentiate different fluorescent dyes and successfully

unmixed mixtures of Atto532, Atto565 and Atto610 whose emission maximums fall within less than 100 nm.

Artifacts in the raw data resulting from rapid object movement or due to tissue absorption will cause spectral artifacts in the component images. In this thesis, the novel T-score metric was introduced to indicate unmixing artifacts.

The prototype system detects fluorescence images in 6 spectral channels and thus theoretically up to 6 different fluorescent dyes can be unmixed. In practice, it is nevertheless favorable to use a smaller number of dyes than available channels. Any additional dye typically increases the amount of spectral mixing and therefore causes an additional amplification of noise in unmixing. Moreover, to be able to compute the T-score, the number of detection channels needs to be higher than the number of components (dyes).

To further optimize the unmixing performance, the exact design of the complementary multiband filter pair can be optimized for a specific scenario. Additional color channels besides the conventional RGB pixels could be added to the sensors. The spectral sensitivity curve of these pixels could be optimized for better dye distinction. For very challenging unmixing scenarios, additional phases can be introduced to separate dyes by excitation multiplexing. However, each additional phase reduces the photon yield during other phases as the integration times need to be shortened.

In brief, unmixing multiple dyes is a very delicate procedure which may amplify noise and introduce artifacts. Noise amplification can be controlled by the spectral design of the system. Unmixing artifacts cannot be avoided, but can be indicated using the T-score.

8.2.3 *Flickering and ambient light*

For the prototype presented in this work, images could only be recorded with up to maximally 100 fps. High framerates lead to shorter integration time because the cameras need a higher fraction of the available time for the sensor readout.

As a result, framerates between 10 fps and 50 fps are chosen for experiments with the prototype system to allow longer fluorescence integration times. Undoubtedly, the flickering of the illumination at these framerates is perceived as very disruptive. In conclusion, an openly operated clinical system requires higher framerates of at least 100 fps. Nevertheless, fast movements of the surgeon still appear disturbing and call for even higher framerates. Recent developments in the field of CMOS sensor technology combine high-resolution, high dynamic range, fast global shutter sensor readout at high framerates and powerful image processing on a FPGA close to the sensor. Therefore, future developments promise a technical solution to this issue and will make the method even more attractive.

Ambient light, which is shined onto the object or directly enters the imaging system will result in artifacts. As a matter of fact, fluorescent light is usually at least 3 orders of magnitude weaker than the ambient light. Thus, relatively weak ambient light can bias the weak fluorescent image even though it does not interfere with the color image.

8.2.4 *Clinical usability*

So far, the system has been tested in technical experiments with fluorescent phantoms containing a scatterer. However, the effect of light absorption has not been investigated in this work. Tissue absorption is wavelength dependent and may therefore change the spectrum of the excitation light and of the emitted fluorescence light. In a first step, the effect of the most common absorbers in the human body on a specific unmixing scenario need to be schematically investigated in phantom experiments. Subsequently, it is desirable to find an algorithm which can unmix the used dyes independent of the tissue absorption and minimize artifacts. Alternatively, the knowledge gained from the phantom experiments can be used to optimize the spectral design for robust unmixing in the presence of absorption. In a next step, the capacity of the system to reliably image the used dyes and the impact of perturbations both need to be tested in preclinical experiments to generate conditions as close as possible to the clinical scenario. Finally, clinical experiments are required to analyze the medical benefits of the imaging scenario and the system.

The prototype system is designed for technical laboratory experiments and initial preclinical experiments. It is evident that the prototype system does not yet fulfill the requirements for clinical use. For instance, the design does not fulfill sterility requirements such as smooth edges of the casing to prevent damage to the required sterile drapes. Yet another issue to be solved is the temperature stabilization of the used sensors. In case of cooling tubes, any leakage of cooling liquid to the surgical field must be prevented. Alternative air cooling with a fan inside a sterile drape is also problematic.

In addition, current surgical lights are not designed to be triggered or spectrally filtered. While spectral filtering remains an unsolved issue, triggering of modern surgical LED lights is technically feasible. Current neurosurgical systems for imaging of PPIX do not harmonize fluorescence detection with the ambient room illumination. Consequently, their usability is seriously impeded.

An easy and intuitive user concept needs to be developed to integrate well with the surgical work-flow. An additional key aspect is to intuitively combine the fluorescence information with the color image video stream. Elliott *et al.* [170] have compared different methods to overlay the information. However, more conclusive studies are

required to fuse the diagnostic fluorescence information with color images. The key question is how to intuitively and reliably display the fluorescence information while maintaining all the relevant color image information.

To summarize, a series of efforts related to product design are required for full clinical compatibility of the prototype system.

8.3 IDEAL DEVICE AND TECHNICAL LIMITATIONS

When designing the prototype system which is presented and evaluated in this work, compromises due to technical constrains were made to match the design requirements. This chapter will ignore all constrains and discuss how an ideal system using the described method would look like and how the ideal sensors, filters, optics and lights would influence the system performance.

Timing

Frame rates higher than 60 fps will most likely not further improve the surgical outcome as described in detail in Section 3.1.6. However, in open surgery the surgical room lights need to be triggered at the same frequency than the sensor. Flickering lights at 60 Hz will be perceived as very disturbing. Higher framerates can eliminate this effect. Additionally, higher frequencies reduce artifacts caused by object movement.

Therefore, an ideal sensor should acquire images at very high framerates, for example at 1200 fps or even higher. At sensor acquisition of 1200 fps, a complete multispectral image data set is acquired at 600 fps, but the video stream only needs to be presented to the surgeon at 60 fps. So, a moving average filter will smooth the image information of 10 subsequent images. The time difference between the acquisition of the two sensors is then 10% of the time, which is used for the total acquisition of the combined image presented to the surgeon. Movement artifacts will thus be reduced and the perceived flickering will vanish.

The moving average filter will maintain the shot noise (which is the dominating source of noise in this work) at the same level as if acquiring the image for a longer time, because in total the same number of photons is collected. However, other sources of noise (whose contributions were minor in this work), need to be reconsidered. Besides, applying a moving standard deviation filter can replace the model based noise estimation required to calculate the T-score by an actual measurement.

If the signal to noise ratio of the video stream is not sufficient, it can be digitally improved by increasing the number of images of the moving average filter without changing sensor readout frequencies.

Recent sensor development has enabled image acquisition at 960 fps for consumer products, but only for a very short time [208, 209]. These developments show that the required feature seems to be technically feasible in future. The filters can be implemented within the camera electronics and thus the data stream between camera and computer can even be reduced.

Sensor

The used RGB Bayer pattern has shown two major limitations: it reduces the detection efficiency by more than 50% compared to monochrome silicon sensors and causes unmixing artifacts on strong intensity variations of the object.

Thus, an ideal sensor may exhibit a pixel structure in which the detection elements for the individual channels (like RGB) are stacked. In this way, each pixel detects all the sensor channels and no demosaicing is required. If each channel only absorbs the photons to be detected and transmits the other photons to the next layer detecting a specific channel, the efficiency could in theory be up to 100%. Also, more than three channels could be realized per pixel. To ensure high-quality color imaging, it must be possible to express the spectral channel sensitivities as a linear transformation of the color matching functions $\overline{x}$, $\overline{y}$ and $\overline{z}$. One appealing example would be to have three channels for the color detection and additional channels with sensitivity in the IR region.

Extensive research has been conducted in this field of sensor development. One example of a commercially available color sensor using three stacked channels is the Foveon X3 [207]. Sensors with a higher number of channels have been proposed and prototypes have been realized. A summary can be found in a review by Hagen *et al.* [72].

Sensors with stacked channels promise higher sensitivity and no artifacts compared to micro-structured filters, but they do not yet play a significant role in the color sensor market. Though, the system could benefit greatly from such sensors.

Filter

Increasing the number of filter bands arbitrarily does not result in an improved detection as demonstrated with numerical optimization in Chapter 7. In contrast, the information acquired in the two phases will become more and more identical resulting in worse spectral separation between dyes compared to filters with fewer bands.

The other extreme would be to implement only one or two transmission bands per filter. In that case, the distinction between fluorophores is mainly based on the smooth color sensitivity curves. This would not result in ideal separation.

In practice, separation between dyes works best if the bandwidths correspond to the width of the excitation spectrum, the emission spectrum and the Stokes shift. Optimization of an example scenario showed best unmixing performance if the number of bands matches the number of dyes (excitation was neglected).

The most critical characteristic of the multiband filters is the angular dependence of the spectral transmission profile. To avoid leakage of excitation light into the fluorescence detection, gaps are required between adjacent bands. Though, the gaps reduce the detection efficiency.

All in all, an ideal filter would show strong blocking bands of 6 orders of magnitude, steep transitions between the bands and show no angular dependence. Such filters would simplify the optical setup dramatically and allow the use of high aperture imaging optics and thus high transmission angles. This would simplify the filter design and allow the design of a more compact and miniaturized system. Angular invariance of the excitation filters makes illumination design without a collimated path possible and thus facilitates more simple and compact illumination. Ultimately, this allows to increase the LED surface and thus the illumination intensity.

Most importantly, the band structure of the filters should best be chosen for optimal separation of the fluorescent dyes relevant for the application.

Optics

The optical lens assembly is supposed to be as compact as possible, while maintaining high optical performance. If the setup is equipped with a color sensor relying on a Bayer pattern, the PSF should not be smaller than the pitch between pixels. Optical smoothing reduces interpolation artifacts but limits the optical performance. For best filter performance, the optical concept should allow to place the beam splitter and filter in an infinity corrected optical path.

Commercially available solutions with high apertures and an infinity corrected path exist in the field of microscopy aiming at high magnification and close object distance. Macroscopic objectives which fulfill the required magnification and working distance do not offer an infinity corrected imaging space for filter placement. A custom design promises a good compromise within theoretical limitations.

Light sources

The ideal light source intensity would be freely scalable for excitation at maximum permissible radiation limits. Additionally, is should exhibit the spectral characteristics matching the emission band structure, therefore making excitation filters obsolete. The spatial power

distribution on the object must be identical for both phases to allow spatially invariant unmixing. To minimize specular reflections of wet tissue, the illumination should be diffuse.

The selected light sources are suitable for the application but do not offer enough power to fully exploit the maximum tolerable power limits for tissue. Also, they require bandpass filters to avoid leakage into the fluorescence detection bands. All lights are unified in one single fiber to make the illumination during different phases as equal as possible and enable spatially invariant unmixing.

8.4 RELATED WORK

The field of fluorescence guided surgery is well-established and thus numerous publications in the field are available. However, to my knowledge no other system has been published which fulfills the design requirements specified in this thesis. Even though many other systems outperform the prototype in one aspect, they perform weaker in other aspects or do not investigate those.

This section compares the prototype with other technologies and systems. First, related work focusing on combining fluorescence and color imaging in a clinical setting is collected and compared. However, these systems generally do not allow to image multiple fluorophores. Therefore, the second part presents systems developed for the recording of multispectral images and relates them to the prototype. These systems generally perform very well in acquiring multispectral data, but in contrast do not allow to record color and fluorescence in videorate.

8.4.1 *Clinical fluorescence imaging devices*

This section compares available fluorescence imaging devices for clinical and preclinical use with the prototype system and discusses the differences.

Spectral splitting

Several devices to image ICG have been presented and are also commercially available for clinical use [74]. These devices usually split the spectral range into two parts: the VIS part is used for color reflectance imaging and the NIR part is used for fluorescence imaging.

Possibly the biggest advantage of these systems is that the two imaging modalities are mostly autonomous. Parameters like framerate, illumination intensity or even pixel size and optical magnification can be chosen independently. This allows to combine very different imaging modalities in one device. Accordingly, these devices show higher sensitivity for IR dyes than the prototype device presented in

this work. Nevertheless, they are not flexible and most only allow to image one single dye. Many of these devices can be combined with room lights, run at video rate and are already translated to the clinical environment. The disadvantage is that these devices do not offer the capacity for multispectral imaging and at least imaging of multiple dyes in the visible is excluded per se.

In future, clinical fluorescence imaging with targeted fluorescent agents will focus on the NIR, because tissue absorption is relatively low in this region [5, 42]. Thus, a device with color imaging capacity in the visible and multispectral fluorescence imaging capacity in the NIR might be a promising scenario for multispectral fluorescence guided surgery. In that case, the method of spectral and temporal multiplexing presented here could be adapted to just cover the NIR part.

Overall, splitting the spectral range into one for color imaging and one for fluorescence imaging is very effective, if applicable for the required scenario. For the example of imaging only ICG, this solution is chosen for the clear majority of devices on the market and shows overall good performance. However, the devices miss the essential requirement to image multispectral fluorescence over the VIS/NIR spectral range.

Temporal splitting

The second well-established approach to unify fluorescence and color imaging in one device is to temporarily split the two modalities. This approach is popular for PPIX imaging in surgical microscopy and cystoscopy. For both applications, most clinical systems require manual switching between the two modes. This means that the surgeon will have to push a pedal to toggle between fluorescence and color imaging mode.

Various systems of this type have already been presented for clinical use. In this regard, these systems lead over the prototype in the sense that they are already translated and adapted to match clinical demands. However, the surgeon only sees either color or fluorescence. In consequence, the surgeon needs to memorize the fluorescence image during cancer resection, switch to color mode and continue resection using the memorized information. In contrast, the prototype combines fluorescence and reflectance imaging and offers real-time combination of the images.

Several approaches to accelerate the switching have been reported [84, 85]. In this respect, these systems use electronic switching like the prototype. However, they also share one common issue: flickering illumination will be disruptive for the user, unless it cannot be perceived anymore. Thus, this approach is most promising for endoscopic applications where the illumination light is not seen by the surgeon. Besides, the presented systems are usually designed to im-

age only one fluorescent dye, they are not developed for multispectral imaging.

Placing a filter permanently in front of the sensor is the simplest optical solution to block the fluorescence excitation light. If the excitation light source is a laser, a single spectrally narrow blocking band is required. The influence on color images is supposed to be minimal, because the spectral width of the filter gap can be made very small compared to the typical width of color reflectance spectra. However, if multiple dyes should be excited with LEDs, the blocking will be significant and the color images may be altered.

In short, systems which use temporal switching to image fluorescence and color have been developed and are commercially available. Even though they may show superior performance to image one single dye, they do not allow flexible multispectral imaging as required for this work.

8.4.2 *Multispectral image acquisition*

Macroscopic point scanning

In comparison to the prototype system point scanning systems are very flexible. Excitation and emission paths can be easily reconfigured as needed. However, traditional systems with galvanometric mirrors scanning the optical beam across the sample are not fast enough for video-rate imaging. Our prototype system clearly outperforms scanning systems such as the one presented by Constantinuou *et al.* in terms of speed [115]. In contrast, this system has a numerical aperture of $NA = 0.35$ and thus collects approximately 1000 times more photons than the prototype system.

Recent developments in the fabrication process of micro electromechanical systems (MEMS) allow the production of miniaturized scanning mirrors. These MEMS devices promise scanning at video rate and in HD resolution [156]. However, such resolutions require a pixel clock frequency between 100 MHz and 1 GHz and thus leave very little integration time to collect photons for each individual pixel. Moreover, technical aspects like mirror size and scan angles still require to be harmonized with scanning systems.

To sum up briefly, point scanning with galvanometric mirrors will not be fast enough to realize a system for clinical use, but novel MEMS devices may be a game changer in future.

Scanning fiber endoscopy

Fiber endoscopes using a single fiber to deliver light and piezo actuators to scan the object have been presented with diameters as low as 1 mm [40]. Up until now, no chip-on-the-tip endoscope with such

a small diameter has been presented [40] and most likely fiber scanning endoscopes will continue to spearhead technical development in this field. From the current point of view, the presented prototype system can be further miniaturized, but not down to a 1 mm diameter endoscope.

Endoscopes with such small diameter might be beneficial for some applications. However, sub-millimeter endoscopes have to be handled with caution to not accidentally perforate tissue. Colonoscopes and cystoscopes for example do not require dramatic further miniaturization of the instrument diameter. Still, the smaller the imaging channel, the more room remains for the working channels and instruments.

Fluorescence detection requires collecting as many photons as possible. A major factor for the photon collection capability of any system is the size of the first lens. Consequently, a miniaturized detection lens is problematic for fluorescence imaging as it opposes high photon collection efficiencies.

The presented fiberscopes run at video framerate (30 fps), but only has an image size of 196 kpx.

The main advantage of any point scanning setup is the flexibility in building a suitable detection unit.

All in all, scanning fiber endoscopes are a promising technology. In scenarios where space is the fundamental limitation (diameter $\leq$ 1 mm), scanning fiber endoscopes are the first choice. Having said that, for high-resolution fluorescence endoscopy at video-rate with permissible catheter diameters around 1 cm, the prototype system remains the technology of choice.

Line scanning

In retrospect, the image size of line scanning systems is comparable to the presented prototype system [117, 118, 120]. Though, their superior spectral resolution comes at the expense of framerate. In this regard, none of the compared systems runs close to the required framerate of 30 fps and can therefore not be seen as a potential replacement technology. The high-quality of the spectral information of the system for example presented in Luthman *et al.* allows to unmix challenging scenarios in vivo using multiple dyes which are close together [120]. It would be very interesting to directly compare the images produced by such a system as a reference mark with the images produced by the presented prototype.

Snapshot hyperspectral imaging

In terms of spatial resolution, the presented prototype system outperforms the clear majority of snapshot hyperspectral imaging systems.

These systems generally distribute all the multispectral data points on a 2D monochrome sensor using various methods.

As an effect, the spatial resolution of these snapshot systems tends to be far below 1 MP because many pixels are used to record spectral information. An extreme choice is for example a fiberscope published by Lim *et al.* claiming to record images of 10×10 pixels with each having 756 spectral bands [93]. However, more suitable selections can also be made: Basiri *et al.* distribute 9 MP into 18 spectral images of 0.5 MP each.

Framerates of the related work and of the prototype should be comparable as they purely depend on the sensor readout time and sensor electronics.

As many different snapshot technologies are available, the size of the setup varies. CTIS, for example, allows the building of comparably compact HSI setups. Most of the snapshot HSI methods are efficient in terms of photon detection. If all wavelengths need to be detected simultaneously, it is not very suitable to block most of the wavelengths as it is often done by scanning techniques.

So far, none of the snapshot HSI technologies dominates the field. Future research is necessary to push forward these technologies.

However, high-resolution sensors with up to 150 MP are projected to enter the sensor market in 2018 [210]. As a result, it would be possible to record hyperspectral data with an image size of 5 MP at 30 spectral bands simultaneously. For such sensors, the data transfer is expected to be the bottleneck. This issue can be solved by processing the images directly in the camera with FPGAs and transferring only the relevant diagnostic image data from the sensor to the computer and screen.

Snapshot imaging technologies are expected to become increasingly popular as they complement with developments on the sensor market. They are likely candidates to prevail in medical applications, especially because movement does not result in artifacts.

Spectral scanning with filter wheels

Comparing in retrospect the presented prototype system with systems allowing to record multispectral fluorescence with filter wheels reveals that the prototype outperforms the other systems in terms of recording speed by far [70, 71]. By contrast, systems with filter wheels can be reconfigured with different filters very flexibly. Changing one band of the prototype system requires the redesign of all multiband filters.

Although the prototype system is of the same size as published setups with filter wheels [70, 71], the prototype system can be miniaturized. In contrast, the size of filter wheels cannot be easily reduced.

The system of Benavides *et al.* uses a color sensor and two different excitation lights for time multiplexing [70]. The prototype system allows rapid acquisition of fluorescence images with different excitation lights. Thus, the concept could be translated. Numerical simulations of the scenario would show the optimal multiband filter structure for the prototype system (analogously to Chapter 7). The results would also allow to judge about the system performance for the example to identify cervical neoplasia by autofluorescence detection.

Spectral scanning with liquid crystal tunable filters

Recent publications present systems for scanning the spectral range using LCTFs instead of filter wheels [63, 104–106]. The achievable spectral resolution is far superior than that of the prototype system, the spatial resolution is acceptable or can easily be fixed by replacing the sensor. Framerates (if reported) are below video-rate, but still better than using filter wheels. As LCTF blocks most of the light when scanning over the spectrum, the technique is generally not very suitable for fluorescence imaging. Also, current LCTF are not suitable to be miniaturized for example in chip-on-the-tip endoscopes.

In brief, LCTF systems do not fulfill the systems design requirements and therefore cannot replace the system. Nevertheless, they allow to build high-quality systems which are necessary for initial clinical experiments. For example, Valdes *et al.* demonstrated clinical advantages of multispectral fluorescence guided glioblastoma resection with such a system. It is of high interest to see if the same results could be achieved with an adapted version of the prototype system.

Spectral scanning with acousto optical tunable filters

The fastest spectral scanning systems work with AOTFs to filter specific wavelength ranges (compared to filter wheels or LCTF). The presented systems [111–114] show framerates up to 5 fps and are thus quite close to fulfilling the requirements in terms of framerate (only a factor 6 is missing). The crystals inside the filters themselves are very small so they could also potentially be miniaturized. However, a major part of the photons is eliminated in this technique and thus the detection efficiency is supposed to be limited. Additionally, motion will lead to spectral artifacts. At the same time, out of all the available spectral scanning techniques, it is so far the most promising one. Future work will show if the technology is competitive and can be introduced into the medical device market.

8.5 OUTLOOK

This section gives an outlook on the next steps for follow-up projects. These are categorized by topic into clinical translation, technical advances, algorithm development and miniaturization for endoscopy.

Clinical translation

Future work in translating the system to clinical applications promises good results. This thesis has worked out a method to combine fluorescence and color imaging and has analyzed its implications. To translate the method for an introduction into clinical practice, application specific systems are required. In this process, firstly, the imaging scenario needs to be specified. This includes fixing the dyes to be distinguished. Secondly, numerical simulation and optimization of the spectral system characteristics will provide optimal spectral design parameters for the system and predict how well the system will be able to distinguish the dyes of interest. Even though an intuitive choice of spectral bands may result in a performance close to optimal, it is not possible to predict how well the dyes can be separated and thus how much noise will be amplified by unmixing. Thirdly, a prototype needs to be designed, realized, tested and potentially improved. This loop of improvement needs to be continued until the test results are satisfactory. For testing, technical laboratory experiments should be performed. This step will be followed by preclinical and finally clinical experiments. It is desirable for efficiency, simplicity and for ethical reasons to keep this order and to only progress to the next step when the system has successfully passed all tests. Searching for system components when designing the prototype should be oriented toward the vision of an ideal system described in Section 8.3.

So far, established clinical applications for fluorescence guided surgery are based on imaging one single dye only. New clinically approved (NIR-) dyes and staining scenarios using multiple dyes are waiting to be translated to the clinics. In the meantime, combining clinically established and approved dyes, for example imaging PPIX, ICG and FITC simultaneously for glioma resection is a promising direction.

Moreover, preclinical experiments suggest that multispectral detection of PPIX itself can improve the diagnostic information for glioma resection.

Another example where initial clinical experiments promise superior diagnostic performance is multispectral autofluorescence detection for diagnosis of cervical neoplasia.

These are example applications in which clinical translation can already be brought forward and do not require to wait for admission

of novel agents. In future, clinical dyes in the NIR imaging region are expected to be available for clinical use.

Technical improvements

The prototype system has shown to fulfill the design requirements. However, the extensive testing and technological progress point to possible future improvements.

The used sensors Fairchild CIS2521 have shown a good, but not overwhelming color imaging performance. It seems that superior micro color filters could further improve the color imaging quality.

Unfortunately, the sensor has a fixed readout time per frame in which no new frame can be recorded. At high framerates this increasingly reduces the system efficiency. Novel sensors which have overcome this obstacle are already available on the market.

The current pixel design of color sensors is a 2×2 R-G-G-B Bayer pattern. Other designs such as R-G-IR-B (replacing one green by an IR pixel) or R-G-M-B (replacing one green by a monochrome pixel) can be imagined. The final aim would be to find a pixel design which improves color reproduction, enhances the spectral separation between dyes and has a high detection efficiency.

The optics of the prototype performed within the specifications. The development was focused on flexibility and high-quality filtering of the emission light and thus leaves space for improvement. A custom optics design promises a more compact setup which would ideally combine good filtering with a high photon collection efficiency and superior image quality.

Algorithm development

A big field of future work lies in the direction of algorithm development. Here, potential regions of work are identified for the fields of improved numerical system optimization, artifact free unmixing, accurate color correction and finding the limitations of the T-score algorithm.

The numerical simulations of the spectral performance allow finding the optimal spectral design and to estimate the system performance for the respective application. The simulation can be further extended optimizing even more parameters like excitation lights or the RGB sensor sensitivity curves. This leads to a high dimensional optimization problem which requires studying the problem more rigorously in order to find the global optimum.

In this work, the fluorescent dyes were unmixed using linear unmixing based on the spectral images. These images have been acquired at different times and the spectral information has been interpolated in the debayering process. Both effects have shown to result

in unmixing artifacts. In future, a novel algorithm which takes the temporal, spectral and spatial shift of information in the raw data into account, can be developed for improved unmixing performance.

The T-score metric has been developed in this thesis and has demonstrated in initial experiments to spot unmixing artifacts. However, it is not directly clear if any unmixing error must necessarily result in a higher T-score. Therefore, future work is required to determine which artifacts can be spotted well and to find the limitations of the algorithm. Along this development, the statistical interpretation of the T-score can be developed to convert the score into statistical statements.

Another field in which new algorithms promise a better performance is color correction.

The linear correction approach results in sufficiently corrected images, but literature has shown that adding constant parameters or higher order polynomials may further improve color correction. Even though literature has not yet found superior performance using neural networks, new insights in this dynamic field may also improve their performance for color correction.

Estimating the best set of parameters for color correction was computationally expensive and the algorithm may only converge to a local optimum.

The color correction algorithm used in this work tries to reproduce the colors as perceived by the human eye when illuminated with sunlight. Alternatively, algorithms which increase color contrast between specific tissue types could be developed. A historic example for a visualization which sacrifices color reproduction for the benefit of enhancing features is narrow band imaging. Recording six channel color information might be sufficient to develop similar algorithms to aid the surgeon.

All in all, work on algorithms development for color correction is still pending and shows promises for advancement.

Endoscopy & miniaturization

The prototype system was designed for open surgery imaging. However, the concept can also be adopted to realize a chip-on-the-tip endoscope. Beam splitting in chip-on-the-tip endoscopes has already been established in commercial solutions. Thus, the technical challenge to place a beam splitter and two sensors in the tip of an endoscope (diameter approx. 1 cm) has been solved. However, combining these setups with the necessary emission filters requires further work on the optical imaging design. The illumination can be filtered and realized outside the endoscope and then guided to the tip in optical fibers. Overall, miniaturization seems feasible but poses a challenge to optical design.

8.6 CONCLUSION

Recent preclinical and clinical experiments indicate the potential of fluorescence guided surgery to improve surgical outcome. These advances include improved cancer margin delineation or identification of anatomical or functional structures. For instance, cancer cells can be stained with one fluorescent dye whereas muscular tissue, nerves or blood vessels can be targeted by other dyes and allow distinction beyond conventional color vision.

However, current imaging methods and the equipment do not yet fully exploit the potential of fluorescence guided surgery. Therefore, this work is dedicated to developing an imaging method and present a prototype device which allows combined multispectral fluorescence and color imaging over the entire VIS/NIR spectrum in video-rate. Additionally, the method must allow seamless integration into the current medical work-flow.

Prototype performance

The selected method explores combined spectral and temporal multiplexing to allow recording of fluorescence and reflectance images over the entire VIS/NIR range. The spectral multiplexing is realized with complementary multi-bandpass filters, the temporal multiplexing by illuminating the object in two subsequent phases with the two complementary multiband lights. As only two temporal phases are necessary to record fluorescence and conventional reflectance images over the entire spectral range, the system can run at video-rate.

All in all, the performance of the prototype system satisfies the requirements very well. Colors can be accurately reproduced even for varying illumination which can be adjusted for best fluorescence detection. Likewise, experiments have shown good unmixing performance even for challenging scenarios such as three fluorescent dyes with strong spectral overlap. The good separation power of the system is attributed to the combined excitation and emission multiplexing.

Live artifact diagnostics

Imaging multiple dyes with spectral overlap always requires a mathematical transformation to separate the unmixed signals. In this work, linear unmixing as the most common method to separate the signals is used. As a matter of fact, the algorithm will always provide some result independent of the correctness. Effects like wrongful calibration, tissue absorption or ambient light may lead to artifacts and arbitrarily falsify the result. Consequently, all information must be treated by the surgeon with extreme caution, as no guarantee on the quality of the information can be given.

In this work, a new score, called T-score, is developed. It provides a consistency check on the unmixed images on a per pixel and per image basis. Thus, the T-score image can be calculated for each individual image of the video-stream. The algorithm requires the raw image data, the unmixing coefficients, which are needed in any case for unmixing, and a noise model of the detection process as input. Structures with a high T-score indicate the occurrence of unmixing artifacts and tell the surgeon to treat the signal of that image region with caution.

The unique feature of this work is that the signal noise is estimated on basis of a single measurement. This allows calculating the T-score in video rate for each pixel and each frame. To my knowledge, there is so far no diagnostic method established, which allows to judge on the unmixing quality at video-rate for multispectral imaging applications.

Undoubtedly, the method is one of the fundamental developments of this work and can be reused for any multispectral imaging application.

Towards clinical application

For some applications, such as bladder cancer resection, fluorescence guided surgery is already clinically established. Moreover, numerous experimental clinical and preclinical experiments using fluorescence targeting with multiple dyes have been reported. Since these targeting techniques complement the work of this thesis very well, their clinical translation will boost the impact of the developed imaging system.

In future, the prototype system needs to be adapted for each application individually. For example, the optical design needs to be different for laparoscopic applications versus open surgery. However, an application specific spectral design is equally important as the power of the system to separate different dyes strongly depends on the spectral characteristics of the system. Thus, after fixing a medical use case, it is worth to optimize the spectral design.

Yet another point of future work is further miniaturization of the prototype system to make it more attractive for its use in a clinical environment. It is technically feasible to miniaturize the setup up to the point of a chip-on-the-tip endoscope. Besides, implementation of stronger light sources, faster sensor readout in global shutter mode and a custom optics with higher numerical aperture can improve the performance.

Next generation fluorescence guided surgery

In short, recent advances in molecular biotechnology provide state-of-the-art staining techniques. These techniques are expected to be translated into clinical practice in the next decade. The developed imaging

method allows realizing miniaturized devices which combine reliable diagnostic fluorescence information with high-quality color imaging.

All in all, combining novel fluorescent drugs with the developed imaging method can pave the way for next generation fluorescence guided surgery.

A

APPENDIX

A.1 MATHEMATICAL FORMULATION OF MULTISPECTRAL IMAGE PROCESSING

A.1.1 *Fluorescence detection and unmixing*

An imaging sensor counts the number of photons $X(\xi)$ emitted by a dye on a pixel location ξ in the image during the integration time t_{int}. The number of detected photons is described by the Poisson statistics with the parameter $\mu_Y(\xi)$:

$$Y(\xi) \sim \mathcal{P}\Big(\mu_Y(\xi)\Big) \tag{A.1}$$

with probability density

$$f_Y\Big(y, \mu_Y(\xi)\Big) = \frac{\mu_Y(\xi)^y}{y!} \exp^{-\mu_Y(\xi)}. \tag{A.2}$$

Photon count numbers are Poisson distributed because coherent effects can be neglected which means that the individual photons are independent.

This consideration can be generalized to the case when the fluorescent dyes $f = 1 \dots N_f$ emit $Y(f, \xi)$ photons at the pixel location ξ. The number of photons emitted by each dye f are independently Poisson distributed with the parameters $\mu_X(f, \xi)$

$$X(f, \xi) \sim \mathcal{P}\Big(\mu_X(f, \xi)\Big). \tag{A.3}$$

The photons of the dyes add up when being detected as

$$Y(\xi) = \sum_{f=1}^{N_f} X(f, \xi) \sim \sum_{f=1}^{N_f} \mathcal{P}\Big(\mu_X(f, \xi)\Big) \stackrel{\mathrm{d}}{=} \mathcal{P}\Big(\mu_Y(\xi)\Big), \tag{A.4}$$

which is again a Poisson distribution with

$$\mu_Y(\xi) = \sum_{f=1}^{N_f} \mu_X(f, \xi). \tag{A.5}$$

and d means equality in distribution. Additionally, it is important to consider that the photons emitted from each fluorophore are split into N_c detector channels $c = 1 \dots N_c$ as each channel has its own spectral detection sensitivity. The random variable $Y(c, \xi)$ describing

the number of photons detected in each channel c is calculated as the weighted sum

$$Y(c,\xi) = \sum_{f=1}^{N_f} m(c,f) \cdot X(f,\xi) \tag{A.6}$$

and accordingly

$$\mu_Y(c,\xi) = \sum_{f=1}^{N_f} m(c,f) \cdot \mu_X(f,\xi). \tag{A.7}$$

The same set of equations can be written in matrix notation where $\boldsymbol{m}$ is the mixing matrix with coefficients $m(c,f)$, $\boldsymbol{\mu}_Y(\cdot)$ and $\boldsymbol{\mu}_X(\cdot)$ are the parameter vectors of the Poisson distributions:

$$\boldsymbol{\mu}_Y(\xi) = \boldsymbol{m} \cdot \boldsymbol{\mu}_X(\xi). \tag{A.8}$$

If a photon is detected by the sensor, it needs to be detected by one of the sensor channels. Therefore, the mixing matrix is normalized as

$$\sum_{c=1}^{N_c} m(c,f) = 1. \tag{A.9}$$

With this normalization the number of photons which are detected by the sensor in different channels is maintained. Of course, not all photons emitted by a dye will be detected as they can for example not be imaged onto the sensor or not trigger an electron due to the finite detection efficiency of the detector.

If the number of sensor channels N_c is greater or equal than the number of dyes N_f, a generalized inverse of the mixing matrix is computed using the Moore-Penrose pseudoinverse [211, p. 409]. In case of $N_c > N_f$, this corresponds to the least squares solution of the overdetermined linear equation system [205]. This allows to obtain the fluorescence intensity originating from each dye:

$$\boldsymbol{\mu}_X(\xi) = \boldsymbol{u} \cdot \boldsymbol{\mu}_Y(\xi), \tag{A.10}$$

where

$$\boldsymbol{u} = \boldsymbol{m}^{+}. \tag{A.11}$$

In this work, the parameter $\hat{\boldsymbol{\mu}}_Y(\xi)$ is estimated using the maximum likelihood estimator (MLE). As the number of detected photons of an observation $\boldsymbol{Y}_i(\xi)$ is Poisson distributed, the MLE $\hat{\boldsymbol{\mu}}_Y(\xi)$ of the distribution parameter $\boldsymbol{\mu}_Y(\xi)$ is determined by the mean (empirical expectation value) of N observations:

$$\hat{\boldsymbol{\mu}}_Y(\xi) = \frac{1}{N} \sum_{i=1}^{N} \boldsymbol{Y}_i(\xi). \tag{A.12}$$

In real-time imaging applications it is not feasible to record multiple values $\boldsymbol{Y}_i(\xi)$. Instead, only one ($N = 1$) observation is used to estimate $\hat{\boldsymbol{\mu}}_Y(\xi)$.

An image with values $\boldsymbol{Y}(\xi)$ correspond to the number of electrons triggered by incoming photons, which are distributed around a mean $\boldsymbol{\mu}_Y(\xi)$. To obtain the image $\boldsymbol{Y}(\xi)$, the raw image $\boldsymbol{Y}'(\xi)$ needs to be corrected for dark signal $\boldsymbol{\mu}_d(\xi)$ and the conversion factor (see Figure A.1). Therefore, the noise $\boldsymbol{\Sigma}_Y(\xi)$ of an image $\boldsymbol{Y}(\xi)$ is no longer purely Poisson distributed, but also contains noise contributions from the readout process, the dark current and from quantization. These effects are described in detail in Section A.1.3.

Nevertheless, mixing and unmixing of components can be performed as is, since the mean $\boldsymbol{\mu}_Y(\xi)$ corresponds to the mean number of triggered electrons in the sensor.

A.1.2 *Fitting spectral signatures*

In order to unmix fluorescent images, the spectral signature of the individual fluorescent dyes needs to be determined. This section describes how the image data is mathematically processed to obtain the signatures from experimental data of pure samples. For this purpose technical phantoms with pure dyes are imaged to produce data with only one single dye signature contained per pixel. The image data used for the spectral calibration is manually selected.

In an ideal scenario, in which neither systematic nor statistical errors are present, the detected signal $\boldsymbol{Y}(\xi)$ of a single fluorescent dye at a certain location ξ is proportional to the signature $\boldsymbol{\kappa}$

$$\boldsymbol{Y}(\xi) = \alpha(\xi) \cdot \boldsymbol{\kappa}, \tag{A.13}$$

where the scalar scaling factor $\alpha(\xi)$ represents the total intensity of the fluorescent signal.

To obtain the spectral signature $\boldsymbol{\kappa}$ of a fluorescent dye, the pure sample data $\boldsymbol{Y}(\xi)$ is fitted for the selected data points ξ using the linear model (see Equation A.13) by minimizing the residuals

$$\min_{\boldsymbol{\kappa} \in \left\{ \Re_{\geq 0}^{N_c} \mid \sum_{c=1}^{N_c} \kappa(c) = 1 \right\}} \left(\sum_{\xi} \sum_{c=1}^{N_c} \left(Y(c, px) - \alpha(\xi) \cdot \kappa(c) \right)^2 \right), \tag{A.14}$$

where the scaling factor $\alpha(\xi)$ is determined by the scalar product $\alpha(\xi) = \boldsymbol{Y}(\xi) \cdot \boldsymbol{\kappa}$ and the total length of each signature is fixed as $\sum_{c=1}^{N_c} \kappa(c) = 1$.

The mixing matrix $\boldsymbol{m}$ (see Equation A.6) is obtained by concatenating the spectral signatures $\boldsymbol{\kappa}(f_{(\cdot)})$ of the fluorescent dyes $f_1, f_2, \ldots, f_{N_f}$:

$$\boldsymbol{m} = \left[\boldsymbol{\kappa}(f_1), \boldsymbol{\kappa}(f_2), \ldots, \boldsymbol{\kappa}(f_{N_f}) \right]. \tag{A.15}$$

This minimization approach corresponds to orthogonal distance regression, which in case of a linear relation is equivalent to the first component of principle component analysis. Therefore, the pre-implemented MATLAB principle component analysis function `pca` was used to fit the sample data.

The minimized orthogonal distance residuals are mainly due to image noise, but may also be due to systematical errors such as absorption. The statistical error of the spectral signatures can be estimated calculating the confidence bounds by bootstrapping [212]. These confidence bounds are estimated by statistical variation in the data. However, the procedure does not take into account systematic errors. The statistical variation in the data can be minimized as the number of data points used for the fit can be increased by recording multiple pictures of the pure samples. Thus, the systematic error will then finally govern the signature uncertainty.

The most robust way to obtain a reliable spectral signature is to record the calibration data with exactly the same system configuration and set of parameters as for the desired imaging scenario. Additionally, it is desirable to record pure fluorescent data of each dye ranging over the entire dynamic range of the sensor. If this cannot be realized during one sensor integration, multiple scenarios with different excitations or different dye concentrations can be combined.

Such additional scenarios can also be used trying to estimate the systematic error in the spectral signature.

A.1.3 *Imaging noise*

This section introduces a mathematical description of the noise that will be present in the sensor data and how this noise propagates through unmixing. The used sCMOS sensor model CIS2521 (Fairchild) can be described well by the EMVA 1288 standard [200, 203]. This standard describes a noise model which is scalar with respect to sensor channels. In contrast, each pixel of a multispectral image is described by a vector and accordingly the noise of the vector is described by the associated covariance matrix $\mathbf{\Sigma}_Y(\xi)$. It is assumed to be diagonal with elements

$$\Sigma_Y(c, c, \xi) = \operatorname{var}\left[Y(c, \xi)\right] = \operatorname{cov}\left[Y(c, \xi), Y(c, \xi)\right] \tag{A.16}$$

for all channels $c = 1 \dots N_c$. According to the EMVA 1288 standard, the main sources of noise are:

SHOT NOISE The detected photons are Poisson distributed. In the same way, the electrons triggered by the photons are Poisson distributed. For high intensities (and thus high number of photons), this is the dominant source of noise which cannot be over-

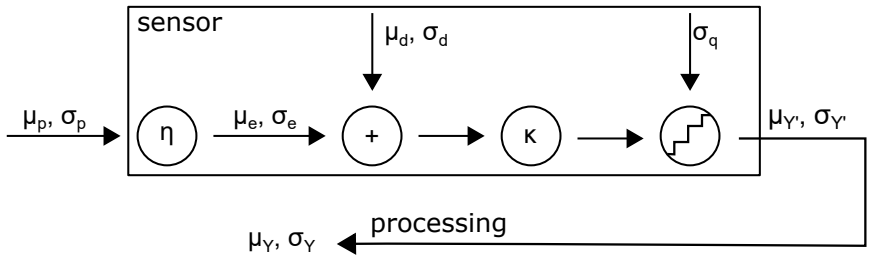

Figure A.1: Sensor noise model according to the EMVA 1288 standard [200]. The figure describes the noise contributions for one sensor pixel. Incident photons are temporally Poisson distributed with mean μ_p and variance σ_p^2. The quantum efficiency of the sensor $\eta(\lambda)$ reduces the number of electrons (e^-), triggered by the incident photons, to μ_e and variance σ_e^2 (also Poisson distributed). A dark image with a mean μ_d and variance σ_d^2 is added to the signal during the detection process. The dark effects can be approximated by two separate processes: a dark readout image and variance at zero integration time and a dark current which increases signal and variance linearly with integration time. Subsequently the signal is amplified by a conversion factor and digitalized. Digitalization adds a quantization noise σ_q^2 since the signal is binned to a finite grid of output values. The raw image values are distributed with a mean $\mu_{Y'}$ and a variance $\sigma_{Y'}^2$. The signal is processed so that $\mu_Y = \mu_e$, because this signal is proportional to the number of incident photons and is in units of electrons [e^-] which determine the Poisson noise of the signal. However, the variance σ_Y^2 is also affected by the dark noise and the quantization noise.

come [15]. The diagonal elements of the covariance matrix are described by the detected intensity:

$$\Sigma_{Y,S}(c,c,\xi) = \boldsymbol{\mu}_Y(c,\xi). \tag{A.17}$$

for all channels $c = 1 \ldots N_c$. Off diagonal elements are assumed to be zero.

For high signal intensities the Poisson distribution $\mathcal{P}\Big(\mu\Big)$ can be approximated by the normal distribution $\mathcal{N}\Big(\mu, \sigma^2 = \mu\Big)$. Consequently, the rules of Gaussian error propagation apply for high signal intensities.

DARK NOISE If no photon hits the sensor, the sensor will show some signal μ_d value and also contain dark some noise σ_d^2. Dark noise originates from two major sources: readout noise and dark current noise.

The raw images only allow positive values. Therefore, the baseline for zero counts is set to a positive readout value μ_R in order not to crop the noise signal at zero values. During the integra-

tion, dark current additionally triggers electrons due to thermal effects: $\mu_I = I_d \cdot t_{\text{int}}$. These two effecs add up to

$$\mu_d = \mu_R + \mu_I. \tag{A.18}$$

Assuming independence between the noise sources, the two separate sources of noise add up:

$$\sigma_d^2 = \sigma_R^2 + \sigma_I^2. \tag{A.19}$$

READOUT NOISE The readout noise corresponds to the noise of a dark image with zero integration time. It is depends on the sensor model, readout mode and may other factors [15, 200]. The diagonal elements of the covariance matrix are

$$\Sigma_R(c, c, \xi) = \sigma_0^2 \tag{A.20}$$

for all channels $c = 1 \dots N_c$.

DARK CURRENT NOISE Dark current noise is caused by electrons which are counted in the sensor during the integration time and which are not triggered due to incident photons. These electrons, which are triggered by thermal effects are also Poisson distributed: $\sigma_I^2 = \mu_I$. The diagonal elements of the covariance matrix can be expressed as

$$\Sigma_R(c, c, \xi) = I_{dark} \cdot t_{\text{int}}. \tag{A.21}$$

QUANTIZATION NOISE The signal is amplified in the sensor by a factor K and subsequently digitalized to a finite quantity. Quantization to digital values g with equidistant spacing $\Delta g = 1$ results in a covariance matrix

$$\Sigma_Q(c, c, \xi) = \frac{1}{12} \cdot \frac{1}{K^2}, \tag{A.22}$$

which is independent of the signal intensity itself [204]. The constant K describes the number of triggered electrons in the sensor for one digital count value $\Delta g = 1$.

IMAGE NOISE The individual covariance matrices of the discussed noise sources are added in the same way as the variances in the EMVA 1288 noise model [200]:

$$\Sigma_Y(c, c, \xi) = \Sigma_{Y,S}(c, c, \xi) + \Sigma_R(c, c, \xi) + \Sigma_R(c, c, \xi) + \Sigma_Q(c, c, \xi). \tag{A.23}$$

SPATIAL NOISE All the described noise contributions are so assumed to be identical for each pixel of the sensor grid. Though, in reality the sensor measurements show spatial dependencies. Two

major effects are described by the EMVA 1288 standard: photo response non-uniformity (PRNU) and dark signal non-uniformity (DSNU). PRNU characterizes the variation in sensor sensitivity between dark image and a 50% saturated image over the different pixel locations [200]. Spatial variations of the dark image are described by the DSNU. Both effects are neglected in this work because for the relevant imaging scenarios, shot noise dominates [171].

Both DSNU and PRNU are spatial standard deviations which do not exhibit signal and noise dependency at a certain spatial frequency. Effects with low spatial frequency may originate from variations in the sensor production or for example from illumination. In contrast, variations at high frequencies can be caused by interferences of the readout electronics [200].

A.1.4 *Unmixing in subspaces*

The recorded complete dataset $\boldsymbol{Y}(\xi)$ contains all the information that is recorded in a single image, but it is hard to explore the data. This may result in unspotted artifacts as the multi-dimensional image data is invisible to the users. In case of wrongful unmixing users will only see the finally estimated unmixed dye concentrations with artifacts, but not the nature of the spectral artifacts. Therefore, a method to reduce the dimensionality of the spectral image information is presented here. In this process, the image data is transformed orthonormally to a subspace of the detector space. Here it is mathematically derived how the fluorescence components can be unmixed after being transformed to the subspace.

First of all, the spectral information of the data $\boldsymbol{Y}_n(\xi)$ is split from the intensity information $I(\xi)$ for each pixel of the recorded data $\boldsymbol{Y}(\xi)$:

$$I(\xi) = \sum_{c=1}^{N_c} Y(c, \xi) \tag{A.24}$$

and

$$\boldsymbol{Y}_n(\xi) = \frac{1}{I(\xi)} \cdot \boldsymbol{Y}(\xi). \tag{A.25}$$

The reason to split intensity from spectral information is to reduce the dimensionality by one and additionally to make it more suitable to be analyzed by algorithms. The subspace is spanned by the N_s orthonormal vectors ς in the detector channel space. These can be determined by various methods including principle component analysis (PCA) or phasor analysis. PCA finds the vectors that maximally separate the spectral spread in the data, whereas phasor analysis takes Fourier components as basis vectors [127, 205].

The normalized fluorescence image data $\boldsymbol{Y}_n(\xi)$ is projected to the subspace by

$$\boldsymbol{Z}_n(\xi) = \boldsymbol{s} \cdot \boldsymbol{Y}_n(\xi) \tag{A.26}$$

with the transformation matrix $\boldsymbol{s}$ formed by the orthonormal subspace basis vectors $\boldsymbol{\varsigma}_{(\cdot)}$

$$\boldsymbol{s} = \left[\boldsymbol{\varsigma}_1, \boldsymbol{\varsigma}_2, \ldots, \boldsymbol{\varsigma}_{N_s}\right]. \tag{A.27}$$

In order to unmix in the subspace, the spectral signatures of the fluorescent dyes $f_{(\cdot)}$ in the subspace $\boldsymbol{\nu}(f_{(\cdot)})$ need to be determined to find the subspace mixing matrix $\boldsymbol{n}$. One option is to directly determine the signatures experimentally, visually if the data can for example be plotted in a 2D histogram or by image analysis algorithms. The individual contributions are concatenated to the mixing matrix

$$\boldsymbol{n} = \left[\boldsymbol{\nu}(f_1), \boldsymbol{\nu}(f_2), \ldots, \boldsymbol{\nu}(f_{N_f})\right]. \tag{A.28}$$

Alternatively, if the dye mixing matrix $\boldsymbol{m}$ is known, it can be directly transformed to the subspace

$$\boldsymbol{n} = \boldsymbol{s} \cdot \boldsymbol{m}. \tag{A.29}$$

To unmix the subspace data for the normalized fluorescent dye contributions $\boldsymbol{X}_n(\xi)$, the following equation system needs to be solved:

$$\begin{bmatrix} n(f_1,1) & n(f_2,1) & \ldots & n(f_{N_f},1) \\ n(f_1,2) & n(f_2,1) & & n(f_{N_f},2) \\ \vdots & & \ddots & \\ n(f_1,N_s) & & & n(f_{N_f},N_s) \\ 1 & 1 & \ldots & 1 \end{bmatrix} \cdot \boldsymbol{X}_n(\xi) = \begin{bmatrix} Z_n(1,\xi) \\ Z_n(2,\xi) \\ \vdots \\ Z_n(N_s,\xi) \\ 1 \end{bmatrix} \tag{A.30}$$

or in matrix notation

$$\begin{bmatrix} \boldsymbol{n} \\ 1 \end{bmatrix} \cdot \boldsymbol{X}_n(\xi) = \begin{bmatrix} \boldsymbol{Z}_n(\xi) \\ 1 \end{bmatrix} \tag{A.31}$$

This corresponds to the equation system in Equation A.6 extended by the last equation necessary to also take into account the information that the spectral data is normalized.

After finding the solution for $\boldsymbol{X}_n(\xi)$, the intensity of the normalized unmixed fluoresence data $\boldsymbol{X}(\xi)$ can be restored as

$$\boldsymbol{X}(\xi) = I(\xi) \cdot \boldsymbol{X}_n(\xi). \tag{A.32}$$

If the subspace is N_s dimensional, the data can be unmixed for up to $N_f = N_s + 1$ fluorescent dyes.

The normalization in this procedure is mathematically not necessary. But it has the advantage that the data has one dimension less and thus it is easier to visualize the data and intuitively explore it while no information is lost.

Table A.1: Detection efficiency of the system for a selection of fluorescent dyes depending on the emission maximum wavelength. Fluorescence emission maximum wavelength and emission width as standard deviation are listed with the computed efficiencies of the individual sensor channels (η_{R1}, η_{G1}, η_{B1}, η_{R2}, η_{G2} and η_{B2}) and combined efficiencies (η_{S1} and η_{S2}) per channel as well as the overall detection efficiency of the system η_S. A detailed description of the calculation can be found in Section 5.1.2. At the beginning of the table the mean, median, maximum and minimum over all dyes listed in Section A.3 are presented for each column.

			S1				S2				
DYE	λ_{em}	std(λ)	η_{R1}	η_{G1}	η_{B1}	η_{S1}	η_{R2}	η_{G2}	η_{B2}	η_{S2}	η
mean	595 nm	34.3 nm	11.9	9.3	5.9	9.1	3.4	6.0	2.8	4.5	13.6
median	582 nm	32.5 nm	12.0	8.3	4.9	8.7	3.2	5.0	2.3	4.5	14.2
min	407 nm	13.4 nm	0.9	1.9	0.8	2.0	0.0	0.0	0.0	0.0	5.1
max	900 nm	119.4 nm	35.1	24.3	22.3	22.9	15.5	24.5	16.3	15.5	23.1
ATTO 390	482 nm	33.2 nm	2.1	7.9	6.4	6.1	1.7	9.3	10.9	7.8	13.9
ATTO 425	484 nm	36.1 nm	2.8	8.8	4.9	6.3	2.1	10.7	11.6	8.8	15.1
ATTO 430LS	547 nm	47.3 nm	9.1	10.2	4.5	8.5	3.6	10.9	3.6	7.2	15.7
ATTO 465	507 nm	47.3 nm	5.8	11.5	5.4	8.5	2.6	10.1	6.6	7.4	15.9
ATTO 488	525 nm	32.2 nm	6.1	16.1	6.8	11.3	2.5	9.1	2.5	5.8	17.0
ATTO 490LS	667 nm	52.2 nm	15.2	7.3	5.0	8.7	4.8	1.6	1.1	2.3	11.0
ATTO 495	527 nm	41.9 nm	7.7	13.3	5.8	10.0	3.0	9.8	2.8	6.4	16.4
ATTO 514	533 nm	29.2 nm	5.9	12.5	4.9	9.0	2.9	10.9	2.8	6.9	15.9

Table A.1: (continuation) Detection efficiency (in %) of existing fluorescent dyes

			S1				S2				
DYE	λ_{em}	std(λ)	η_{R1}	η_{G1}	η_{B1}	η_{S1}	η_{R2}	η_{G2}	η_{B2}	η_{S2}	η
ATTO 520	545 nm	29.8 nm	6.7	5.9	2.3	5.2	4.2	15.9	4.1	10.0	15.2
ATTO 532	555 nm	34.0 nm	8.4	4.5	2.0	4.8	5.1	17.8	4.6	11.3	16.2
ATTO 550	576 nm	34.7 nm	14.8	6.7	3.1	7.8	4.6	10.0	2.8	6.8	14.6
ATTO 565	592 nm	40.6 nm	21.1	9.2	4.5	11.0	3.6	3.3	1.2	2.9	13.9
ATTO 590	624 nm	41.0 nm	17.6	6.8	4.1	8.8	5.4	1.6	1.2	2.4	11.2
ATTO 594	629 nm	40.0 nm	16.3	6.2	3.9	8.1	5.8	1.6	1.2	2.6	10.7
ATTO 610	634 nm	39.1 nm	12.5	5.1	3.4	6.6	7.1	2.0	1.5	3.2	9.7
ATTO 620	642 nm	38.6 nm	11.0	4.8	3.3	6.0	8.2	2.4	1.8	3.7	9.7
ATTO 633	658 nm	46.0 nm	11.9	6.1	4.4	7.1	6.8	1.9	1.5	3.0	10.1
ATTO 635	658 nm	39.4 nm	11.9	5.9	4.1	6.9	6.6	1.9	1.4	2.9	9.9
ATTO 647N	671 nm	49.1 nm	13.9	7.0	5.2	8.3	3.9	1.2	0.9	1.8	10.0
ATTO 647	670 nm	45.7 nm	14.9	7.8	5.8	9.1	3.3	1.0	0.7	1.5	10.5
ATTO 655	683 nm	45.4 nm	18.9	10.1	7.5	11.7	0.8	0.3	0.2	0.4	12.0
ATTO 665	685 nm	33.5 nm	20.0	9.9	6.9	11.7	0.7	0.2	0.2	0.3	12.0
ATTO 680	700 nm	44.9 nm	18.6	10.9	8.2	12.2	0.1	0.1	0.0	0.1	12.3
ATTO 700	719 nm	43.4 nm	12.9	9.0	7.2	9.5	0.1	0.1	0.0	0.0	9.6
ATTO 725	753 nm	42.5 nm	12.0	10.0	8.7	10.1	0.0	0.0	0.0	0.0	10.1
ATTO 740	763 nm	40.8 nm	14.0	11.5	9.6	11.6	0.0	0.0	0.0	0.0	11.6
ATTO Oxa12	681 nm	49.5 nm	17.0	9.0	6.7	10.4	1.6	0.5	0.4	0.7	11.1

Table A.1: (continuation) Detection efficiency (in %) of existing fluorescent dyes

			S1				S2				
DYE	λ_{em}	std(λ)	η_{R1}	η_{G1}	η_{B1}	η_{S1}	η_{R2}	η_{G2}	η_{B2}	η_{S2}	η
ATTO Rho101	608 nm	38.2 nm	22.9	9.1	4.8	11.5	3.7	1.4	0.9	1.8	13.3
ATTO Rho11	600 nm	37.0 nm	23.4	9.9	4.9	12.0	3.4	1.8	0.9	2.0	14.0
ATTO Rho12	608 nm	38.2 nm	22.9	9.1	4.8	11.5	3.7	1.4	0.9	1.8	13.3
ATTO Rho13	626 nm	40.4 nm	16.7	6.4	4.0	8.4	5.6	1.6	1.2	2.5	10.9
ATTO Rho14	650 nm	38.1 nm	9.9	4.6	3.2	5.6	9.0	2.5	1.9	4.0	9.6
ATTO Rho3B	593 nm	39.3 nm	21.8	9.6	4.6	11.4	3.6	2.8	1.1	2.6	14.0
ATTO Rho6G	561 nm	38.5 nm	10.3	4.9	2.3	5.6	5.2	16.7	4.3	10.8	16.3
ATTO Thio12	607 nm	42.5 nm	22.8	9.2	4.9	11.6	3.7	1.3	0.8	1.8	13.3
Fluorescein	541 nm	30.8 nm	6.7	8.0	3.1	6.4	3.7	13.6	3.5	8.6	15.1
Methylene Blue	692 nm	41.8 nm	18.9	10.4	7.7	11.9	0.6	0.2	0.1	0.3	12.1
NADH	476 nm	47.7 nm	3.1	7.9	8.6	6.9	1.7	8.0	7.0	6.2	13.1
Riboflavin	539 nm	55.4 nm	8.7	10.7	4.9	8.8	3.3	9.8	4.2	6.8	15.6
Protoporphyrin IX	637 nm	29.9 nm	13.0	5.9	4.0	7.2	6.1	1.7	1.3	2.7	9.9

A.3 DYE LIST

This list contains the names of all the fluorescent dyes from the library of TU Graz which are used for numerical calculations in Section 5.1.2: AAA, APC-Seta-750, APC, ATTO 390, ATTO 425, ATTO 430LS, ATTO 465, ATTO 488, ATTO 490LS, ATTO 495, ATTO 514, ATTO 520, ATTO 532, ATTO 550, ATTO 565, ATTO 590, ATTO 594, ATTO 610, ATTO 620, ATTO 633, ATTO 635, ATTO 647N, ATTO 647, ATTO 655, ATTO 665, ATTO 680, ATTO 700, ATTO 725, ATTO 740, ATTO Oxa12, ATTO Rho101, ATTO Rho11, ATTO Rho12, ATTO Rho13, ATTO Rho14, ATTO Rho3B, ATTO Rho6G, ATTO Thio12, Acridine Orange, Acridine Yellow, Adams Apple Red 680, Adirondack Green 520, Alexa Fluor 350, Alexa Fluor 405, Alexa Fluor 430, Alexa Fluor 480, Alexa Fluor 488, Alexa Fluor 488 hydrazide, Alexa Fluor 500, Alexa Fluor 514, Alexa Fluor 532, Alexa Fluor 546, Alexa Fluor 555, Alexa Fluor 568, Alexa Fluor 594, Alexa Fluor 610-R-PE, Alexa Fluor 610, Alexa Fluor 633, Alexa Fluor 635, Alexa Fluor 647-R-PE, Alexa Fluor 647, Alexa Fluor 660, Alexa Fluor 680-APC, Alexa Fluor 680-R-PE, Alexa Fluor 680, Alexa Fluor 700, Alexa Fluor 750, Alexa Fluor 790, Allophycocyanin, AmCyan1, Aminomethylcoumarin, Amplex Gold (product), Amplex Red Reagent, Amplex UltraRed, AsRed2, Auramine O, Azami Green, B-phycoerythrin, BCECF, BO-PRO-1, BO-PRO-3, BOBO-1, BOBO-3, BODIPY-DiMe, BODIPY-Phenyl, BODIPY-TMSCC, BODIPY 630 650-X, BODIPY 650/665-X, BODIPY FL, BODIPY R6G, BODIPY TMR-X, BODIPY TR-X pH 7.0, Bex1, Birch Yellow 580, Blue-green algae, C-Phycocyanin, C3-Indocyanine, C3-Oxacyanine, C3-Thiacyanine, C5-Indocyanine, C5-Oxacyanine, C5-Thiacyanine, C545T, C7-Indocyanine, C7-Oxacyanine, CBQCA, CF405M, CF405S, CF488A, CF543, CF555, CFP, CFSE, CHOxAsH-CCXXCC, CM-H2DCFDA, Calcein, Calcein red-orange, Calcium Crimson, Calcium Green-1, Calcium Orange, Calcofluor white 2MR, Carboxy SNARF-1 pH 6.0, Carboxy SNARF-1 pH 9.0, Carboxynaphthofluorescein, Cascade Blue, Cascade Yellow, Catskill Green 540, CellMask Orange, CellTrace BODIPY TR methyl ester, CellTrace calcein violet, CellTracker Blue, CellTracker Red CMTPX, CellTracker Violet BMQC, Chlorophyll A, Chlorophyll B, Chromeo 488, Chromeo 494, Chromeo 505, Chromeo 546, Chromeo 642, Citrine (Campbell Tsien 2003), ClOH C12 aza-BODIPY, ClOH butoxy aza-BODIPY, Coumarin 1, Coumarin 30, Coumarin 314, Coumarin 334, Coumarin 343, Coumarin 6, Coumarine 545T, Cresyl Violet Perchlorate, CryptoLight CF1, CryptoLight CF2, CryptoLight CF3, CryptoLight CF4, CryptoLight CF5, CryptoLight CF6, Crystal Violet, Cumarin153, Cy2, Cy3.5, Cy3B, Cy3Cy5 ET, Cy3, Cy5.5, Cy5, Cy7, CyQUANT GR, CyTrak Orange, Cyanine3 NHS ester, Cyanine5 NHS ester, Cyanine5 carboxylic acid, CypHer5 pH 9.15, DAF-FM, DAMC, DAPI, DCI, DCM, DDAO, DM-NERF pH 4.0, DOCI, DPP pH-Probe 590-11.0, DPP pH-Probe 590-7.5, DPP pH-Probe 590-9.0, DRAQ5, DY-350XL,

DY-480, DY-485, DY-490XL MegaStokes, DY-490, DY-500, DY-520, DY-547, DY-554, DY-555, DY-557, DY-590, DY-615, DY-630, DY-631, DY-633, DY-635, DY-636, DY-647, DY-649P1, DY-650, DY-651, DY-656, DY-673, DY-675, DY-676, DY-680, DY-681, DY-700, DY-701, DY-730, DY-731, DY-750, DY-751, DY-776, DY-782, Dabcyl SE, Dansyl Glycine (Dioxane), Dapoxyl (2-aminoethyl)sulfonamide, Deep Purple, DiA, DiClOH C12 aza-BODIPY, DiClOHbutoxy aza-BODIPY, DiD, DiI, DiIC18(3), DiO, DiR, Diversa Cyan-FP, Diversa Green-FP, Doxorubicin, Dragon Green, DsRed-Express, DsRed-Express T1, DsRed, DyLight 488, DyLight 549, DyLight 633, DyLight 649, DyLight 680, Dye-1041, Dye-28, Dye-304, Dye-33, Dye-45, E2-Crimson, E2-Orange, E2-Red/Green, EBFP, ECFP, ECF, ECL Plus, EGFP, ELF 97, ER-Tracke Blue-White DPX, EVOblue-30, EYFP, Emerald, Envy Green, Eosin Y, Eosin, EqFP611, Erythrosin-5-isothiocyanate, Ethidium bromide, Ethyl Eosin, Ethyl Nile Blue A, Eu (Soini), Eu(tta)3DEADIT, Eu_2O_3 nanoparticles, EvaGreen, FAD, FITC, FM 1-43, FM 4-64, FM4-64 in CTC, FM4-64 in SDS, FlAsH, FlAsH-CCPGCC, FlAsH-CCXXCC, Flash Red EX, Fluo-3, Fluo-4, Fluo-5F, FluoSpheres blue, FluoSpheres crimson, FluoSpheres dark red, FluoSpheres orange, FluoSpheres red, FluoSpheres yellow-green, Fluorescein, Fluorol 5G, Fort Orange 600, Fura-2 Ca free, Fura Red Ca free, Fura Red, Gadodiamide, Gd-Dtpa-Bma, H9-40, HCS CellMask Deep Red, HCS CellMask Red, HCS LipidTOX Deep Red, HCS LipidTOX Green neutral lipid stain, HCS LipidTOX Green phospholipidosis detection reagent, HCS LipidTOX Red neutral lipid stain, HCS LipidTOX Red phospholipidosis detection reagent, HPTS (pH 2.0), HPTS (pH 1.0), , HPTS (HCl), HPTS (pH 12.0), Haematococcus pluvialis – Flotow, HcRed1, Hemo Red 720, Heteractis magnifica GFP, HiLyte Fluor 488, HiLyte Fluor 555, HiLyte Fluor 647, HiLyte Fluor 680, HiLyte Fluor 750, HiLyte Plus 555, HiLyte Plus 647, HiLyte Plus 750, HmGFP, Hoechst-33258, Hoechst-33258, Hoechst 33258, Hoechst 33342, Hops Yellow 560, IR-775 chloride, IR-806, Indo-1 Ca free, Ir(Cn)2 (acac), Ir(Cs)2 (acac), Ir-OEP-CO-Cl, Isochrysis galbana – Parke, JC-1, JOJO-1, Jonamac Red Evitag T2, Kaede Green, Kaede Red, LDS 751, LIVE DEAD Fixable Aqua Dead Cell Stain, LIVEDEAD Fixable Blue Dead Cell Stain, LIVE DEAD Fixable Far Red Dead Cell Stain, LIVE DEAD Fixable Green Dead Cell Stain, LIVE DEAD Fixable Near-IR Dead Cell Stain, LIVE DEAD Fixable Red Dead Cell Stain, LIVE DEAD Fixable Violet Dead Cell Stain, LOLO-1, Lake Placid 490, Lissamine Rhodamine (Weiss), Lucifer Yellow CH Dilitium salt, Lucifer Yellow CH, Lumio Green, Lumio Red, Lumogen F Orange, Lumogen Red F300, LysoSensor Blue DND-192, LysoSensor Green DND-153, LysoSensor Green DND-153, LysoSensor YellowBlue DND-160, LysoSensor Yellow/Blue DND-160 pH 3, LysoTracker Blue DND-22, LysoTracker Green DND-26, LysoTracker Red DND-99, LysoTracker Yellow HCK-123, Macoun Red Evitag T2, Macrolex Fluorescence Red G, Macrolex Fluorescence Yellow 10GN, Magnesium Green, Magne-

sium Octaethylporphyrin, Magnesium Orange, Magnesium Phthalocyanine, Magnesium Tetramesitylporphyrin, Maple Red-Orange 620, Marina Blue, Merocyanine 540, Methylene Blue, Methyl green, MitoTracker Deep Red 633, MitoTracker Green FM, MitoTracker Orange CMTMRos, MitoTracker Red CMXRos, Monochlorobimane, Monoraphidium, NADH, NBD-X, NIR1, NIR2, NIR3, NIR4, NIR820, N,N-Bis(2,4,6-trimethylphenyl) -3,4:9,10- perylenebis (dicarboximide), Naphthofluorescein, NeuroTrace 500525, Nilblau perchlorate, Nile Blue (EtOH), Nile Red, Nileblue A, Nile red, OHC12 aza-BODIPY, OH butoxy aza-BODIPY, Octaethylporphyrin, Orange Fluorescent Protein, Oregon Green 488 DHPE, Oregon Green 488, Oregon Green 514, Oxazin1, Oxazin 750, Oxazine 170, Oxazine 1, P4-3, PA-GFP (post-activation), PA-GFP (pre-activation), PO-PRO-1, PO-PRO-3, POPO-1, POPO-3, POPOP, PTIR475/UF, PTIR545/UF, Pacific Orange, Palladium(II) meso - tetraphenyl - tetrabenzoporphyrin, PdOEPK, PdTFPP, PerCP-Cy5.5, Perylene Green Tag pH-Probe 720-6.0, Perylene Green pH-Probe 720-5.5, Perylene Orange Tag 550, Perylene Orange pH-Probe 550-2.0, Perylene Red pH-Probe 600-5.5, Perylene, Perylene bisimide pH-Probe 550-5.0, Perylene bisimide pH-Probe 550-5.5, Perylene bisimide pH-Probe 550-6.5, Perylenediimid, Perylne Green pH-Probe 740-5.5, Phaeodactylum tricornutum – Bohlin, Phthalocyanine, PicoGreen dsDNA quantitation reagent, Pinacyanol-Iodide, Piroxicam, Platinum(II) tetraphenyltetrabenzoporphyrin, Plum Purple, Pontamine fast scarlet 4B, Porphin, Pro-Q Diamond, Pro-Q Diamond phosphoprotein gel stain, Pro-Q Emerald, Proflavin, PromoFluor-350, PromoFluor-405, PromoFluor-415, PromoFluor-488LSS, PromoFluor-488 Premium, PromoFluor-488, PromoFluor-500LSS, PromoFluor-505, PromoFluor-510LSS, PromoFluor-514LSS, PromoFluor-520LSS, PromoFluor-532, PromoFluor-546, PromoFluor-555, PromoFluor-590, PromoFluor-610, PromoFluor-633, PromoFluor-647, PromoFluor-670, PromoFluor-680, PromoFluor-700, PromoFluor-750, PromoFluor-770, PromoFluor-780, PromoFluor-840, Protoporphyrin IX, PtOEPK, PtOEP, PtTFPP, QD525, QD565, QD585, QD605, QD655, QD705, QD800, QD903, QD PbS 950, QDot 525, QDot 545, QDot 565, QSY 21, QSY 35, QSY 7, QSY 7, QSY 9, Qdot 585, Qdot 605, Qdot 625, Qdot 655, Qdot 705, Qdot 800, QpyMe2, Quinine sulfate, R-phycoerythrin, ReAsH-CCPGCC, ReAsH-CCXXCC, Red Beads (Weiss), Redmond Red, Resorufin, Rhodamin 700 perchlorate, Rhodamine 101, Rhodamine 123, Rhodamine 6G, Rhodamine 6G, Rhodamine B, Rhodamine Green, Rhodamine Red-X, Rhodamine pH-Probe 585-7.0, Rhodamine pH-Probe 585-7.5, Rhodamine phalloidin, Rhodol Green, Riboflavin, Rose Bengal, SBFI Zero Na, SBFI, SNIR1, SNIR2, SNIR3, SNIR4, SYBR Gold nucleic acid gel stain, SYBR Green I, SYBR Safe DNA gel stain, SYPRO Ruby, SYTO 11, SYTO 13, SYTO 16, SYTO 17, SYTO 45, SYTO 59, SYTO 60, SYTO 61, SYTO 62, SYTO 82, SYTO 9, SYTO RNASelect, SYTOX Blue, SYTOX Green, SYTOX Orange, SYTOX Red, Sapphire, Scenedesmus sp., SeTau-380-NHS, SeTau-647-

NHS, SensiLight PBXL-1, SensiLight PBXL-3, Seta 633-NHS, Snake-Eye Red 900, Sodium Green, Solophenyl flavine 7GFE 500, Spectrum Aqua, Spectrum Blue, Spectrum FRed, Spectrum Gold, Spectrum Green, Spectrum Orange, Spectrum Red, Squarylium dye III, Stains All, Stilben derivate, Styryl8 perchlorate, Sulfo-Cyanine3 NHS ester, Sulfo-Cyanine3 carboxylic acid, Sulfo-Cyanine5 carboxylic acid, Sulforhodamine 101, Sulforhodamine B, Sulforhodamine G, Suncoast Yellow, SuperGlo BFP, SuperGlo GFP, Surf Green EX, Synechocystis sp. PCC 6803, T-Sapphire, TMRE, TO-PRO-1, TO-PRO-3, TOTO-1, TOTO-3, TRITC (Weiss), TRITC Dextran (Weiss), Tb (Soini), Terrylen, Terrylendiimid, Tetra-t-Butylazaporphine, Tetra-t-Butylnaphthalocyanine, Tetracen, Tetramesitylporphyrin, Tetramethylrhodamine, Texas Red, ThiolTracker Violet, Thionin acetate, Topaz, Tris(2,2 -Bipyridyl)Ruthenium(II) chloride, Tris(4,4-diphenyl-2,2-bipyridine)ruthenium(II) chloride, Tris(4,7-diphenyl-1,10-phenanthroline)ruthenium(II) TMS, Vex1, Vybrant DyeCycle Green stain, Vybrant DyeCycle Orange stain, Vybrant DyeCycle Violet stain, WEGFP (post-activation), WellRED D2, WellRED D3, WellRED D4, WtGFP, X-rhod-1, YFP, YO-PRO-1, YO-PRO-3, YOYO-1, YOYO-3, Yakima Yellow, YoYo-1, YoYo-1 dsDNA, YoYo-1 ssDNA, Zinc Octaethylporphyrin, Zinc Phthalocyanine, Zinc Tetramesitylporphyrin, Zinc Tetraphenylporphyrin, ZsYellow1, dTomato, dansyl cadaverine, di-8-ANEPPS, eGFP, epicocconone, ethidium homodimer-1, fluoro-emerald, fura-2, indo-1, kusabira orange, lucifer yellow CH, mBBr, mBanana, mCherry, mHoneyDew, mOrange, mOrange2, mPlum, mRFP1.2, mRFP1, mRFP, mRaspberry, mStrawberry, mTangerine, malachite green isothiocyanate, monobromobimane, nile blue, nile red, pHrodo succinimidyl ester, propidium iodide, quinine, resorufin, rhod-2, rhodamine 110, rhodamine 123, rhodamine, sulforhodamine 101, tCO, tdTomato, tetramethylrhodamine, (CS)2Ir(µ-Cl)2Ir(CS)2, 1-anilinonaphthalene-8-sulfonic acid, 1,1 -Diethyl-4,4 -carbocyanine iodide, 1,2-Diphenylacetylene, 1,6-Diphenylhexatriene, 2-Di-1-ASP, 2-dodecylresorufin, 2 ,7 -Dichlorofluorescein, 3,3-Diethylthiadi-carbocyanine iodide, 4-Dimethylamino-4 -Nitrostilbene, 5(6)-Carboxy-fluorescein, 5(6)-Carboxynaphtofluorescein, 5-(N-hexadecanoyl) aminoeosin, 5-(and-6)-carboxy-2′,7′-dichloro-fluorescein, 5-(and-6)-carboxy-2,7-dichloro-fluorescein, 5-FAM, 5-ROX, 5-TAMRA, 5-chloromethylfluorescein, 6-HEX, 6-JOE, 6-TET, 6-carboxyrhodamine 6G, 6,8-difluoro-7-hydroxy-4-methylcoumarin, 7-Benzylamino-4-Nitrobenz-2-Oxa-1,3-Diazole, 7-aminoactinomycin D, 8-Benzyloxy-5,7-diphenylquinoline (protonated), 9,10-Bis(Phenylethynyl) Anthracene

BIBLIOGRAPHY

[1] Bernard Stewart and Christopher Wild. "World cancer report 2014". In: *World Health Organization* (Dec. 2014) (cit. on pp. 1, 33).

[2] Rafael Lozano et al. "Global and regional mortality from 235 causes of death for 20 age groups in 1990 and 2010: a systematic analysis for the Global Burden of Disease Study 2010". In: *The Lancet* 380.9859 (Dec. 2012), pp. 2095–2128. DOI: 10.1016/S0140-6736(12)61728-0 (cit. on p. 1).

[3] Ralph Weissleder and Mikael J. Pittet. "Imaging in the era of molecular oncology". In: *Nature* 452.7187 (Apr. 2008), pp. 580–589. DOI: 10.1038/nature06917 (cit. on pp. 1, 16).

[4] John V. Frangioni. "New technologies for human cancer imaging". In: *Journal of Clinical Oncology* 26.24 (Aug. 2008), pp. 4012–4021. DOI: 10.1200/JCO.2007.14.3065 (cit. on p. 1).

[5] Alexander L. Vahrmeijer, Merlijn Hutteman, Joost R. van der Vorst, Cornelis J. H. van de Velde, and John V. Frangioni. "Image-guided cancer surgery using near-infrared fluorescence". In: *Nature Reviews Clinical Oncology* 10.9 (July 2013), pp. 507–518. DOI: 10.1038/nrclinonc.2013.123 (cit. on pp. 1, 2, 12, 17, 179).

[6] E. De Boer, N. J. Harlaar, A. Taruttis, W. B. Nagengast, E. L. Rosenthal, V. Ntziachristos, and G. M. Van Dam. "Optical innovations in surgery". In: *British Journal of Surgery* 102.2 (Jan. 2015), e56–72. DOI: 10.1002/bjs.9713 (cit. on pp. 1, 2, 7).

[7] Quyen T. Nguyen, Emilia S. Olson, Todd A. Aguilera, Tao Jiang, Miriam Scadeng, Lesley G. Ellies, and Roger Y. Tsien. "Surgery with molecular fluorescence imaging using activatable cell-penetrating peptides decreases residual cancer and improves survival." In: *Proceedings of the National Academy of Sciences of the United States of America* 107.9 (Mar. 2010), pp. 4317–22. DOI: 10.1073/pnas.0910261107 (cit. on pp. 1, 13).

[8] Iris D. Nagtegaal and Phil Quirke. "What is the role for the circumferential margin in the modern treatment of rectal cancer?" In: *Journal of Clinical Oncology* 26.2 (Jan. 2008), pp. 303–312. DOI: 10.1200/JCO.2007.12.7027 (cit. on p. 1).

[9] Zohar A. Dotan, Kathryn Kavanagh, Ofer Yossepowitch, Matt Kaag, Semra Olgac, Machele Donat, and Harry W. Herr. "Positive Surgical Margins in Soft Tissue Following Radical Cystectomy for Bladder Cancer and Cancer Specific Survival". In:

Journal of Urology 178.6 (Dec. 2007), pp. 2308–2313. DOI: 10.1016/j.juro.2007.08.023 (cit. on p. 1).

[10] S. Eva Singletary. "Surgical margins in patients with early-stage breast cancer treated with breast conservation therapy." In: *American Journal of Surgeryurgery* 184.5 (Nov. 2002), pp. 383–393. DOI: 10.1016/S0002-9610(02)01012-7 (cit. on p. 1).

[11] Nader Sanai and Mitchel S. Berger. "Glioma extent of resection and its impact on patient outcome". In: *Neurosurgery* 62.4 (Apr. 2008), pp. 753–764. DOI: 10.1227/01.neu.0000318159.21731.cf (cit. on pp. 1, 9).

[12] Walter Stummer, Uwe Pichlmeier, Thomas Meinel, Otmar Dieter Wiestler, Friedhelm Zanella, and Hans Jürgen Reulen. "Fluorescence-guided surgery with 5-aminolevulinic acid for resection of malignant glioma: a randomised controlled multicentre phase III trial". In: *Lancet Oncology* 7.5 (May 2006), pp. 392–401. DOI: 10.1016/S1470-2045(06)70665-9 (cit. on pp. 2, 7, 9).

[13] Martin Kriegmair, Reinhold Baumgartner, Ruth Knuchel, Herbert Stepp, Ferdinand Hofstadter, and Alfons Hofstetter. "Detection of Early Bladder Cancer by 5-Aminolevulinic Acid Induced Porphyrin Fluorescence". In: *The Journal of Urology* 155.1 (Jan. 1996), pp. 105–110. DOI: 10.1016/S0022-5347(01)66559-5 (cit. on pp. 2, 7, 10).

[14] Dieter Jocham, Herbert Stepp, and Raphaela Waidelich. "Photodynamic Diagnosis in Urology: State-of-the-Art". In: *European Urology* 53.6 (2008), pp. 1138–1150. DOI: 10.1016/j.eururo.2007.11.048 (cit. on pp. 2, 7, 10).

[15] Suman B. Mondal, Shengkui Gao, Nan Zhu, Rongguang Liang, Viktor Gruev, and Samuel Achilefu. "Real-time fluorescence image-guided oncologic surgery". In: *Advances in Cancer Research* 124 (2014), pp. 171–211. DOI: 10.1016/B978-0-12-411638-2.00005-7 (cit. on pp. 2, 7, 10, 11, 13, 16, 50, 118, 195, 196).

[16] Thea Helene Degett, Helene Schou Andersen, and Ismail Gögenur. "Indocyanine green fluorescence angiography for intraoperative assessment of gastrointestinal anastomotic perfusion: a systematic review of clinical trials". In: *Langenbeck's Archives of Surgery* 401.6 (Sept. 2016), pp. 767–775. DOI: 10.1007/s00423-016-1400-9 (cit. on p. 2).

[17] Eben L. Rosenthal et al. "Successful Translation of Fluorescence Navigation During Oncologic Surgery: A Consensus Report". In: *Journal of Nuclear Medicine* 57.1 (Jan. 2016), pp. 144–150. DOI: 10.2967/jnumed.115.158915 (cit. on p. 2).

[18] Guosong Hong, Alexander L. Antaris, and Hongjie Dai. "Near-infrared fluorophores for biomedical imaging". In: *Nature Biomedical Engineering* 1.1 (Jan. 2017), p. 0010. DOI: 10.1038/s41551-016-0010 (cit. on pp. 2, 10, 12, 42).

[19] Shenglin Luo, Erlong Zhang, Yongping Su, Tianmin Cheng, and Chunmeng Shi. "A review of NIR dyes in cancer targeting and imaging". In: *Biomaterials* 32.29 (2011), pp. 7127–7138. DOI: 10.1016/j.biomaterials.2011.06.024 (cit. on p. 2).

[20] Boudewijn E. Schaafsma, J. Sven D Mieog, Merlijn Hutteman, Joost R. Van Der Vorst, Peter J K Kuppen, Clemens W G M Löwik, John V. Frangioni, Cornelis J H Van De Velde, and Alexander L. Vahrmeijer. "The clinical use of indocyanine green as a near-infrared fluorescent contrast agent for image-guided oncologic surgery". In: *Journal of Surgical Oncology* 104.3 (Sept. 2011), pp. 323–332. DOI: 10.1002/jso.21943 (cit. on pp. 2, 10).

[21] Quyen T. Nguyen and Roger Y. Tsien. "Fluorescence-guided surgery with live molecular navigation — a new cutting edge". In: *Nature Reviews Cancer* 13.9 (Aug. 2013), pp. 653–662. DOI: 10.1038/nrc3566 (cit. on pp. 2, 13, 42).

[22] Gooitzen M van Dam et al. "Intraoperative tumor-specific fluorescence imaging in ovarian cancer by folate receptor-α targeting: first in-human results". In: *Nature Medicine* 17.10 (Oct. 2011), pp. 1315–1319. DOI: 10.1038/nm.2472 (cit. on pp. 2, 3, 11, 18).

[23] Michael A Whitney, Jessica L Crisp, Linda T Nguyen, Beth Friedman, Larry A Gross, Paul Steinbach, Roger Y Tsien, and Quyen T Nguyen. "Fluorescent peptides highlight peripheral nerves during surgery in mice". In: *Nature Biotechnology* 29.4 (Apr. 2011), pp. 352–356. DOI: 10.1038/nbt.1764 (cit. on pp. 2, 3, 13, 14, 42).

[24] Kenneth M. Tichauer, Kimberley S. Samkoe, Kristian J. Sexton, Jason R. Gunn, Tayyaba Hasan, and Brian W. Pogue. "Improved tumor contrast achieved by single time point dual-reporter fluorescence imaging". In: *Journal of Biomedical Optics* 17.6 (June 2012), p. 066001. DOI: 10.1117/1.JBO.17.6.066001 (cit. on pp. 2, 3, 15, 42).

[25] George E. Moore, William T. Peyton, Lyle A. French, and Walter W. Walker. "The Clinical Use of Fluorescein in Neurosurgery". In: *Journal of Neurosurgery* 5.4 (July 1948), pp. 392–398. DOI: 10.3171/jns.1948.5.4.0392 (cit. on pp. 7, 11, 16).

[26] Philip I. Haigh and Armando E. Giuliano. "Intraoperative lymphatic mapping and sentinel lymphadenectomy for breast cancer". In: *Operative Techniques in General Surgery* 2.2 (Sept. 2000), pp. 161–165. DOI: 10.1053/otgn.2000.7063 (cit. on p. 7).

[27] Walter Stummer, Susanne Stocker, Simon Wagner, Herbert Stepp, Clemens Fritsch, Claudia Goetz, Alwin E. Goetz, Rainer Kiefmann, and Hans J. Reulen. "Intraoperative detection of malignant gliomas by 5-aminolevulinic acid- induced porphyrin fluorescence". In: *Neurosurgery* 42.3 (Mar. 1998), pp. 518–526. DOI: 10.1097/00006123-199803000-00017 (cit. on p. 7).

[28] Walter Stummer, Alexander Novotny, Herbert Stepp, Claudia Goetz, Karl Bise, and Hans Jürgen Reulen. "Fluorescence-guided resection of glioblastoma multiforme utilizing 5-ALA-induced porphyrins: a prospective study in 52 consecutive patients". In: *Journal of Neurosurgery* 93.6 (2000), pp. 1003–1013. DOI: 10.3171/jns.2000.93.6.1003 (cit. on p. 7).

[29] Ji Yi and Vadim Backman. "Imaging a full set of optical scattering properties of biological tissue by inverse spectroscopic optical coherence tomography". In: *Optics Letters* 37.21 (Nov. 2012), p. 4443. DOI: 10.1364/OL.37.004443 (cit. on p. 8).

[30] Elena Salomatina, Brian Jiang, John Novak, and Anna N. Yaroslavsky. "Optical properties of normal and cancerous human skin in the visible and near-infrared spectral range". In: *Journal of Biomedical Optics* 11.6 (2006), p. 064026. DOI: 10.1117/1.2398928 (cit. on p. 8).

[31] Steven L Jacques. "Optical properties of biological tissues: a review". In: *Physics in Medicine and Biology* 58.11 (June 2013), R37–R61. DOI: 10.1088/0031-9155/58/11/R37 (cit. on pp. 8, 42).

[32] B. J. Tromberg, O. Coquoz, J. B. Fishkin, T. Pham, E. R. Anderson, J. Butler, M. Cahn, J. D. Gross, V. Venugopalan, and D. Pham. "Non-invasive measurements of breast tissue optical properties using frequency-domain photon migration". In: *Philosophical Transactions of the Royal Society B: Biological Sciences* 352.1354 (June 1997), pp. 661–668. DOI: 10.1098/rstb.1997.0047 (cit. on p. 8).

[33] Dorota B. Jakubowski, Albert E. Cerussi, Frédéric Bevilacqua, Natasha Shah, David Hsiang, John Butler, and Bruce J. Tromberg. "Monitoring neoadjuvant chemotherapy in breast cancer using quantitative diffuse optical spectroscopy: a case study". In: *Journal of Biomedical Optics* 9.1 (2004), p. 230. DOI: 10.1117/1.1629681 (cit. on p. 8).

[34] Te-Yu Tseng, Chun-Yu Chen, Yi-Shan Li, and Kung-Bin Sung. "Quantification of the optical properties of two-layered turbid media by simultaneously analyzing the spectral and spatial information of steady-state diffuse reflectance spectroscopy". In: *Biomedical Optics Express* 2.4 (Apr. 2011), p. 901. DOI: 10.1364/BOE.2.000901 (cit. on p. 8).

[35] Scott Prahl. *Optical Absorption of Hemoglobin*. 1998. URL: http://omlc.ogi.edu/spectra/hemoglobin/ (visited on 10/25/2017) (cit. on p. 8).

[36] George M. Hale and Marvin R. Querry. "Optical Constants of Water in the 200-nm to 200-μm Wavelength Region". In: *Applied Optics* 12.3 (Mar. 1973), p. 555. DOI: 10.1364/AO.12.000555 (cit. on p. 8).

[37] R. L. P. van Veen, H. J. C. M. Sterenborg, A. Pifferi, A. Torricelli, E. Chikoidze, and R. Cubeddu. "Determination of visible near-IR absorption coefficients of mammalian fat using time- and spatially resolved diffuse reflectance and transmission spectroscopy". In: *Journal of Biomedical Optics* 10.5 (2005), p. 054004. DOI: 10.1117/1.2085149 (cit. on p. 8).

[38] Brian W. Pogue, Summer L. Gibbs-Strauss, Pablo A. Valdés, Kimberley S. Samkoe, David W. Roberts, and Keith D. Paulsen. "Review of neurosurgical fluorescence imaging methodologies". In: *IEEE Journal on Selected Topics in Quantum Electronics* 16.3 (May 2010), pp. 493–505. DOI: 10.1109/JSTQE.2009.2034541 (cit. on p. 7).

[39] Ryan K. Orosco, Roger Y. Tsien, and Quyen T. Nguyen. "Fluorescence Imaging in Surgery". In: *IEEE Reviews in Biomedical Engineering* 6 (Jan. 2013), pp. 178–187. DOI: 10.1109/RBME.2013.2240294 (cit. on pp. 7, 10).

[40] Bernard T. Lee, Merlijn Hutteman, Sylvain Gioux, Alan Stockdale, Samuel J. Lin, Long H. Ngo, and John V. Frangioni. "The FLARE Intraoperative Near-Infrared Fluorescence Imaging System: A First-in-Human Clinical Trial in Perforator Flap Breast Reconstruction". In: *Plastic and Reconstructive Surgery* 126.5 (Nov. 2010), pp. 1472–1481. DOI: 10.1097/PRS.0b013e3181f059c7 (cit. on pp. 7, 54, 180, 181).

[41] Stefanie Kudszus, Christian Roesel, Alexander Schachtrupp, and Jörg J. Höer. "Intraoperative laser fluorescence angiography in colorectal surgery: A noninvasive analysis to reduce the rate of anastomotic leakage". In: *Langenbeck's Archives of Surgery* 395.8 (Nov. 2010), pp. 1025–1030. DOI: 10.1007/s00423-010-0699-x (cit. on p. 7).

[42] Seok Hyun Yun and Sheldon J. J. Kwok. "Light in diagnosis, therapy and surgery". In: *Nature Biomedical Engineering* 1 (Jan. 2017), pp. 1–16. DOI: 10.1038/s41551-016-0008 (cit. on pp. 9, 45, 88, 179).

[43] Michael J. Colditz, Karin Van Leyen, and Rosalind L. Jeffree. "Aminolevulinic acid (ALA)-protoporphyrin IX fluorescence guided tumour resection. Part 2: Theoretical, biochemical and practical aspects". In: *Journal of Clinical Neuroscience* 19.12 (2012),

pp. 1611–1616. DOI: 10.1016/j.jocn.2012.03.013 (cit. on p. 9).

[44] Nicholas F. Marko, Robert J. Weil, Jason L. Schroeder, Frederick F. Lang, Dima Suki, and Raymond E. Sawaya. "Extent of resection of glioblastoma revisited: Personalized survival modeling facilitates more accurate survival prediction and supports a maximum-safe-resection approach to surgery". In: *Journal of Clinical Oncology* 32.8 (2014), pp. 774–782. DOI: 10.1200/JCO.2013.51.8886 (cit. on p. 9).

[45] Bruno Montcel, Laurent Mahieu-Williame, Xavier Armoiry, David Meyronet, and Jacques Guyotat. "Two-peaked 5-ALA-induced PpIX fluorescence emission spectrum distinguishes glioblastomas from low grade gliomas and infiltrative component of glioblastomas". In: *Biomedical Optics Express* 4.4 (Apr. 2013), pp. 548–558. DOI: 10.1364/BOE.4.000548 (cit. on pp. 10, 14, 43).

[46] Thomas Filbeck, Uwe Pichlmeier, Ruth Knuechel, Wolf F Wieland, and Wolfgang Roessler. "Clinically relevant improvement of recurrence-free survival with 5-aminolevulinic acid induced fluorescence diagnosis in patients with superficial bladder tumors." In: *The Journal of Urology* 168.1 (July 2002), pp. 67–71. DOI: 10.1016/S0022-5347(05)64833-1 (cit. on p. 10).

[47] W. Loidl, J. Schmidbauer, M. Susani, and M. Marberger. "Flexible Cystoscopy Assisted by Hexaminolevulinate Induced Fluorescence: A New Approach for Bladder Cancer Detection and Surveillance?" In: *European Urology* 47.3 (Mar. 2005), pp. 323–326. DOI: 10.1016/j.eururo.2004.10.025 (cit. on p. 10).

[48] Jarmo T. Alander, Ilkka Kaartinen, Aki Laakso, Tommi Pätilä, Thomas Spillmann, Valery V. Tuchin, Maarit Venermo, and Petri Välisuo. "A Review of Indocyanine Green Fluorescent Imaging in Surgery". In: *International Journal of Biomedical Imaging* 2012 (2012), pp. 1–26. DOI: 10.1155/2012/940585 (cit. on pp. 10, 11, 17).

[49] Ali Majlesara, Mohammad Golriz, Mohammadreza Hafezi, Arash Saffari, Esther Stenau, Lena Maier-Hein, Beat P. Müller-Stich, and Arianeb Mehrabi. "Indocyanine green fluorescence imaging in hepatobiliary surgery". In: *Photodiagnosis and Photodynamic Therapy* 17 (Mar. 2017), pp. 208–215. DOI: 10.1016/j.pdpdt.2016.12.005 (cit. on p. 10).

[50] B Zhu and E M Sevick-Muraca. "A review of performance of near-infrared fluorescence imaging devices used in clinical studies". In: *The British Journal of Radiology* 88 (Jan. 2015), pp. 1–26. DOI: 10.1259/bjr.20140547 (cit. on p. 10).

[51] Susan L. Troyan, Vida Kianzad, Summer L. Gibbs-Strauss, Sylvain Gioux, Aya Matsui, Rafiou Oketokoun, Long Ngo, Ali Khamene, Fred Azar, and John V. Frangioni. "The FLARE™ Intraoperative Near-Infrared Fluorescence Imaging System: A First-in-Human Clinical Trial in Breast Cancer Sentinel Lymph Node Mapping". In: *Annals of Surgical Oncology* 16.10 (2009), pp. 2943–2952. DOI: 10.1245/s10434-009-0594-2 (cit. on pp. 11, 13, 16–18, 57, 58).

[52] Yiping Li, Roberto Rey-Dios, David W. Roberts, Pablo A. Valdés, and Aaron A. Cohen-Gadol. "Intraoperative Fluorescence-Guided Resection of High-Grade Gliomas: A Comparison of the Present Techniques and Evolution of Future Strategies". In: *World Neurosurgery* 82.1-2 (2014), pp. 175–185. DOI: 10.1016/j.wneu.2013.06.014 (cit. on pp. 11, 15).

[53] C. Coles, D. Taggart, B. Choudhary, Y. Abu-Omar, L. Balacumaraswami, and D. Pigott. "The use of a novel imaging technique to evaluate patency of coronary grafts". In: *Anaesthesia* 58.3 (Mar. 2003), pp. 304–308. DOI: 10.1046/j.1365-2044.2003.03093_1.x (cit. on p. 11).

[54] Masao Takahashi, Toshihiro Ishikawa, Koichi Higashidani, and Hiroki Katoh. "SPY: An innovative intra-operative imaging system to evaluate graft patency during off-pump coronary artery bypass grafting". In: *Interactive Cardiovascular and Thoracic Surgery* 3.3 (Sept. 2004), pp. 479–483. DOI: 10.1016/j.icvts.2004.01.018 (cit. on p. 11).

[55] S. Folli, G. Wagnieres, A. Pelegrin, J. M. Calmes, D. Braichotte, F. Buchegger, Y. Chalandon, N. Hardman, C. Heusser, and J. C. Givel. "Immunophotodiagnosis of colon carcinomas in patients injected with fluoresceinated chimeric antibodies against carcinoembryonic antigen." In: *Proceedings of the National Academy of Sciences* 89.17 (Sept. 1992), pp. 7973–7977 (cit. on p. 11).

[56] Aya Matsui, Eiichi Tanaka, Hak Soo Choi, Vida Kianzad, Sylvain Gioux, Stephen J. Lomnes, and John V. Frangioni. "Real-time, near-infrared, fluorescence-guided identification of the ureters using methylene blue". In: *Surgery* 148.1 (July 2010), pp. 78–86. DOI: 10.1016/j.surg.2009.12.003 (cit. on p. 12).

[57] Emilia S. Olson, Tao Jiang, Todd A. Aguilera, Quyen T. Nguyen, Lesley G. Ellies, Miriam Scadeng, and Roger Y. Tsien. "Activatable cell penetrating peptides linked to nanoparticles as dual probes for in vivo fluorescence and MR imaging of proteases." In: *Proceedings of the National Academy of Sciences of the United States of America* 107.9 (Mar. 2010), pp. 4311–4316. DOI: 10.1073/pnas.0910283107 (cit. on p. 13).

[58] Elamprakash N. Savariar, Csilla N. Felsen, Nadia Nashi, Tao Jiang, Lesley G. Ellies, Paul Steinbach, Roger Y. Tsien, and Quyen T. Nguyen. "Real-time in Vivo molecular detection of primary tumors and metastases with ratiometric activatable cell-penetrating peptides". In: *Cancer Research* 73.2 (Jan. 2013), pp. 855–864. DOI: 10.1158/0008-5472.CAN-12-2969 (cit. on p. 13).

[59] Elamprakash N. Savariar, Csilla N. Felsen, Nadia Nashi, Tao Jiang, Lesley G. Ellies, Paul Steinbach, Roger Y. Tsien, and Quyen T. Nguyen. "Real-time in Vivo molecular detection of primary tumors and metastases with ratiometric activatable cell-penetrating peptides". In: *Cancer Research* 73.2 (Jan. 2013), pp. 855–864. DOI: 10.1158/0008-5472.CAN-12-2969 (cit. on p. 13).

[60] Douglas C. Prasher, Virginia K. Eckenrode, William W. Ward, Frank G. Prendergast, and Milton J. Cormier. "Primary structure of the Aequorea victoria green-fluorescent protein". In: *Gene* 111.2 (Feb. 1992), pp. 229–233. DOI: 10.1016/0378-1119(92)90691-H (cit. on p. 13).

[61] Nathan C. Shaner, Robert E. Campbell, Paul A. Steinbach, Ben N. G. Giepmans, Amy E. Palmer, and Roger Y. Tsien. "Improved monomeric red, orange and yellow fluorescent proteins derived from Discosoma sp. red fluorescent protein". In: *Nature Biotechnology* 22.12 (Dec. 2004), pp. 1567–1572. DOI: 10.1038/nbt1037 (cit. on p. 13).

[62] Grigory S Filonov, Kiryl D Piatkevich, Li-Min Ting, Jinghang Zhang, Kami Kim, and Vladislav V Verkhusha. "Bright and stable near-infrared fluorescent protein for in vivo imaging". In: *Nature Biotechnology* 29.8 (July 2011), pp. 757–761. DOI: 10.1038/nbt.1918 (cit. on p. 13).

[63] P. A. Valdés, F. Leblond, A. Kim, B. C. Wilson, K. D. Paulsen, and D. W. Roberts. "A spectrally constrained dual-band normalization technique for protoporphyrin IX quantification in fluorescence-guided surgery". In: *Optics Letters* 37.11 (June 2012), pp. 1817–1819. DOI: 10.1364/OL.37.001817 (cit. on pp. 14, 27, 183).

[64] Pablo A. Valdés, Valerie L. Jacobs, Brian C. Wilson, Frederic Leblond, David W. Roberts, and Keith D. Paulsen. "System and methods for wide-field quantitative fluorescence imaging during neurosurgery". In: *Optics Letters* 38.15 (Aug. 2013), pp. 2786–2788. DOI: 10.1364/OL.38.002786 (cit. on pp. 14, 26, 27).

[65] Pablo A. Valdés, Valerie Jacobs, Brent T. Harris, Brian C. Wilson, Frederic Leblond, Keith D. Paulsen, and David W. Roberts. "Quantitative fluorescence using 5-aminolevulinic acid-induced protoporphyrin IX biomarker as a surgical adjunct in low-grade glioma surgery". In: *Journal of Neurosurgery* 123.3 (2015), pp. 771–780. DOI: 10.3171/2014.12.JNS14391 (cit. on p. 14).

[66] Kristian Sexton, Scott C. Davis, David McClatchy, Pablo A. Valdés, Stephen C. Kanick, Keith D. Paulsen, David W. Roberts, and Brian W. Pogue. "Pulsed-light imaging for fluorescence guided surgery under normal room lighting". In: *Optics Letters* 38.17 (Sept. 2013), pp. 3249–3252. DOI: 10.1364/OL.38.003249 (cit. on pp. 14, 19, 50).

[67] Michael Jermyn et al. "Improved sensitivity to fluorescence for cancer detection in wide-field image-guided neurosurgery". In: *Biomedical Optics Express* 6.12 (2015), pp. 5063–5074. DOI: 10.1364/BOE.6.005063 (cit. on pp. 14, 78).

[68] Walter Stummer, Jörg Christian Tonn, Claudia Goetz, Winfried Ullrich, Herbert Stepp, Andrea Bink, Thorsten Pietsch, and Uwe Pichlmeier. "5-Aminolevulinic acid-derived tumor fluorescence: The diagnostic accuracy of visible fluorescence qualities as corroborated by spectrometry and histology and postoperative imaging". In: *Neurosurgery* 74.3 (Mar. 2014), pp. 310–319. DOI: 10.1227/NEU.0000000000000267 (cit. on p. 14).

[69] Sung K. Chang, Michele Follen, Anais Malpica, Urs Utzinger, Gregg Staerkel, Dennis Cox, E. Neely Atkinson, Calum MacAulay, and Rebecca Richards-Kortum. "Optimal excitation wavelengths for discrimination of cervical neoplasia". In: *IEEE Transactions on Biomedical Engineering* 49.10 (2002), pp. 1102–1111. DOI: 10.1109/TBME.2002.803597 (cit. on pp. 15, 25).

[70] Juan Benavides, Sung Chang, Sun Park, Rebecca Richards-Kortum, Nick Mackinnon, Calum Macaulay, Andrea Milbourne, Anais Malpica, and Michele Follen. "Multispectral digital colposcopy for in vivo detection of cervical cancer." In: *Optics Express* 11.10 (May 2003), pp. 1223–1236. DOI: 10.1364/OE.11.001223 (cit. on pp. 15, 25, 53, 182, 183).

[71] Timothy E. Renkoski, Kenneth D. Hatch, and Urs Utzinger. "Wide-field spectral imaging of human ovary autofluorescence and oncologic diagnosis via previously collected probe data". In: *Journal of Biomedical Optics* 17.3 (2012), pp. 1–13. DOI: 10.1117/1.JBO.17.3.036003 (cit. on pp. 15, 25, 26, 182).

[72] Nathan Hagen and Michael W. Kudenov. "Review of snapshot spectral imaging technologies". In: *Optical Engineering* 52.9 (Sept. 2013), pp. 1–23. DOI: 10.1117/1.OE.52.9.090901 (cit. on pp. 15, 20, 23, 55, 176).

[73] Guolan Lu and Baowei Fei. "Medical hyperspectral imaging: a review". In: *Journal of Biomedical Optics* 19.1 (2014), pp. 1–23. DOI: 10.1117/1.JBO.19.1.010901 (cit. on pp. 15, 20).

[74] Alisha V. DSouza, Huiyun Lin, Eric R. Henderson, Kimberley S. Samkoe, and Brian W. Pogue. "Review of fluorescence guided surgery systems: identification of key performance capabilities beyond indocyanine green imaging". In: *Journal of Biomedical Optics* 21.8 (2016), pp. 1–15. DOI: 10.1117/1.JBO.21.8.080901 (cit. on pp. 17, 42, 44, 46, 49, 50, 80, 81, 86–88, 133, 172, 178).

[75] Chongwei Chi, Yang Du, Jinzuo Ye, Deqiang Kou, Jingdan Qiu, Jiandong Wang, Jie Tian, and Xiaoyuan Chen. "Intraoperative imaging-guided cancer surgery: From current fluorescence molecular imaging methods to future multi-modality imaging technology". In: *Theranostics* 4.11 (2014), pp. 1072–1084. DOI: 10.7150/thno.9899 (cit. on p. 17).

[76] Yang Liu, Adam Q. Bauer, Walter J. Akers, Gail Sudlow, Kexian Liang, Duanwen Shen, Mikhail Y. Berezin, Joseph P. Culver, and Samuel Achilefu. "Hands-free, wireless goggles for near-infrared fluorescence and real-time image-guided surgery". In: *Surgery* 149.5 (2011), pp. 689–698. DOI: 10.1016/j.surg.2011.02.007 (cit. on p. 17).

[77] Yang Liu, Walter J. Akers, Adam Q. Bauer, Suman Mondal, Kyle Gullicksrud, Gail P. Sudlow, Joseph P. Culver, and Samuel Achilefu. "Intraoperative detection of liver tumors aided by a fluorescence goggle system and multimodal imaging". In: *The Analyst* 138.8 (2013), pp. 2254–2557. DOI: 10.1039/c3an00165b (cit. on p. 17).

[78] Yang Liu, Raphael Njuguna, Thomas Matthews, Walter J. Akers, Gail P. Sudlow, Suman Mondal, Rui Tang, Viktor Gruev, and Samuel Achilefu. "Near-infrared fluorescence goggle system with complementary metal–oxide–semiconductor imaging sensor and see-through display". In: *Journal of Biomedical Optics* 18.10 (May 2013), pp. 1–7. DOI: 10.1117/1.JBO.18.10.101303 (cit. on p. 17).

[79] Jeffrey R. Watson, Christian F. Gainer, Nikolay Martirosyan, Jesse Skoch, G. Michael Lemole, Rein Anton, and Marek Romanowski. "Augmented microscopy: real-time overlay of bright-field and near-infrared fluorescence images". In: *Journal of Biomedical Optics* 20.10 (2015), pp. 1–9. DOI: 10.1117/1.JBO.20.10.106002 (cit. on p. 17).

[80] Christina R. Vargas, John T. Nguyen, Yoshitomo Ashitate, Joseph Angelo, Vivek Venugopal, Frank Kettenring, Florin Neacsu, John V. Frangioni, Sylvain Gioux, and Bernard T. Lee. "Intraoperative Hemifacial Composite Flap Perfusion Assessment

Using Spatial Frequency Domain Imaging". In: *Annals of Plastic Surgery* 76.2 (Feb. 2016), pp. 249–255. DOI: 10.1097/SAP.0000000000000631 (cit. on p. 17).

[81] Akira Nakayama, Federica Del Monte, Roger J. Hajjar, and John V. Frangioni. "Functional near-infrared fluorescence imaging for cardiac surgery and targeted gene therapy". In: *Molecular Imaging* 1.4 (2002), pp. 365–377. DOI: 10.1162/15353500200221333 (cit. on p. 18).

[82] Merlijn Hutteman, Joost R. van der Vorst, Katja N. Gaarenstroom, Alexander A.W. Peters, J. Sven D Mieog, Boudewijn E. Schaafsma, Clemens W.G.M. Löwik, John V. Frangioni, Cornelis J.H. van de Velde, and Alexander L. Vahrmeijer. "Optimization of near-infrared fluorescent sentinel lymph node mapping for vulvar cancer". In: *American Journal of Obstetrics and Gynecology* 206.1 (Jan. 2012), 89.e1–89.e5. DOI: 10.1016/j.ajog.2011.07.039 (cit. on p. 18).

[83] George Themelis, Jung Sun Yoo, Kwang-Sup Soh, Ralf Schulz, and Vasilis Ntziachristos. "Real-time intraoperative fluorescence imaging system using light-absorption correction". In: *Journal of Biomedical Optics* 14.6 (2009), pp. 1–9. DOI: 10.1117/1.3259362 (cit. on p. 18).

[84] Daniel C. Gray, Evgenia M. Kim, Victoria E. Cotero, Anshika Bajaj, V. Paul Staudinger, Cristina A. Tan Hehir, and Siavash Yazdanfar. "Dual-mode laparoscopic fluorescence image-guided surgery using a single camera". In: *Biomedical Optics Express* 3.8 (Aug. 2012), p. 1880. DOI: 10.1364/BOE.3.001880 (cit. on pp. 18, 179).

[85] John Fengler, Paul Westwick, Arthur E. Bailey, and Paul Cottle. "Imaging System for combined full-color reflectance and near-infrared imaging". Patent US 2011/0063427. Mar. 2009 (cit. on pp. 19, 179).

[86] Banghe Zhu, John C. Rasmussen, and Eva M. Sevick-Muraca. "Non-invasive fluorescence imaging under ambient light conditions using a modulated ICCD and laser diode". In: *Biomedical Optics Express* 5.2 (2014), pp. 562–572. DOI: 10.1364/BOE.5.000562 (cit. on pp. 19, 50).

[87] Zhenyue Chen, Nan Zhu, Shaun Pacheco, Xia Wang, and Rongguang Liang. "Single camera imaging system for color and near-infrared fluorescence image guided surgery". In: *Biomedical Optics Express* 5.8 (2014), pp. 2791–2797. DOI: 10.1364/BOE.5.002791 (cit. on pp. 19, 24).

[88] Mihaela Antonina Calin, Sorin Viorel Parasca, Dan Savastru, and Dragos Manea. "Hyperspectral imaging in the medical field: Present and future". In: *Applied Spectroscopy Reviews* 49.6

(Aug. 2014), pp. 435–447. DOI: 10.1080/05704928.2013.838678 (cit. on p. 20).

[89] Liang Gao, Robert T. Kester, Nathan Hagen, and Tomasz S. Tkaczyk. "Snapshot Image Mapping Spectrometer (IMS) with high sampling density for hyperspectral microscopy". In: *Optics Express* 18.14 (2010), pp. 14330–14344. DOI: 10.1364/OE.18.014330 (cit. on p. 21).

[90] Robert T Kester, Liang Gao, and Tomasz S Tkaczyk. "Development of image mappers for hyperspectral biomedical imaging applications". In: *Applied Optics* 49.10 (Apr. 2010), pp. 1886–1899. DOI: 10.1364/AO.49.001886 (cit. on p. 21).

[91] Robert T. Kester, Noah Bedard, Liang Gao, and Tomasz S. Tkaczyk. "Real-time snapshot hyperspectral imaging endoscope". In: *Journal of Biomedical Optics* 16.5 (2011), pp. 1–12. DOI: 10.1117/1.3574756 (cit. on p. 21).

[92] Zeno Lavagnino, Jason Dwight, Alessandro Ustione, Thuc Uyen Nguyen, Tomasz S. Tkaczyk, and David W. Piston. "Snapshot Hyperspectral Light-Sheet Imaging of Signal Transduction in Live Pancreatic Islets". In: *Biophysical Journal* 111.2 (2016), pp. 409–417. DOI: 10.1016/j.bpj.2016.06.014 (cit. on p. 21).

[93] Hoong-Ta Lim and Vadakke Matham Murukeshan. "A four-dimensional snapshot hyperspectral video-endoscope for bio-imaging applications". In: *Scientific Reports* 6 (Apr. 2016), pp. 1–10. DOI: 10.1038/srep24044 (cit. on pp. 22, 182).

[94] Jason G. Dwight and Tomasz S. Tkaczyk. "Lenslet array tunable snapshot imaging spectrometer (LATIS) for hyperspectral fluorescence microscopy". In: *Biomedical Optics Express* 8.3 (Mar. 2017), p. 1950. DOI: 10.1364/BOE.8.001950 (cit. on p. 22).

[95] William R. Johnson, Daniel W. Wilson, Wolfgang Fink, Mark Humayun, and Greg Bearman. "Snapshot hyperspectral imaging in ophthalmology". In: *Journal of Biomedical Optics* 12.1 (2007), pp. 1–7. DOI: 10.1117/1.2434950 (cit. on p. 22).

[96] Christy Fernandez Cull, Kerkil Choi, David J. Brady, and Tim Oliver. "Identification of fluorescent beads using a coded aperture snapshot spectral imager". In: *Applied Optics* 49.10 (Apr. 2010), B59–B70. DOI: 10.1364/AO.49.000B59 (cit. on p. 23).

[97] Joel Kaluzny, Hao Li, Wenzhong Liu, Peter Nesper, Justin Park, Hao F. Zhang, and Amani A. Fawzi. "Bayer Filter Snapshot Hyperspectral Fundus Camera for Human Retinal Imaging". In: *Current Eye Research* 42.4 (2017), pp. 629–635. DOI: 10.1080/02713683.2016.1221976 (cit. on pp. 24, 57).

[98] Hao Li, Wenzhong Liu, Biqin Dong, Joel V. Kaluzny, Amani A. Fawzi, and Hao F. Zhang. "Snapshot hyperspectral retinal imaging using compact spectral resolving detector array". In: *Journal of Biophotonics* 10.6 (2017), pp. 830–839. DOI: 10.1002/jbio.201600053 (cit. on p. 24).

[99] Scott A. Mathews. "Design and fabrication of a low-cost, multispectral imaging system". In: *Applied Optics* 47.28 (Oct. 2008), F71–F76. DOI: 10.1364/AO.47.000F71 (cit. on p. 24).

[100] Ali Basiri, Marjan Nabili, Scott Mathews, Alex Libin, Suzanne Groah, Herke J. Noordmans, and Jessica C. Ramella-Roman. "Use of a multi-spectral camera in the characterization of skin wounds". In: *Optics Express* 18.4 (2010), pp. 3244–3257. DOI: 10.1364/OE.18.003244 (cit. on p. 24).

[101] Jessica C. Ramella-Roman and Scott A. Mathews. "Spectroscopic measurements of oxygen saturation in the retina". In: *IEEE Journal on Selected Topics in Quantum Electronics* 13.6 (2007), pp. 1697–1703. DOI: 10.1109/JSTQE.2007.911312 (cit. on p. 24).

[102] Andres F. Zuluaga, Urs Utzinger, Anthony Durkin, Fuchs Holger, Ann Gillenwater, Rhonda Jacob, Bonnie Kemp, James Fan, and Rebecca Richards-Kortum. "Fluorescence Excitation Emission Matrices of Human Tissue: A System for in Vivo Measurement and Method of Data Analysis". In: *Applied Spectroscopy* 53.3 (1999), pp. 302–311 (cit. on p. 25).

[103] Daron G. Ferris, Raymond A. Lawhead, Eileen D. Dickman, Nina Holtzapple, Jill A. Miller, Stephanie Grogan, Shabbir Bambot, Anant Agrawal, and Mark L. Faupel. "Multimodal hyperspectral imaging for the noninvasive diagnosis of cervical neoplasia". In: *Journal of Lower Genital Tract Disease* 5.2 (2001), pp. 65–72. DOI: 10.1046/j.1526-0976.2001.005002065.x (cit. on p. 25).

[104] Steven C. Gebhart, Reid C. Thompson, and Anita Mahadevan-Jansen. "Liquid-crystal tunable filter spectral imaging for brain tumor demarcation". In: *Applied Optics* 46.10 (2007), pp. 1896–1910. DOI: 10.1364/AO.46.001896 (cit. on pp. 27, 53, 183).

[105] Brian S. Sorg, Benjamin J. Moeller, Owen Donovan, Yiting Cao, and Mark W. Dewhirst. "Hyperspectral imaging of hemoglobin saturation in tumor microvasculature and tumor hypoxia development". In: *Journal of Biomedical Optics* 10.4 (2005), pp. 1–11. DOI: 10.1117/1.2003369 (cit. on pp. 27, 183).

[106] Kinshuk Mitra, James Melvin, Shufang Chang, Kyoungjin Park, Alper Yilmaz, Scott Melvin, and Ronald X. Xu. "Indocyanine-green-loaded microballoons for biliary imaging in cholecystec-

tomy". In: *Journal of Biomedical Optics* 17.11 (Nov. 2012), pp. 1–8. DOI: 10.1117/1.JBO.17.11.116025 (cit. on pp. 27, 183).

[107] Pablo A. Valdés, Frederic Leblond, Valerie L. Jacobs, Brian C. Wilson, Keith D. Paulsen, and David W. Roberts. "Quantitative, spectrally-resolved intraoperative fluorescence imaging". In: *Scientific Reports* 2 (Nov. 2012), pp. 1–7. DOI: 10.1038/srep00798 (cit. on pp. 27, 43, 45, 46, 53, 121).

[108] Pablo A. Valdés, Anthony Kim, Marco Brantsch, Carolyn Niu, Ziev B. Moses, Tor D. Tosteson, Brian C. Wilson, Keith D. Paulsen, David W. Roberts, and Brent T. Harris. "δ-aminolevulinic acid-induced protoporphyrin IX concentration correlates with histopathologic markers of malignancy in human gliomas: The need for quantitative fluorescence-guided resection to identify regions of increasing malignancy". In: *Neuro-Oncology* 13.8 (Aug. 2011), pp. 846–856. DOI: 10.1093/neuonc/nor086 (cit. on p. 27).

[109] Pablo A. Valdés et al. "Quantitative fluorescence in intracranial tumor: implications for ALA-induced PpIX as an intraoperative biomarker". In: *Journal of Neurosurgery* 115.1 (July 2011), pp. 11–17. DOI: 10.3171/2011.2.JNS101451 (cit. on p. 27).

[110] Arjen Amelink, Dominic J. Robinson, and Henricus J. C. M. Sterenborg. "Confidence intervals on fit parameters derived from optical reflectance spectroscopy measurements". In: *Journal of Biomedical Optics* 13.5 (2008), pp. 1–14. DOI: 10.1117/1.2982523 (cit. on p. 27).

[111] Thomas Arnold, Martin De Biasio, and Raimund Leitner. "High-sensitivity hyper-spectral video endoscopy system for intra-surgical tissue classification". In: *Proceedings of IEEE Sensors* (2010), pp. 2612–2615. DOI: 10.1109/ICSENS.2010.5690205 (cit. on pp. 27, 28, 53, 183).

[112] Seong G. Kong, Matthew Martin, and Tuan Vo-Dinh. "Hyperspectral Fluorescence Imaging for Mouse Skin Tumor Detection". In: *ETRI Journal* 28.6 (Dec. 2006), pp. 770–776. DOI: 10.4218/etrij.06.0106.0061 (cit. on pp. 27, 28, 53, 183).

[113] Matt E. Martin, Musundi Wabuyele, Masoud Panjehpour, Bergein Overholt, Robert Denovo, Steve Kennel, Glenn Cunningham, and Tuan Vo-Dinh. "An AOTF-based dual-modality hyperspectral imaging system (DMHSI) capable of simultaneous fluorescence and reflectance imaging". In: *Medical Engineering and Physics* 28.2 (Mar. 2006), pp. 149–155. DOI: 10.1016/j.medengphy.2005.04.022 (cit. on pp. 27, 28, 183).

[114] Raimund Leitner, Martin De Biasio, Thomas Arnold, Cuong Viet Dinh, Marco Loog, and Robert P.W. Duin. "Multi-spectral video endoscopy system for the detection of cancerous tissue".

In: *Pattern Recognition Letters* 34.1 (Jan. 2013), pp. 85–93. DOI: 10.1016/j.patrec.2012.07.020 (cit. on pp. 27, 28, 53, 183).

[115] Paul Constantinou, Trudey Nicklee, David W. Hedley, Savvas Damaskinos, and Brian C. Wilson. "A high-resolution MACROscope with differential phase contrast, transmitted light, confocal fluorescence, and hyperspectral capabilities for large-area tissue imaging". In: *IEEE Journal on Selected Topics in Quantum Electronics* 11.4 (July 2005), pp. 766–777. DOI: 10.1109/JSTQE.2005.857708 (cit. on pp. 28, 180).

[116] Abhinav Kumar, Sonal Saxena, Sameer Shrivastava, Vandana Bharti, Upendra Kumar, and Kuldeep Dhama. "Hyperspectral imaging (HSI): applications in animal and dairy sector". In: *Journal of Experimental Biology and Agricultural Sciences* 4.4 (June 2016), pp. 448–461. DOI: 10.18006/2016.4(4).448.461 (cit. on p. 29).

[117] Eivind L. P. Larsen, Lise L. Randeberg, Elisabeth Olstad, Olav A. Haugen, Astrid Aksnes, and Lars O. Svaasand. "Hyperspectral imaging of atherosclerotic plaques in vitro". In: *Journal of Biomedical Optics* 16.2 (2011), pp. 1–11. DOI: 10.1117/1.3540657 (cit. on pp. 29, 181).

[118] Bahram Khoobehi, James M. Beach, and Hiroyuki Kawano. "Hyperspectral Imaging for Measurement of Oxygen Saturation in the Optic Nerve Head". In: *Investigative Ophthalmology & Visual Science* 45.5 (May 2004), pp. 1464–1472. DOI: 10.1167/iovs.03-1069 (cit. on pp. 30, 181).

[119] Bahram Khoobehi, Jinfeng Ning, Elise Puissegur, Kimberly Bordeaux, Madhusudhanan Balasubramanian, and James Beach. "Retinal oxygen saturation evaluation by multi-spectral fundus imaging". In: *Proc. SPIE 6511, Medical Imaging 2007: Physiology, Function, and Structure from Medical Images, 65110B (March 29, 2007)*. Ed. by Armando Manduca and Xiaoping P. Hu. Vol. 6511. Mar. 2007, 65110B. DOI: 10.1117/12.710030 (cit. on p. 30).

[120] Anna Siri Luthman, Sebastian Dumitru, Isabel Quiros-Gonzalez, James Joseph, and Sarah E. Bohndiek. "Fluorescence hyperspectral imaging (fHSI) using a spectrally resolved detector array". In: *Journal of Biophotonics* 10.6-7 (2017), pp. 840–853. DOI: 10.1002/jbio.201600304 (cit. on pp. 30, 181).

[121] Cameron M. Lee, Christoph J. Engelbrecht, Timothy D. Soper, Fritjof Helmchen, and Eric J. Seibel. "Scanning fiber endoscopy with highly flexible, 1 mm catheterscopes for wide-field, full-color imaging". In: *Journal of Biophotonics* 3.5-6 (Mar. 2010), pp. 385–407 (cit. on pp. 30, 31).

[122] David L. MacAdam. "Visual Sensitivities to Color Differences in Daylight". In: *Journal of the Optical Society of America* 32.5 (May 1942), pp. 247–274. DOI: 10.1364/JOSA.32.000247 (cit. on p. 35).

[123] Gaurav Sharma. *Digital color imaging handbook*. CRC Press LLC, 2003 (cit. on pp. 36, 76, 99, 100, 103, 110, 111).

[124] Andrew M. Smith, Michael C. Mancini, and Shuming Nie. "Bioimaging: Second window for in vivo imaging". In: *Nature Nanotechnology* 4.11 (Nov. 2009), pp. 710–711. DOI: 10.1038/nnano.2009.326 (cit. on p. 42).

[125] Kenneth M. Tichauer, Kimberley S. Samkoe, Jason R. Gunn, Stephen C. Kanick, P. Jack Hoopes, Richard J. Barth, Peter A. Kaufman, Tayyaba Hasan, and Brian W. Pogue. "Microscopic lymph node tumor burden quantified by macroscopic dual-tracer molecular imaging". In: *Nature Medicine* 20.11 (Oct. 2014), pp. 1348–1353. DOI: 10.1038/nm.3732 (cit. on pp. 42, 46).

[126] Richard A. Neher, Mišo Mitkovski, Frank Kirchhoff, Erwin Neher, Fabian J. Theis, and André Zeug. "Blind Source Separation Techniques for the Decomposition of Multiply Labeled Fluorescence Images". In: *Biophysical Journal* 96.9 (May 2009), pp. 3791–3800. DOI: 10.1016/j.bpj.2008.10.068 (cit. on p. 43).

[127] Farzad Fereidouni, Arjen N. Bader, and Hans C. Gerritsen. "Spectral phasor analysis allows rapid and reliable unmixing of fluorescence microscopy spectral images". In: *Optics Express* 20.12 (2012), pp. 12729–12741. DOI: 10.1364/OE.20.012729 (cit. on pp. 43, 197).

[128] Hideki Shirakawa and Shunichi Miyazaki. "Blind spectral decomposition of single-cell fluorescence by parallel factor analysis." In: *Biophysical Journal* 86.3 (Mar. 2004), pp. 1739–52. DOI: 10.1016/S0006-3495(04)74242-3 (cit. on p. 43).

[129] Ivica Kopriva, Antun Peršin, Neira Puizina-Ivić, and Lina Mirić. "Robust demarcation of basal cell carcinoma by dependent component analysis-based segmentation of multi-spectral fluorescence images". In: *Journal of Photochemistry and Photobiology B: Biology* 100.1 (2010), pp. 10–18. DOI: 10.1016/j.jphotobiol.2010.03.013 (cit. on p. 43).

[130] Richard A. Neher and Erwin Neher. "Optimizing imaging parameters for the separation of multiple labels in a fluorescence image". In: *Journal of Microscopy* 213.1 (2004), pp. 46–62. DOI: 10.1111/j.1365-2818.2004.01262.x (cit. on pp. 44, 155).

[131] Michael Dobosz, Vasilis Ntziachristos, Werner Scheuer, and Steffen Strobel. "Multispectral Fluorescence Ultramicroscopy: Three-Dimensional Visualization and Automatic Quantification of Tumor Morphology, Drug Penetration, and Antiangiogenic Treatment Response". In: *Neoplasia* 16.1 (Jan. 2014), pp. 1–13. DOI: 10.1593/neo.131848 (cit. on p. 45).

[132] Eben L. Rosenthal, Jason M. Warram, Kirby I. Bland, and Kurt R. Zinn. "The Status of Contemporary Image-Guided Modalities in Oncologic Surgery". In: *Annals of Surgery* 261.1 (2015), pp. 46–55. DOI: 10.1097/SLA.0000000000000622 (cit. on pp. 45, 46).

[133] Jonathan T.C. Liu, Mike W. Helms, Michael J. Mandella, James M. Crawford, Gordon S. Kino, and Christopher H. Contag. "Quantifying cell-surface biomarker expression in thick tissues with ratiometric three-dimensional microscopy". In: *Biophysical Journal* 96.6 (Mar. 2009), pp. 2405–2414. DOI: 10.1016/j.bpj.2008.12.3908 (cit. on p. 46).

[134] Yang Yang, Jun Ming, and Nenghai Yu. "Color image quality assessment based on CIEDE2000". In: *Advances in Multimedia* 2012 (2012), pp. 1–6. DOI: 10.1155/2012/273723 (cit. on pp. 47, 114).

[135] Jaques Marescaux and Francesco Rubino. "Transcontinental robot-assisted remote telesurgery, feasibility and potential applications". In: *Teleophthalmology* 235.4 (Apr. 2006), pp. 261–265. DOI: 10.1007/3-540-33714-8_31 (cit. on p. 47).

[136] Asli Kumcu, Lotte Vermeulen, Shirley A. Elprama, Pieter Duysburgh, Ljiljana Platiša, Yves Van Nieuwenhove, Nele Van De Winkel, An Jacobs, Jan Van Looy, and Wilfried Philips. "Effect of video lag on laparoscopic surgery: correlation between performance and usability at low latencies". In: *The International Journal of Medical Robotics and Computer Assisted Surgery* 13.2 (June 2016), pp. 1–10. DOI: 10.1002/rcs.1758 (cit. on pp. 47, 48).

[137] T. Kim, P. M. Zimmerman, M. J. Wade, and C. A. Weiss. "The effect of delayed visual feedback on telerobotic surgery". In: *Surgical Endoscopy and Other Interventional Techniques* 19.5 (May 2005), pp. 683–686. DOI: 10.1007/s00464-004-8926-6 (cit. on p. 47).

[138] Mitchell J.H. Lum, Jacob Rosen, Hawkeye King, Diana C.W. Friedman, Thomas S. Lendvay, Andrew S. Wright, Mika N. Sinanan, and Blake Hannaford. "Teleoperation in surgical robotics - Network latency effects on surgical performance". In: *Proceedings of the 31st Annual International Conference of the IEEE Engineering in Medicine and Biology Society: Engineering the Fu-*

ture of Biomedicine, EMBC 2009 (2009), pp. 6860–6863. DOI: 10.1109/IEMBS.2009.5333120 (cit. on p. 47).

[139] M. Perez, F. Quiaios, P. Andrivon, D. Husson, M. Dufaut, J. Felblinger, and J. Hubert. "Paradigms and experimental set-up for the determination of the acceptable delay in Telesurgery". In: *Annual International Conference of the IEEE Engineering in Medicine and Biology - Proceedings* (2007), pp. 453–456. DOI: 10.1109/IEMBS.2007.4352321 (cit. on p. 47).

[140] Kajal T. Claypool and Mark Claypool. "On frame rate and player performance in first person shooter games". In: *Multimedia Systems* 13.1 (2007), pp. 3–17. DOI: 10.1007/s00530-007-0081-1 (cit. on pp. 47, 48).

[141] R. Rayman, K. Croome, N. Galbraith, R. McClure, R. Morady, S. Peterson, S. Smith, V. Subotic, A. Van Wynsberghe, and S. Primak. "Long-distance robotic telesurgery: A feasibility study for care in remote environments". In: *International Journal of Medical Robotics and Computer Assisted Surgery* 2.3 (Sept. 2006), pp. 216–224. DOI: 10.1002/rcs.99 (cit. on p. 47).

[142] Manuela Perez, Song Xu, Sanket Chauhan, Alyssa Tanaka, Khara Simpson, Haidar Abdul-Muhsin, and Roger Smith. "Impact of delay on telesurgical performance: study on the robotic simulator dV-Trainer". In: *International Journal of Computer Assisted Radiology and Surgery* 11.4 (Apr. 2016), pp. 581–587. DOI: 10.1007/s11548-015-1306-y (cit. on p. 47).

[143] Bing Wu, Sung Hun Sim, Andinet Enquobahrie, and Ricardo Ortiz. "Effects of visual latency on visual-haptic experience of stiffness". In: *2015 Seventh International Workshop on Quality of Multimedia Experience (QoMEX)*. IEEE, May 2015, pp. 1–6. DOI: 10.1109/QoMEX.2015.7148129 (cit. on pp. 47, 48).

[144] Mary C. Potter, Brad Wyble, Carl Erick Hagmann, and Emily S. McCourt. "Detecting meaning in RSVP at 13 ms per picture". In: *Attention, Perception, & Psychophysics* 76.2 (Feb. 2014), pp. 270–279. DOI: 10.3758/s13414-013-0605-z (cit. on pp. 47, 48).

[145] George B. Hanna, Sami M. Shimi, and Alfred Cuschieri. "Task Performance in Endoscopic Surgery Is Influenced by Location of the Image Display". In: *Annals of Surgery* 227.4 (Apr. 1998), pp. 481–484. DOI: 10.1097/00000658-199804000-00005 (cit. on p. 49).

[146] Carl Zeiss Meditec AG. *OPMI PENTERO 900 von ZEISS - Die nächste Generation*. Tech. rep. Carl Zeiss Meditec AG, 2015, pp. 1–7 (cit. on pp. 49, 51).

[147] *Stay Focused with with Leica M530 OH6*. Tech. rep. Heerbrugg: Leica Microsystems (Schweiz) AG, 2015, pp. 1–4 (cit. on p. 49).

[148] W. Fleischer. "Erste Hilfe für das Herzstück". In: *Deutsches Ärzteblatt* 109 (50).50 (2012), pp. 2555–2556 (cit. on p. 50).

[149] Thomas Busse. *OP-Management: Grundlagen*. 4th ed. medhochzwei, 2010, pp. 1–243 (cit. on p. 50).

[150] A. Guirao, C. González, M. Redondo, E. Geraghty, S. Norrby, and P. Artal. "Average optical performance of the human eye as a function of age in a normal population." In: *Investigative Ophthalmology & Visual Science* 40.1 (Jan. 1999), pp. 203–213 (cit. on p. 50).

[151] Pablo Artal and Rafael Navarro. "Monochromatic modulation transfer function of the human eye for different pupil diameters: an analytical expression". In: *Journal of the Optical Society of America A* 11.1 (1994), pp. 246–249. DOI: 10.1364/JOSAA.11.000246 (cit. on p. 50).

[152] Carl Zeiss Meditec AG. *OPMI PENTERO 900 from ZEISS - Integrated Video Solutions*. URL: https://www.zeiss.com/meditec/int/products/neurosurgery/surgical-microscopes/opmi-pentero-900.html (visited on 02/24/2017) (cit. on p. 51).

[153] Leica Microscystems. *Intra-operative fluorescence-guided tumor resection in oncology - 400 nm/blue Leica FL400*. URL: http://www.leica-microsystems.com/products/surgical-microscopes/neurosurgery-spine/details/product/leica-fl400/ (visited on 02/24/2017) (cit. on p. 51).

[154] Olympus Europa SE & CO. KG. *Endoskopiesystem VISERA 4K UHD bietet Chirurgen vier Mal höhere Auflösung*. 2015 (cit. on p. 51).

[155] Olympus Europa SE & CO. KG. *Olympus Europa - Visera 4k UHD*. 2017. URL: www.olympus.eu/4k (visited on 02/24/2017) (cit. on p. 51).

[156] Sven T.S. Holmström, Utku Baran, and Hakan Urey. "MEMS laser scanners: A review". In: *Journal of Microelectromechanical Systems* 23.2 (2014), pp. 259–275. DOI: 10.1109/JMEMS.2013.2295470 (cit. on pp. 54, 180).

[157] Erek S. Barhoum, Richard S. Johnston, and Eric J. Seibel. "Optical modeling of an ultrathin scanning fiber endoscope, a preliminary study of confocal versus non-confocal detection". In: *Optics Express* 13.19 (2005), pp. 7548–7562. DOI: 10.1364/OPEX.13.007548 (cit. on p. 54).

[158] Bahadir K. Gunturk, John Glotzbach, Yucel Altunbasak, Ronald W. Schafer, and Russell M. Mersereau. "Demosaicking: Color filter array interpolation". In: *IEEE Signal Processing Magazine* 22.1 (Jan. 2005), pp. 44–54. DOI: 10.1109/MSP.2005.1407714 (cit. on p. 57).

[159] Glen C. Gerhard. "A multispectral image sensor array". In: *Proceedings of the IEEE* 59.12 (1971), p. 1718. DOI: 10.1109/PROC.1971.8535 (cit. on p. 58).

[160] A. Rogalski, J. Antoszewski, and L. Faraone. "Third-generation infrared photodetector arrays". In: *Journal of Applied Physics* 105.9 (2009), pp. 1–45. DOI: 10.1063/1.3099572 (cit. on p. 58).

[161] X. C. Sun, J. J. Hu, C. Y. Hong, J. F. Viens, X. M. Duan, R. Das, A. M. Agarwal, and L. C. Kimerling. "Multispectral pixel performance using a one-dimensional photonic crystal design". In: *Applied Physics Letters* 89 (Nov. 2006), pp. 1–3. DOI: 10.1063/1.2400069 (cit. on p. 58).

[162] Pascale Parrein, Norbert Moussy, Ludovic Poupinet, and Pierre Gidon. "Multilayer structure for a spectral imaging sensor". In: *Applied Optics* 48.3 (Jan. 2009), pp. 653–657. DOI: 10.1364/AO.48.000653 (cit. on p. 58).

[163] P. Mitra, F. C. Case, J. H. McCurdy, S. A. Zaidel, and L. T. Claiborne. "Multispectral long-wavelength quantum-well infrared photodetectors". In: *Applied Physics Letters* 82.19 (May 2003), pp. 3185–3187. DOI: 10.1063/1.1573354 (cit. on p. 58).

[164] Antonio Longoni, Federico Zaraga, Giacomo Langfelder, and Langfelfer Bombelli. "The transverse field detector (TFD): A novel color-sensitive CMOS device". In: *IEEE Electron Device Letters* 29.12 (Dec. 2008), pp. 1306–1308. DOI: 10.1109/LED.2008.2006284 (cit. on p. 58).

[165] Jianfei Wang, Juejun Hu, Xiaochen Sun, Anu Agarwal, and Lionel C Kimerling. "Cavity-enhanced multispectral photodetector using phase-tuned propagation: Theory and design". In: *Optics Letters* 35.5 (Mar. 2010), pp. 742–744. DOI: 10.1364/OL.35.000742 (cit. on p. 58).

[166] Nikolas Dimitriadis, Bartłomiej Grychtol, Lars Maertins, Tobias Behr, George Themelis, and Nikolaos C. Deliolanis. "Simultaneous real-time multicomponent fluorescence and reflectance imaging method for fluorescence-guided surgery". In: *Optics Letters* 41.6 (2016), p. 1173. DOI: 10.1364/OL.41.001173 (cit. on pp. 61, 87–89, 99, 116, 121, 122, 125, 170).

[167] Nikolas Dimitriadis, Bartłomiej Grychtol, Martin Theuring, and Nikolaos C. Deliolanis. "Spectral and Temporal Multiplexing for Multispectral Fluorescence and Reflectance Imaging using two Color Sensors". In: *Optics Express* 25.11 (May 2017), pp. 12812–12829. DOI: 10.1364/OE.25.012812 (cit. on pp. 61, 76, 81, 89–91, 96, 99, 116, 117, 119, 121, 123, 124, 133, 137, 139, 144, 148, 149, 153).

[168] Nikolas Dimitriadis and Nikolaos Deliolanis. "Methods And Means For Multispectral Imaging". Patent WO 2015/185661. Dec. 2015 (cit. on p. 61).

[169] Nikolas Dimitriadis and Nikolaos Deliolanis. "Methods And Means For Multispectral Imaging". Patent WO 2015/185662. Dec. 2015 (cit. on p. 61).

[170] Jonathan T. Elliott, Alisha V. Dsouza, Scott C. Davis, Jonathan D. Olson, Keith D. Paulsen, David W. Roberts, and Brian W. Pogue. "Review of fluorescence guided surgery visualization and overlay techniques". In: *Biomedical Optics Express* 6.10 (2015), p. 3765. DOI: 10.1364/BOE.6.003765 (cit. on pp. 72, 174).

[171] PCO AG. *Data Sheet pco. edge 5.5*. Tech. rep. 2017, pp. 1–10 (cit. on pp. 76, 91, 141–143, 197).

[172] *Color Camera Sensor Review Q2 2016*. Tech. rep. Point Grey, 2016, pp. 1–11 (cit. on p. 76).

[173] Robert Luther. "Aus dem Gebiet der Farbreizmetrik". In: *Zeitschrift für technische Physik* (1927), pp. 540–558 (cit. on pp. 76, 99, 100, 103).

[174] Eric R. Fossum et al. *Multi-frame correspondence estimation using subspace constraints*. Ed. by Junichi Nakamura. Optical Science and Engineering. CRC Press, 2006 (cit. on pp. 76, 99, 100, 103, 105, 142).

[175] Tobias Behr. "Entwicklung der optischen Strahlführung eines Doppelkamerasystems für die multispektrale klinische Fluoreszenzbildgebung". MA thesis. Karlsruher Institut für Technologie, 2015 (cit. on pp. 85, 127, 128, 131–133).

[176] Hamamatsu. *Light Source*. Tech. rep. 2014, pp. 1–23 (cit. on p. 86).

[177] Schott. *Machine Vision System solutions for Machine Vision lighting*. Tech. rep., pp. 1–12 (cit. on p. 86).

[178] Omicron Laserage Laserprodukte GmbH. *LedHUB - Multicolor LED Light Engine with up to six TEC-cooled LED Modules*. Tech. rep. 2016, pp. 1–2 (cit. on p. 88).

[179] CoolLED. *pE-4000*. Tech. rep. 2017, p. 1 (cit. on p. 88).

[180] Lumencore. *SPECTRA X light engine*. Tech. rep. 2015, pp. 1–2 (cit. on p. 88).

[181] Semrock Inc. *Semrock Homepage*. 2017. URL: https://www.semrock.com/ (visited on 03/02/2017) (cit. on p. 90).

[182] *Database of Fluorescent Dyes, Properties and Applications*. URL: http://www.fluorophores.tugraz.at/ (visited on 03/22/2017) (cit. on p. 95).

[183] Phil Green and Lindsay MacDonald. *Colour Engineering: Achieving Device Independent Colour*. John Wiley & Sons, 2002 (cit. on pp. 98, 99).

[184] Guowei Hong, M. Ronnier Luo, and Peter A. Rhodes. "A study of digital camera colorimetric characterization based on polynomial modeling". In: *Color Research & Application* 26.1 (2001), pp. 76–84. DOI: 10.1002/1520-6378(200102)26:1<76::AID-COL8>3.0.CO;2-3 (cit. on pp. 98, 110).

[185] Vien Cheung, Stephen Westland, David Connah, and Caterina Ripamonti. "A comparative study of the characterisation of colour cameras by means of neural networks and polynomial transforms". In: *Coloration Technology* 120.1 (2004), pp. 19–25. DOI: 10.1111/j.1478-4408.2004.tb00201.x (cit. on pp. 98, 110).

[186] T. Smith and J. Guild. "The C.I.E. colorimetric standards and their use". In: *Transactions of the Optical Society* 33.3 (Jan. 1932), pp. 73–134. DOI: 10.1088/1475-4878/33/3/301 (cit. on p. 100).

[187] Arthur D. Broadbent. "A critical review of the development of the CIE1931 RGB color-matching functions". In: *Color Research and Application* 29.4 (2004), pp. 267–272. DOI: 10.1002/col.20020 (cit. on p. 100).

[188] Christine Fernandez-Maloigne, ed. *Advanced Color Image Processing and Analysis*. Springer, 2013, pp. 1–515. DOI: 10.1007/978-1-4419-6190-7 (cit. on pp. 100, 105, 110).

[189] Jun Jiang, Dengyu Liu, Jinwei Gu, and Sabine Susstrunk. "What is the space of spectral sensitivity functions for digital color cameras?" In: *Proceedings of IEEE Workshop on Applications of Computer Vision* (Jan. 2013), pp. 168–179. DOI: 10.1109/WACV.2013.6475015 (cit. on pp. 102, 109, 114).

[190] M. R. Luo, G. Cui, and B. Rigg. "The development of the CIE 2000 colour-difference formula: CIEDE2000". In: *Color Research and Application* 26.5 (2001), pp. 340–350. DOI: 10.1002/col.1049 (cit. on p. 104).

[191] Jouni Hiltunen. *Munsell colors matt (spectrofotometer measured)*. URL: http://www.uef.fi/web/spectral/munsell-colors-matt-spectrofotometer-measured (visited on 04/03/2017) (cit. on p. 105).

[192] CIE - International Commission on Illumination. *Selected Colorimetric Tables*. 2017. (Visited on 04/03/2017) (cit. on pp. 105, 111).

[193] Jussi Kinnunen. *Artificial lights*. 2007. URL: http://www.uef.fi/web/spectral/artificial-lights (visited on 09/26/2017) (cit. on p. 105).

[194] Javier Vazquez-Corral, David Connah, and Marcelo Bertalmío. "Perceptual Color Characterization of Cameras". In: *Sensors* 14.12 (Dec. 2014), pp. 23205–23229. DOI: 10.3390/s141223205 (cit. on pp. 109, 114).

[195] Junfei Shen, Huihui Wang, Yisi Wu, An Li, Chi Chen, and Zhenrong Zheng. "Surgical lighting with contrast enhancement based on spectral reflectance comparison and entropy analysis". In: *Journal of Biomedical Optics* 20.10 (Oct. 2015), pp. 1–7. DOI: 10.1117/1.JBO.20.10.105012 (cit. on p. 110).

[196] Huihui Wang, Raymond H. Cuijpers, Ming Ronnier Luo, Ingrid Heynderickx, and Zhenrong Zheng. "Optimal illumination for local contrast enhancement based on the human visual system". In: *Journal of Biomedical Optics* 20.1 (2015), pp. 1–8. DOI: 10.1117/1.JBO.20.1.015005 (cit. on p. 110).

[197] Junfei Shen, Shengqian Chang, Huihui Wang, and Zhenrong Zheng. "Optimal illumination for visual enhancement based on color entropy evaluation". In: *Optics Express* 24.17 (Aug. 2016), pp. 19788–19000. DOI: 10.1364/OE.24.019788 (cit. on p. 110).

[198] Richard T. Bryan, Lucinda J. Billingham, and D. M A Wallace. "Narrow-band imaging flexible cystoscopy in the detection of recurrent urothelial cancer of the bladder". In: *BJU International* 101.6 (Mar. 2008), pp. 702–705. DOI: 10.1111/j.1464-410X.2007.07317.x (cit. on p. 110).

[199] CIE. *Colorimetry - part 2: CIE standard illuminants CIE S 014-2/E:2008 (ISO 11664-2:2007)*. Tech. rep. International Organization for Standardization, 2007, pp. 1–14 (cit. on p. 111).

[200] European Machine Vision Association. *EMVA Standard 1288 Standard - Standard for Characterization of Image Sensors and Cameras*. Tech. rep. 2016, pp. 1–39 (cit. on pp. 118, 140–143, 194–197).

[201] Leica Microsystems. *Leica Zoom Systems - Technical Information*. Tech. rep. 2013, pp. 1–16 (cit. on pp. 129, 133, 134).

[202] Egbert Buhr, Susanne Guenther-Kohfahl, and Ulrich Neitzel. "Simple method for modulation transfer function determination of digital imaging detectors from edge images". In: *Medical Imaging 2003: Physics of Medical Imaging, 877*. Ed. by Martin J. Yaffe and Larry E. Antonuk. San Diego, June 2003, pp. 877–884. DOI: 10.1117/12.479990 (cit. on p. 131).

[203] Bernd Jähne and Martin Schwarzbauer. "Noise equalisation and quasi loss-less image data compression - Or how many bits needs an image sensor?" In: *Technisches Messen* 83.1 (Jan. 2016), pp. 16–24. DOI: 10.1515/teme-2015-0093 (cit. on pp. 141, 194).

[204] Bernd Jähne. *Digital Image Processing*. 6th ed. Springer Science & Business Media, 2005, pp. 1–607. DOI: 10.1007/3-540-27563-0 (cit. on pp. 142, 143, 196).

[205] Roger J. Barlow. *Statistics: A Guide to the Use of Statistical Methods in the Physical Sciences*. John Wiley & Sons, 2008 (cit. on pp. 146, 192, 197).

[206] Paolo de Leva. *Multiple matrix multiplications, with array expansion enabled*. URL: https://de.mathworks.com/matlabcentral/fileexchange/8773 (cit. on p. 147).

[207] Allen Rush and Paul Hubel. "X3 sensor characteristics". In: *The Society of Photographic Science and Technology of Japan* 66.1 (2003), pp. 57–60. DOI: 10.11454/photogrst1964.66.57 (cit. on pp. 171, 176).

[208] Sony Corporation. *Sony Develops the Industry's First 3-Layer Stacked CMOS Image Sensor with DRAM for Smartphones*. Tech. rep. Sony Semiconductor Solutions, 2017 (cit. on p. 176).

[209] Sony Corporation. *Sony Releases a High-Speed Vision Sensor that Makes Detection and Tracking of Objects at 1,000 fps Possible*. 2017. URL: https://www.sony.net/SonyInfo/News/Press/201705/17-051E/index.html (visited on 06/26/2016) (cit. on p. 176).

[210] Sony Semiconductor Solutions Corporation. *Roadmap*. Tech. rep. 2017, pp. 1–7 (cit. on p. 182).

[211] Paul Fieguth. *Statistical Image Processing and Multidimensional Modeling*. Information Science and Statistics. Springer, Nov. 2011, pp. 1–465. DOI: 10.1007/978-1-4419-7294-1 (cit. on p. 192).

[212] Dennis D Boos. "Introduction to the Bootstrap World". In: *Statistical Science* 18.2 (May 2003), pp. 168–174. DOI: 10.1214/ss/1063994971 (cit. on p. 194).

ACKNOWLEDGEMENTS

First and most importantly, I would like to express my gratitude to Prof. Dr. Marcus Motzkus for supervising my thesis. He inspired me by asking questions and at the same time supported me to keep focused. After discussing with him, I always felt eager to answer all the new research questions. I feel very lucky to benefit from his supervision.

Moreover, I would like to thank Prof. Dr. Bernd Jähne for his effort to referee this thesis as well as Prof. Dr. Joerg Jaeckel and Prof. Dr. Selim Jochim for their work as examiners of the committee.

The daily lab-work for this thesis took place within the Fraunhofer research team centered around Dr. Nikolaos Deliolanis in Mannheim. Special thanks go to him for supervising the thesis, sending me to conferences and supporting publications. Furthermore, many thanks go to all my colleagues, especially Bartłomiej Grychtol and Martin Theuring for their input and all our fruitful discussions. Additionally, I want to acknowledge the Fraunhofer Society for providing the research budget for this work.

Besides, I want to thank Tobias Behr for the great time and his commitment to write a Master's thesis under my supervision. Also, I would like to thank all the students that supported me during my PhD, espeically Vaibhav Dixit, Christian Heblich and Christian Sippel.

In addition, my thanks go to all the proofreaders suffering from all my mistakes: Kristin Grußmayer, Nina Bernges, Sabrina Schubert, David Puga and Timo Dimitriadis.

Finally, I would like to thank all my friends and family for supporting me during the PhD time.